



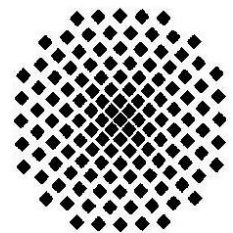
Max-Planck-Institut für Festkörperforschung
Stuttgart

New Ternary and Quaternary Metal Oxides of Ruthenium and Osmium

Kailash M. Mogare

Dissertation an der Universität Stuttgart

Stuttgart, 2006



New Ternary and Quaternary Metal Oxides of Ruthenium and Osmium

Von der Fakultät Chemie der Universität Stuttgart
zur Erlangung der Würde eines Doktors der Naturwissenschaften
(Dr. rer. nat.) genehmigte Abhandlung

Vorgelegt von

Kailash M. Mogare

aus Dahivali, Indien

Hauptberichter:	Prof. Dr. Dr. h. c. Martin Jansen
Mitberichter:	Prof. Dr. Thomas Schleid
Mitprüfer und Prüfungsvorsitzender:	Prof. Dr. Helmut Bertagnolli
Tag der mündlichen Prüfung:	17 th August 2006

Max-Planck-Institut für Festkörperforschung, Stuttgart
Universität Stuttgart
2006

**Dedicated to
my uncle (Late) Madhav kaka, parents and
family members**

Table of Contents

1 Introduction	5
2 General	9
2.1 Synthesis under high oxygen pressure in autoclaves	9
2.1.1 Thermodynamic view and pressure regulation of solid state synthesis under high oxygen pressure.....	9
2.1.2 Schematic of the oxygen high pressure autoclave.....	11
2.1.3 Investigatory procedure	12
2.2 Working under inert atmosphere	13
2.2.1 Vacuum and inert gas glass apparatus.....	13
2.2.2 Glove box.....	15
2.3 Piston cylinder press	15
2.4 Physical properties.....	16
2.4.1 X-ray diffraction methods.....	16
Powder X-ray diffraction	16
Single crystal diffraction	17
2.4.2 Neutron diffraction	18
2.4.3 Energy Dispersive X-ray Spectrometry (EDX)	18
2.4.4 Raman and infrared spectroscopy	19
2.4.5 Thermal analysis methods, DTA / TG / MS and DSC	19
2.4.6 Magnetic susceptibility measurements.....	19
2.4.7 Conductivity measurements.....	20
3 Alkali metal ruthenates	21
3.1 Na ₂ RuO ₄ , Sodium oxo-ruthenate (VI)	22
3.1.1 Synthesis	22
3.1.2 Thermal analysis.....	22
3.1.3 Raman and infrared spectroscopy	23
3.1.4 X-ray diffraction.....	24
3.1.5 Structure description.....	26
3.1.6 Magnetic measurements	29
3.1.7 Neutron diffraction studies	30
3.2 K ₂ RuO ₄ and Rb ₂ RuO ₄	37
3.2.1 Synthesis	37
3.2.2 X-ray diffraction.....	37
3.2.3 Magnetic measurements	37
3.3 K ₃ Na(RuO ₄) ₂ and Rb ₃ Na(RuO ₄) ₂ , Ruthenium Glaserites.....	40
3.3.1 Synthesis	40
3.3.2 Thermal analysis.....	41
3.3.3 Raman spectroscopy	41
3.3.4 X-ray diffraction.....	42
3.3.5 Structure description.....	45
3.3.6 Magnetic measurements	55
3.3.7 Conductivity measurements.....	56
3.4 Magnetism in hexavalent alkali oxo-ruthenates	57
3.5 Na ₂ RuO ₃ , Sodium oxo-ruthenate (IV)	58
3.5.1 Synthesis	58
3.5.2 Infrared spectroscopy	58

3.5.3 X-ray diffraction	58
3.5.4 Structure description	60
3.5.5 Magnetic measurements	62
3.5.6 Conductivity measurements	62
4 Alkali metal osmates	63
4.1 K_2OsO_5 , Potassium osmate(VIII).....	64
4.1.1 Synthesis.....	64
4.1.2 Thermal analysis	64
4.1.3 Raman and infrared spectroscopy	65
4.1.4 X-ray diffraction	66
4.1.5 Structure description	68
4.1.6 Magnetic measurements	72
4.1.7 Conductivity measurements	72
4.2 $K_2NaOsO_{5.5}$, a double perovskite	73
4.2.1 Synthesis.....	73
4.2.2 Thermal analysis	73
4.2.3 Raman and infrared spectroscopy	74
4.2.4 X-ray diffraction	74
4.2.5 Structure description	76
4.2.6 Magnetic measurements	78
4.2.7 Conductivity measurements	78
4.3 Na_3OsO_5 , Sodium osmate(VII)	79
4.3.1 Synthesis.....	79
4.3.2 Thermal analysis	80
4.3.3 Raman spectroscopy.....	80
4.3.4 X-ray diffraction	80
4.3.5 Structure description	82
4.3.6 Magnetic measurements	86
4.4 $CsOsO_4$, Cesium osmate(VII)	87
4.4.1 Synthesis.....	87
4.4.2 Thermal analysis	87
4.4.3 Raman spectroscopy.....	87
4.4.4 X-ray diffraction	88
4.4.5 Structure description	90
4.4.6 Magnetic measurements	94
4.5 $K_3NaOs_2O_9$, a triple perovskite	95
4.5.1 Synthesis.....	95
4.5.2 Thermal analysis	95
4.5.3 Raman spectroscopy.....	95
4.5.4 X-ray diffraction	96
4.5.5 Structure description	98
4.5.6 Magnetic measurements	100
4.5.7 Conductivity measurements	101
5 Double perovskite	102
5.1 Sr_2CrOsO_6	102
5.1.1 Synthesis.....	102
5.1.2 Thermal analysis	103
5.1.3 Raman spectroscopy.....	103
5.1.4 X-ray diffraction, neutron diffraction and crystal structure	104

5.1.5 Magnetic measurements	106
Summary	109
Zusammenfassung	115
Outlook.....	121
List of Figures	123
List of Tables.....	126
List of Abbreviations	128
References	129
Appendix	137
Acknowledgements	142
List of Publications	144

1 Introduction

Solid state chemistry is the study of synthesis, structure, mechanical, electronic, magnetic and optical properties of materials in the solid state, and also includes their reactivity in the crystalline, amorphous and glassy state.

A large number of inorganic solids are non-molecular and their crystal structure is determined by the manner in which the atoms or ions are packed together in three dimensions. The knowledge of the crystal structure of any material is indispensable in order to study its chemical, physical and electronic properties. The inorganic solid state compounds display a variety of complex structure types (such as pyrochlore, scheelite, perovskite etc). These structure types exhibit interesting properties ranging from semi-conducting to metallic to even superconducting one. Most of the compounds contain defects of some kind which influence their properties such as electrical conductivity and chemical reactivity [1,2].

Among all the structure types, the compounds crystallising in the perovskite type structure are almost the ones which are most studied as they exhibit diverse electronic properties. A simple cubic perovskite ABO_3 ($SrTiO_3$) consists of a twelve-fold coordinated large A cation and a relatively smaller sized B cation coordinated to 6 oxygen atoms. An ordered double perovskite $A_2BB'O_6$ is formed when the substitution occurs at the site of the B cation resulting in the 1:1 ordering of the cations. The symmetry of the simple ABO_3 perovskite or a double perovskite can be estimated using the Goldschmidt's tolerance factor (t) [3] based on Shannon's ionic radii [4]. When t is equal to unity the structure is cubic and when t is between 0.8 to 1, a variety of structures with lower symmetry are possible. Thus, the factor helps in knowing the symmetry a particular perovskite oxide may adopt. It also helps to select the appropriate alkali/alkaline earth metals to stabilise unusual and possibly a new high oxidation state. Almost any element in the periodic table can be incorporated into the perovskite lattice.

The perovskite structure type is adopted by many oxides and has plenty of technological applications such as ferroelectrics, sensors and superconductors. In the late 1980's and during the 1990's perovskites have attracted a lot of attention because of their ability to support superconductivity above the boiling point of liquid nitrogen (77 K). In the beginning of 1990's rare earth manganese oxides displayed magnetic phase transition close to room temperature accompanied by a metal-to-insulator transition [5-7]. This

process results in a huge or better known as “colossal”, magnetoresistance in the case of manganites. The discovery of $\text{Sr}_2\text{FeMoO}_6$ [8], an ordered double perovskite displaying magnetoresistance above room temperature and a Curie temperature of around 415 K, has triggered a lot of activities in exploring new double perovskites. $\text{Sr}_2\text{FeMoO}_6$ shows a pronounced negative CMR at lower magnetic fields and higher temperatures, compared to the doped manganites. This has aroused a great interest in looking for new perovskite materials displaying Giant-Magneto-Resistance (GMR) around room temperature. Very recently, another new ferromagnetic semiconductor, $\text{La}_2\text{NiMnO}_6$, which displays magnetoresistance near to room temperature, was reported [9]. The search for new perovskite type oxides is continued to explore new materials exhibiting a variety of magnetic and electronic properties, ionic conductivity, ferroelectricity and spintronics (spin-polarized electronics). Spintronics is a new emerging technology which combines electronics and magnetics through manipulation of electron spins. This technology offers the potential for non volatile memories, faster data processing speeds and large storage capacity, which is not possible with conventional semiconductor devices. Also majority of catalysts used in modern chemical industries are based on perovskite type mixed metal oxides [10].

All elements in the periodic table have certain unique properties and thus the course is continued ahead in the sea of these elements looking for new materials by aiming to extend the boundaries of the known compounds in their reduced, mixed valent and highly oxidised states. The oxidation state of a metal plays a crucial role in designing a particular property of any material.

In solid state chemistry most reactions are carried out in solid state at elevated temperatures. By combining various elements in different compositions a number of mixed valent as well as unusual high oxidised compounds are discovered till now. Amongst these, the mixed valent transition metal oxides containing Cu(II)/Cu(III) displayed superconductivity [11]. A number of new high and unusual oxidation state compounds have been explored, mostly as fluorides such as, Cs_2KAgF_6 containing trivalent silver (Ag^{3+}) [12], Au^{5+} in fluoro complexes, Cu^{4+} in Cs_2CuF_6 [13]. In solutions, high oxidation states have been stabilised by using oxidising (potassium persulphate, H_2O_2 , HBr , O_3) or complexing substances, or by electrochemical oxidation [14]. In the area of oxide materials, a number of high oxidation state compounds have been explored, especially of iridium under high pressure by Demazeau and co-workers [15,16]. A recent review is also

reported concerning the coordination of iridium in oxo-iridate compounds [17]. However, this area of high oxidation state compounds, stabilised as their oxides, still remains to be explored to a fuller extent.

The perovskite lattice is favoured to stabilise highly oxidised compounds mainly due to two reasons. Firstly, the electronic configuration fits well in the local site of octahedral symmetry, and secondly, the corresponding electronic configuration formed would be isotropic [18]. However, in some cases no stabilisation can take place as the octahedral site is not appropriate to the anisotropic electronic configuration or the size of cations does not fit, so this structure type is not realised. Various factors and problems involved in the stabilisation of oxidation states are reviewed and discussed in the literature [19].

One goal of this work was to synthesise high oxidation state compounds, especially, looking for those containing a 5d transition metal. Transition metal oxides constitute an interesting class of materials. Due to the presence of valence d-orbitals, there is a strong tendency of these metals to lose electrons easily. The 5d transition elements have high crystal field energy and low ionisation energy in comparison to the 3d and 4d transition elements. Thus, these elements show a higher tendency to form new high oxidation state compounds. The higher the oxidation state of metal the shorter is its bond with the ligand (oxygen). This results to an increase in the covalent character of these bonds giving rise to more pronounced super-exchange interactions. These high oxidation state compounds would open a new door in the quest of materials exhibiting a variety of phenomena such as ferroelectricity, ferromagnetism and superconductivity. To serve this purpose, the monovalent alkali metals and the divalent alkaline earth metals are best suited to stabilise high oxidation states of a particular transition metal.

The challenge of stabilising elements in high oxidation is of great importance in chemistry and also from the applied point of view. The high oxidation state compounds are often unstable and thus great efforts are being taken to promote and enhance the stability of such compounds. Different methods are in use such as the traditional ones in the solid state chemistry, starting with the calcination of nitrates or carbonates of the respective alkali/alkaline earth metal and heating them at high temperatures with intermittent grindings. This process involves several steps with long reaction times to obtain a pure compound. Another method is the use of hydroxide flux-growth technique based on the Lux-Flood acid-base concept [20,21] which has come out to be highly appropriate to

stabilise and produce high quality crystals of high oxidation state compounds. Another method implied in this work is starting with the pure oxides and/or peroxides of alkali and alkaline earth metals. The starting materials are allowed to react under oxygen pressure in autoclaves, at varying temperatures and pressures. Firstly, the advantage of using oxides is in avoiding unwanted elements (such as C, N and H) in the final phase. Secondly, these starting materials are powerful oxidants at relatively low temperatures to attain the desirable high oxidation state. Also, these elements are more electropositive in character giving good stabilising environment of higher oxidation state for the neighbouring cation. Other synthetic routes have also been used in carrying out the reactions such as reactions under oxygen flow, in sealed quartz ampoules and also in a piston cylinder apparatus.

In this work, the investigation of ternary and quaternary systems of alkali metal ruthenates and alkali metal osmates is described. Attempts have been made to look for new perovskite type oxides and to achieve high and unusual oxidation states for ruthenium and osmium. However, a number of new compounds with different structures have been found for both the elements, along with some double and triple perovskites in the case of osmium. Besides the alkali metal systems, one more double perovskite has been re-investigated which displays robust ferromagnetism. The various compounds explored are discussed in the respective chapters based on the hierarchy of the oxidation states of the respective group VIII metal.

2 General

2.1 Synthesis under high oxygen pressure in autoclaves

To ensure acceptable reaction times in solid state chemistry, the experiments have to be performed at higher temperatures. However, with reactions of oxides and/or peroxides of alkali and alkaline earth metals along with the heavier transition metals (in particular noble metals) at such higher temperatures, one has to prevent the decomposition of these thermally unstable compounds. Thus, an oxygen pressure higher than the partial pressure above the respective oxides has to be applied.

2.1.1 Thermodynamic view and pressure regulation of solid state synthesis under high oxygen pressure

For the simplification of the thermodynamic considerations the activity is equated with the concentration of oxygen. The thermal decomposition of an oxide can be given by the following reaction



The equilibrium constant K of this decomposition reaction is obtained from the Law of mass action, using the concentration c_j the component j :

$$K = \frac{c(M)^x c(O_2)^{\frac{y}{2}}}{c(M_xO_y)} \quad (2.2)$$

The situation of the heterogeneous equilibrium exclusively depends on the oxygen partial pressure above the thermally decomposed oxide, and therefore follows

$$K = p(O_2)^{\frac{y}{2}} \quad (2.3)$$

The temperature dependence of the equilibrium constants of the decomposition reaction is described by van't Hoff's reaction isochore. The change in the internal energy is calculated as

$$\left(\frac{\delta \ln K}{\delta T} \right) = \frac{\Delta U}{RT^2} \quad (2.4)$$

The internal energy U is approximately constant over a relatively large range of temperature, therefore, by integration with C as integration constant a linear correlation between $\ln K$ and $1/T$ can be written as

$$\ln K = -\left(\frac{\Delta U}{R}\right)\frac{1}{T} + c \quad (2.5)$$

The $\ln K$ to $y/2 \ln p(\text{O}_2)$ is equivalent for a linear temperature rise and, the oxygen partial pressure above an oxide increases exponentially.

In first approximation the dominant pressure in autoclaves can be determined by the van der Waals equation

$$p = \frac{nRT}{V_{\text{eff}} - nb} - \frac{n^2 a}{V_{\text{eff}}^2} \quad (2.6)$$

p Pressure in bars

V_{eff} Effective autoclave volume ($2 \times 10^{-5} \text{ m}^3$)

n Number of moles

R Gas constant ($8.314 \text{ J mol}^{-1} \text{ K}^{-1}$)

T Temperature in K

a, b Van der Waals constants for O_2 [22] : $a = 1.378 \text{ bar L}^2 \text{ mol}^{-2}$, $b = 0.03183 \text{ L mol}^{-1}$

The molecular quantity of condensed oxygen is calculated by the volume of liquid oxygen using the following equation

$$n = \frac{\rho V}{M} \quad (2.7)$$

ρ Density of O_2 at 77 K ($1.20 \times 10^3 \text{ kg m}^{-3}$) [22]

V Condensed volume of oxygen in m^3

M Molecular mass of O_2 ($31.99 \times 10^{-3} \text{ kg mol}^{-1}$)

A diagram illustrating the dependence of the autoclave internal pressure on temperature and condensed volume of oxygen is shown in Figure 2-1.

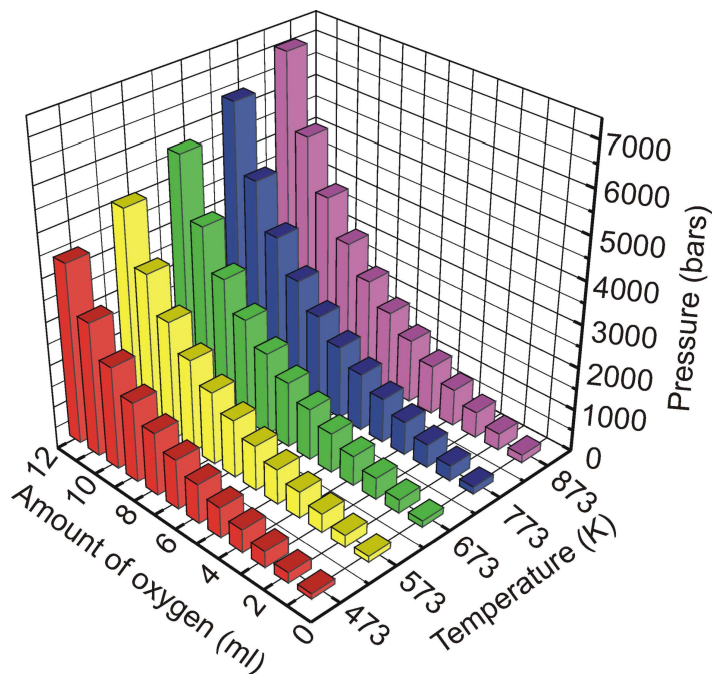
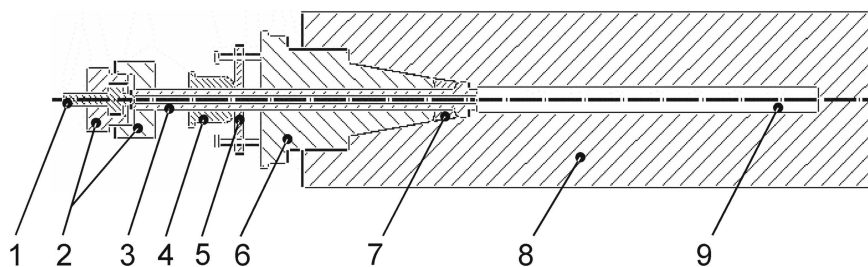


Figure 2-1 Internal pressure in the autoclave using oxygen for high pressure syntheses with an effective autoclave volume of 0.02 litres

2.1.2 Schematic of the oxygen high pressure autoclave

The cross-section of an oxygen high pressure autoclave is shown in Figure 2-2 and pictures of the individual parts of an autoclave are shown in Figure 2-3.



- | | |
|------------------|-----------------------------|
| 1 Sealing Plug | 6 Conical Pressure Screw |
| 2 Coupling | 7 Modified Bridgman Sealing |
| 3 Spindle | 8 Pressure Holding Unit |
| 4 Pressure Screw | 9 Reaction Area |
| 5 Pressure Plate | |

Figure 2-2 Schematic of the structure of oxygen high pressure autoclave

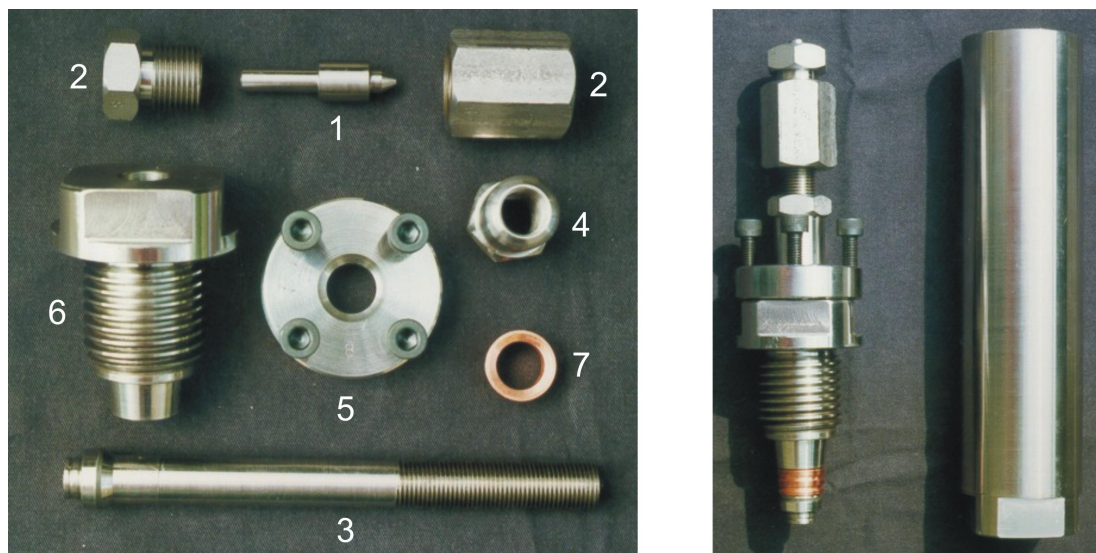


Figure 2-3 Oxygen high pressure autoclave (a) sub-assemblies; and (b) the assembled autoclave. The autoclave is manufactured using a high-temperature resistant, scale-free Cr-Ni-high-grade steel ATS 351 (Company: Thyssen). These autoclaves have self sealing ability and are developed according to the principle of Bridgman. The maximum operating conditions are at a temperature of 873 K and a simultaneous oxygen pressure of 6 kbar.

2.1.3 Investigatory procedure

The blended reaction mixture is filled in silver or gold crucibles which are then placed in the reaction area of the autoclave. The one-way seal made of copper is heated, cooled in ethanol and inserted in the pressure screw. The autoclave is further clutched with this sealing and screwed together. For easy opening after the reaction the conical pressure screw is treated with a special high temperature stable lubricant (COPASLIP, Company: Tribo-Technik GmbH, Rodgau). The autoclave is now attached with the pressure screw to the filling equipment, Figure 2-4, and cooled down using liquid nitrogen bath. Subsequently, by opening the valves 'a' and 'b' the required amount of oxygen from the cylinder is condensed into the measuring tube which is also cooled using liquid nitrogen. After locking the valve 'a', valve 'c' to the autoclave is opened and the nitrogen bath of the measuring tube is removed so that the oxygen over-condenses from the measuring tube into the autoclave. Finally the autoclave is screwed up tightly and placed into a tube furnace with the intended temperature program.

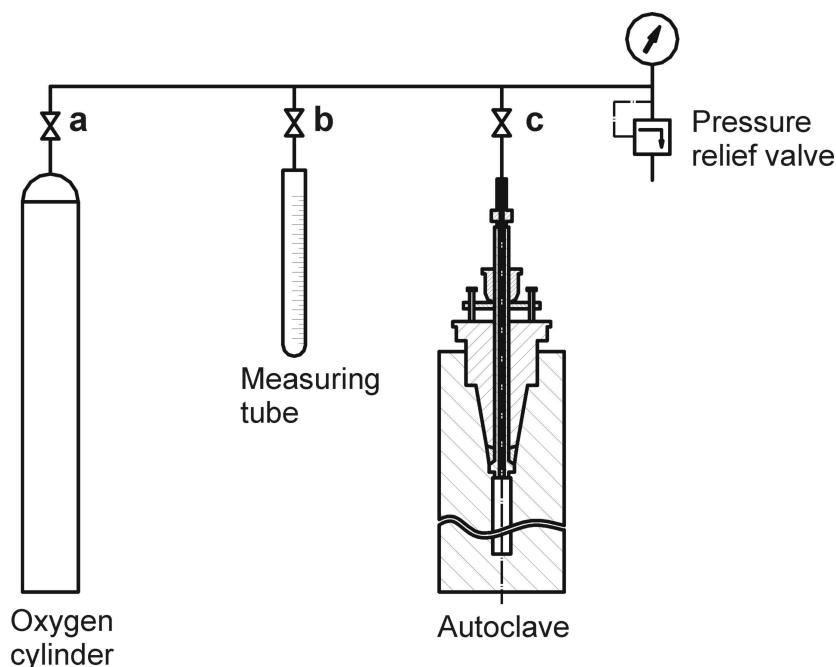


Figure 2-4 Mechanism of generating oxygen pressure in the autoclave

2.2 Working under inert atmosphere

2.2.1 Vacuum and inert gas glass apparatus

The low temperature service department (Max-Planck Institute, Stuttgart, Germany) supplies the argon through copper tubes. The apparatus as shown in Figure 2-5 is made from Duran glass and is attached to a rotary valve oil pump (Type: RD4, Company: Vacuubrand). The quality of vacuum is controlled by a Pirani manometer (Thermovac TM 20, Company: Leybold) within a range of 10^{-3} - 10^3 mbar. This apparatus is filled with either argon or oxygen. Before use, the gas is passed through four successive drying towers of blue gel, potassium hydroxide, molecular sieve (mesh size 3 Å) and phosphorous pentoxide on an inert substrate (Sicapent, Company: Merck), respectively. This arrangement is used to remove the humidity from the gas. The flow rate can be controlled as per the requirement. To find leakage in the glass tubes, a high frequency vacuum examiner (VP 201, Company G. Lauer) is used. L-shaped angled glasses connect the glass apparatus. Equipments connected by glass spirals or angled glasses can be evacuated and filled with argon by opening the concerned valve. The joints are sealed with silicone grease (Company: Wacker). Before use, the necessary glassware is heated under vacuum and is immediately rinsed with dried argon. The process of evacuating, heating, and refilling with argon is repeated a couple of times to ensure that the apparatus is completely inert and free from moisture.

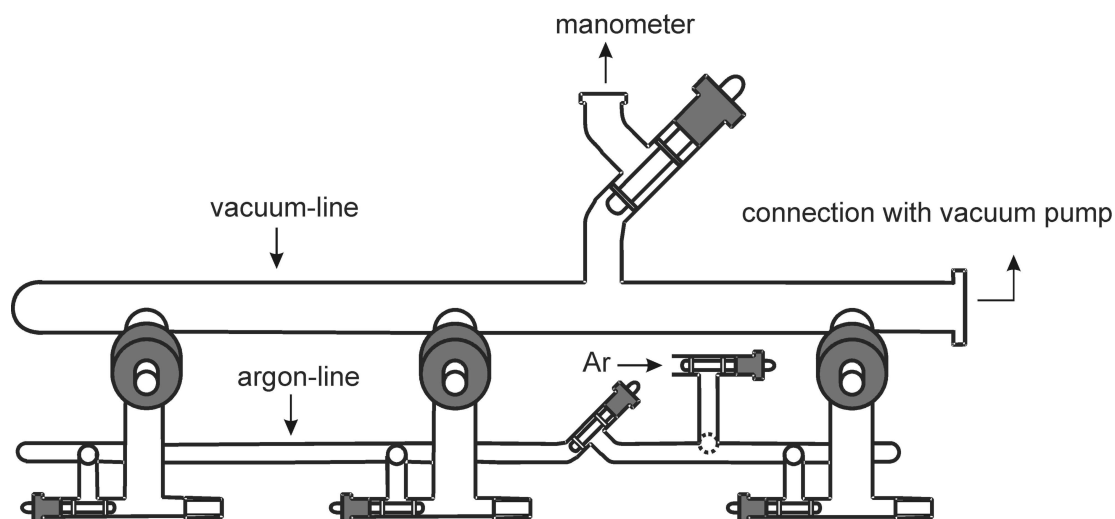


Figure 2-5 Vacuum line

The samples to be handled under inert conditions are dealt with the apparatus as shown in Figure 2-6. This technique was developed by Schlenk [23], especially for handling air sensitive substances. This equipment favours the homogenisation of the substances by crushing them into powder with the use of a dried glass rod. The apparatus also helps in filling the substances into glass or quartz capillaries of various diameters (under flow of argon), which are further used for X-ray analysis. The remaining substance is sealed in small glass ampoules.

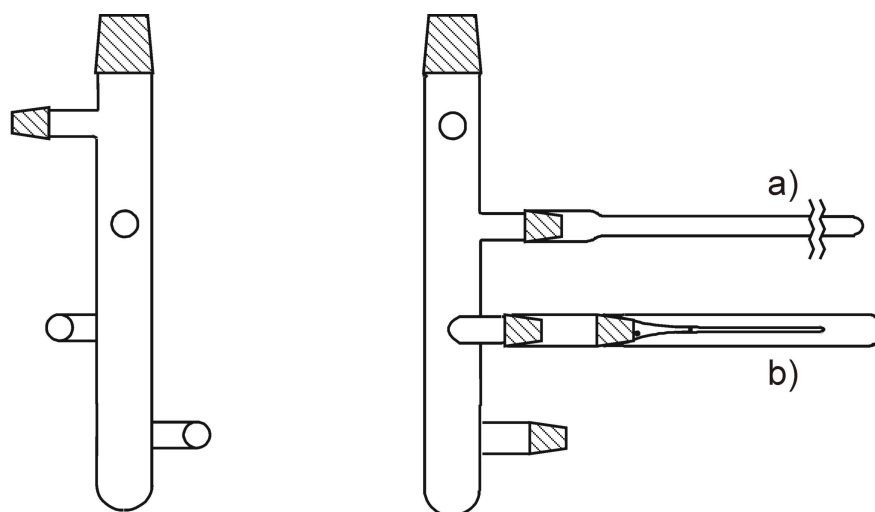


Figure 2-6 Schlenk apparatus (upper cross sections: LV of 29, remaining cross sections LV 14.5), a = ampoules sealing unit and b = capillary filling unit

2.2.2 Glove box

The glove box apparatus is normally used for handling the air and/or moisture sensitive compounds, picking single crystals and pressing the pellets for infrared (IR) spectroscopy. On the other hand, glove box is the best tool to grind and pelletize air sensitive starting mixtures especially containing alkali and alkaline earth metal oxides/peroxides. The model of glove box compartment available is MT 200 (Company: M. Braun). The cleaning of the inert gas is done by passing it over the molecular sieves and its quality is judged by the gas analyzers. The water content inside the glove box compartment is maintained below 0.2 ppm while the oxygen content below 0.5 ppm. Apparatus or samples can be taken inside or outside the glove box compartment through airtight evacuation chambers (big and small). The chambers are filled with argon and evacuated a number of times (big chamber for 45 minutes and small chamber for 10 minutes) to ensure the atmosphere inside the chamber and the glove box is completely inert.

2.3 Piston cylinder press

The piston cylinder press is used to carry out experiments at high pressures up to 2.5 GPa and temperatures up to 1073 K. The press is powered using a fluid medium. By a hydraulic system (oil) the high pressure piston is pressed on the stamp. The stamp shifts downward by the steel plates and transfers the pressure to the pressure cell and the sample. The steel plates consist of a cylinder with a core of tungsten carbide which is surrounded by rings of hardened steel. The pressure cell consists of different parts which transfer pressure to the sample. Sodium chloride is used as the pressure transmitting medium. An electrically heated thin graphite tube serves as the furnace around the sample. The temperature is controlled over a thermocouple.

2.4 Physical properties

2.4.1 X-ray diffraction methods

This is an indispensable, non destructive research method to examine the crystal structures from single crystals as well as from polycrystalline samples [24-27]. The measurement of a single crystal gives primarily the solution of the atomic structure of a substance, while the powder method is used to check the purity, for rapid substance identification and to investigate phase transitions in substances. The powder method is also used to solve and refine structures from powder data. The structure models of the powder or single crystal samples are visualised with the help of the program DIAMOND [28].

Powder X-ray diffraction

To identify a substance and examine the purity of polycrystalline samples, a Stadi P powder diffractometer (Company: Stoe & Cie, Darmstadt) was used. The crystalline sample was applied either to a surface carrier between two X-ray-amorphous polyethylene foils or filled into a glass capillary and rotated in the path of X-rays. The X-rays are produced in a fine focus tube with Cu anode using Ge(111)-single crystal as a monochromator (Cu-K_{α1}-radiation $\lambda = 1.54.06 \text{ \AA}$). A position sensitive detector (PSD) was used as a proportional counter with an opening angle 2θ of 6° (linear PSD, resolution $\Delta 2\theta = 0.06^\circ$, precision measurement) and a image plate detector with an opening angle 2θ of 140° (IP-PSD, Company: Stoe & Cie, Darmstadt, resolution $\Delta 2\theta = 0.12^\circ$, routine investigation). The correction of measured values was achieved by using elemental Si as an external standard. Identification of the substances was accomplished by comparing with the database (e.g. ICSD or ICDD-JCPDS) [29,30] of powder diffractograms for already explored substances. The evaluation of the diffractograms was carried out using WinXPow [31] program. To collect the diffractograms at higher temperatures the Guinier Simon technique was used in which the sample was rotated in a rotary quartz capillary during the measurement at a pre-defined temperature program. The control program coupled with the feed motion of the videodisc was evaluated using the Aida 2.0 [32] software. For this purpose a Guinier Simon camera (FR 553, Company: Enraf Nonius, Delft, Netherlands) with CuK_{α1}-radiation (Johansson Monochromator: Quartz cylinder, parallel to (1011)) was used. Scattering of powder samples gives one-dimensional images of the reciprocal lattice. Because of the limited resolution of the involved detectors at the recording of powder patterns, the information about the intensity of some reflections can be lost due to the

overlapping of closely situated reflections. The overlapping of symmetrically non-equivalent reflections occurs particularly in structures with low symmetry or with large lattice constants. Owing to this, methods of structure refinement that are ground on the calculation of structure factors based on powder data intensities are usually not used for solution of complex structures. However, if a structure model exists, the problem of overlapping of reflections can be circumvented by a method developed by Rietveld [33,34]. Here, not only the integrated intensities, but also the single data points of the measurement are used in the calculations. The refinement is based on the variation of profile parameters, background coefficients and structure parameters with the least squares method until the calculated profile matches with the observed powder pattern as precise as possible. The structure refinement from powder data was carried out by using either GSAS [35] or Fullprof [36,37].

Single crystal diffraction

For the preparation of single crystal photographs a crystal is glued onto the tip of a capillary with the help of a special wax obtained from the lime tree and fixed onto a goniometer head for adjustment into the X-ray beam. Diffraction experiments on single crystals collect the reflexes in the three-dimensional area individually and thus make a simpler task to solve crystal structures in contrast to powder diffraction. By means of film methods all reflexes of one layer can be collected at the same time and thus elementary cell, Laue group and extinction conditions are easily accessible. For the determination of integral reflection intensities additionally a single crystal diffractometer is used. The measurements on the single crystals are carried out with a dual circuit plane detector diffractometer IPDS II (Company: Stoe & Cie, Darmstadt) and a three circle diffractometer AXS Smart with CCD 1000-Detector (Company: Bruker, Karlsruhe), both with a fine focus tube with Mo-anode (Mo-K α - radiation: $\lambda = 71.073$ pm) as source of X-rays and a graphite single crystal monochromator. From the experimentally measured reflections and intensities the data are processed using the programs X-area [38] or SMART32 [39], further the data reductions are performed using the programs X-red [40] or SAINT32 [41] and finally the absorption corrections are carried out with the programs X-shape [42] or SADABS [43]. The structures are solved with the help of direct methods using SHELXS-97 [44] and SHELXTL [45], or by using SIR-97 [46]. The refinements of structures determined are carried out by the least squares refinement procedure with the help of the SHELXTL [45] program package, or with the minimisation of the difference of the squares

on the basis of the structure refinement program, JANA2000 [47]. Analysis of the existing pseudo symmetry of a substance for the recognition of possibly existing structure is accomplished with the program PSEUDO [48].

2.4.2 Neutron diffraction

Neutron diffraction is an important tool in the determination of atomic structures and especially in studying the magnetic structure of compounds. As neutrons are not charged they do not interact with the electron cloud surrounding the nucleus (unlike X-rays). They interact only with the nucleus of the atom. Neutrons penetrate deeply into most of the materials and interact with the unpaired electrons in the magnetic ions/atoms and thus have a unique ability to probe the magnetic structure of the compound. Neutron diffraction is also helpful in locating the exact position of light atoms in the unit cell. The neutron powder diffraction patterns were obtained from the SINQ spallation source of Paul Scherrer Institute (PSI), Laboratory for Neutron Scattering, ETHZ & PSI, CH-5232 Villigen PSI, Switzerland. The crystal structure determination was carried out on the data collected from the high-resolution HRPT diffractometer [49] while the data on the magnetic ordering were obtained by means of the DMC powder diffractometer [50] situated at a super mirror coated guide for cold neutrons at SINQ ($\lambda = 2.567 \text{ \AA}$). The neutron diffraction studies were also carried out on the E9 line, FIREPOD (Fine-Resolution Powder Diffractometer), at the Hahn-Meitner-Institute, Berlin.

2.4.3 Energy Dispersive X-ray Spectrometry (EDX)

Energy Dispersive X-ray Spectroscopy (EDX) is based on the interaction of incident electrons (electron beam) with inner-shell electrons of the sample. The characteristic X-rays are produced when a material is bombarded with electrons in an electron beam instrument, such as a scanning electron microscope (SEM). During the ionisation process, a high-energy electron ejects an electron from the inner-shell of the atom, leaving a vacancy in the shell. The excited atom returns to its initial state filling the vacant place with an electron from an outer-shell (recombination). Because of the difference in bonding-energy, the recombination process results in the emission of characteristic X-rays. The intensity and the wave length of this X-rays yield quantitative and qualitative information on the elements present in the sample. Scanning electron microscopy and Energy dispersive microanalysis was carried out on XL 30 TMP (Company: Philips,

Eindhoven, NL), equipped with a energy dispersive unit for microanalysis (Model: Phoenix, Company: EDAX, Mahwah, NJ, USA).

2.4.4 Raman and infrared spectroscopy

Raman spectra were recorded with a microscope laser Raman system (Jobin-Yvon, LabRam) operating at the laser lines of a He-Ne- (632.8 nm) and a Diode-Laser (784.7 nm) at 20 mW. Infrared measurements were performed with a Fourier-Transform-Spectrometer (IFS 113v, Bruker). A silicon carbide globar was used as a radiation source and a DTGS (deuterated triglycine sulphate) detector was used for detection. Samples were prepared by mixing 1-2 mg of substance with ca. 400 mg of KBr (Aldrich, 99+%, dried in vacuum at 473 K).

2.4.5 Thermal analysis methods, DTA / TG / MS and DSC

The difference thermal analysis (DTA) and thermogravimetry (TG) were performed simultaneously, up to a temperature of 1673 K with a Thermoanalyser STA 409 C (Company: Netzsch, Selb). The change in the mass of the sample due to its decomposition was studied by heating the sample to a controlled temperature program in oxygen/argon atmosphere. The decomposition products were detected with a coupled quadruple mass spectrometer QMS 421 (Company: Balzers, Hudson, NH, USA). For these research methods the substance was weighed into a corundum crucible and compared with the measurement of a blank probe. For the analysis of phase conversion at different temperatures a Differential Scanning Calorimeter (DSC) Pyris 1 (Company: Perkin Elmer) was used. The sample to be examined was taken in a powder form in a flat aluminium crucible sealed tightly in a small press.

2.4.6 Magnetic susceptibility measurements

Measurement of the magnetic susceptibility of any substance gives an idea about the presence of the unpaired electrons in that substance. Depending upon the kind of the magnetic moment one can distinguish between diamagnetic, paramagnetic, ferromagnetic and antiferromagnetic and also the ferrimagnetic substances. The determination of the magnetic susceptibility was achieved in a spin quantum interference device (SQUID magnetometer), MPMS 5.5 (Company: Quantity Design, San Diego, CA, USA). For sample preparation the substance to be examined was inserted in a gelatine capsule (in powder form) or into a quartz capillary sealed under helium in the case of air sensitive samples. The diamagnetic susceptibility is composed of the sum in the literature [51].

2.4.7 Conductivity measurements

The conductivity σ (S m^{-1} , or $\Omega^{-1} \text{m}^{-1}$) of a material differs and depends upon the investigated substances around several orders of magnitude. For metals it is about $10^6 - 10^4 \text{ S m}^{-1}$ (Ag: $62.5 \cdot 10^6 \text{ S m}^{-1}$) [52], for semiconductors around $100 - 10^{-6} \text{ S m}^{-1}$ (Si: $4.3 \cdot 10^{-4} \text{ S m}^{-1}$) [52] and for isolators below $10^{-10} \text{ S m}^{-1}$ [53]. A further distinguishing characteristic is the temperature dependence of the conductivity. For metals the conductivity decreases during rise in temperature, and for semiconductors the resistivity drops down (positive and/or negative temperature coefficient α). The measurement is carried out on a pressed pellet in contact with gold foil at the bearing positions of the test electrodes (platinum). The conductivity is determined afterwards according to the four probe method with an in-built measuring system. The ionic conductivity [54] of a substance can be calculated by subtraction of the electronic conductivity from the total conductivity and by resistance tests. This resistance (impedance) can be determined with the help of the impedance spectroscopy; the measurement of the ionic conductivity is carried out by the use of an alternating voltage (AC) instead of a direct voltage (DC), as compared to the earlier one. Further, the conductivity equipment [55] permits the data collection of direct current and alternating current starting from ambient temperature to 973 K. The pressed powder is in contact with the platinum electrode inside the measurement cell [56]. The controlling and analysis of the data is carried out with the programs Sigma measurement [57], Sigma evaluation [58], and Equivalent Circuit [59].

3 Alkali metal ruthenates

Ruthenium, the group VIII, 4d transition element, is a hard white metal occurring in different modifications. It exhibits ten oxidation states ranging from -2 , 0 and $+1$ (as in carbonyls and carbonyl halides) to $+8$ (only RuO_4 till date). Ruthenium compounds crystallise in a variety of structure types such as pyrochlore, hollandite, scheelite and perovskite, exhibiting a variety of interesting electronic and magnetic properties. In the case of ruthenium oxides, RuO_4 is prepared by heating the metal with sodium peroxide or with fused KOH and KNO_3 and then treating the melt with Cl_2 or KMnO_4 in acid. RuO_4 is volatile, toxic and a strong oxidizing agent and can be reduced by HCl into Ru^{4+} and by alkali into Ru^{6+} [60]. Alkali metal oxo-ruthenates(VI) have been known since long time but not much has been revealed about their crystal structures and properties. The compounds are hygroscopic, containing Ru^{6+} cation. One of the early works found in the literature on these alkali metal ruthenates is from J. L. Howe and co-workers in first quarter of the 20th century [61,62], by oxidation of ruthenium metal in presence of alkali metal oxide/peroxide/hydroxide in aqueous solution. Different alkali ruthenates studied and predicted are mentioned in Gmelin's Handbook [63]. The current interest in oxides of the transition metals adopting crystal structures with low-dimensional building units as characteristic features is driven by the intriguing physical properties, in particular magnetic and conducting, exhibited by several members of this extended family of compounds [64-66]. The strong directionality of low-dimensional structures can produce highly anisotropic physical properties since interactions between electrons, such as magnetic coupling can strongly depend on the crystallographic axes along which they occur [67]. On the other hand, electrons in ruthenium compounds are expected to display an itinerant behaviour as in recent years it has been shown that ferromagnetic, antiferromagnetic and diamagnetic states in ruthenates are energetically close to each other. Recently, the alkali ruthenium hollandites, KRu_4O_8 and RbRu_4O_8 , were studied which displayed metallic conductivity [68]. In this chapter, attempts to synthesise ternary and quaternary alkali oxides containing ruthenium in higher oxidation states in order to have short distances between the spin bearing ruthenium cations are discussed.

3.1 Na₂RuO₄, Sodium oxo-ruthenate (VI)

In the system Na-Ru-O, only the single crystal structure of NaRu₂O₄ and Na_{3-x}Ru₄O₉ [69] were investigated earlier. I. S. Shaplygin and co-workers [70] reported the solid state reactions of Na₂CO₃ or Na₂O₂ with RuO₂, which yielded the phases Na₄RuO₄, NaRu₄O₉, Na₂Ru₉O₁₉, Na₂Ru₄O₉, Na₄Ru₃O₈ and, Na₂RuO₃. These were identified and characterised by X-ray diffraction, thermal analysis and electrical conductivity. Recently, the crystal structures of Na₃RuO₄ [71] (isostructural to Na₃NbO₄ [72]), NaRu₂O₄ and Na_{2.7}Ru₄O₉ were studied by neutron powder diffraction [73]. However, no structural investigations have been carried out on the sodium ruthenates containing ruthenium in higher than +5 oxidation states. The oxo-ruthenates have been found to express various interesting electronic features [74,75], therefore, a study on the alkali ruthenates was carried out systematically, including high oxygen pressure preparations in order to realise higher oxidation states of ruthenium. In this section the synthesis, crystal structure and properties of Na₂RuO₄ are described. The neutron diffraction studies of the same are also discussed.

3.1.1 Synthesis

Na₂RuO₄ was prepared by solid state reaction of sodium peroxide and ruthenium dioxide applying an elevated oxygen pressure. Equimolar amounts of Na₂O₂ (p.a., > 95 %, Merck) and RuO₂ {prepared from ruthenium(III) chloride hydrate (Sigma-Aldrich) under an oxygen flow at 923 K for 20 h} were finely ground and pressed into pellets. These pellets were put into gold crucibles which were sealed from one side and mechanically closed from the other. Alternatively, this phase can also be obtained by heating the same starting mixture in gold crucibles at 898 K under oxygen flow for 2 days. Crystalline samples of Na₂RuO₄ were obtained in stainless steel autoclaves under an oxygen pressure of 220 MPa, using sodium hydroxide as mineralizer. The samples were kept at a temperature of 873 K for 4 days and then cooled down to room temperature with a rate of 12 K/h. Single crystals suitable for X-ray diffraction studies were selected in a glove box and sealed into glass capillaries of 0.3 mm diameter.

3.1.2 Thermal analysis

The thermal analysis of Na₂RuO₄ was carried out using the DTA/TGA equipment (STA 409, Netzsch, Selb) coupled with a quadruple mass spectrometer. The sample was heated at the rate of 10 K/min in a corundum crucible under argon atmosphere. The thermal

degradation proceeds in several steps accompanied by a loss of oxygen and finally forming Na₂RuO₃ at 1123 K.

3.1.3 Raman and infrared spectroscopy

A Raman spectrum of Na₂RuO₄ was recorded with a Confocal Microscope Laser Raman System (Jobin-Yvon, excitation line 632 nm, power 4 mW). The spectrum obtained is shown in Figure 3-1. Several Raman modes were obtained. The strong mode at 804.6 cm⁻¹ is same as the mode reported for [RuO₄]²⁻ in the literature [76]. The spectrum was also compared with reference Raman spectra of K₂RuO₄ [77], containing isolated RuO₄ tetrahedra, the modes 339 cm⁻¹, 779 cm⁻¹, 812 cm⁻¹ and 837 cm⁻¹ are similar as observed in K₂RuO₄. However, as Na₂RuO₄ consists of RuO₅ trigonal bipyramids, the possibility of assigning the strong mode at 801 cm⁻¹ and medium modes at 443 cm⁻¹ and 756 cm⁻¹ to the chain of trigonal bipyramids cannot be ruled out.

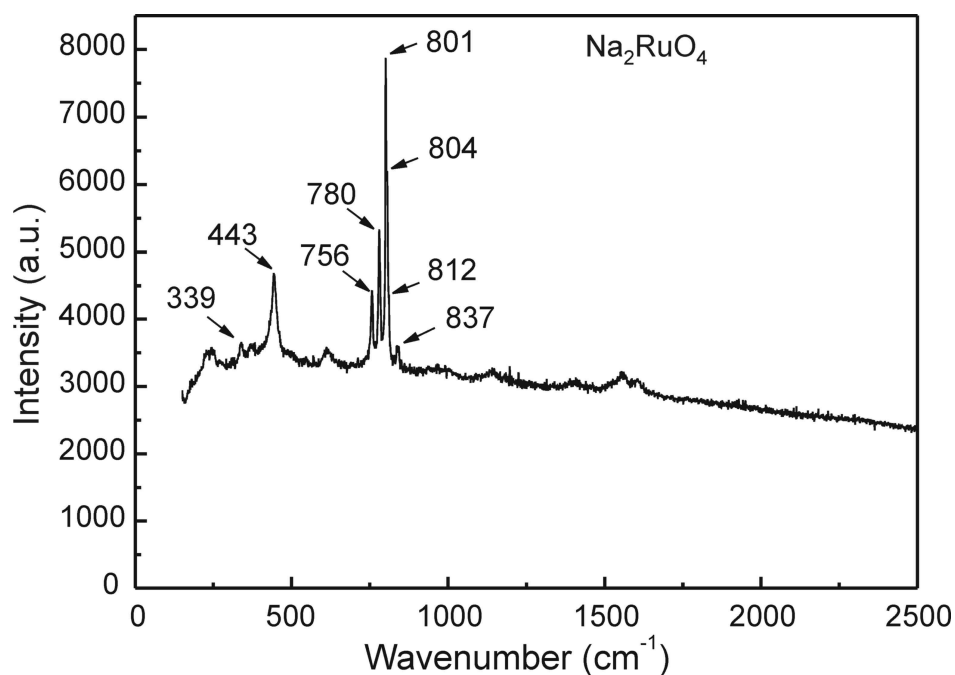


Figure 3-1 Raman spectrum of Na₂RuO₄

Infrared measurements of Na₂RuO₄ were performed with a Fourier-Transform-Spectrometer (IFS 113v, Bruker). 1-2 mg of the sample and 400 mg of KBr (Aldrich, 99+%, dried in vacuum at 473 K) were pressed into a pellet. Modes obtained are 497 cm⁻¹-(w), 567 cm⁻¹-(m), 768 cm⁻¹-(m), 801 cm⁻¹-(m), 809 cm⁻¹-(s), 832 cm⁻¹-(s), 1104 cm⁻¹-(w) and 1264 cm⁻¹-(w). The medium mode at 801 cm⁻¹ is the same as observed in the raman measurements. Another medium mode at 832 cm⁻¹ is near to the mode reported in

literature [78]. However, as the structure consists of RuO₅ trigonal bipyramids, no reference data are reported till date on such type of coordination. Thus, the spectra can be considered as a finger print for this type of coordination.

3.1.4 X-ray diffraction

Single crystal data of Na₂RuO₄ were collected on a Stoe IPDS II (MoK_α 1st run: $\varphi = 0^\circ$, $\omega = 0 - 180^\circ$, $\Delta \omega = 1^\circ$; 2nd run: $\varphi = 90^\circ$, $\omega = 0 - 180^\circ$, $\Delta \omega = 1^\circ$; time per frame = 5 min). X-ray diffraction powder data were collected with a Stoe Stadi-P diffractometer (Cu K_α1, Ge monochromator, linear PSD) in steps of 0.01° over a 2 θ range from 0 to 90° for approximately 24 h with the samples sealed in glass capillaries of 0.2 mm diameter.

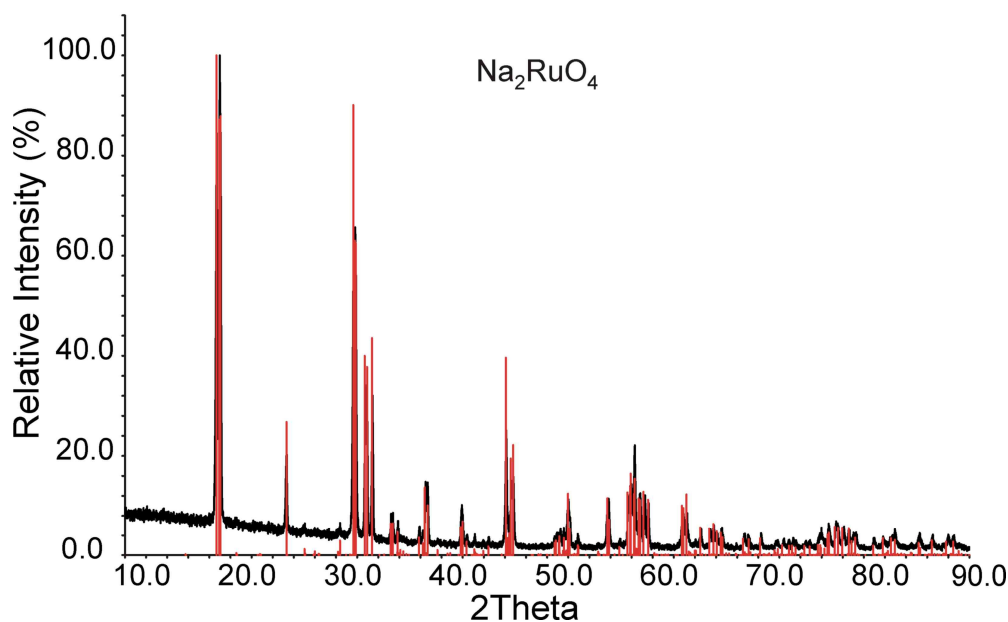


Figure 3-2 X-ray pattern of Na₂RuO₄ (reflections in red is the pattern calculated from the single crystal structure determination)

The obtained X-ray pattern is shown in Figure 3-2. All information concerning the data collection and processing, the crystallographic parameters, as well as details on structure solution and refinement are given in Table 3.1

Table 3.1 Crystallographic data and details on the structure determination of Na₂RuO₄

Empirical formula	Na₂RuO₄
Crystal system	Monoclinic
Space group (no.)	<i>P</i> 2 ₁ /c (no. 14)
Lattice parameters at 293 K from 1129 reflections with 2θ _{min} = 9.52 ° and 2θ _{max} = 64.58°	a = 10.721(6) Å b = 7.033(4) Å c = 10.871(6) Å β = 119.10(4)°
Formula units	8
Cell volume / Å ³	716.2
X-ray density / g·cm ⁻³	3.91
Molar mass /amu	422.2
Diffractometer	Stoe IPDS II
Wavelength	Mo-Kα (λ = 0,71073 Å)
Monochromator	Germanium
Crystal size	0.10 x 0.15 x 0.20 mm
Temperature	293 K
Data collection mode	Omega-scan
Reciprocal lattice segments	Full sphere
2θ-region /°	2,86 < 2θ < 64,80
hkl _{min} – hkl _{max}	–16, –10, –16 to 16, 10, 16
Data collection software	X-Area (Stoe & CIE, 1998)
Data reduction software	X-Red (Stoe & CIE, 1998)
Integration parameters	Coefficient A = 12.0 Coefficient B = 2.0 EMS = 0.01
Number of measured reflections	9312
Number of unique reflections	2503
Number of reflections > 3σ	1998
R _{int} (obs/all)	0.0432 / 0.0435
Absorption coefficient / mm ⁻¹	4.47
Absorption correction	Gaussian [79] (Coppens, 1970)
Crystal approximated by	20 faces
T _{min} , T _{max}	0.235, 0.410
Structure solution	Direct Methods: Sir97 (Altomare et. al., 1997)
Structure refinement	Full matrix least-squares; Jana2000 (Petříček & Dušek, 2000)
R(obs), R(all)	0.0766, 0.0488
R _w (obs), R _w (all)	0.0853, 0.0488
Weighting scheme	1/s(Fobs) ²
Extinction correction	Isotropic [79] (Coppens, 1970)
Extinction coefficient	0.33(2)
Difference density min./max. [e · Å ⁻³]	–2.75 / 1.71

3.1.5 Structure description

According to a single crystal structure determination, Na₂RuO₄ contains two crystallographic independent Ru atoms which are coordinated by five oxygen atoms in the form of trigonal bipyramids. Within the experimental errors (3 \times e.s.d), the point group is D_{3h}. The Ru-O distances range from 1.766-1.80 Å for equatorial and from 1.975-1.998 Å for axial oxygen atoms, respectively. An analysis of the pseudo symmetry with the program PSEUDO [48] shows that the Ru- and Na-partial structures are pseudo-hexagonal and pseudo-trigonal, respectively, see Figure 3-3, while the oxygen substructure shows no further pseudo-symmetry. The RuO₅ polyhedra are connected via common apical vertices, resulting in infinite chains of bipyramids along the [010] direction as seen in Figure 3-4. While the O_{ax}-Ru-O_{ax} angles are approximately linear (178.9° and 179.3°), the bipyramids are tilted significantly with respect to the neighbouring polyhedra (Ru-O_{ax}-Ru angles 123.3° and 124.4°). The Na cations, connecting the pseudo-hexagonally close packed ¹_∞[RuO₃O_{2/2}] chains shown in Figure 3-4, are coordinated by 6 (Na4) or 7 (Na1-Na3) oxygen atoms with distances between 2.334 to 2.829 Å (for details see Table 3.2 and Table 3.3).

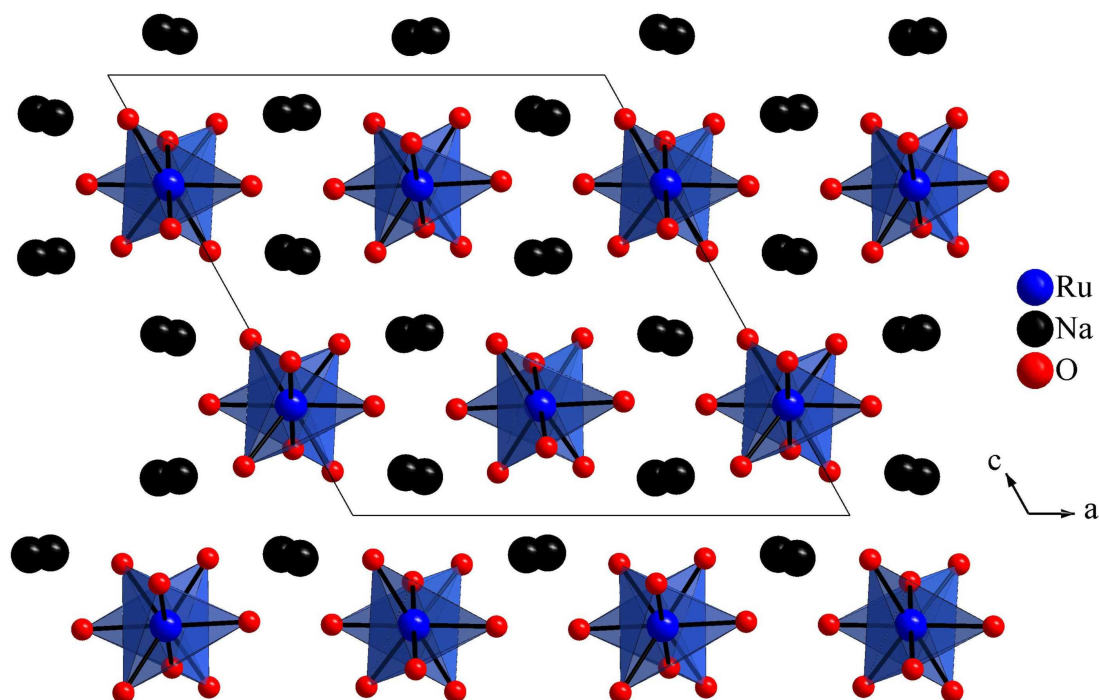


Figure 3-3 View of the crystal structure of Na₂RuO₄ along [010]. RuO₅ units are drawn as polyhedra. The ¹_∞[RuO₃O_{2/2}] chains are arranged in a pseudo-hexagonal rod packing

Odd coordination numbers appear to be rare, particularly, in complexes of transition elements with monoatomic ligands. Correspondingly, in tetra-oxo-metallates of general formulae A₂MO₄ or AMO₄ virtually exclusively tetrahedral or octahedral complex oxo-anions have been encountered so far. Thus, when synthesising and characterising Na₂RuO₄, it was expected to contain tetrahedral oxo-anions and iso-structural to Na₂MoO₄ [80]. As Ru⁶⁺ has a slightly smaller ionic radius than Mo⁶⁺, it came as a surprise that in Na₂RuO₄, ruthenium(VI) adopts an even larger uneven coordination sphere than Mo⁶⁺ in Na₂MoO₄.

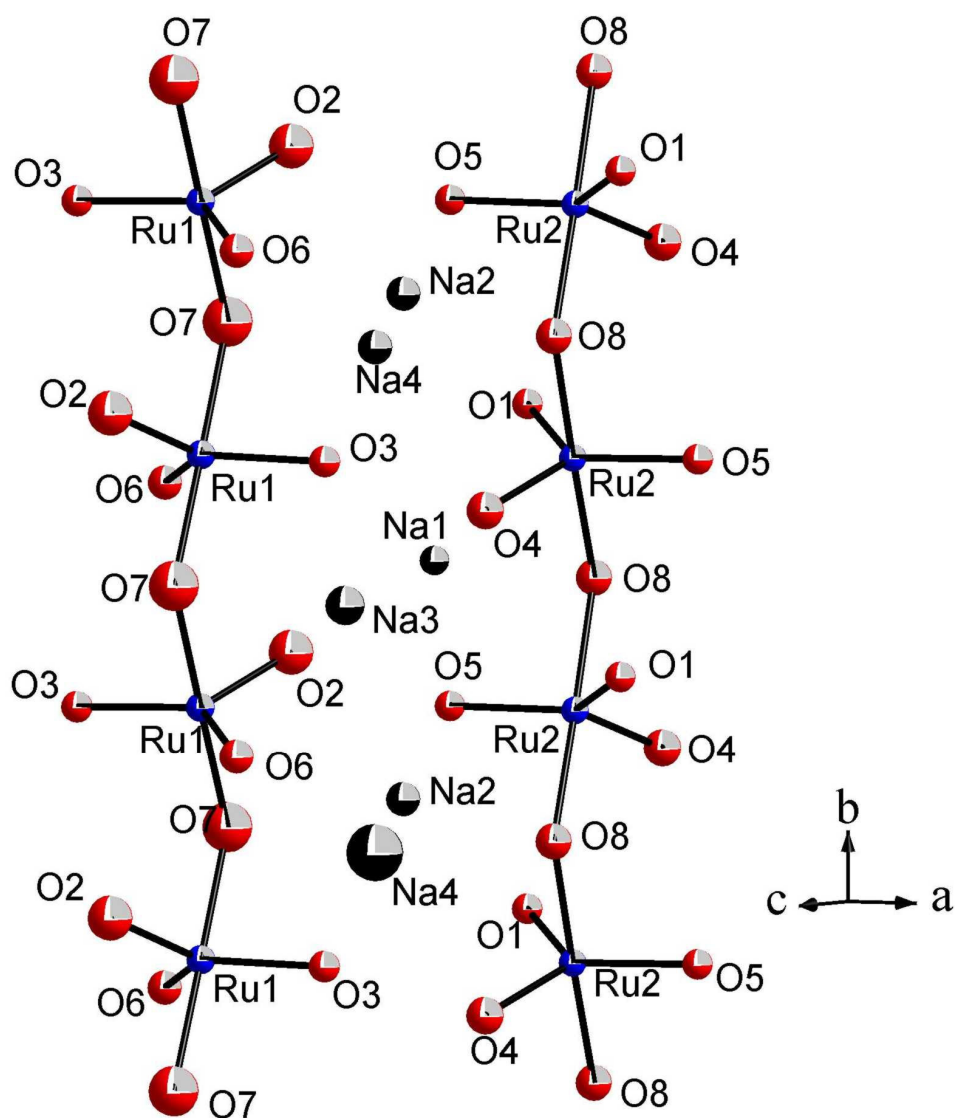


Figure 3-4 Schematic drawing of two parallel $^{1-}_{\infty}[\text{RuO}_3\text{O}_{2/2}]$ chains. The connecting Na⁺ cations are indicated. Displacement ellipsoids have been drawn at the 50% probability level

Table 3.2 Atomic coordinates and isotropic displacement parameters U_{iso} in Å² of Na₂RuO₄ with standard deviations in parentheses; U_{iso} is defined as $\exp[-8\pi^2 U(\sin^2\theta/\lambda^2)]$

Atom	x	y	z	U_{iso}
Ru1	0.5003(1)	0.24486(8)	0.2510(1)	0.0170(3)
Ru2	0.0006(1)	0.23202(8)	0.2486(1)	0.0165(3)
Na1	0.3051(6)	0.4632(7)	0.4106(5)	0.025(2)
Na2	0.3501(6)	0.5609(7)	0.9149(5)	0.030(2)
Na3	0.1875(7)	0.5152(7)	0.0879(6)	0.028(2)
Na4	0.1547(7)	0.0049(7)	0.0972(6)	0.028(2)
O1	0.1646(9)	0.1455(9)	0.3887(8)	0.025(3)
O2	0.4818(10)	0.6489(9)	0.3897(8)	0.026(3)
O3	0.3278(11)	0.2512(10)	0.2411(10)	0.026(3)
O4	0.0084(10)	0.3212(10)	0.0998(8)	0.027(3)
O5	0.1643(11)	0.7294(9)	0.2476(9)	0.024(3)
O6	0.3404(9)	0.6789(10)	0.5977(8)	0.027(3)
O7	0.4659(13)	0.0064(8)	0.6555(10)	0.031(4)
O8	0.0454(10)	0.4809(8)	0.3497(8)	0.018(3)

Table 3.3 Selected bond distances (Å) and angles (°) for Na₂RuO₄ with standard deviations in parentheses

Bond	Distance	Bond	Distance
Ru1-O2 ⁱ	1.766(10)	Ru2-O1	1.782(7)
Ru1-O3	1.800(13)	Ru2-O4	1.774(10)
Ru1-O6 ⁱⁱ	1.783(10)	Ru2-O5 ^v	1.787(12)
Ru1-O7 ⁱⁱⁱ	1.975(7)	Ru(2)-O8	1.997(6)
Ru1-O7 ^{iv}	1.982(7)	Ru2-O8 ^v	1.998(6)
Na1-O2 ⁱⁱ	2.394(8)	Na3-O1 ⁱⁱⁱ	2.347(11)
Na1-O2	2.401(12)	Na3-O4 ^{ix}	2.394(8)
Na1-O6	2.415(10)	Na3-O5	2.402(12)
Na1-O3	2.473(13)	Na3-O4	2.410(12)
Na1-O5	2.514(9)	Na3-O3	2.459(9)
Na1-O8	2.532(12)	Na3-O6 ^x	2.675(10)
Na(1)-O1	2.640(9)	Na3-O7 ⁱⁱⁱ	2.709(16)
Na(2)-O7 ^{vi}	2.334(11)	Na4-O8 ⁱⁱⁱ	2.357(10)
Na2-O1 ^{vi}	2.365(11)	Na4-O6 ⁱⁱⁱ	2.372(12)
Na2-O5 ^{vii}	2.435(9)	Na4-O3	2.463(9)
Na2-O7 ^{viii}	2.468(17)	Na4-O8 ^v	2.484(14)
Na2-O2 ^{vii}	2.570(11)	Na4-O5 ^{xi}	2.505(11)
Na2-O6 ^{vii}	2.740(11)	Na4-O4	2.730(11)
Na2-O3 ^{vi}	2.829(11)		
Angles			
O7 ⁱⁱⁱ -Ru1-O7 ^{iv}	179.3(4)	Ru1-O7 ^{iv} -Ru1 ⁱ	124.4(5)
O8-Ru2-O8 ^v	178.9(4)	Ru2-O8-Ru2 ^{xiii}	123.3(4)

Symmetry codes: (i) 1-x, -0.5+y, 0.5-z; (ii) 1-x, 1-y, 1-z; (iii) x, 0.5-y, -0.5+z; (iv) 1-x, -y, 1-z; (v) -x, 0.5+y, 0.5-z; (vi) x, 0.5-y, 0.5+z; (vii) x, 1.5-y, 0.5+z; (viii) 1-x, 0.5+y, 1.5-z; (ix) -x, 1-y, -z; (x) x, 1.5-y, -0.5+z; (xi) x, -1-y, z; (xii) -x, 0.5+y, 0.5-z

In general, the peculiar five-fold coordination of ruthenium in Na₂RuO₄ is a consequence of minimising the total energy of its collective structure, and singular pertinent influences are impossible to extract unambiguously. Yet, a qualitative interpretation can be successfully footed on selected effects of major influence, in particular, when comparing

the results with related compounds. Firstly, the effective size of the central atom has to be considered which, for a given valence state, increases when moving to the heavier homologues within a group, and by shifting to lower atomic numbers within a period, of the periodic system. Secondly, the counter-cations are of crucial impact and thus reducing their sizes favours higher coordination numbers. Finally, the electronic structure of the central atom can direct towards a characteristic coordination through e.g. ligand field stabilisation. While Na₂RuO₄ is in accordance with the trends as expected within the group, including oxo-ferrates(VI), ruthenates(VI) and osmates(VI), and within the A₂RuO₄ family (A = K, Rb and Cs induce a tetrahedral coordination of ruthenium(VI)), there is a striking inconsistency when comparing to Na₂MoO₄. Obviously, the electronic configurations (d⁰ and d², respectively) are responsible for this difference. However, both the complex-anions under consideration (T_d, D_{3h}) experience a ligand field stabilisation for a d² configuration. In both cases the resulting lowest lying occupied ruthenium centred orbital is degenerate (of E (T_d) or E" (D_{3h}) symmetry) and leads to a ³A ground state. So the decisive effect is the magnitude of the ligand field splitting which is larger for the trigonal bipyramidal coordination as compared to the tetrahedral coordination [74,75]. This preference seems to be small, since the size effect caused by substituting potassium for sodium in Na₂RuO₄ is sufficient for the tetrahedral coordination being preferred over the fivefold one. Taking together all oxo-ruthenates(VI) known to date, which include A₂RuO₄ (A = K, Rb, Cs [81]) containing ruthenium in tetrahedral coordination and CsK₅Ru₂O₉ [82], K₂RuO₃(OH)₂ [83] and Ag₂RuO₄ [84] containing ruthenium in a trigonal bipyramidal coordination, makes the two coordination geometries winning equal weights.

3.1.6 Magnetic measurements

The magnetisation of Na₂RuO₄ was investigated using a SQUID magnetometer (Quantum Design MPMS; 5-330 K). The magnetic properties indicate a largely one dimensional spin system showing an onset of significant exchange interactions at around 200 K and a three dimensional antiferromagnetic ordering below 50 K as shown in Figure 3-5. The magnetic moment of 2.80 μ_B as determined from the high temperature data is in full agreement with the expectation for a ³A ground state.

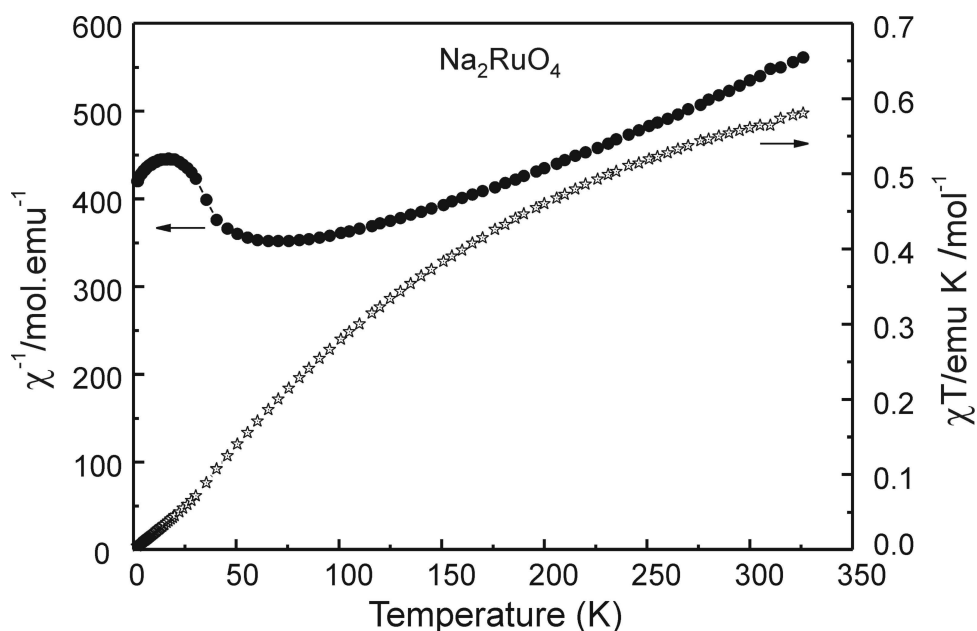


Figure 3-5 Magnetic susceptibility of Na₂RuO₄ represented as χ^{-1} versus T and χT versus T

To evaluate the low temperature behaviour and the magnetic structure, neutron diffraction experiments have been carried out on Na₂RuO₄ which are discussed ahead.

3.1.7 Neutron diffraction studies

The crystal and magnetic structures of sodium (VI) ruthenate was studied by neutron powder diffraction in the temperature range of 1.5 to 200 K. Polycrystalline samples of Na₂RuO₄ were prepared in different batches from equimolar amounts of sodium peroxide and ruthenium dioxide under oxygen flow at 898 K, as described earlier. Approximately 5 grams of Na₂RuO₄ was synthesised and sealed inside a 6mm diameter vanadium container, under argon flow for the neutron studies. Neutron powder diffraction experiments in the temperature range 1.5 K-200 K were carried out at the SINQ spallation neutron source of the Paul Scherrer Institute. The crystal structure parameters of Na₂RuO₄ were refined from the powder patterns taken with the high-resolution diffractometer HRPT [49] which was operated in a High Intensity mode with the neutron wavelength $\lambda = 1.886 \text{ \AA}$. The data on the magnetic ordering were obtained with the powder diffractometer DMC50 located on a super mirror coated guide for cold neutrons at SINQ (neutron wavelength used was $\lambda = 4.20 \text{ \AA}$). The Fullprof Suite of Programs was used for Rietveld refinements.

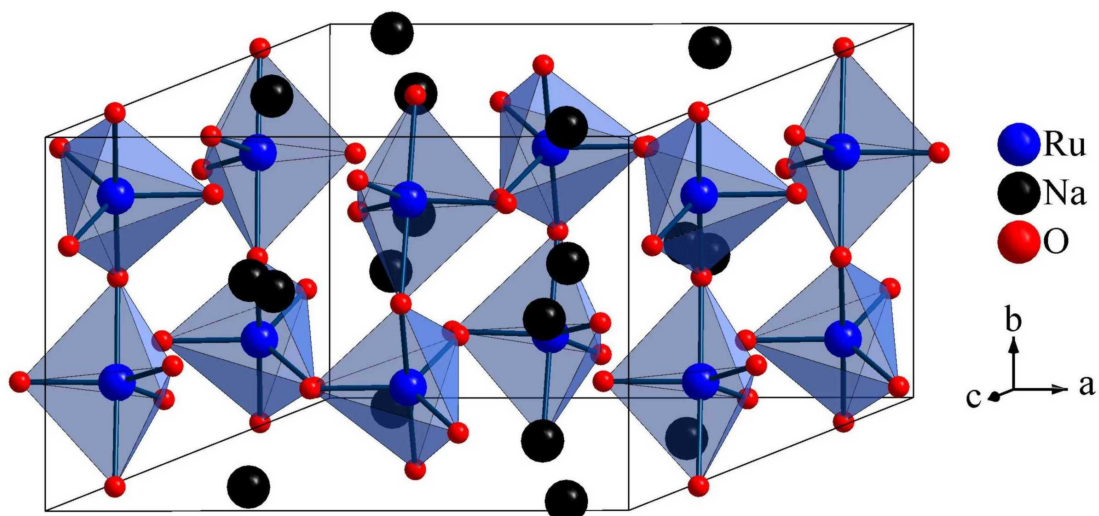


Figure 3-6 Schematic of the Na₂RuO₄ crystal structure. RuO₅ trigonal bipyramids sharing apical oxygen atoms form one dimensional chains running along the b-axis

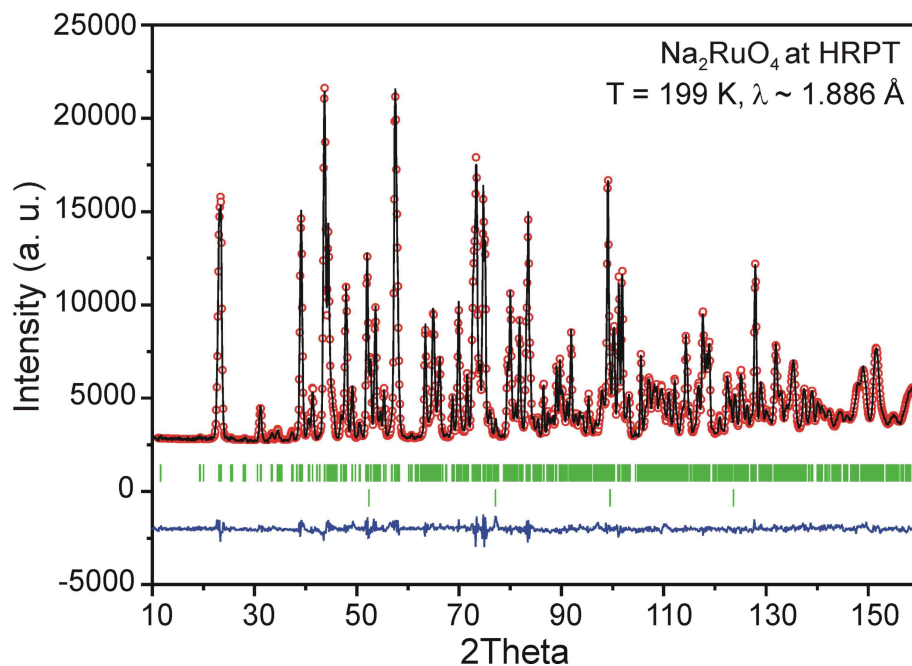


Figure 3-7 Rietveld refinement of Na₂RuO₄ powder neutron diffraction data from HRPT ($\lambda = 1.886 \text{ \AA}$) at 199 K. Experimental points, calculated profile and the difference curve are shown. The two rows of ticks at the bottom indicate the calculated peak positions for the main phase and the vanadium from the container material

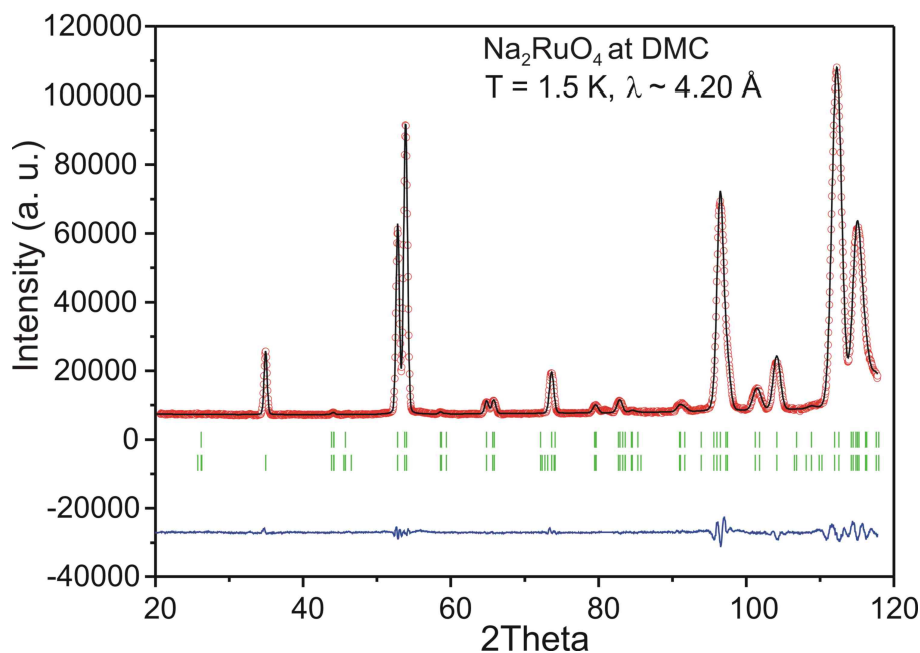


Figure 3-8 Rietveld refinement of Na₂RuO₄ powder neutron diffraction data from DMC ($\lambda = 4.20 \text{ \AA}$) at 1.5 K. The experimental points, calculated profile and the difference curve are shown. Two rows of the ticks at the bottom indicate the calculated peak positions for the crystal and magnetic structures of Na₂RuO₄

The Rietveld refinements of the HRPT powder patterns have yielded the precise values of the structural parameters in the wide temperature range (1.5–200 K). The results proved and confirmed the known model of the crystal structure of Na₂RuO₄ (space group $P 2_1/c$) and did not display any structural phase transformations to 1.5 K. The schematic representation of the crystal structure of Na₂RuO₄ is given in Figure 3-6. Examples of the Rietveld refinement fits of the HRPT data (at 199 K) and DMC data (at 1.5 K) are shown in Figure 3-7 and Figure 3-8, respectively. The crystal structure parameters at two selected temperatures (1.5 K and 199 K), where the higher statistics acquisitions were done are listed in Table 3.4. There is not much variation in the Ru-O distances at 2 K and 199 K, listed in Table 3.5.

Table 3.4 Crystal structure parameters of Na₂RuO₄ at T = 1.5 K and 199 K, refined from HRPT powder neutron data, space group P 21/c. The thermal parameters for the atoms of each sort were constrained to equality in the refinements

	T = 1.5 K				T = 199 K	
a, Å	10.65122 (8)				10.68366 (8)	
b, Å	7.01135 (4)				7.02334 (5)	
c, Å	10.82996 (8)				10.85282 (9)	
β, deg.	119.1978 (4)				119.1884 (5)	
Vol, Å ³	706.013 (9)				710.936 (9)	
Ru1 (x, y, z)	0.5004 (4)	0.2417 (4)	0.2511 (5)	0.5010 (4)	0.2431 (5)	0.2507 (5)
Ru2 (x, y, z)	-0.0002 (4)	0.2294 (4)	0.2476 (5)	-0.0008(4)	0.2312 (4)	0.2481 (5)
B(Ru1,Ru2), Å ²	0.12 (3)				0.36 (3)	
Na1 (x, y, z)	0.3008 (8)	0.4573 (9)	0.4104 (8)	0.3031(10)	0.4610(10)	0.4108(10)
Na2 (x, y, z)	0.3505 (8)	0.5717 (9)	0.9153 (8)	0.3490 (9)	0.5646 (9)	0.9137 (9)
Na3 (x, y, z)	0.1893 (7)	0.5103 (13)	0.0885 (7)	0.1912 (9)	0.5143(14)	0.0885 (9)
Na4 (x, y, z)	0.1520 (7)	0.0003 (11)	0.0993 (6)	0.1519 (8)	0.0022(12)	0.0995 (8)
B(Na-Na4), Å ²	0.46 (4)				0.97 (5)	
O1 (x, y, z)	0.1642 (4)	0.1422 (6)	0.3860 (4)	0.1626 (5)	0.1429 (6)	0.3861 (5)
O2 (x, y, z)	0.4818 (5)	0.6432 (6)	0.3904 (4)	0.4820 (5)	0.6473 (6)	0.3861 (5)
O3 (x, y, z)	0.3273 (5)	0.2502 (5)	0.2384 (5)	0.3296 (6)	0.2507 (5)	0.2401 (6)
O4 (x, y, z)	0.0069 (5)	0.3193 (7)	0.1001 (4)	0.0069 (5)	0.3204 (7)	0.0997 (5)
O5 (x, y, z)	0.1648 (4)	0.7234 (7)	0.2472 (6)	0.1656 (6)	0.7253 (5)	0.2485 (7)
O6 (x, y, z)	0.3420 (5)	0.6821 (7)	0.5953 (4)	0.3407 (5)	0.6812 (8)	0.5958 (4)
O7 (x, y, z)	0.4679 (4)	0.0108 (6)	0.6533 (4)	0.4677 (5)	0.0072 (6)	0.6538 (5)
O8 (x, y, z)	0.0484 (5)	0.4773 (5)	0.3512 (4)	0.0493 (5)	0.4784 (5)	0.3513 (5)
B (O1-O8), Å ²	0.22(2)				0.56(2)	
R _p , %	4.56				5.18	
R _{wp} , %	5.27				5.73	
χ ²	3.28				3.54	

Table 3.5 Bond lengths of Ru-O in Å at selected temperatures

Bond	Distance (Å)	Bond	Distance(Å)
At 2 K			
Ru1 - O6	1.774	Ru2 - O4	1.752
Ru1 - O2	1.778	Ru2 - O1	1.769
Ru1 - O3	1.785	Ru2 - O5	1.783
Ru1 - O7	1.971	Ru2 - O8	1.998
Ru1 - O7	1.995	Ru2 - O8	1.999
At 199 K			
Ru1 - O6	1.757	Ru2 - O4	1.759
Ru1 - O2	1.764	Ru2 - O1	1.781
Ru1 - O3	1.781	Ru2 - O5	1.771
Ru1 - O7	1.976	Ru2 - O8	1.992
Ru1 - O7	1.992	Ru2 - O8	2.013

Upon cooling the sample below $T_N \sim 37.2$ K, the appearance of the new reflections (see Figure 3-9) in the neutron diffraction pattern indicates the onset of the long-range magnetic ordering of Ru⁶⁺ ions. For easier understanding, only the portions of the Na₂RuO₄ neutron diffraction patterns taken at the DMC diffractometer with the $\lambda = 4.20$ Å neutrons at $T = 39$ K (just above the magnetic transition temperature, lower curve) and $T = 1.5$ K (saturated magnetic state) are presented. The total Bragg intensity at $T = 39$ K is originating from nuclear scattering by the atoms of the nuclear crystal structure cell of Na₂RuO₄, while almost all the intensity of the (012) and (210)/(-212) peaks, as well as exactly all the intensity of the (010) peak (since this one is prohibited for the space group $P 2_1/c$ of the crystal structure) are coming from the neutron scattering on the long-range ordered lattice of magnetic Ru⁶⁺ ions. The hkl-indices (referring to the axes of the chemical unit cell) are mentioned for clarity near the magnetic diffraction peaks. All additional lines originating from the neutron diffraction on the system of the ordered Ru⁶⁺ magnetic moments can be indexed with integer indices within a parent unit cell of the crystal structure of Na₂RuO₄, though some of them are prohibited by its crystal symmetry.

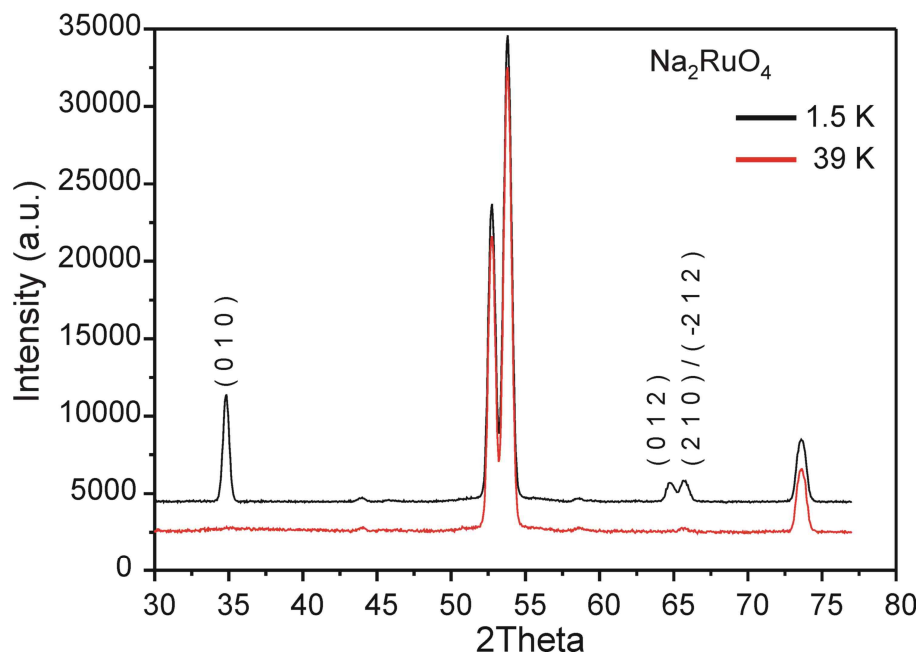


Figure 3-9 Portions of HRPT neutron diffraction patterns of Na₂RuO₄ collected at 1.5 K and 39 K and normalized to comparable scale

From the results obtained with the high-resolution thermal neutrons diffractometer HRPT, one interesting fact is observed. The temperature dependences of the unit cell constants of Na₂RuO₄ are all smooth in the whole temperature range, see Figure 3-10. From the

refinements of the DMC powder data at various temperatures, the temperature dependence of the ordered magnetic Ru⁶⁺ moment magnitude was derived, see Figure 3-11.

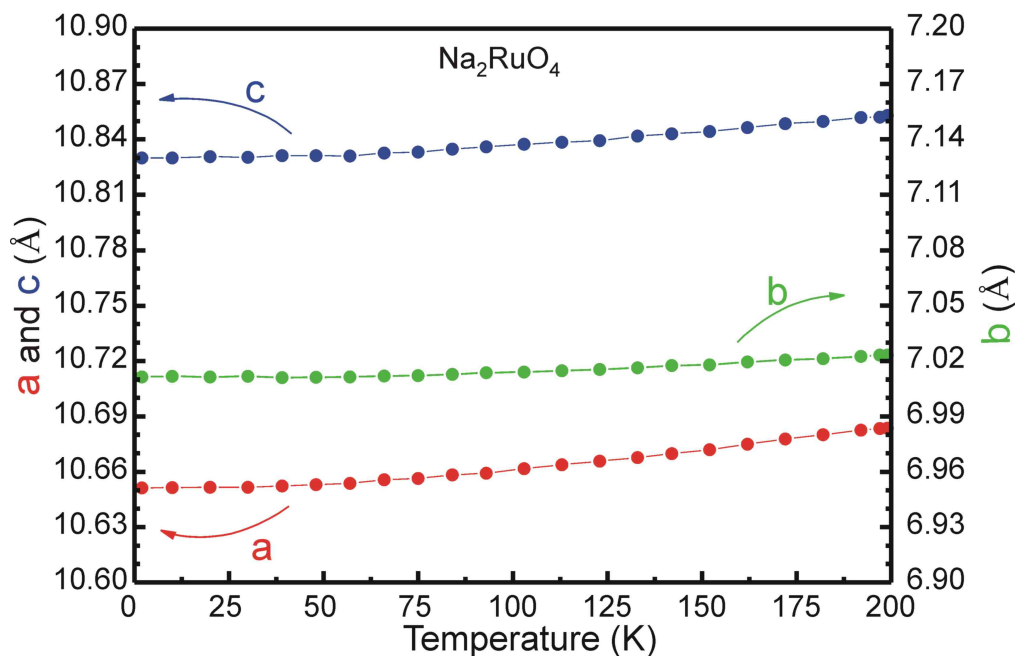


Figure 3-10 Temperature dependencies of the unit cell parameters a, b and c of Na₂RuO₄

In order to estimate the antiferromagnetic transition temperature, the data of $M_{\text{Ru}}(T)$ were fitted to an empirical formula:

$$M(T) = M_0 \left[1 - (T/T_N)^\alpha \right]^\beta \quad (3.1)$$

with four free parameters, where M_0 is the saturated magnetic moment at $T=0$, T_N is the Néel temperature, α and β are the refineable exponential parameters. The fit (see the solid curve in figure 3.11), has yielded the following parameters: the saturated low-temperature Ru⁶⁺ magnetic moment magnitude $M_0 = 1.656 \pm 0.003 \mu\text{B}$, antiferromagnetic transition temperature $T_N = 37.22 \pm 0.06 \text{ K}$, the exponents $\alpha = 5.4 \pm 0.2$, and $\beta = 0.364 \pm 0.018$.

The detailed analysis concerning the magnetic form factor for Ru⁶⁺, the symmetry analysis of the low temperature magnetic structure and the whole concept is discussed elsewhere [85].

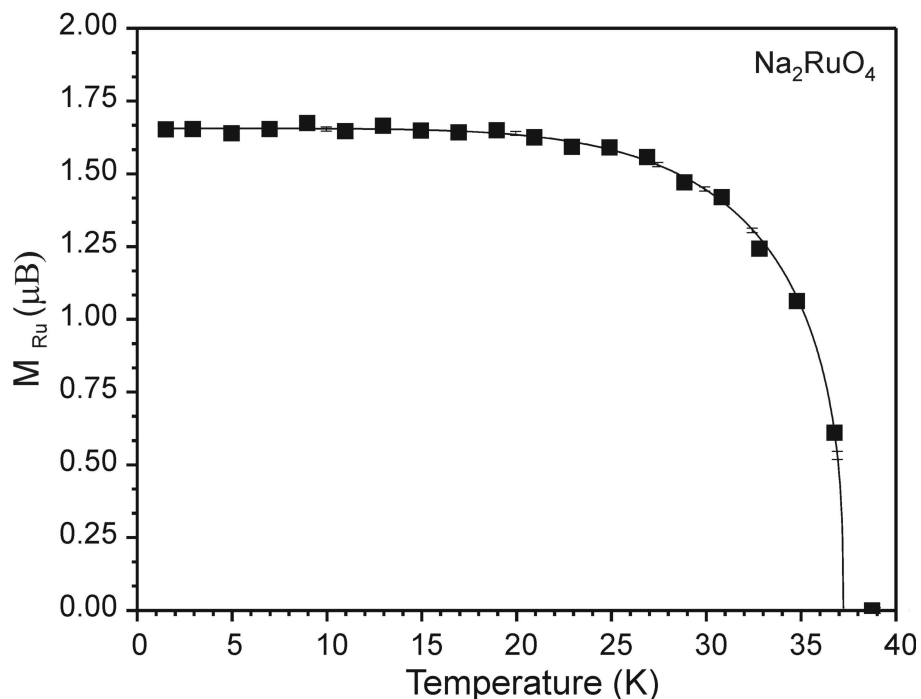


Figure 3-11 Temperature dependence of the ordered Ru⁶⁺ magnetic moment magnitude in Na₂RuO₄. Error bars are comparable to the symbol sizes, except for last few points (above 36 K) and are not shown for clarity. The solid line is a fit of the $M_{Ru}(T)$ data to the empirical formula explained in equation (3.1) in the text

In conclusion, the Ru magnetic moments are aligned ferromagnetically along the a-axis and antiferromagnetically along the b-axis, along which the RuO₅ chains are aligned. The low temperature magnetic structure of Na₂RuO₄ is shown in Figure 3-12

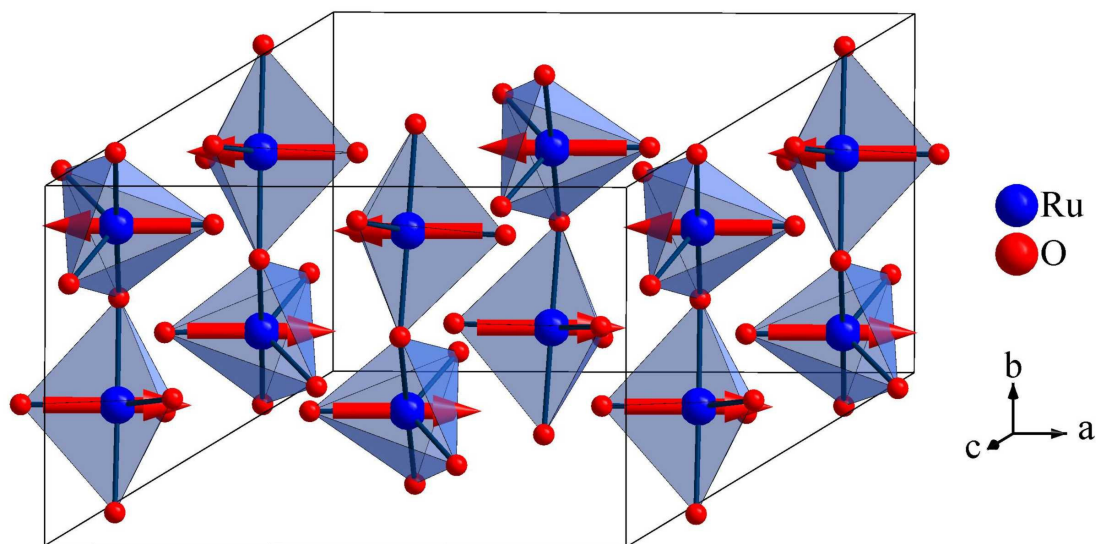


Figure 3-12 Low-temperature magnetic structure of Na₂RuO₄. The antiferromagnetically ordered chains of Ru ions are couple ferromagnetically between each other. The magnetic Ru moments are aligned in the a-c plane with the dominant a- and minor c- components

3.2 K₂RuO₄ and Rb₂RuO₄

The alkali oxo-ruthenates of potassium, rubidium and cesium [81] were studied more than a decade ago by Hoppe and Fischer [86]. The structures are of β -K₂SO₄ type, with ruthenium in four-fold coordination with oxygen forming isolated RuO₄ tetrahedra. The mixed alkali metal ruthenate, CsK₅[RuO₄][RuO₅] [82] further studied, contains isolated RuO₄ tetrahedra and RuO₅ trigonal bipyramids. However, the magnetism in all these ruthenates was not explored. In the course of this thesis, K₂RuO₄ and Rb₂RuO₄ were synthesised in order to investigate and compare their magnetic behaviour with Na₂RuO₄, and overall to see the trend in magnetism as the oxygen coordination of ruthenium changes from cesium to sodium. As the structures of these compounds are already studied, only the alternative synthesis, X-ray diffraction and magnetic measurements are discussed. The other purpose of synthesising these compounds was to prepare pure phases of quaternary ruthenium containing oxides; these results are discussed in section 3.3.

3.2.1 Synthesis

Polycrystalline samples of K₂RuO₄ and Rb₂RuO₄ were synthesised from KO₂ and RuO₂ in a molar ratio of 2 : 1 for K₂RuO₄ and from RbO₂ and RuO₂ in a molar ratio of 2 : 1 for Rb₂RuO₄. The mixtures were placed in gold ampoules which were flame sealed at one end and mechanically closed at the other. The reactions were carried out under an oxygen flow at 898 K for 2 days and subsequent cooling to room temperature at a rate of 20 K per hour.

3.2.2 X-ray diffraction

X-ray powder diffractograms were recorded on a STOE-Stadi P diffractometer with a germanium monochromator on the primary beam, CuK α ₁ radiation ($\lambda = 1.54056 \text{ \AA}$) and a linear position sensitive detector. The batches were confirmed as single phases without any impurity and the lattice constants, as compared with the literature, were found to be similar as reported [86].

3.2.3 Magnetic measurements

Magnetic measurements were performed on polycrystalline powder samples using a SQUID-Magnetometer (MPMS 5.5, Quantum Design) between 5 and 350 K in the magnetic fields up to 5 T. Measurements of the inverse magnetic susceptibilities obey the Curie-Weiss law down to about 70 K. The plots of susceptibility and inverse susceptibility versus temperature for K₂RuO₄ and Rb₂RuO₄ are shown in Figure 3-13 and Figure 3-14,

respectively, in an applied field of 5 T. The inverse magnetic susceptibilities obey the Curie-Weiss Law down to about $T = 60$ K. Fitting the Curie and Weiss constants the values obtained are $C = 0.9$ emu K/mol for both compounds, and θ around -19 K for Rb₂RuO₄ and -30 K for K₂RuO₄. Effective magnetic moments are $\mu_{eff} = 2.68\mu_B$ for both compounds, which is 95 % of $\mu_{SO} = 2.83 \mu_B$, the ideal moment for the spin-only d^2 ($S = 1$) configuration, thus confirming the oxidation state +6 for ruthenium. Below 60 K, the inverse susceptibility curves diverge remarkably from the linear behaviour indicating the presence of antiferromagnetic interactions in both compounds, with $T_N = 14$ K and 4 K (2 transitions) for K₂RuO₄ and with $T_N = 9$ K for Rb₂RuO₄.

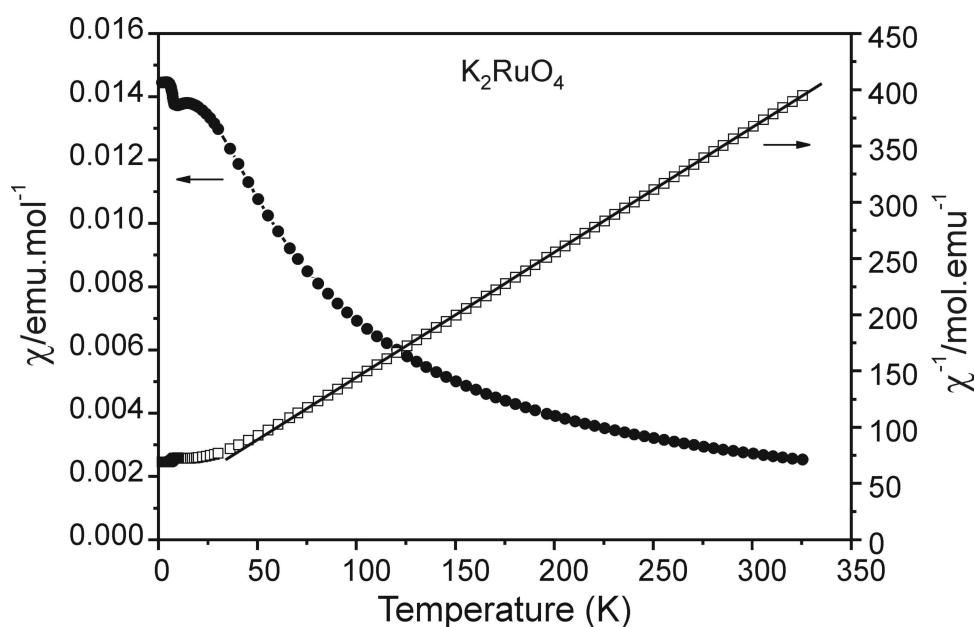


Figure 3-13 Magnetic susceptibility of K₂RuO₄ represented as χ vs. T (circles) and χ^{-1} vs. T (squares) in an applied field of 5 T. The full line represents the linear fit using the Curie-Weiss law

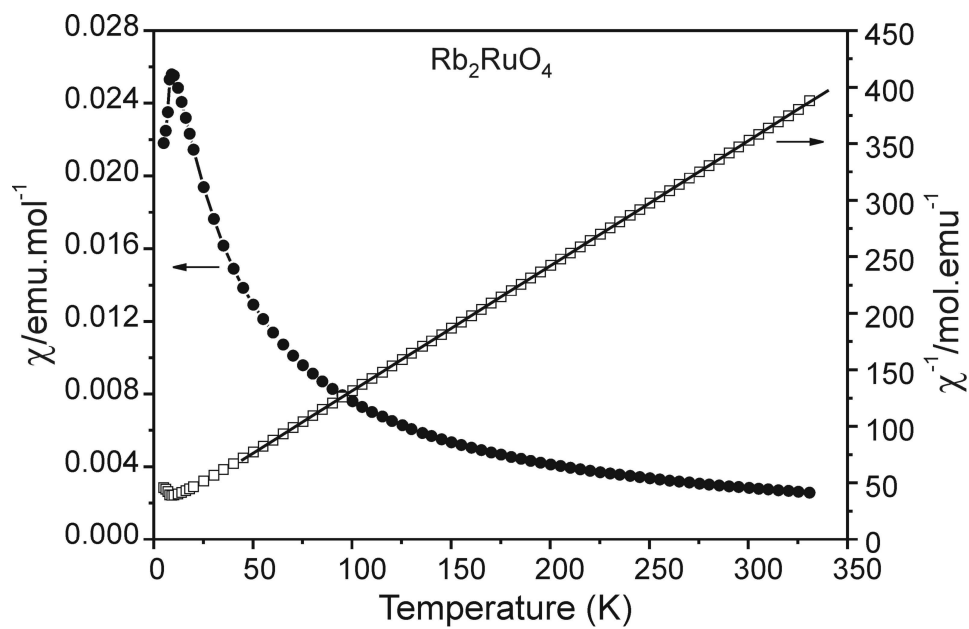


Figure 3-14 Magnetic susceptibility of Rb₂RuO₄ represented as χ vs. T (circles) and χ^{-1} vs. T (squares) in an applied field of 5 T. The full line represents the linear fit using the Curie-Weiss law

This can be correlated with the distances between the ruthenium tetrahedra, which are closer for K₂RuO₄ than for Rb₂RuO₄ giving rise to more pronounced interactions. Thus, the shortening of Ru - Ru distances in these compounds increases the magnetic transition temperature. The comparison of all hexavalent ruthenates explored in this work is discussed in section 3.4.

3.3 $K_3Na(RuO_4)_2$ and $Rb_3Na(RuO_4)_2$, Ruthenium Glaserites

The quaternary mixed alkali metal oxoruthenates are not much explored till date. Only $CsK_5Ru_2O_9$ is known [82], which contains RuO_5 trigonal bipyramids and RuO_4 tetrahedra as described earlier. The same type of coordination is also observed in $K_2RuO_3(OH)_2$ (OH groups in axial positions) [83], but the RuO_x polyhedra are isolated in each case. As described in earlier sub-chapter, the crystal structure of Na_2RuO_4 represents a unique structure type and differs significantly from the other alkali oxo-ruthenates(VI) known so far (A_2RuO_4 with $A = K, Rb, Cs$ which adopt the β - K_2SO_4 type of structure). Obviously the occurrence of different structure types and, in particular, coordination numbers is strongly influenced by variation of the size of the alkali metal cation. This behaviour is known from e.g. the tellurates(VI), where Cs_2TeO_4 [87] consists of isolated TeO_4 tetrahedra, while the A_2TeO_4 with $A = Li, Na, Ag$ contain different polyanionic TeO_4 chains with condensed octahedral units [88-90]. Nevertheless, in the case of the ruthenates some contributions in form of attractive interactions between unpaired electrons must be taken into account, otherwise the crystal structure of Na_2RuO_4 should be more similar to the corresponding phase containing the similar sized hexavalent molybdenum, Na_2MoO_4 [80]. Thus, decreasing the alkali metal radius is resulting in shortening the distances between the spin bearing transition metal atoms and, in particular, their coordination number. So, attempts were made to insert one more alkali cation (potassium and rubidium) in the unusual structure of Na_2RuO_4 , to follow the coordination of ruthenium and to see if it displays any interesting properties. The new compounds obtained were found to crystallise in the glaserite type [91] of structure. The syntheses, crystal structures and magnetic properties of $K_3Na(RuO_4)_2$ and $Rb_3Na(RuO_4)_2$ are discussed ahead.

3.3.1 Synthesis

Black hygroscopic samples of $K_3Na(RuO_4)_2$ and $Rb_3Na(RuO_4)_2$ were prepared by solid state reactions using stoichiometric amounts of RuO_2 , Na_2O_2 , and KO_2 or RbO_2 , in autoclaves under oxygen pressure. KO_2 and RbO_2 were synthesised from the respective alkali metal and O_2 [92]. Na_2O_2 (p.a., >95%, Merck) was finely ground before use. RuO_2 was prepared from ruthenium(III) chloride hydrate (Sigma-Aldrich) under oxygen atmosphere at 923 K. All manipulations were carried out under purified argon in the glove-box. In a typical experiment, crystalline samples were obtained in stainless steel autoclaves under oxygen pressure of 175 MPa after 8 days at 873 K followed by cooling down to

room temperature within two days. Although crystals sufficient for structure determination were obtained in autoclaves, the phase always contained small amounts of Na_2RuO_4 . For pure microcrystalline samples, stoichiometric amounts of the pre-synthesised ternary ruthenates(VI), Na_2RuO_4 [93] and K_2RuO_4 and Rb_2RuO_4 [94], respectively, were intimately mixed in the ratio 3 : 1, pressed into pellets, and put into gold crucibles (1 cm diameter and 3 cm long), which were sealed from one side and crimped from the other. The reaction was carried out under oxygen flow at 898 K for 50 hours followed by cooling down to room temperature at a rate of 15 K per hour. The obtained samples were handled and stored in inert atmosphere for further characterisation.

3.3.2 Thermal analysis

The thermal analysis of $K_3Na(RuO_4)_2$ and $Rb_3Na(RuO_4)_2$ was carried out by using the DTA/TGA equipment (STA 409, Netzsch, Selb) coupled with a quadruple mass spectrometer. The samples were heated at the rate of 10 K/min in a corundum crucible under a flow of dry argon. No thermal degradation was observed and no residue was left for further analysis after 1573 K.

3.3.3 Raman spectroscopy

A Raman spectrum was recorded with a Confocal Microscope Laser Raman System (Jobin-Yvon, excitation line 632 nm, power 4 mW). The different modes obtained are shown in Figure 3-15. The strong mode at 807 cm^{-1} in $K_3Na(RuO_4)_2$ and 802 cm^{-1} in $Rb_3Na(RuO_4)_2$ are close to the mode reported for $[RuO_4]^{2-}$ ions in the literature [76]. The modes observed in both the compounds are similar. However, $Rb_3Na(RuO_4)_2$ which crystallises trigonal has more Raman active modes as compared to the monoclinic $K_3Na(RuO_4)_2$.

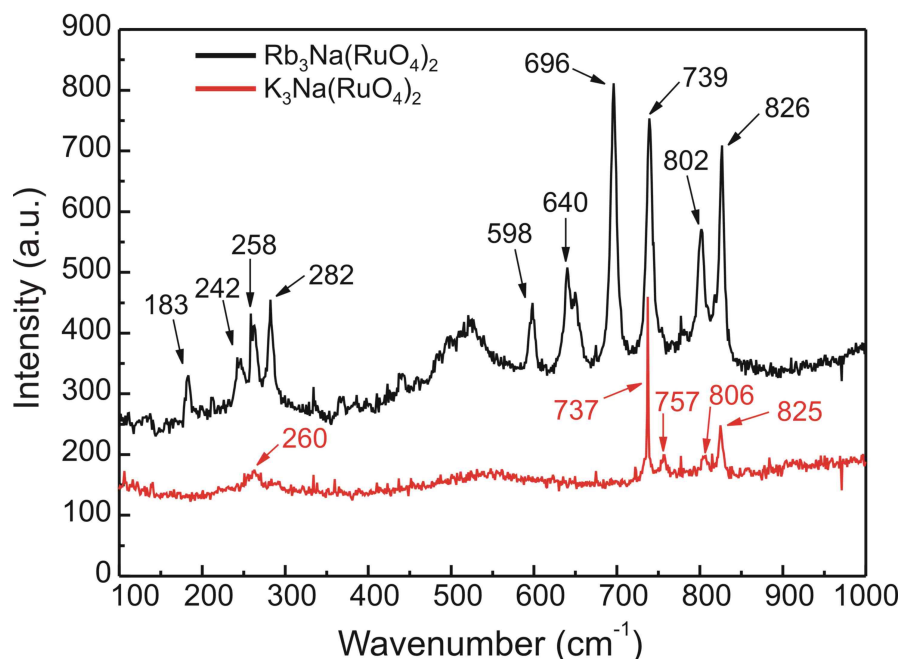


Figure 3-15 Raman spectra of K₃Na(RuO₄)₂ (red) and Rb₃Na(RuO₄)₂ (black)

3.3.4 X-ray diffraction

X-ray powder diffractograms were recorded on a STOE-Stadi P diffractometer with a germanium monochromator on the primary beam, CuK α ₁ radiation ($\lambda = 1.54056 \text{ \AA}$) and a linear position sensitive detector. Silicon was used as an external standard. The measured X-ray pattern is shown in Figure 3-16.

High temperature X-ray powder diffraction was also carried out on K₃Na(RuO₄)₂ in a quartz capillary using a hot air blower, on a molybdenum X-ray source. The X-ray diffractograms were collected starting from room temperature to 623 K in steps of 50 K. It can be seen from Figure 3-17 that the reflections marked as asterisk (*) diminish going from room temperature to 573 K. Single crystal data were collected on a Bruker AXS with SMART-CCD (APEX) (MoK α Graphite monochromator, semi-empirical absorption correction with the program SADABS.

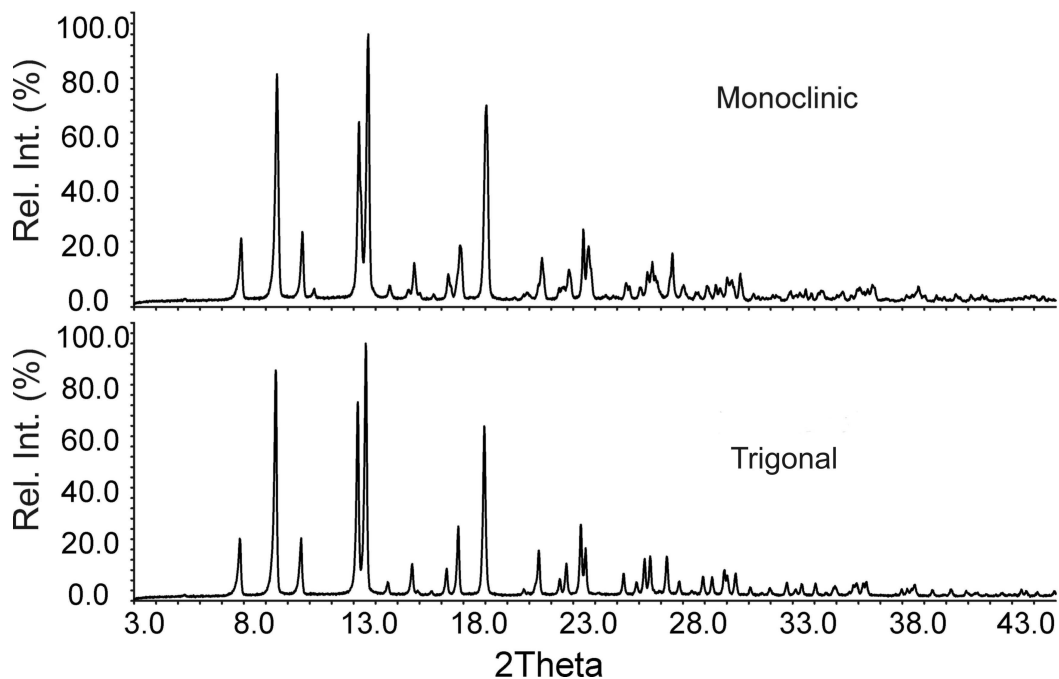


Figure 3-16 Measured X-ray pattern of $(K_3NaRuO_4)_2$. Room temperature (upper pattern) and 473 K (lower pattern)

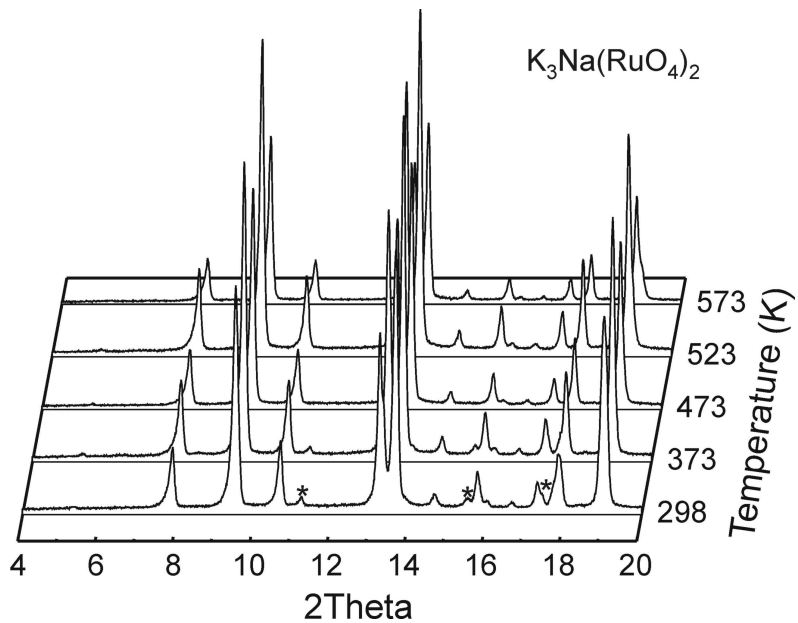


Figure 3-17 X-ray diffraction patterns of $K_3Na(RuO_4)_2$ at different temperatures, asterisk (*) indicates the reflections responsible for the phase transition

Table 3.6 Experimental X-ray powder data for $K_3Na(RuO_4)_2$ at RT with $d > 1.4 \text{ \AA}$.

$d_{obs} [\text{\AA}]$	I/I_0	h	k	l	$d_{obs} [\text{\AA}]$	I/I_0	h	k	l	$d_{obs} [\text{\AA}]$	I/I_0	h	k	l
5.1741	25.4	$\begin{Bmatrix} 1 & 1 & 0 \\ 2 & 0 & 0 \end{Bmatrix}$			2.5465	4.9	0	0	6	1.7281	22.3	$\begin{Bmatrix} 3 & 3 & 0 \\ 5 & 1 & 4 \end{Bmatrix}$		
4.2848	85.6	$\begin{Bmatrix} -1 & 1 & 2 \\ -2 & 0 & 2 \\ 1 & 1 & 2 \end{Bmatrix}$			2.4511	4.8	2	2	2	1.6129	8.8	$\begin{Bmatrix} -3 & 1 & 8 \\ 0 & 2 & 8 \end{Bmatrix}$		
3.8205	27.4	0	0	4	2.3573	12.2	$\begin{Bmatrix} -3 & 1 & 4 \\ 0 & 2 & 4 \end{Bmatrix}$			1.6032	7.5	$\begin{Bmatrix} 3 & 1 & 8 \\ 3 & 3 & 4 \end{Bmatrix}$		
3.6379	6.7	-1	1	3	2.2856	23.2	$\begin{Bmatrix} -2 & 0 & 6 \\ 1 & 1 & 6 \end{Bmatrix}$			1.5546	12.8	$\begin{Bmatrix} -5 & 1 & 6 \\ 1 & 3 & 6 \end{Bmatrix}$		
3.0778	68.9	-1	1	4	2.1454	74.5	-4	0	4	1.5418	16.0	$\begin{Bmatrix} -4 & 0 & 8 \\ -2 & 2 & 8 \end{Bmatrix}$		
3.0577	43.4	2	0	4	1.9089	8.1	0	0	8	1.5341	11.6	$\begin{Bmatrix} 2 & 2 & 8 \\ 4 & 0 & 8 \end{Bmatrix}$		
2.9859	100.0	$\begin{Bmatrix} 0 & 2 & 0 \\ 3 & 1 & 0 \end{Bmatrix}$			1.8951	17.8	$\begin{Bmatrix} 1 & 3 & 2 \\ -4 & 2 & 2 \\ -5 & 1 & 2 \\ 4 & 2 & 2 \end{Bmatrix}$			1.4915	19.7	$\begin{Bmatrix} 0 & 4 & 0 \\ 6 & 2 & 0 \end{Bmatrix}$		
2.7856	8.0	-3	1	2	1.8291	7.1	-1	3	3	1.4653	7.9	1	1	10
2.6298	6.3	$\begin{Bmatrix} -1 & 1 & 5 \\ 1 & 1 & 5 \end{Bmatrix}$			1.7938	13.7	$\begin{Bmatrix} -2 & 0 & 8 \\ -1 & 1 & 8 \end{Bmatrix}$			1.4114	7.7	$\begin{Bmatrix} -2 & 4 & 2 \\ -5 & 3 & 2 \end{Bmatrix}$		
2.5879	16.2	$\begin{Bmatrix} 2 & 2 & 0 \\ 4 & 0 & 0 \end{Bmatrix}$			1.7446	28.9	$\begin{Bmatrix} -1 & 3 & 4 \\ -4 & 2 & 4 \end{Bmatrix}$							
2.5192	6.7	-1	1	3										
2.3873	20.6	1	3	2										

Table 3.7 Experimental X-ray powder data for $Rb_3Na(RuO_4)_2$ with $d > 1.3 \text{ \AA}$

$d_{obs} [\text{\AA}]$	I/I_0	h	k	l	$d_{obs} [\text{\AA}]$	I/I_0	h	k	l	$d_{obs} [\text{\AA}]$	I/I_0	h	k	l
5.2618	17.5	1	0	0	2.1895	41.9	2	0	2	1.5796	9.1	2	0	4
4.3790	32.7	1	0	1	1.9895	5.9	1	1	3	1.5194	15.8	2	2	0
3.9486	14.9	0	0	2	1.9750	2.9	0	0	4	1.5132	6.6	1	0	5
3.1582	75.7	1	0	2	1.9288	6.2	2	1	1	1.4602	2.9	3	1	0
3.0376	100.0	1	1	0	1.8614	5.2	2	0	3	1.4354	3.0	3	1	1
2.8354	4.8	1	1	1	1.8487	9.4	1	0	4	1.4182	4.7	2	2	2
2.6315	13.6	$\begin{Bmatrix} 0 & 0 & 3 \\ 2 & 0 & 0 \end{Bmatrix}$			1.7766	28.4	2	1	2	1.4020	10.8	2	1	4
					1.7543	20.0	3	0	0	1.3694	10.9	3	1	2
2.4959	7.0	2	0	1	1.6559	4.7	1	1	4	1.3547	4.5	2	0	5
2.4081	8.0	1	1	2	1.6030	3.2	3	0	2	1.3165	3.5	2	2	3
2.3543	17.1	1	0	3	1.5873	9.5	2	1	3	1.3113	2.5	3	0	4

The measured intensities of both compounds at room temperature are listed in Table 3.6 and Table 3.7, respectively. The structure refinement was performed using the GSAS program package [35]. The details on the powder refinement data are given in Table 3.8.

Table 3.8 Powder refinement data of HT-K₃Na(RuO₄)₂

Compound	HT-K ₃ Na(RuO ₄) ₂
temperature	473 K
molar mass	470.42 g/mol
density (calculated)	3.242 g/cm ³
Least squares refinement data	
parameters refined	14
measurement range 2θ	2.99 – 44.98°
hkl -range	$0 \leq h \leq 5, 0 \leq k \leq 3, -8 \leq l \leq 8$
measured reflections	4053
w R _p	8.56 %
R _p	6.49 %
Reduced χ^2	2.13
R (F ²)	18.00
depository number	CSD-416040

The phase transition is complete in the X-ray pattern at 473 K which was refined as a high temperature hexagonal phase. The Rietveld refinement plot of this high temperature phase of K₃Na(RuO₄)₂ is shown in Figure 3-18.

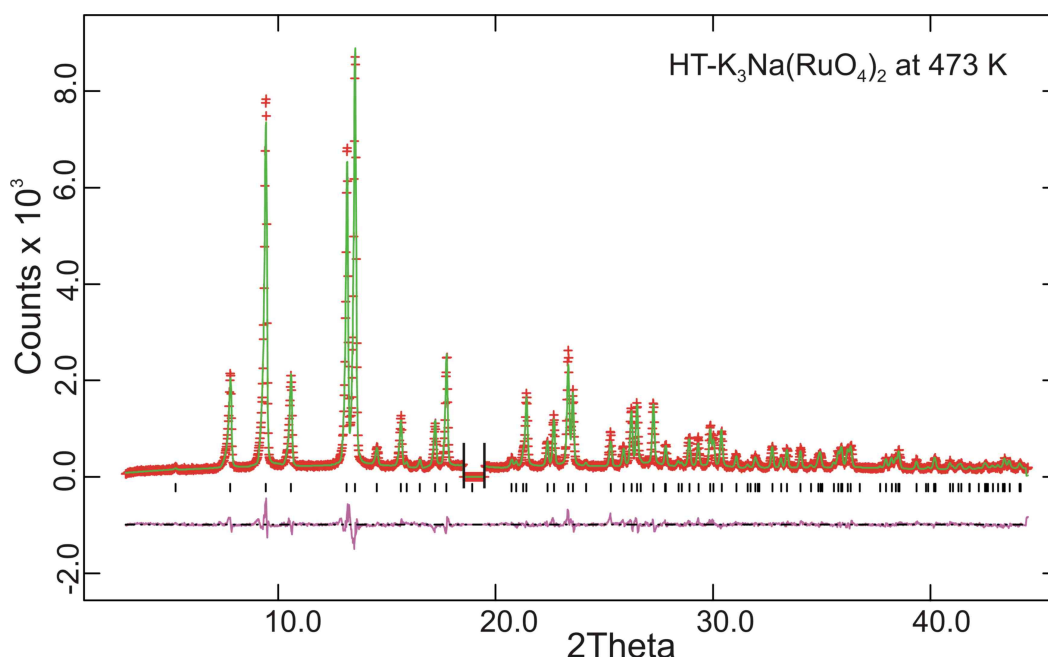


Figure 3-18 Rietveld refinement of the HT phase of K₃Na(RuO₄)₂ (excluded region at $\sim 2\theta = 19^\circ$ is to avoid the spurious reflection arising from the detector)

3.3.5 Structure description

According to the crystal structure solutions both the compounds consist of isolated RuO₄ tetrahedra. In K₃Na(RuO₄)₂, the RuO₄ tetrahedra are separated by sodium and potassium cations, see Figure 3-19. All oxygen atoms are bound to one ruthenium atom. While in the trigonal phase one threefold symmetry axis of the tetrahedra is identical with the

crystallographic *c*-axis (see Figure 3-19a), the RuO₄ tetrahedra in the LT-phase are tilted and not aligned parallel to [001] anymore (see Figure 3-19b), so the threefold symmetry is destroyed here. In both phases the Ru-O1 bond parallel or almost parallel to *c* is distinctly shorter than the other Ru-O bonds. The Ru-O1 distance in the HT phase is obviously too short.

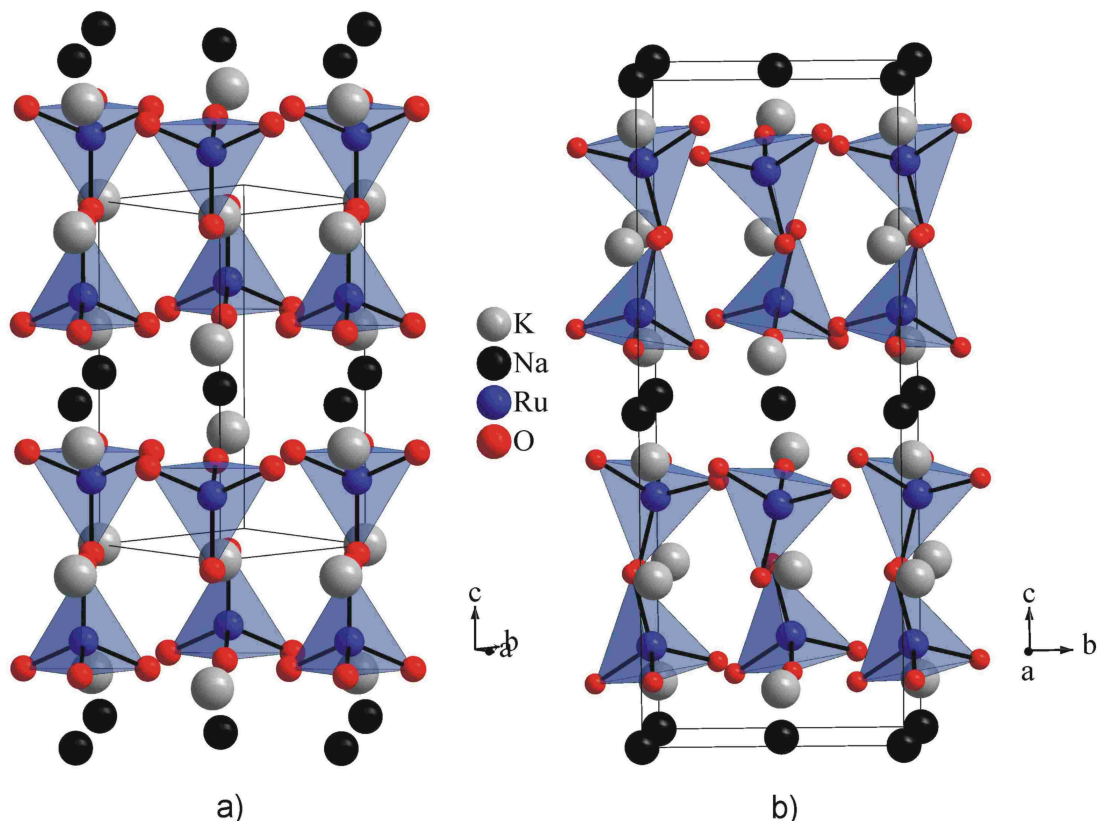


Figure 3-19 Crystal structure of K₃Na(RuO₄)₂: a) HT phase above 467 K, view along [-110]; b) LT phase at room temperature, view along [-100]

During the powder refinement, this distance was fixed with the LT value at first and released after all parameters were refined into stable values. Nevertheless it went into the given value. Obviously, an averaging effect has to be accounted for the RuO₄ tetrahedra tumbling along the *c* axis, causing short distances. Shifting the O1 atom by 0.29 Å within the *a/b* plane (a bit off-centred) from its refined position gives the expected Ru-O1 distance of 1.72 Å and K2-O1 distance of 2.60 Å, or shifting the O1 atom from its refined position along the *c* axis in the direction of K2 atom also results in expected distances. While the first coordination spheres of Na (six oxygen atoms in form of a slightly distorted octahedron) and Ru are less affected from the phase transition, the coordination polyhedra of the potassium atoms differ significantly in both the phases. In the HT-phase the two

crystallographically independent potassium ions are surrounded by twelve K1 and ten K2 oxygen atoms, respectively. For each KO_x polyhedron six oxygen atoms are in plane with the centring cation forming a regular hexagon which is capped by two triangles forming an elongated trigonal anti-prism (K1, Figure 3-20a), or by one single oxygen atom and a triangle of oxygen atoms (K2, Figure 3-20b). In the LT-phase they are shifted away from the centres (see Figure 3-20c and Figure 3-20d) resulting in smaller coordination numbers, 8+2 instead of 12 for K1 and 9 instead of 10 for K2. The rest of the formerly coordinating oxygen atoms are now situated in distances of 4.053 Å (K1) and 3.623 Å (K2) and have lost direct contact.

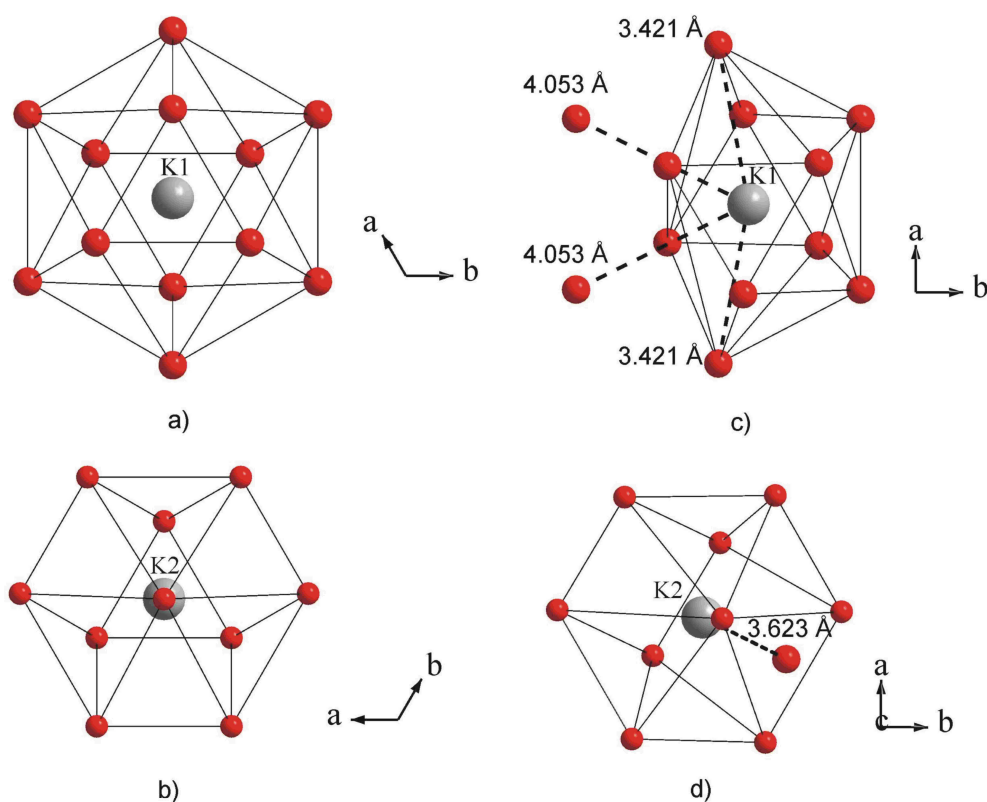


Figure 3-20 Oxygen coordination of K^+ ions in a), b) HT phase and c), d) LT phase of $K_3Na(RuO_4)_2$, respectively

Crystallographic data and the details from the single crystal X-ray diffraction are given in Table 3.9 and Table 3.10, respectively. Atomic coordinates and isotropic displacement parameters are given in Table 3.11, while anisotropic displacement parameters are listed in Table 3.12.

Table 3.9 Crystallographic data of K₃Na(RuO₄)₂, at room temperature and at 473 K (HT), and Rb₃Na(RuO₄)₂ at room temperature

Phase	RT-K ₃ Na(RuO ₄) ₂	HT-K ₃ Na(RuO ₄) ₂	Rb ₃ Na(RuO ₄) ₂
space group	<i>C2/c</i> (No. 15)	<i>P</i> $\bar{3}$ <i>m1</i> (No. 164)	<i>P</i> $\bar{3}$ <i>m1</i> (No. 164)
a	10.323(8) Å	6.0163(7) Å	6.0784(3) Å
b	5.989(4) Å	a	a
c	15.278(7) Å	7.6855(14) Å	7.8994(6) Å
β	90.49(5)°	90°	90°
unit cell volume V	944.5(7) Å ³	240.92(5) Å ³	252.76(3) Å ³
no. of formula units Z	4	1	1

Table 3.10 Details of the single crystal refinement of K₃Na(RuO₄)₂ and Rb₃Na(RuO₄)₂

Compound	K ₃ Na(RuO ₄) ₂	Rb ₃ Na(RuO ₄) ₂
temperature	room temperature	room temperature
molar mass	470.43 g/mol	609.54 g/mol
density (calculated)	3.308 g/cm ³	4.005 g/cm ³
diffractometer	Bruker SMART-APEX CCD	Bruker SMART-APEX CCD
wavelength	Mo-K α (λ = 0.71073 Å)	Mo-K α (λ = 0.71073 Å)
monochromator	Graphite	Graphite
absorption coefficient μ	4.576 mm ⁻¹	17.391 mm ⁻¹
measurement range 2θ	2.66 - 55.98°	5.16 - 57.09°
<i>hkl</i> -range	-13 $\leq h \leq$ 13 -7 $\leq k \leq$ 7 -20 $\leq l \leq$ 20	-8 $\leq h \leq$ 8 -8 $\leq k \leq$ 8 -10 $\leq l \leq$ 10
measured reflections	4974	4596
R _{int}	5.53 %	10.33 %
domain fractions $f_1 / f_2 / f_3$	77.67 / 9.87 / 12.46	-
independent reflections	1231	281
independent reflections ($I > 2\sigma(I)$)	1038	276
parameters	68	21
R(F) ($I > 2\sigma(I)$)	4.27 %	2.35 %
R _w (F ²) ($I > 2\sigma(I)$)	8.95 %	5.51 %
R(F) (all data)	5.11 %	2.39 %
R _w (F ²) (all data)	9.23 %	5.53 %
goodness-of-fit ($I > 2\sigma(I)$)	1.072	1.213
goodness-of-fit (all data)	1.072	1.213
extinction coefficient	-	0.025(3)
max./min. residual electron density	1.13 / -1.06 e ⁻ Å ⁻³	0.65 / -1.02 e ⁻ Å ⁻³
weighting scheme w	$q_1 = 0.0242$ $q_2 = 12.6983$	$q_1 = 0.0155$ $q_2 = 0.7646$
depository number	CSD-416039	CSD-416038

Beneath the short Ru-O bond mentioned above, another striking short distance is found between K2 and O1. In the HT-phase both short bonds are parallel to the *c*-axis and are part of the first coordination sphere of the same oxygen atom O1, so the Ru-O1-K2 angle is 180°. In the LT-phase this angle is decreased to 154.6°. The HT-phase of K₃Na(RuO₄)₂ is isotypic to glaserite, K₃Na(SO₄)₂ [95], and some related compounds, e.g. K₃Na(SeO₄)₂ [96-98] are exhibiting a similar phase transition.

$K_3Na(RuO_4)_2$ and $Rb_3Na(RuO_4)_2$, Ruthenium Glaserites

Table 3.11 Atomic coordinates and isotropic displacement parameters U_{iso} in \AA^2 of $K_3Na(RuO_4)_2$ (LT and HT) and $Rb_3Na(RuO_4)_2$, U_{eq} is defined as $\exp[-8\pi^2 U(\sin^2\theta/\lambda^2)]$

LT-$K_3Na(RuO_4)_2$					
Atoms	Wyckoff Position	x	y	z	U_{eq}
K1	4e	0	0.0509(5)	1/4	0.0329(6)
K2	8f	0.3298(2)	0.0211(3)	0.08126(10)	0.0254(3)
Na	4a	0	0	0	0.0198(7)
Ru	8f	0.16409(7)	0.51827(8)	0.14232(3)	0.01524(16)
O1	8f	0.1745(9)	0.4446(11)	0.2520(3)	0.0443(17)
O2	8f	0.3161(6)	0.5317(12)	0.0918(5)	0.0374(17)
O3	8f	0.0780(7)	0.7657(10)	0.1175(4)	0.0308(14)
O4	8f	0.0846(7)	0.2973(10)	0.0842(4)	0.0266(13)
HT-$K_3Na(RuO_4)_2$					
Atoms	Wyckoff Position	x	y	z	U_{eq}
K1	1a	0	0	0	0.0460(2)
K2	2d	2/3	1/3	0.3410(4)	0.0384(1)
Na	1b	0	0	1/2	0.0321(4)
Ru	2d	2/3	1/3	0.78551(16)	0.0171(3)
O1	2d	2/3	1/3	0.0009(13)	0.1253(2)
O2	6i	0.3596(9)	0.1798(4)	0.6948(6)	0.0402(2)
$Rb_3Na(RuO_4)_2$					
Atoms	Wyckoff Position	x	y	z	U_{eq}
Rb1	1a	0	0	0	0.0294(3)
Rb2	2d	2/3	1/3	0.34149(9)	0.0196(2)
Na	1b	0	0	1/2	0.0172(8)
Ru	2d	2/3	1/3	0.78011(7)	0.0139(2)
O1	2d	2/3	1/3	0.9973(9)	0.050(2)
O2	6i	0.3549(6)	0.1774(3)	0.6933(5)	0.0272(7)

Table 3.12 Anisotropic displacement parameters of LT- $K_3Na(RuO_4)_2$ and $Rb_3Na(RuO_4)_2$. The U_{ij} are defined as $-2\pi^2 (U_{11}h^2a^{*2} + U_{22}k^2b^{*2} + U_{33}l^2c^{*2} + U_{12}hka^*b^* + U_{13}hla^*c^* + U_{23}klb^*c^*)$

$K_3Na(RuO_4)_2$	U_{11}	U_{22}	U_{33}	U_{23}	U_{13}	U_{12}
K1	0.0462(18)	0.0303(13)	0.0223(11)	0	0.0034(12)	0
K2	0.0286(10)	0.0278(9)	0.0199(7)	0.0032(6)	0.0001(7)	-0.0007(8)
Na	0.020(2)	0.018(2)	0.0221(17)	0.0018(15)	0.0023(19)	-0.0014(18)
Ru	0.0181(3)	0.0143(3)	0.0133(2)	-0.0004(2)	0.0002(2)	0.0006(3)
O1	0.073(6)	0.045(4)	0.015(3)	0.005(3)	-0.004(3)	-0.003(4)
O2	0.021(3)	0.042(4)	0.050(4)	-0.015(3)	0.012(3)	0.001(3)
O3	0.039(4)	0.025(3)	0.028(3)	0.001(2)	-0.009(3)	0.013(3)
O4	0.030(4)	0.028(3)	0.022(3)	-0.008(2)	-0.008(3)	-0.006(3)
$Rb_3Na(RuO_4)_2$	U_{11}	U_{22}	U_{33}	U_{23}	U_{13}	U_{12}
Rb1	0.0339(4)	0.0339(4)	0.0203(6)	0	0	0.0170(2)
Rb2	0.0202(3)	0.0202(3)	0.0183(4)	0	0	0.01010(15)
Na	0.0143(12)	0.0143(12)	0.023(2)	0	0	0.0071(6)
Ru	0.0138(2)	0.0138(2)	0.0139(3)	0	0	0.00692(12)
O1	0.066(3)	0.066(3)	0.016(3)	0	0	0.0331(17)
O2	0.0154(15)	0.0252(12)	0.0378(17)	-0.0033(7)	-0.0066(14)	0.0077(7)

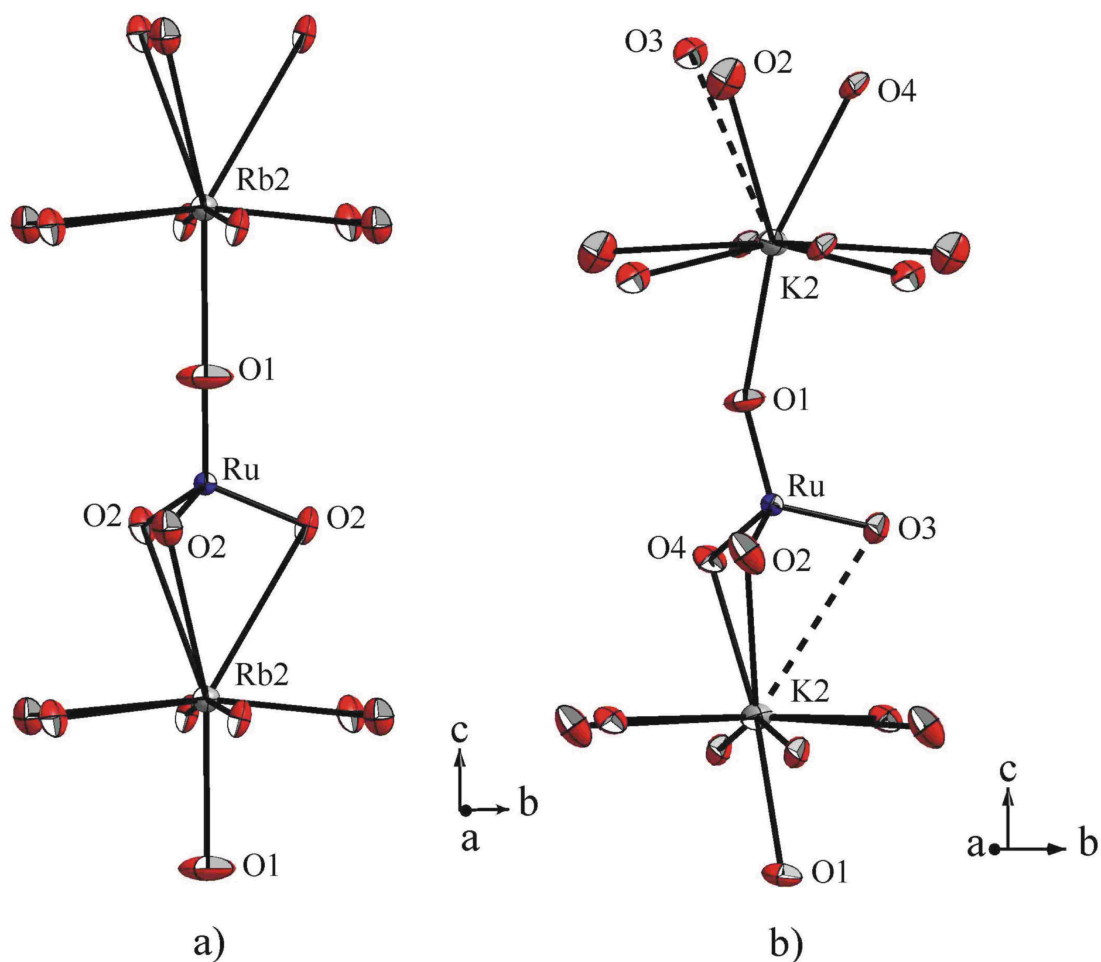


Figure 3-21 Sequence of RuO_4 and AO_x coordination polyhedra parallel to the c axis in a) $Rb_3Na(RuO_4)_2$ and b) $LT-K_3Na(RuO_4)_2$

$Rb_3Na(RuO_4)_2$ is also isotypic to glaserite (see Figure 3-22) and to the HT-phase of $K_3Na(RuO_4)_2$, but the compound does not show a structural phase transition in the investigated temperature range down to 100 K. Ru-O and Na-O bond lengths are almost identical to those in the potassium compound. Similar to $K_3Na(RuO_4)_2$, $Rb_3Na(RuO_4)_2$ also shows characteristic structural features such as short Ru-O1 and Rb2-O1 distances parallel to the c -axis (see Table 3.13).

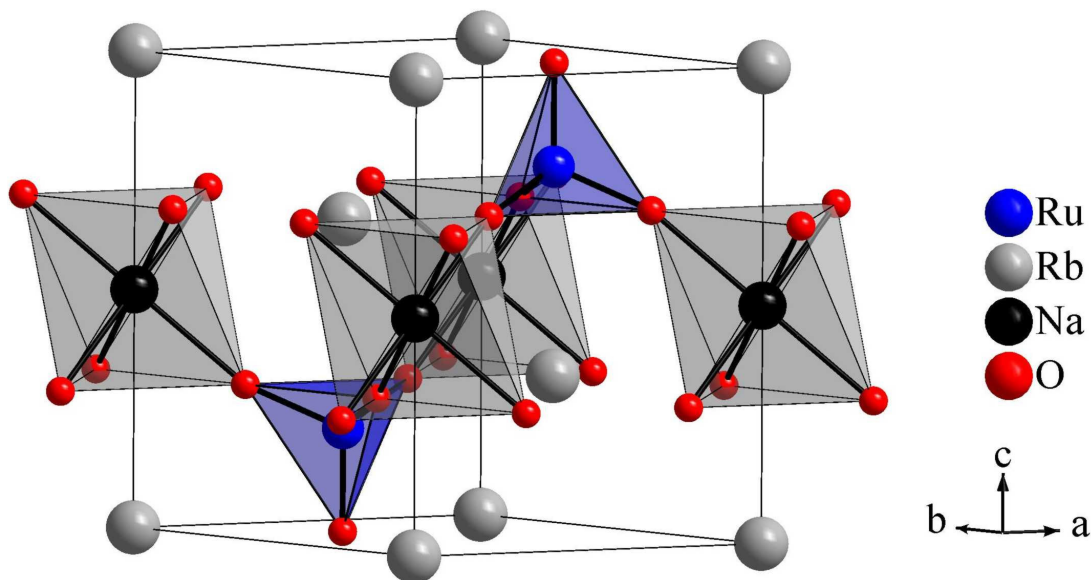


Figure 3-22 Unit cell of $Rb_3Na(RuO_4)_2$

$K_3Na(RuO_4)_2$ shows phase transitions at 430 K and at 467 K indicated by specific heat measurements (Figure 3-23) and by high temperature X-ray diffraction. As observed from the specific heat measurements, the symmetry decreases from trigonal to monoclinic during the step at 467 K, and the HT-phase crystallises in space group $P\bar{3}m1$, while the LT-phase can be described in the monoclinic space group $C2/c$. With the transition into the monoclinic phase, the threefold axis is lost, the length of the c axis is doubled, and each of the mirror planes (related to each respective domain) is transformed into the glide plane c . The symmetry decrease can be split into two steps, one *translationengleichen* of index 3 and one *klassengleichen* of index 2. Due to the former one a triple twinned domain pattern develops.

Table 3.13 Selected bond lengths (Å) for LT- and HT-K₃Na(RuO₄)₂ and for Rb₃Na(RuO₄)₂

LT-K₃Na(RuO₄)₂					
Atoms	Distance [Å]	Atoms	Distance [Å]	Atoms	Angle
K1–O3 ⁱ	2.773(6) [2x]	K2–O2	3.065(8)	O1–Ru–O2	112.8(4)°
K1–O1	2.967(9) [2x]	K2–O3 ⁱ	3.070(8)	O1–Ru–O3	116.6(3)°
K1–O2 ⁱⁱ	3.063(8) [2x]	K2–O3 ⁱⁱⁱ	3.623(6)	O1–Ru–O4	108.4(3)°
K1–O4	3.065(6) [2x]	Na–O4	2.360(5) [2x]	O2–Ru–O3	108.5(3)°
K1–O1 ⁱⁱ	3.421(10) [2x]	Na–O2 ⁱⁱⁱ	2.378(6) [2x]	O2–Ru–O4	102.9(3)°
K1–O1 ⁱ	4.053(8) [2x]	Na–O3 ⁱ	2.412(5) [2x]	O3–Ru–O4	106.6(3)°
K2–O1 ⁱⁱ	2.589(6)	Ru–O1	1.735(5)	Ru–O1–K2 ^v	154.6(4)°
K2–O4 ⁱⁱⁱ	2.897(6)	Ru–O2	1.756(6)		
K2–O2 ⁱ	2.939(8)	Ru–O3	1.767(5)		
K2–O4 ^{iv}	2.952(8)	Ru–O4	1.789(5)		
K2–O3 ^{iv}	2.999(8)				
K2–O4	3.024(8)	Ru–K2 ⁱⁱⁱ	3.425(2)		
K2–O2 ⁱⁱⁱ	3.048(8)				
HT-K₃Na(RuO₄)₂					
Atoms	Distance [Å]	Atoms	Distance [Å]	Atoms	Angle
K1–O2 ^{vi}	3.002(5) [6x]	Na–O2	2.398(5) [6x]	O1–Ru–O2	113.54(2)° [3x]
K1–O1 ^{vi}	3.474(1) [6x]	Ru–O1	1.655(10)	O2–Ru–O2 ^{ix}	105.17(2)° [3x]
K2–O1 ^{vi}	2.614(11)	Ru–O2	1.745(5) [3x]	Ru–O1–K2 ^{viii}	180°
K2–O2 ^{vii}	3.024(4) [6x]				
K2–O2	3.155(5) [3x]	Ru–K2 ^{viii}	3.4146(3)		
Rb₃Na(RuO₄)₂					
Atoms	Distance [Å]	Atoms	Distance [Å]	Atoms	Angle
Rb1–O2 ^{vi}	3.060(4) [6x]	Na–O2	2.412(4) [6x]	O1–Ru–O2	112.68(13)° [3x]
Rb1–O1 ^{vi}	3.5094(2) [6x]	Ru–O1	1.715(7)	O2–Ru–O2 ^{ix}	106.08(15)° [3x]
Rb2–O1 ^{vi}	2.719(7)	Ru–O2	1.779(3) [3x]	Ru–O1–Rb2 ^{viii}	180°
Rb2–O2 ^{vii}	3.0537(4) [6x]				
Rb2–O2	3.227(4) [3x]	Ru–Rb2 ^{viii}	3.4649(9)		

Symmetry codes: (i) $x, y-1, z$; (ii) $-x+0.5, y-0.5, -z+0.5$; (iii) $-x+0.5, -y+0.5, -z$; (iv) $x+0.5, y-0.5, z$; (v) $-x+0.5, y+0.5, -z+0.5$; (vi) $x, y, z-1$; (vii) $-x+1, -y, -z+1$; (viii) $x, y, z+1$; (ix) $-y+1, x-y, z$

The trend in phase transition for K₃Na(RuO₄) is similar to the phase transition as observed for K₃Na(SeO₄)₂ [96] with the formation of an intermediate monoclinic or orthorhombic phase in both the compounds. In this study the intermediate transition was not explored. Apart from Na₂RuO₄, all these alkali ruthenates mentioned above realise the same structure types as the corresponding sulphates, i. e. β-K₂SO₄ and glaserite, K₃Na(SO₄)₂ [91,95], which have been studied owing to their interesting crystal chemistry [99-101].

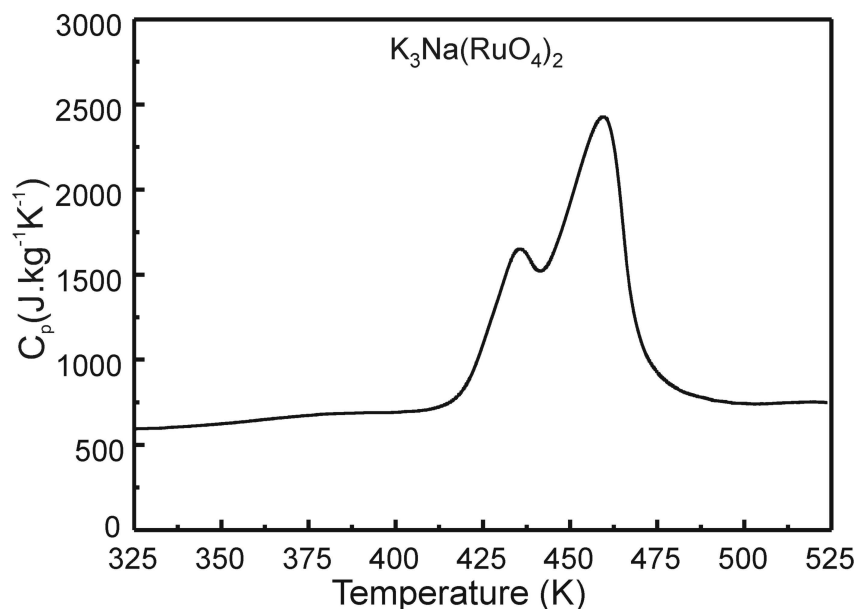


Figure 3-23 Specific heat of K₃Na(RuO₄)₂

Glaserites have the general formula $A_3B(TO_4)_2$, where A usually is significantly larger than B , but sometimes of the same size [102]. Among others, K₃Na(SeO₄)₂ [96-98], K₃Na(CrO₄)₂ [103,104], K₃Na(MoO₄)₂ [105], Na₃Fe(PO₄)₂ [106], K₃V(VO₄)₂ [107] and K₃Na(BeF₄)₂ [108] are crystallising in the glaserite type of structure, and some of these compounds show a similar phase transition as K₃Na(RuO₄)₂ performs. During this phase transition the main structural changes from the trigonal HT into the monoclinic LT form are the tilting of the TO_4 tetrahedra and the decrease of the coordination number of both the potassium atoms (due to a shift off the centre of the trigonal KO₁₂/KO₁₀ polyhedra). These changes should be the main driving forces for the phase transition.

Obviously the transition temperature correlates strongly with the size of the “ A ” cation for a given further composition, which is clearly seen for the first time from these results. So while K₃Na(RuO₄)₂ performs a transition at 467 K, the slightly larger Rb⁺ cation stabilises the trigonal structure for Rb₃Na(RuO₄)₂ in the whole investigated temperature range down to 100 K. This is reasonable due to the fact that the voids are filled by A cations more sufficiently by larger cations, and a reduction of the coordination numbers, as observed in the monoclinic phase, is disadvantageous. The same correlation was found for the corresponding molybdate, K₃Na(MoO₄)₂, where an excess of the remarkably smaller sodium in K_{2.5}Na_{1.5}(MoO₄)₂, occupying mainly the tenfold coordinated positions, prevents the transition, so the monoclinic structure is stable [105]. Another dependence of the phase transition temperature is found to the size of the TO_4 anion. Within the group of

K₃Na(TO₄)₂ compounds, the transition temperatures correspond with the radii of the hexavalent *T* cations and roughly with the average *T*-O bond lengths, see Table 3.14. Small deviations of the bond lengths sequence from that of the cationic radii should mainly indicate different degrees of thermal libration movements (or possibly differences in crystal qualities) which is also outlined from the strong differences in the short K2-O1 distances and thus must be considered carefully. The transition temperature of K₃Na(RuO₄)₂ is close below that of the molybdate, as expected from the ionic radii. Considering the TO₄ tetrahedra it has to be noticed that for all the glaserites performing a phase transition, the *T*-O1 bond along the *c* axis is significantly shorter than the other three. For the only exception, K₃Na(SO₄)₂, no phase transition has been detected. Together with the thermal displacement parameters being the largest for O1 in all these compounds (see Figure 12) the short bonds are an expression of a strong librational movement. The short *T*-O1 bond, the striking short K2-O1 distance of around 2.55 Å parallel to the *c* axis found in all compounds considered here, and, further following the *c* axis, an unfavourable face-sharing of the TO₄ and KO₁₀ polyhedra, seem to indicate the existence of a remarkable internal strain, which is relaxed below the transition temperature. With a shift of the K⁺ ions off the centre, the heavy thermal libration of the TO₄ tetrahedra is partially hindered or frozen, the threefold symmetry is broken and a tilting of the TO₄ tetrahedra results, including a distortion of the KO_x polyhedra and a change of the face sharing into edge sharing TO₄ and KO_x polyhedra. As a support for this interpretation serves the permanence or even a slight elongation of the interatomic distances parallel to [001], although the *c* axis is shortened slightly stronger than *a* and *b*. A decrease of the size of the *T*⁶⁺ cation as well as an increase of the radius of the monovalent “A” cations, in particular on the twelve-fold coordinated sites, should stabilise the trigonal symmetry, what is observed for K₃Na(SO₄)₂ and Rb₃Na(RuO₄)₂.

The crystal structure of Na₂RuO₄ exhibits infinite chains of RuO₅ trigonal bipyramids connected by common vertices. In contrast to Na₂RuO₄, the crystal structures of these new compounds, K₃Na(RuO₄)₂ and Rb₃Na(RuO₄)₂, consist of isolated tetrahedral RuO₄ units and resemble to K₂RuO₄ and the ruthenates of the heavier alkali metals. Thus, variations of the synthetic approach resulted in mixtures of Na₂RuO₄ and the respective A₃Na(RuO₄)₂ (A = K, Rb) compound. No hints for other compositions A_{3-x}Na_{1+x}(RuO₄)₂, possibly adopting the Na₂RuO₄ structure type, were found.

Table 3.14 M-O bond lengths at room temperature and phase transition temperatures of some compounds crystallising in the glaserite type of structure

Compound	Average T-O bond length [Å]	K(2)-O(1) bond length [Å]	Radii ⁴ of T ⁶⁺ in tetrahedral coordination	Phase transition temperature
K ₃ Na(SO ₄) ₂ [95]	1.472	2.547	0.26	-
K ₃ Na(CrO ₄) ₂ [103]	1.639 (230 K)	2.595 (230 K)	0.40	239 K
K ₃ Na(SeO ₄) ₂ [96]	1.631	2.557	0.42	346 K
K ₃ Na(RuO ₄) ₂ [this work]	1.762	2.589	~0.54 ^{a)}	467 K
K ₃ Na(MoO ₄) ₂ [105]	1.756	2.553	0.55	513 K
K ₃ Na(WO ₄) ₂ [109]	1.848	2.557	0.42	523 K
Rb ₃ Na(RuO ₄) ₂ [this work]	1.763	2.719 (Rb-O)	~0.54 ^{a)}	-

^{a)} estimated by extrapolation from given values of Mo, W, Re, Ru, and Os in penta-, hexa-, and heptavalent state [4]

3.3.6 Magnetic measurements

Magnetic measurements were performed on polycrystalline powder samples using a SQUID-Magnetometer (MPMS 5.5, Quantum Design) between 5 and 350 K in magnetic fields up to 5 T. Measurements of the inverse magnetic susceptibilities obey the Curie-Weiss law down to about 70 K, see Figure 3-24 and Figure 3-25. Fitting the Curie and Weiss constants the values obtained are $C = 1.0215$ emu K/mol and $\theta \sim -49$ K for K₃Na(RuO₄)₂, and $C = 0.9941$ emu K/mol and $\theta \sim -35$ K for Rb₃Na(RuO₄)₂, in an applied field of 5 T. The effective magnetic moments of $\mu_{eff} = 2.85 \mu_B$ and $\mu_{eff} = 2.82 \mu_B$ for K₃Na(RuO₄)₂ and Rb₃Na(RuO₄)₂, respectively, are close to the ideal moment for the spin-only d^2 ($S = 1$) configuration, $\mu_{so} = 2.83 \mu_B$, thus confirming the hexavalent oxidation state for ruthenium. At temperatures below 60 K, the inverse susceptibility curves diverge from the linear behaviour indicating the presence of antiferromagnetic interactions with $T_N \sim 28$ K in K₃Na(RuO₄)₂ and $T_N \sim 11$ K in Rb₃Na(RuO₄)₂.

Thus from the measurements of magnetic susceptibility weak antiferromagnetic interactions between the d^2 centres are observed. These findings are similar to that of the ternary alkali oxo-ruthenates(VI) as described in earlier respective sections. As expected, the strength of the antiferromagnetic interactions indicated by the Néel temperature is correlated to the crystal structure, especially to the interatomic distances between the paramagnetic ruthenium atoms.

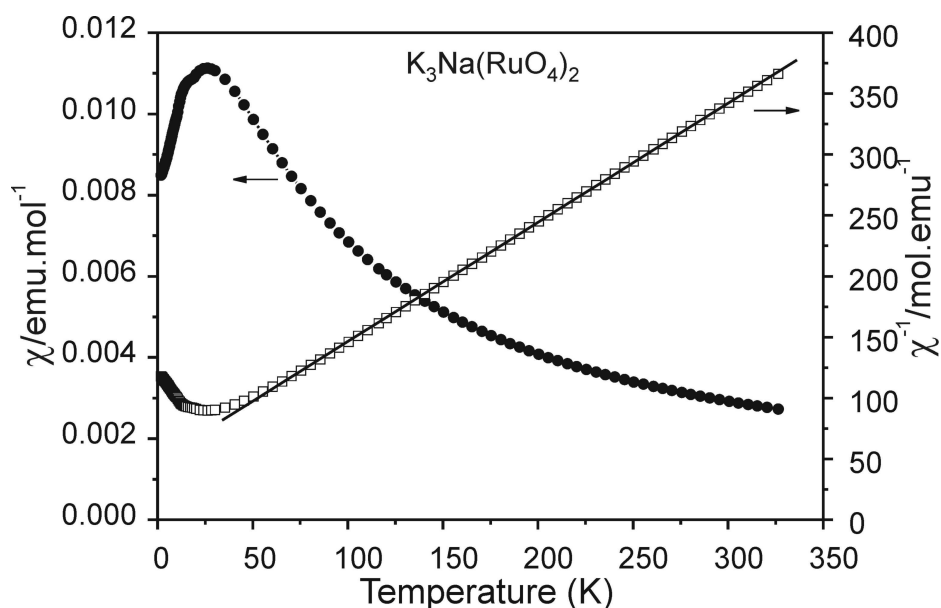


Figure 3-24 Magnetic susceptibility of $K_3Na(RuO_4)_2$ represented as χ vs. T (circles) and χ^{-1} vs. T (squares) in an applied field of 5 T. The full line represents the linear fit using the Curie-Weiss law

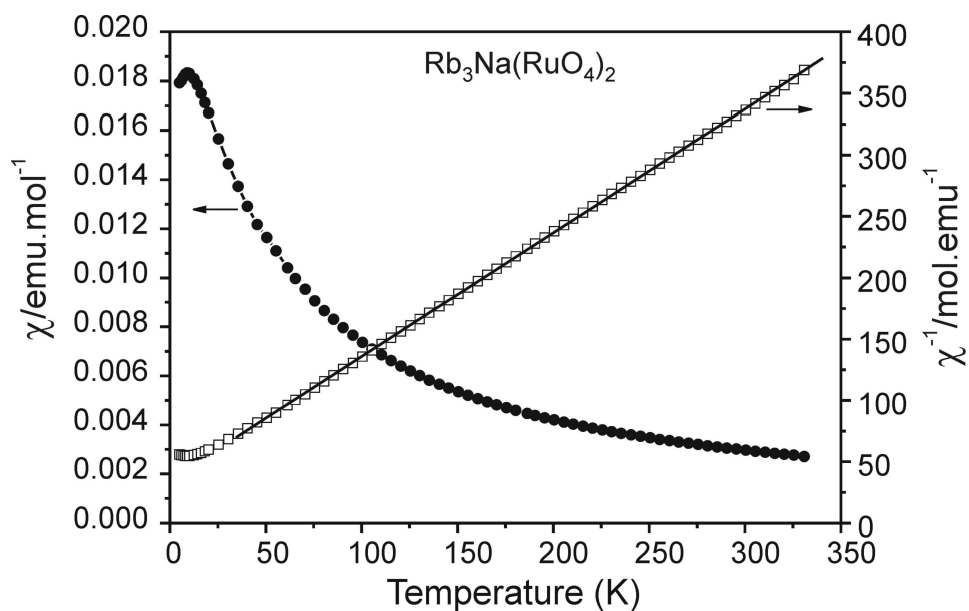


Figure 3-25 Magnetic susceptibility of $Rb_3Na(RuO_4)_2$ represented as χ vs. T (circles) and χ^{-1} vs. T (squares) in an applied field of 5 T. The full line represents the linear fit using the Curie-Weiss law

3.3.7 Conductivity measurements

The conductivity measurements were carried out on polycrystalline powder samples with the standard four point probe method. The resistance remains constant up to 100 K in both the compounds and above 100 K the compounds display a semi-conducting behaviour.

3.4 Magnetism in hexavalent alkali oxo-ruthenates

The magnetic phenomena in all these new alkali hexavalent oxo-ruthenates exhibit an interesting correlation with respect to the alkali metal cation and to the distances between the spin bearing ruthenium cations. As seen from the above sections, the magnetic transition temperature varies with respect to the size of the alkali metal cation. In the case of A_2RuO_4 compounds ($A = Cs, Rb, K, Na$), as the ruthenium tetrahedrons are packed more closely going from cesium to sodium, the Ru-Ru distances are shortened which results in the increase of Neél temperatures. Finally, the tetrahedral coordination of ruthenium is lost in Na_2RuO_4 which contains interconnected $[RuO_5]$ trigonal bipyramids linked via oxygen atoms.

Also, a comparison of the ternary alkali oxo-ruthenates is made with the quaternary alkali metal ruthenium glaserites. Here again the shortening of the Ru-Ru distances is observed which enhances the Neél temperature, see Table 3.15. The neutron diffraction study of the compound with highest Neél temperature, Na_2RuO_4 , is described in the respective section.

Table 3.15 Neél-Temperatures and shortest Ru–Ru distances in some alkali ruthenates.

Compound	Shortest Ru–Ru distance	Neél-Temperature
Cs_2RuO_4 [81]	5.36 Å	Not investigated
Rb_2RuO_4	5.03 Å	9 K
$Rb_3Na(RuO_4)_2$	4.93 Å	11 K
K_2RuO_4	4.82 Å	14 K, 4 K
$K_3Na(RuO_4)_2$	4.73 Å	28 K
Na_2RuO_4	3.51 Å	35.5 K

This interesting trend is quite convincing how the magnetic interactions are enhanced on reduction of the distances between the metal atoms (in this case ruthenium). Hence, it would be interesting to reveal the coordination of ruthenium with oxygen in the smallest alkali metal analogue (lithium), to have a complete overview on the family of these compounds.

3.5 Na₂RuO₃, Sodium oxo-ruthenate (IV)

Na₂RuO₃ was reported to be orthorhombic in the studies of I. S. Shaplygin and co-workers [70]. Only powder diffraction was studied whereas no structural details were investigated. This compound was initially obtained by the thermal decomposition Na₂RuO₄ under argon atmosphere, as mentioned in the respective chapter. Thus, a bulk amount of this compound was synthesised to closely investigate its crystal structure and properties. The crystal structure obtained from powder refinement and the magnetic properties are discussed ahead.

3.5.1 Synthesis

Na₂RuO₃ was obtained by the thermal decomposition of Na₂RuO₄ under argon atmosphere. The compound was obtained by heating Na₂RuO₄ at 1123 K for 2 days under the flow of argon. A black homogenous powder of Na₂RuO₃ was obtained, but attempts to obtain single crystals by annealing were unsuccessful.

3.5.2 Infrared spectroscopy

Infrared measurements of Na₂RuO₃ were performed with a Fourier-Transform-Spectrometer (IFS 113v, Bruker). 1-2 mg of the sample and 400 mg of KBr (Aldrich, 99+%, dried in vacuum at 473 K) were pressed into a pellet. The modes obtained are 528 cm⁻¹(s), 644 cm⁻¹(m), 804 cm⁻¹(m), 880 cm⁻¹(m), 1100 cm⁻¹(m), 1262 cm⁻¹(m) and 1439 cm⁻¹(m). The strong mode observed at 528 cm⁻¹ is similar as observed for RuO₆ octahedra in the literature [78].

3.5.3 X-ray diffraction

X-ray diffraction powder data for Na₂RuO₃ was collected with a Stoe Stadi-P diffractometer (Cu K α ₁, Ge monochromator, linear PSD) in steps of 0.01° over a 2 θ range from 0 to 90° for approximately 24 h with the sample sealed in glass capillaries of 0.2 mm diameter. Further crystallographic data and details on the structure determination are given in Table 3.16. Data reduction was performed using the program WinXPow (Stoe) [31]. Background, peak profiles and lattice parameters were determined by LeBail-type fits, structure refinement was performed by the Rietveld method using the program package GSAS [35] with the atomic coordinates of α -NaFeO₂ and Na₂PtO₃ [110] as starting values. The atomic coordinates and isotropic displacement parameters are given in Table 3.17

while selected bond lengths are listed in Table 3.18. The scattered X-ray intensities of Na₂RuO₃ are shown in Figure 3-26.

Table 3.16 Crystallographic data and details on the structure determination of Na₂RuO₃

Formula	Na ₂ RuO ₃	Na ₂ RuO ₃
	disordered	ordered
Crystal system	trigonal	monoclinic
Space group (no.)	R -3m (166)	C 2/c (15)
Formula wt. /g mol ⁻¹	1560.38	
Unit cell dimensions / Å	<i>a</i> = 3.12360(5) Å <i>c</i> = 16.0370(4) Å	<i>a</i> = 5.4141(4) Å <i>b</i> = 9.3663(6) Å <i>c</i> = 10.8481(4) Å β = 99.636(9)°
Cell volume Å ³	135.003(3)	542.36(6)
Z	2	8
Density calc /g cm ³	4.777	4.777
R- values	<i>R_p</i> : 0.1191, <i>R_{wp}</i> : 0.1535	

Table 3.17 Atomic coordinates and isotropic displacement parameters U_{eq} of the two hypothetical phases of Na₂RuO₃ (see text for explanation). U_{eq} is defined as one third of the trace of the orthogonalised U_{ij} tensor

Atom	Occup.	x	y	z	U _{eq}
monoclinic phase					
Na1	1	0.258(5)	0.613(4)	-0.007(3)	0.0186
Na2	1	0.25	0.25	0	0.0384
Na3	1	0	0.910(3)	0.25	0.0103
Ru1	1	0	0.253(8)	0.25	0.0207
Ru2	1	0	0.581(8)	0.25	0.0337
O1	1	0.134(7)	0.103(11)	0.153(6)	0.0195
O2	1	0.106(7)	0.401(11)	0.153(6)	0.0167
O3	1	0.144(8)	0.730(11)	0.149(7)	0.0149
trigonal phase					
Na1	1	0	0	0	0.0257
Ru1	2/3	0	0	0.5	0.0234
Na2	1/3	0	0	0.5	0.0583
O1	1	0	0	0.2372(4)	0.0185

Table 3.18 Selected bond lengths (Å) for Na₂RuO₃ with standard deviations in parentheses

monoclinic phase			
Ru1-O1 (2x)	1.97(10)	Ru2-O1 (2x)	2.09(5)
Ru1-O2 (2x)	1.89(10)	Ru2-O2 (2x)	2.12(11)
Ru1-O3 (2x)	2.06(5)	Ru2-O3 (2x)	2.01(10)
Na1-O1	2.45(5)	Na2-O1 (2x)	2.33(7)
Na1-O1	2.70(9)	Na2-O2 (2x)	2.41(8)
Na1-O2	2.85(9)	Na3-O3 (2x)	2.46(6)
Na1-O2	2.31(5)	Na3-O1 (2x)	2.26(3)
Na1-O3	2.19(7)	Na3-O2 (2x)	2.22(5)
Na1-O3	2.25(9)	Na3-O3 (2x)	2.22(5)
trigonal phase			
Na1-O1 (6x)	2.373(4)	Na2 / Ru1 - O1 (6x)	2.129(3)

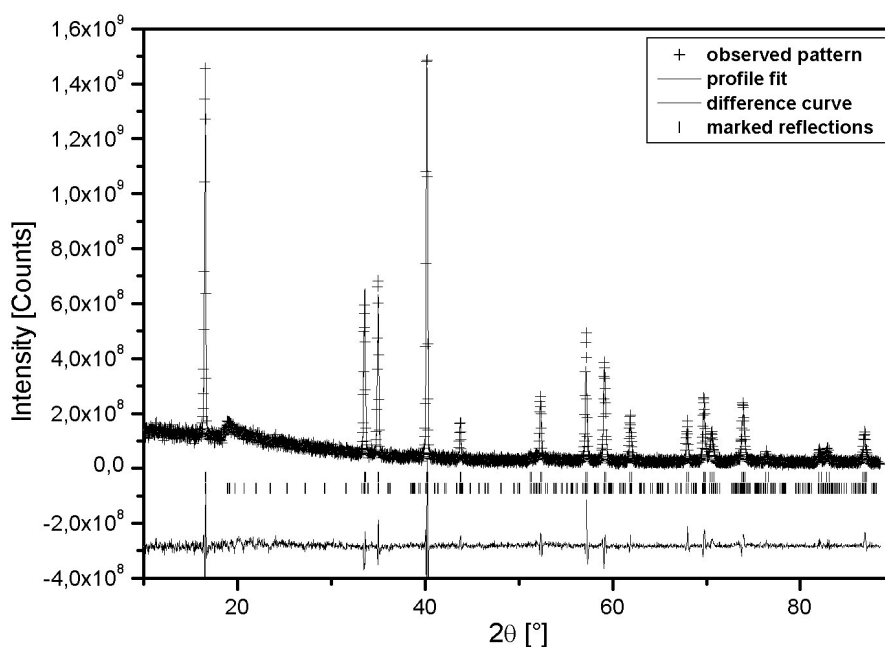


Figure 3-26 Scattered X-ray intensities for Na₂RuO₃ as a function of diffraction angle 2θ . The observed patterns (cross), the best Rietveld fit profiles (line), difference curves (bottom line) are shown. Reflection positions of trigonal (above) and monoclinic phase (below) are marked

3.5.4 Structure description

According to the results from Rietveld refinement, the oxygen atoms in Na₂RuO₃ form a cubic close packing, where all octahedral voids are occupied by the cations resulting in a layered variant of the NaCl-structure type. Along the [111] direction (referring to the cubic NaCl structure type) the cations segregate to form layers consisting of Na⁺ only, and of composition NaRu₂, which stack in an alternating mode (Figure 3-27). This stacking direction defines the *c*-axis of the rhombohedral crystal system of Na₂RuO₃. A comparison

of the lattice parameters suggests that the compound crystallises in the α -NaFeO₂ structure, but striking similarities with the X-ray diffraction pattern of Na₂PtO₃ (Li₂SnO₃ – structure type) [110,111] are also present. Both, the α -NaFeO₂ and the Li₂SnO₃ structure types, are layered variants of the NaCl-type. Yet while in α -NaFeO₂, Na containing layers alternate with Fe containing ones, in Li₂SnO₃ and also in closely related Li₂MnO₃ [112], pure Li-containing layers alternate with others that consist of 1/3 Li + 2/3 Sn (or Mn respectively), in an ordered arrangement.

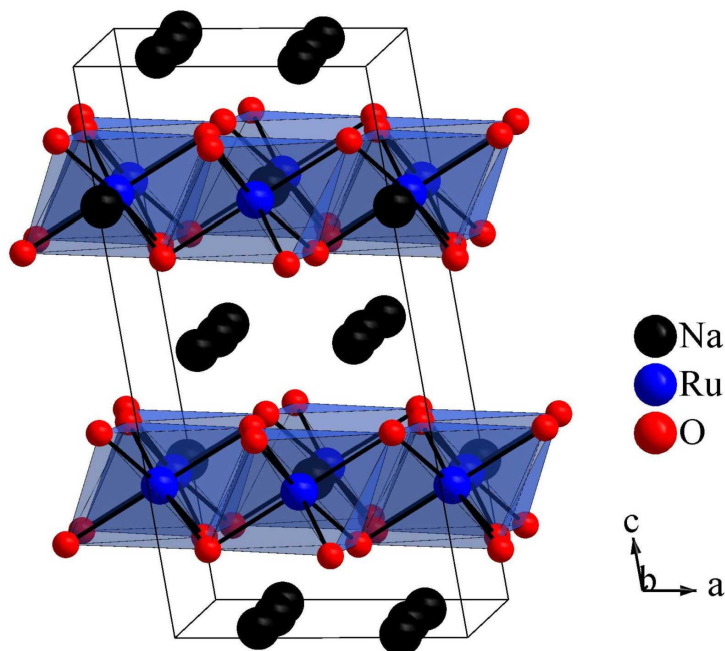


Figure 3-27 Crystal structure of Na₂RuO₃ in a projection along the b-axis. RuO₆ octahedra and Na atoms are drawn

In Na₂RuO₃, the first layer is composed of Na while the second layer contains Na and Ru in relation 1/3 to 2/3. The difference with respect to the other two structure types described above is that the distribution of these two cation types is only partially ordered. To approximate this partially ordered state in the refinement, the existence of two hypothetical phases was assumed, the first one is trigonal which shows a completely statistical distribution of the two cation types. Consequently, all atoms in the layer seem to be equal and the structure corresponds to the α -NaFeO₂ structure type.

The second phase is monoclinic and is characterised by a completely ordered distribution of the two cations, corresponding to the Li₂SnO₃–structure type. The volume contributions of the two phases as obtained from the Rietveld refinement were 8.7 : 1 (NaFeO₂ : Li₂SnO₃) thus indicating a very high degree of disorder in the structure.

Naturally, for these types of problems, the information content of a powder pattern is not sufficient. Single crystal studies, or even more conclusive, HRTEM studies could give a definite answer about the nature of the underlying disorder.

3.5.5 Magnetic measurements

The magnetisation of Na₂RuO₃ was investigated using a SQUID magnetometer (Quantum Design MPMS; 5-330 K). A plot of inverse susceptibility and susceptibility versus temperature is given in Figure 3-28. The inverse magnetic susceptibility obey the Curie-Weiss Law down to about $T = 150$ K. The effective magnetic moment is $\mu_{eff} = 4.63\mu_B$, which is around 94 % of $\mu_{SO} = 4.89 \mu_B$, the ideal moment for the spin-only d^4 ($S = 2$) configuration, thus confirming the oxidation state +4 for ruthenium.

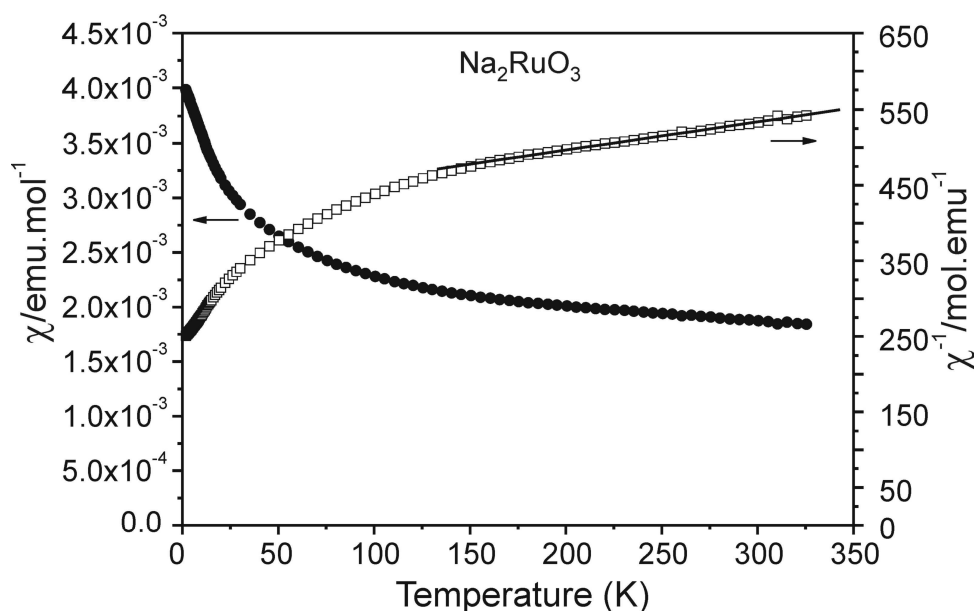


Figure 3-28 Magnetic susceptibility of Na₂RuO₃ represented as χ vs. T (circles) and χ^{-1} vs. T (squares) in an applied field of 5 T. The full line represents the linear fit using the Curie-Weiss law

3.5.6 Conductivity measurements

The conductivity measurements were carried out on powder samples of Na₂RuO₃ with the standard four point probe method. Na₂RuO₃ acts as a semiconductor. The resistance remains constant up to 50 K and above 50 K it displays a semi-conducting behaviour.

4 Alkali metal osmates

Osmium, the group VIII, 5d transition element shows some characteristics in its properties and reactivity. At first, it is one of the rarest elements naturally occurring in the earth's crust and thus is available at a high price. Another disadvantage is regarded to the facile oxidation of osmium metal and some of its compounds to toxic osmium tetroxide (OsO_4), in traces, also in air at room temperature, and hence great care has to be taken while handling osmium reactions. Mainly for these reasons, not much has been explored about the crystal structures and properties of osmium compounds. Nevertheless, due to its unique properties, it has found its way into some valuable applications. Initially, osmium was used as a catalyst in the synthesis of ammonia and later extensively in organic chemistry. Owing to its high-melting point, osmium was also applied as a filament in the light bulb, and thus is responsible for the first part of the company name OSRAM. Osmium exhibits various oxidation states ranging from -2 to $+8$. Within the binary oxides, OsO_2 is the most stable one, but, expressing the tendency of the 5d elements to adopt high oxidation states more facile, OsO_4 is also easily accessible. Though the alkali oxo-osmates were studied since long time they were merely examined in comparison with the alkali oxo-ruthenates. The few known compounds of osmium are hygroscopic with most of them readily giving off OsO_4 when exposed to air. One of the early works on these alkali metal osmates is by Scholder et al. [113]. The various phases predicted and studied are also reported in Gmelin's Handbook [63]. Osmium compounds crystallise in a rich variety of structure types such as pyrochlore, scheelite and perovskite, exhibiting a variety of interesting electronic and magnetic properties. Recently, the defect pyrochlores AOs_2O_6 ($\text{A}=\text{Cs}, \text{Rb}, \text{K}$) were found to display superconductivity [114-116]. The perovskite-related $\text{Ba}_{11}\text{Os}_4\text{O}_{24}$ showed weak ferromagnetic behaviour at around 7 K [117]. The double perovskites explored by zur Loye et al. using the hydroxide flux crystal growth technique exhibit interesting magnetic properties [118]. This has triggered a lot of activities in the osmium containing phases. In this work the ternary systems K-Os-O, Na-Os-O and Cs-Os-O, are investigated in order to achieve compounds containing osmium in higher oxidation state and to probe their properties. On the other hand, no quaternary perovskites of osmium containing both A and B site cations as alkali metals have been explored so far. Thus, quaternary alkali osmium perovskites are also explored. Results of all the ternary and quaternary alkali metal osmates containing octavalent and heptavalent osmium are discussed in this chapter.

4.1 K₂OsO₅, Potassium osmate(VIII)

Recently, a new pyrochlore related compound KOs₂O₆ [114] was found to display superconductivity at 10 K. Before this, only one oxide, KOsO₄ [119] and a few hydrates such as potassium hydroxo-oxo-osmate [K₂OsO₄(OH)₂] [120,121] were reported in the K-Os-O system. Thus, attempts have been made to reveal new interesting oxides in this system. One reason for the lack of known and characterised compounds, as described earlier, could be the problem associated with the possible formation of toxic and volatile OsO₄ during solid state reactions involving osmium oxides. Hence, a closed system is preferred for carrying out such reactions. Within possible closed systems, the oxygen pressure technique in steel autoclaves was implemented. This technique was used to synthesise the only example of ternary oxides containing osmium in the oxidation state +8 explored so far, with an exceptional composition and an unique crystal structure, Ag₁₃OsO₆ [122]. The synthesis, crystal structure and characterisation of another ternary Os(VIII) compound, K₂OsO₅, is discussed in the following sections.

4.1.1 Synthesis

K₂OsO₅ was prepared by the reaction of potassium superoxide and osmium powder at an elevated oxygen pressure. Equimolar amounts of KO₂ (synthesised from K and O₂) [92] and osmium powder (Chempur, 99.9 %) were finely ground in an agate mortar and pressed into pellets. These pellets were put into gold crucibles which were sealed from one side and crimped from the other. Black, polycrystalline samples of K₂OsO₅ were obtained in stainless steel autoclaves under an oxygen pressure of 380 to 420 MPa within the temperature range of 698 to 748 K. Alternatively, the powder sample of this compound can be obtained under oxygen flow at 698 K, but a closed system is favoured to avoid the risk of exposure to toxic OsO₄. In a typical experiment a crystalline sample was obtained by heating the mixture at 698 K applying 386 MPa oxygen pressure for 3 days and further cooling it down to room temperature at a rate of 30 K/h. The sample is hygroscopic and sensitive to air, readily giving out OsO₄ fumes on exposure to atmosphere.

4.1.2 Thermal analysis

The thermal analysis of K₂OsO₅ was carried out by using the DTA/TGA equipment (STA 409, Netzsch, Selb) coupled with a quadruple mass spectrometer. The sample was heated at a rate of 10 K/min in a corundum crucible under a flow of dry argon. The compound starts losing oxygen at around 473 K supposedly forming an intermediate of the

composition K₂OsO₄. Detailed investigation on these decomposition products was not continued further.

4.1.3 Raman and infrared spectroscopy

A Raman spectrum was recorded with a Confocal Microscope Laser Raman System (Jobin-Yvon, excitation line 632 nm, power 4 mW), the spectrum is shown in Figure 4-1. The mode at 914 cm⁻¹ confirms the presence of OsO₅ trigonal bipyramids in the structure as found in the literature [78].

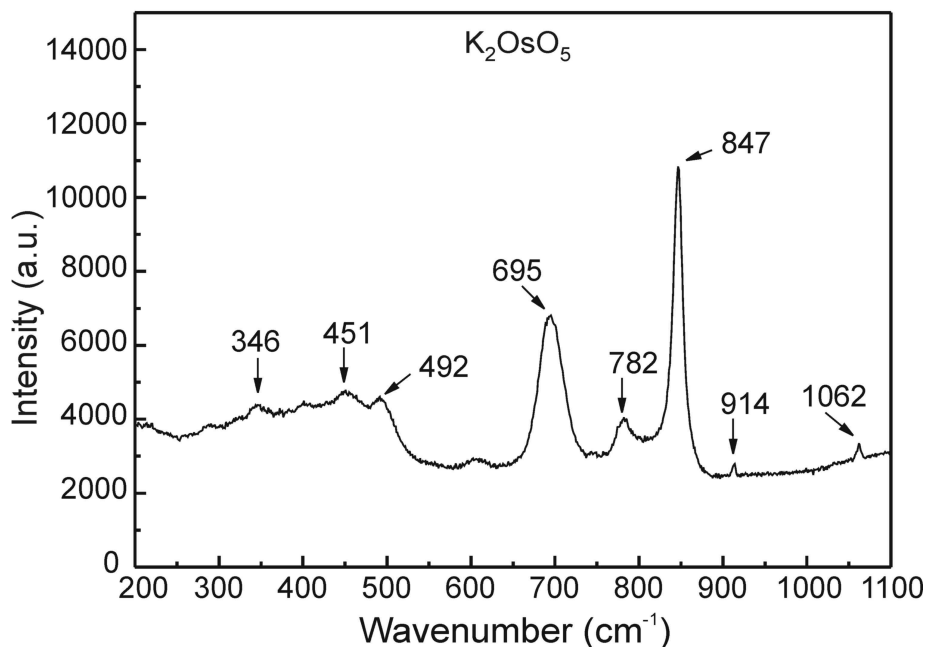


Figure 4-1 Raman spectrum of K₂OsO₅

For the infrared measurement of K₂OsO₅, 1-2 mg of the sample and 400 mg of KBr (Aldrich, 99+%, dried in vacuum at 473 K) were pressed into a pellet. The spectrum was recorded on a Fourier-Transform-Spectrometer (IFS 113v, Bruker). The following modes were obtained: 1414 cm⁻¹ (s), 1262 cm⁻¹ (w), 1099 cm⁻¹ (w), 1021 cm⁻¹ (w), 881 cm⁻¹ (w), 789 cm⁻¹ (s), 752 cm⁻¹ (s), 450 cm⁻¹ (s).

4.1.4 X-ray diffraction

Powder X-ray diffraction data for K₂OsO₅ were collected with a Stoe Stadi-P diffractometer (Cu K α ₁, Ge monochromator, linear PSD) in steps of 0.01° over a 2 θ range of 0 to 90° for approximately 24 h with the samples sealed in glass capillaries of 0.2 mm diameter. The measured X-ray pattern is shown in Figure 4-2.

Single crystal data of K₂OsO₅ were collected on a Stoe IPDS II diffractometer (Mo-K α ₁ Germanium monochromator, semi-empirical absorption correction with the program SADABS). Further information concerning the data collection and processing, the crystallographic parameters, as well as details on structure solution and refinement are given in Table 4.1, the atomic coordinates and isotropic displacement parameters are given in Table 4.2, and the anisotropic displacement parameters are listed in Table 4.3.

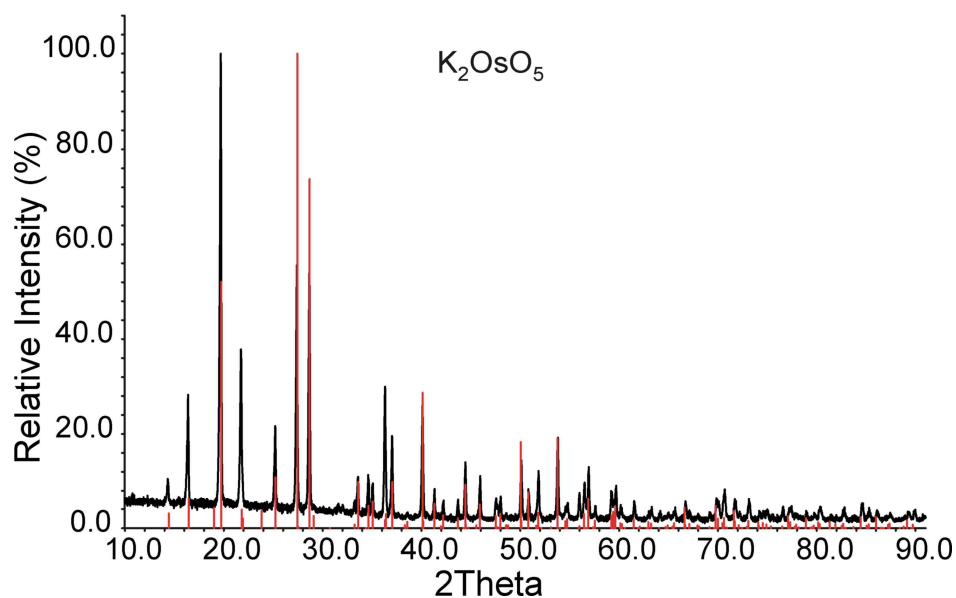


Figure 4-2 X-ray pattern of K₂OsO₅, red peaks are calculated from the result of the crystal structure refinement

Table 4.1 Crystallographic data and details on the structure determination of K₂OsO₅

Space group	P $\bar{6}$ (no. 174)
Lattice parameters at 293 K	a = 10.7730(15) Å c = 8.1453(16) Å
Formula units	6
Cell volume	818.7(2) Å ³
X-ray density	4.24 g·cm ⁻³
Molar mass	348.4
Diffractometer	Stoe IPDS II
Wavelength	Mo-Kα (λ = 0.71073 Å)
Monochromator	Germanium
Temperature	293 K
Data collection mode	ω-Scan
Reciprocal lattice segments	Full sphere
2θ-region	4.36° < 2θ < 54.67°
hkl _{min} - hkl _{max}	-13 ≤ h ≤ 13; -13 ≤ k ≤ 13; -10 ≤ l ≤ 10
Number of measured reflections	8514
Number of unique reflections	1342
Number of reflections > 2σ	1324
Number of parameters	105
R _{int}	5.14%
Absorption coefficient	24.82 mm ⁻¹
R(F)(obs), R(F)(all)	0.0191, 0.0195
R _w (F ²)(obs), R _w (F ²)(all)	0.0459, 0.0461
Difference density min./max.	-0.76 / 1.44 e · Å ⁻³

Table 4.2 Atomic coordinates and isotropic displacement parameters U_{iso} in Å² of K₂OsO₅, U_{iso} is defined as exp[-8π² U(sin²θ/λ²)]

Atom	Wy.Pos.	x	y	z	Occupancy	U _{iso}
K1	2g	0	0	0.2528(6)	1	0.0513(8)
K2	2h	1/3	2/3	0.2521(6)	1	0.05187(8)
K3	2i	2/3	1/3	0.2445(3)	1	0.0276(6)
K4	3j	0.2981(3)	-0.0351(3)	0	1	0.0429(6)
K5	3k	0.3648(2)	0.3333(3)	1/2	1	0.0309(4)
Os1	3k	0.30213(4)	-0.03121(4)	1/2	1	0.02195(9)
O1a	3k	0.2036(9)	0.0600(10)	1/2	1	0.067(4)
O1b	3k	0.3963(10)	-0.1288(10)	1/2	1	0.064(4)
O1c	3k	0.4675(8)	0.1344(8)	1/2	1	0.0247(14)
O1d	6l	0.2135(7)	-0.1190(7)	0.3184(8)	1	0.065(2)
Os2	3j	0.36872(4)	0.33333(5)	0	1	0.02804(10)
O2a	3j	0.1869(9)	0.1969(9)	0	1	0.039(2)
O2b	3j	0.5551(16)	0.4276(15)	0	0.501(15)	0.027(4)
O2c	3j	0.3242(9)	0.4713(9)	0	1	0.040(2)
O2d	6l	0.3743(12)	0.2426(12)	0.1879(14)	0.501(15)	0.036(3)
O2b'	3j	0.4619(17)	0.2430(17)	0	0.499(15)	0.030(4)
O2d'	6l	0.4654(11)	0.4261(11)	0.1870(14)	0.499(15)	0.033(3)

Table 4.3 Anisotropic displacement parameters for K₂OsO₅. The U_{ij} are defined as $-2\pi^2 (U_{11}h^2a^{*2} + U_{22}k^2b^{*2} + U_{33}l^2c^{*2} + U_{12}hka^*b^* + U_{13}hla^*c^* + U_{23}klb^*c^*)$

Atom	U ₁₁	U ₂₂	U ₃₃	U ₂₃	U ₁₃	U ₁₂
K1	0.0618(13)	0.0618(13)	0.0302(16)	0	0	0.0309(6)
K2	0.0622(13)	0.0622(13)	0.0312(16)	0	0	0.0311(6)
K3	0.0266(8)	0.0266(8)	0.0295(15)	0	0	0.0133(4)
K4	0.0268(11)	0.0266(11)	0.0586(17)	0	0	0.0006(8)
K5	0.0293(10)	0.0331(10)	0.0320(12)	0	0	0.0169(10)
Os1	0.0208(2)	0.0208(2)	0.0208(2)	0	0	0.00777(13)
O1a	0.019(4)	0.038(5)	0.145(13)	0	0	0.016(4)
O1b	0.038(5)	0.030(5)	0.129(12)	0	0	0.020(5)
O1c	0.020(3)	0.023(3)	0.022(3)	0	0	0.004(2)
O1d	0.056(4)	0.057(4)	0.039(4)	-0.007(3)	-0.008(3)	-0.005(3)
Os2	0.0253(2)	0.0457(2)	0.0199(2)	0	0	0.0228(2)
O2a	0.039(5)	0.018(3)	0.054(6)	0	0	0.010(4)
O2b	0.011(6)	0.023(7)	0.043(10)	0	0	0.006(5)
O2c	0.042(5)	0.016(3)	0.055(6)	0	0	0.010(3)
O2d	0.039(6)	0.049(7)	0.021(6)	0.008(5)	-0.008(5)	0.023(5)
O2b'	0.021(7)	0.033(8)	0.044(10)	0	0	0.018(7)
O2d'	0.032(6)	0.042(6)	0.022(6)	-0.011(4)	-0.017(4)	0.017(5)

4.1.5 Structure description

K₂OsO₅ crystallises in the hexagonal system in space group $P\bar{6}$ and is constituted of anionic OsO₅²⁻ groups, connected through potassium atoms. For both crystallographically independent Os atoms the two sets of coordinating oxygen atoms form a trigonal bipyramid (see Figure 4-3 and Figure 4-4). The trigonal OsO₅ bipyramids are arranged in such a way that their threefold axes are oriented perpendicular to the crystallographic *c* axis. The osmium atom, one equatorial and the two axial oxygen atoms of each OsO₅ group are located in planes at *z* = 0 and *z* = 1/2, respectively. The remaining oxygen atoms are generated by a mirror plane perpendicular to [001]. For Os1, the mean Os–O distances are 1.773 Å, 1.782 Å (axial) and 1.767 Å (equatorial), see Table 4.4. The angle of Os1 and the two axial O atoms is close to 180°. The three equatorial oxygen atoms ($89.1^\circ \leq O_{ax}-Os-O_{eq} \leq 91.3^\circ$), in plane with Os1, form the O_{eq}–Os–O_{eq} angle with an average value of 120°. So, although unforced by space group restrictions, the symmetry of the polyhedron is close to perfect D_{3h}.

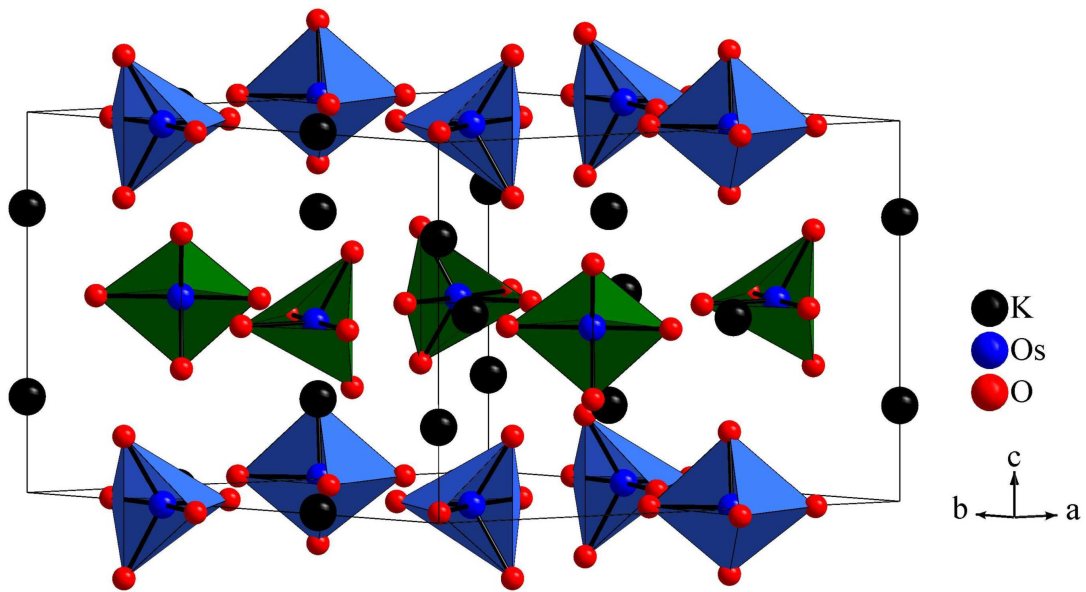


Figure 4-3 Perspective view of K_2OsO_5 along $[110]$. OsO_5 bipyramids and K^+ ions have been drawn, blue polyhedra: $z = 0$, green polyhedra: $z = 1/2$

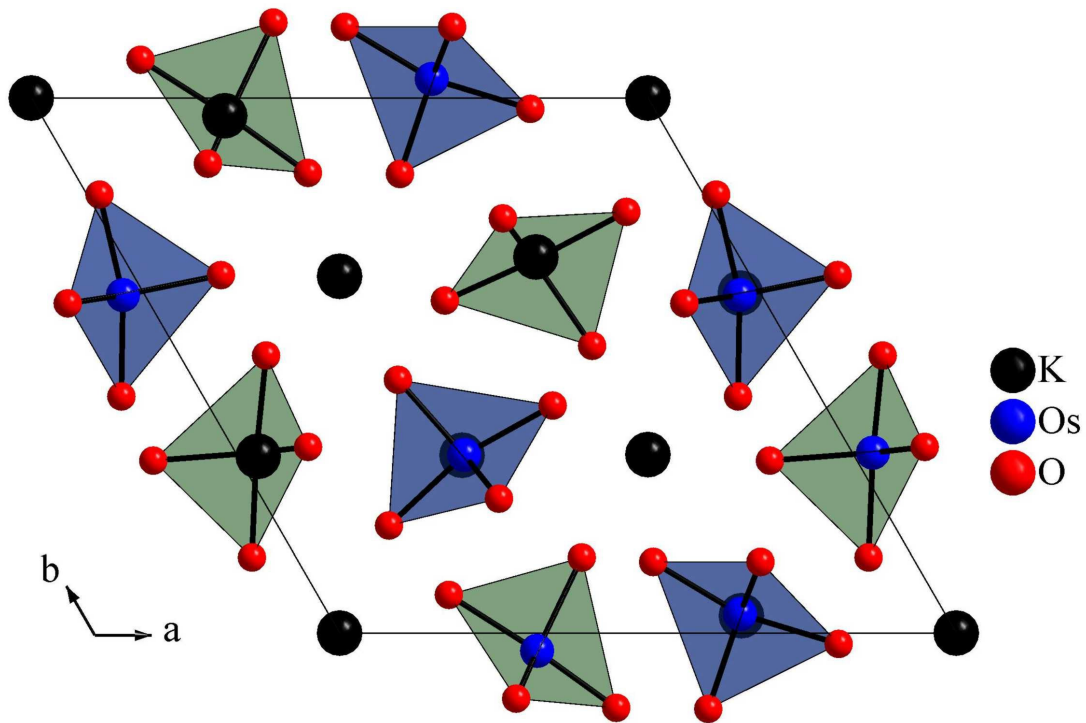


Figure 4-4 View of the crystal structure of K_2OsO_5 along $[00\bar{1}]$. OsO_5 bipyramids and K^+ ions have been drawn, blue polyhedra: $z = 0$, green polyhedra: $z = 1/2$

Table 4.4 Selected bond lengths (Å) for K₂OsO₅.

Atoms	Distances	Atoms	Distances
Os1–O1a	1.773(11)	K3–O2b	2.773(12) [3x]
Os1–O1b	1.792(11)	K3–O2d	2.833(13) [3x]
Os1–O1c	1.780(8)	K3–O2d'	2.845(13) [3x]
Os1–O1d	1.760(7)	K3–O1c	2.990(9) [3x]
Os1–O1d ⁱ	1.760(7)	K4–O2b ^{iv}	2.574(14)
Os2–O2a	1.762(10)	K4–O2b'	2.608(16)
Os2–O2b	1.733(17)	K4–O2a ^v	2.690(9)
Os2–O2c ^v	1.770(10)	K4–O2c ^v	2.698(9)
Os2–O2d	1.832(12)	K4–O1d	2.748(7) [2x]
Os2–O2d ⁱⁱ	1.832(12)	K4–O2d' ^{vi}	3.067(12) [2x]
Os2–O2b'	1.710(19)	K4–O2d	3.084(12) [2x]
Os2–O2d'	1.832(11)	K4–O2c ^{vi}	3.259(9)
Os2–O2d' ⁱⁱ	1.832(11)	K4–O2a	3.268(9)
K1–O1a	2.804(7) [3x]	K5–O1b ⁱⁱⁱ	2.538(10)
K1–O2a	2.920(7) [3x]	K5–O1a	2.564(10)
K1–O1d	3.188(10) [3x]	K5–O2d	2.744(12) [2x]
K2–O1b ⁱⁱⁱ	2.810(7) [3x]	K5–O2d'	2.755(12) [2x]
K2–O2c	2.907(7) [3x]	K5–O1c	2.861(9)
K2–O1d ⁱⁱⁱ	3.205(10) [3x]	K5–O1c	2.866(9)
K3–O2b'	2.766(13) [3x]	K5–O1d	3.030(6) [2x]

Symmetry codes: (i) x, y, -z+1; (ii) x, y, -z; (iii) -x+y+1, -x+1, z; (iv) -y+1, x-y, z; (v) -x+y, -x, z; (vi) -y+1, x-y, z.

Table 4.5 Selected bond angles for K₂OsO₅

Atoms	Angles	Atoms	Angles
O1a–Os1–O1b	178.0(4)°	O1b–Os1–O1d	89.9(4)°
O1a–Os1–O1c	91.3(4)°	O1b–Os1–O1d ⁱ	89.1(4)°
O1a–Os1–O1d	89.1(4)°	O1c–Os1–O1d	122.6(2)°
O1a–Os1–O1d ⁱ	89.1(4)°	O1c–Os1–O1d ⁱ	122.6(2)°
O1b–Os1–O1c	90.3(4)°	O1d–Os1–O1d ⁱ	114.7(2)°
O2a–Os2–O2b	164.4(6)°	O2c–Os2–O2b'	163.2(7)°
O2a–Os2–O2c	92.5(4)°	O2c–Os2–O2a	92.5(4)°
O2a–Os2–O2d	82.7(4)°	O2c–Os2–O2d'	82.0(4)°
O2a–Os2–O2d ⁱⁱ	82.7(4)°	O2c–Os2–O2d' ⁱⁱ	82.0(4)°
O2b–Os2–O2c	103.1(6)°	O2b'–Os2–O2a	104.3(7)°
O2b–Os2–O2d	88.7(5)°	O2b'–Os2–O2d'	88.7(5)°
O2b–Os2–O2d ⁱⁱ	88.7(5)°	O2b'–Os2–O2d' ⁱⁱ	88.7(5)°
O2c–Os2–O2d	122.9(4)°	O2a–Os2–O2d'	123.2(4)°
O2c–Os2–O2d ⁱⁱ	122.9(4)°	O2a–Os2–O2d' ⁱⁱ	123.2(4)°
O2d–Os2–O2d ⁱⁱ	112.9(9)°	O2d'–Os2–O2d' ⁱⁱ	111.9(8)°

Symmetry codes: (i) x, y, -z+1; (ii) x, y, -z.

The second trigonal bipyramid is orientationally disordered, as seen in Figure 4-5, and therefore shows larger deviations from average values for Os–O distances and O–Os–O angles. The trigonal bipyramidal coordination polyhedron has been found in Cs[O₄Os^{VIII}(OH)Os^{VIII}O₄] [123], however, isolated [OsO₅]²⁻ trigonal bipyramids were without precedent so far. Interestingly, the crystal structure of Ba₅(Os^{VII}O₅)₃Cl [124] is closely related to the apatite type of structure and is isotopic with the Re^{VII} compound

[125,126]. It crystallises in space group $P6_3cm$, a supergroup of $P\bar{6}$, with Ba and Cl at the crystallographic sites of K in K₂OsO₅. It consists of isolated [OsO₅]³⁻ complex anions, where the five oxygen ligands of Os form a square pyramid. In K₂OsO₅, the OsO₅ bipyramids are arranged to form a hexagonal close packing. The K⁺ ions, connecting the OsO₅ groups, are situated in the octahedral voids and in the centre of two face sharing tetrahedral voids of the hexagonal close packing of osmium. The partial structure of the cations corresponds to that one found in K₂RuO₄ [86]. The first coordination sphere of the K⁺ ions in K₂OsO₅ is formed by the tricapped distorted trigonal prisms of nine oxygen atoms (K1-K3) or an irregular polyhedra of eight or nine oxygen atoms (K4-K5).

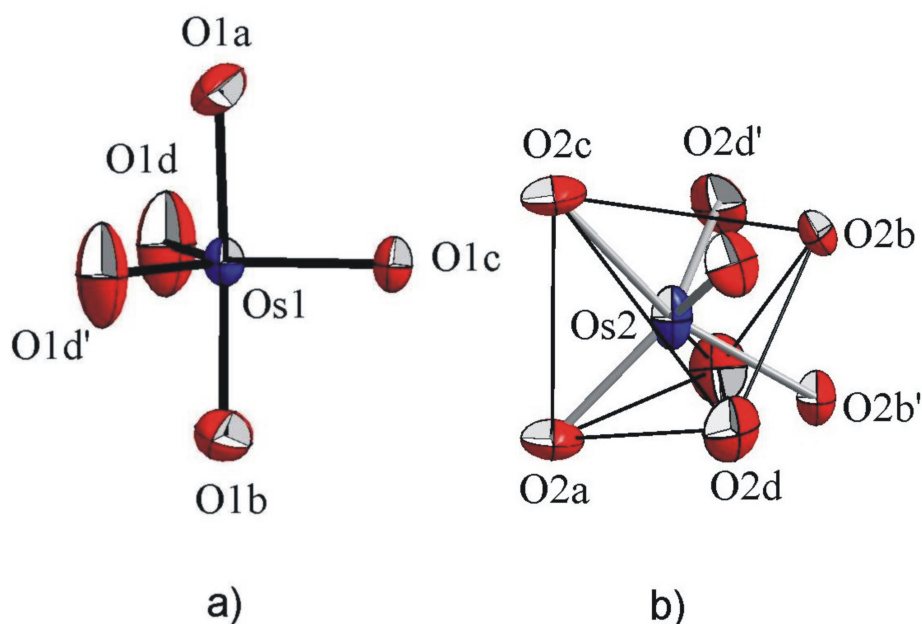


Figure 4-5 Coordination of the two crystallographically independent osmium in K₂OsO₅, a) trigonal bipyramidal OsO₅²⁻ group, b) split atom model of the two superimposed OsO₅ groups around the Os₂ atom

The orientational disorder of the anions is related to specific features of the underlying hexagonal close packing. The OsO₅ groups are arranged in such a way that in each layer one threefold axis parallel to and one mirror plane perpendicular to [001], and additionally mirror planes perpendicular to [210] are fulfilled. According to the threefold axis, three orientations of OsO₅ bipyramids occur in each layer of the hexagonal close packing. For a given arrangement in one layer, there are only two possible orientations in the adjacent layers, the third one being forbidden because then the resulting interlayer O–O distances would be too short. The remaining two orientations are related by a mirror plane perpendicular to [210], and should be equivalent with respect to the first layer. The

combination of the first layer and one of the possible second layers violates the [210] mirror plane. In refining the crystal structure, the resulting disorder was treated in a split atom model, and also in a twin model, choosing the [210] mirror plane as a twin element. The split atom refinement yielded the lower R-values, thus these results are documented here.

There are a number of compounds which are crystallographically related to K₂OsO₅ containing MO₅ bipyramids and especially showing a similar “weakness” of stacking order. For BaHg(RuO₅) ($a = 10.1760 \text{ \AA}$, $c = 8.4121 \text{ \AA}$, $P6_3/m$) [127], the structure solution from powder data lead to a layer multiplicity of 2 with oxygen atom positions at a low reliability, resulting in an irregular shape of the RuO₅ bipyramid. For BaH₂RuO₅ \equiv Ba[RuO₃(OH)₂] ($a = 10.023 \text{ \AA}$, $c = 25.471 \text{ \AA}$, $R\bar{3}c$) [128] a more complicated stacking order ABA'B'A"B" with all possible RuO₅ orientations was found. In the case of K₂OsO₅, neither the single crystal nor the powder data gave any hint for a doubling or tripling of the crystallographic c axis.

4.1.6 Magnetic measurements

Magnetic measurements were performed on polycrystalline powder samples using a SQUID-Magnetometer (MPMS 5.5, Quantum Design) between 5 and 350 K in magnetic fields up to 5 T. K₂OsO₅ has been found to be diamagnetic in accordance with the oxidation state of +8 for osmium as suggested from the structure determination.

4.1.7 Conductivity measurements

Measurements of the electrical conductivity were performed by four-point-probe method (Van-der-Pauw) on pressed pellets (diameter: 6 mm, thickness: 1 mm). The compound behaves as an insulator in the investigated temperature range of 1.5 K to 350 K.

4.2 K₂NaOsO_{5.5}, a double perovskite

Double perovskites are intensively studied due to their interesting physical and chemical properties. Recently a few double perovskites of osmium containing an alkaline earth metal or a lanthanide element as *A* site and alkali metal as the *B* site were reported by zur Loye and co-workers [118,129]. In this system, attempts were made to explore the behaviour of osmium in complex perovskite lattices with alkali metal cations at all additional cationic sites. Two new perovskite phases have been obtained, one double perovskite is discussed below, and the triple perovskite is discussed in section 4.5. Although the valence state of osmium for a double perovskite of any composition must be inappropriate, the title compound of this section has been obtained as an equilibrium product from many experiments. The details of the compound are discussed ahead.

4.2.1 Synthesis

K₂NaOsO_{5.5} phase was initially obtained during the synthesis of K₂OsO₅, described in section 4.1. Using the same starting mixtures as for K₂OsO₅ and just adding sodium hydroxide as a mineralizer, good quality crystals of this cubic phase have been obtained. So, after the initial results, the synthesis was carried out without the hydroxide and the new compound was prepared by reaction of potassium superoxide, sodium peroxide and osmium powder at an elevated oxygen pressure. Stoichiometric amounts of KO₂ (synthesised from K and O₂) [92], Na₂O₂ and osmium powder (Chempur, 99.9 %) were mixed in the ratio 2 : 0.5 : 1, finely ground in an agate mortar and pressed into pellets. These pellets were put into gold crucibles which were sealed from one side and crimped from the other. Black, polycrystalline samples were obtained from the experiments in stainless steel autoclaves under an oxygen pressure of 35 MPa at a temperature of 673 K for a period of 2 days. Alternatively, powder sample of this compound can be also be obtained under oxygen flow at 698 K, however, again a closed system is favoured due to the formation of toxic OsO₄. The compound is hygroscopic and sensitive to air, readily giving out OsO₄ fumes on exposure to atmosphere.

4.2.2 Thermal analysis

The thermal analysis of K₂NaOsO_{5.5} was carried out by using the DTA/TGA equipment (STA 409, Netzsch, Selb) coupled with a quadruple mass spectrometer. The sample was heated at the rate of 10 K/min in a corundum crucible under a flow of dry argon. The compound starts losing oxygen at around 473 K, and supposedly at 773 K forms an

intermediate of the nominal composition K_2NaOsO_5 (based on the weight loss calculations). Further, it decomposes to form $K_2NaOsO_{4.5}$, (based on weight loss calculations starting from the K_2NaOsO_5 intermediate). Detailed investigation on these decomposition products was not continued further.

4.2.3 Raman and infrared spectroscopy

Raman spectrum was recorded with a Confocal Microscope Laser Raman System (Jobin-Yvon, excitation line 632 nm, power 4 mW). The obtained spectrum is shown in Figure 4-6. The medium mode observed at 859 cm^{-1} is similar to the mode observed for OsO_6 octahedra reported in literature [78].

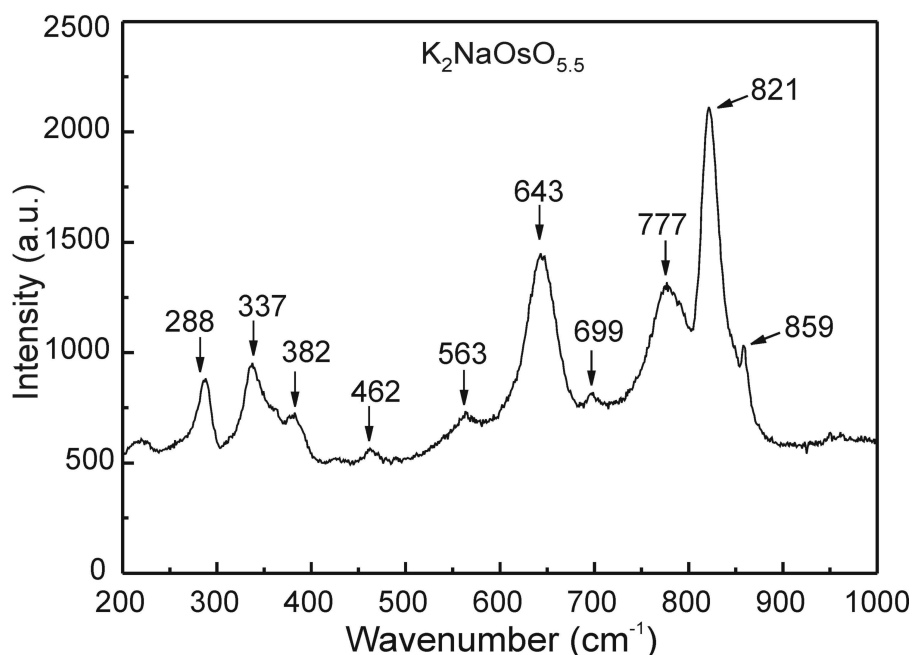


Figure 4-6 Raman spectrum of $K_2NaOsO_{5.5}$

Infrared measurements for this phase were performed with a Fourier-Transform-Spectrometer (IFS 113v, Bruker). 1-2 mg of the sample and 400 mg of KBr (Aldrich, 99+%, dried in vacuum at 473 K) were pressed into a pellet. The measurements were carried out especially on the batch synthesised without using any mineralizer and no indication of the presence of -OH band was observed around 3600 cm^{-1} .

4.2.4 X-ray diffraction

X-ray diffraction powder data were collected with a Stoe Stadi-P diffractometer (Cu $K\alpha_1$, Ge monochromator, linear PSD) in steps of 0.01° over a 2θ range from 0 to 90° for approximately 24 h with the samples sealed in glass capillaries of 0.2 mm diameter. The

measured X-ray pattern is shown in Figure 4-7. Few additional weak reflections are observed in the X-ray pattern of crystalline samples resulting from preparations without mineralizer. These reflections were found to be of the new triple perovskite phase which is discussed in section 4.5.

Single crystal data were collected on a Bruker AXS with SMART-CCD (APEX) (MoK_α Graphite monochromator, semi-empirical absorption correction with the program SADABS). Further information concerning the data collection and processing, the crystallographic parameters, as well as details on structure solution and refinement are given in Table 4.6, the atomic positions and isotropic thermal displacement parameters in Table 4.7 and the anisotropic thermal displacement parameters in Table 4.8.

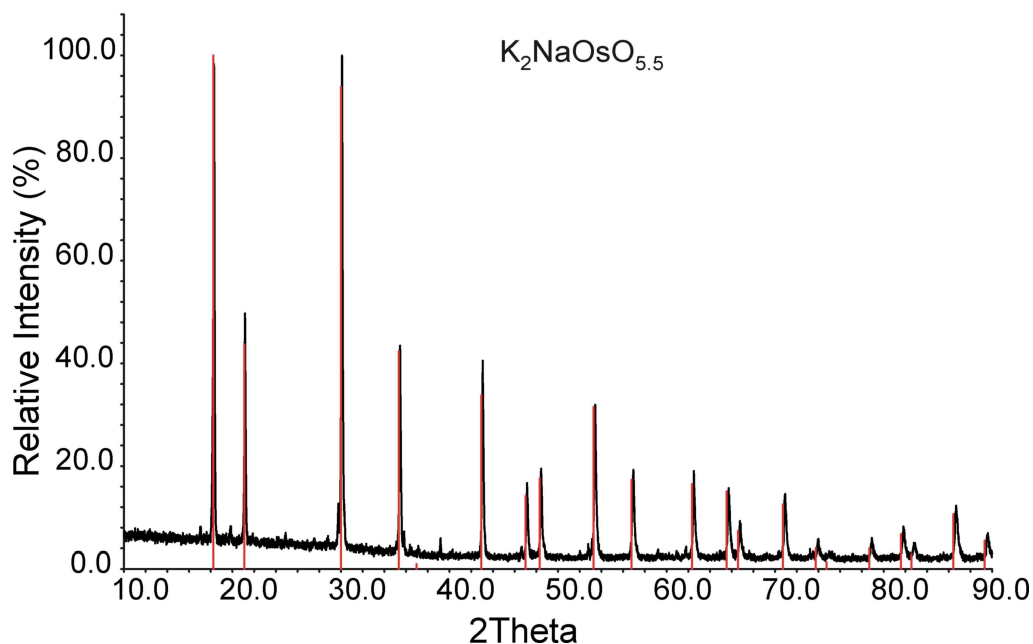


Figure 4-7 Measured X-ray pattern of K₂NaOsO_{5.5}, reflections in red indicate the pattern calculated from the single crystal structure determination. Weak unindexed reflections belong to K₃NaOs₂O₉, see section 4.5

Table 4.6 Crystallographic data and details on the structure determination of K₂NaOsO_{5.5}

Compound	K ₂ NaOsO _{5.5}
Crystal system	cubic
Space group	Fm $\bar{3}$ m (no. 225)
Lattice parameters at 293 K	a = 8.4184(5) Å
Formula units	4
Cell volume	596.61(6) Å ³
X-ray density	4.313 g·cm ⁻³
Molar mass	387.39
Diffractometer	Bruker SMART-APEX CCD
Wavelength	Mo-Kα (λ = 0.71073 Å)
Monochromator	Graphite
Temperature	293 K
Data collection mode	ω-Scan
Reciprocal lattice segments	Full sphere
2θ-region	4.19° < 2θ < 34.93°
hkl _{min} - hkl _{max}	-13 ≤ h ≤ 13; -13 ≤ k ≤ 13; -13 ≤ l ≤ 13
Number of measured reflections	2381
Number of unique reflections	96
Number of reflections > 2σ	96
Number of parameters	8
R _{int}	3.53%
Absorption coefficient	22.803 mm ⁻¹
R(F)(obs), R(F)(all)	0.0140, 0.0140
R _w (F ²)(obs), R _w (F ²)(all)	0.0397, 0.0397
Goodness-of-fit (all data)	1.428
Extinction coefficient	0.0034(4)
Difference density min./max.	-0.838 / 0.682 e · Å ⁻³

Table 4.7 Atomic coordinates and isotropic displacement parameters U_{iso} in Å² of K₂NaOsO_{5.5}. U_{iso} is defined as exp[-8π² U(sin²θ/λ²)]

Atom	Wy.Pos.	x	y	z	Occupancy	U _{iso}
K1	8c	0.25	0.25	0.25	1	0.03603(5)
Na1	4a	0.5	0.5	0.5	1	0.02934(12)
Os1	4b	0	0	0	1	0.02758(3)
O	24e	0.2212(5)	0	0	0.91667	0.02718(8)

Table 4.8 Anisotropic displacement parameters for K₂NaOsO_{5.5}. The U_{ij} are defined as -2π² (U₁₁h²a*² + U₂₂k²b*² + U₃₃l²c*² + U₁₂hka*b* + U₁₃hla*c* + U₂₃kla*b*c*)

Atom	U ₁₁	U ₂₂	U ₃₃	U ₁₂	U ₁₃	U ₂₃
K	0.0360(5)	0.0360(5)	0.0360(5)	0.00000	0.00000	0.00000
Na	0.0293(12)	0.0293(12)	0.0293(12)	0.00000	0.00000	0.00000
Os	0.0276(2)	0.0276(2)	0.0276(2)	0.00000	0.00000	0.00000
O	0.0215(19)	0.0300(13)	0.0300(13)	0.00000	0.00000	0.00000

4.2.5 Structure description

According to a single crystal structure determination, K₂NaOsO_{5.5} crystallises as a cubic double perovskite in space group Fm $\bar{3}$ m. The view along [0 1 0] is shown in Figure 4-8. The structure consists of a rock salt lattice of NaO₆ octahedra and OsO₆ octahedra with

twelve coordinate potassium cations separating the planes of sodium and osmium atoms. In another description, K and O atoms form a cubic close packing, where Na and Os atoms fill one eighth of the octahedral voids, in an ordered way, respectively. The coordinations of Na and Os are perfectly octahedral, while the potassium atom is surrounded by a cub-octahedron of O atoms. The cuboctahedron is slightly distorted due to the different size of the NaO₆ and OsO₆ octahedra, resulting in rectangles instead of squares and equilateral triangles of two different sizes as faces, see Figure 4-9. The selected bond distances are shown in Table 4.9. The Os-O bond distances are 1.862 Å. The magnetic measurements also display a diamagnetic behaviour. These findings, the diamagnetism and the bond lengths, reveal that the oxidation state of osmium is +8.

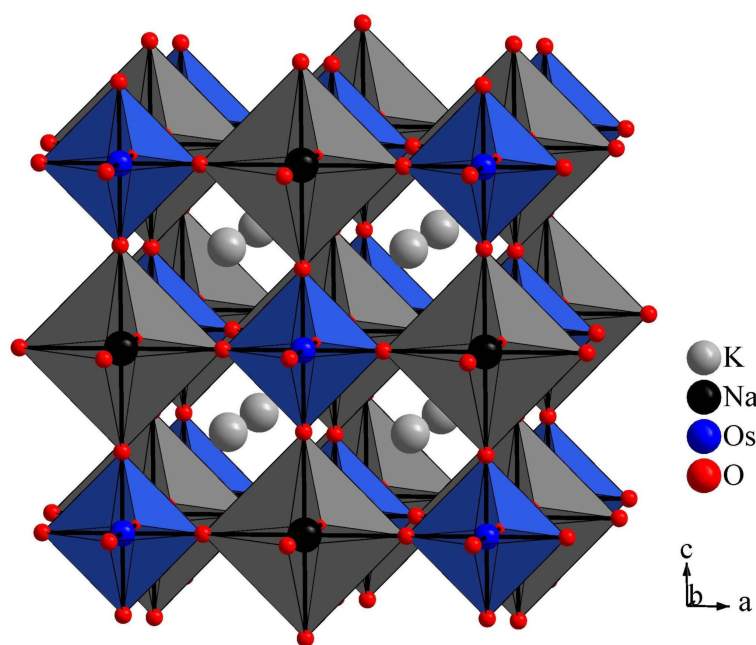


Figure 4-8 Crystal structure of the double perovskite K₂NaOsO_{5.5}

Table 4.9 Selected bond lengths (Å) for K₂NaOsO_{5.5}

Atoms	Distances
Os–O	1.862(4) [6x]
Na–O	2.347(4) [6x]
K–O	2.9862(4) [12x]

Full occupation of all crystallographic sites participating in the double perovskite structure does not satisfy the oxidation state for osmium. Hence, to achieve this, the occupancy of the oxygen atom was fixed to the exact composition K₂NaOsO_{5.5} during the crystal structure refinements. Refinements of the site occupancy of the oxygen atom resulted in

values greater than 1 with $R_1 = 1.0 \%$, corresponding to compositions up to $K_2NaOsO_{6.2}$ and a highly improbable oxidation state of more than +9 for osmium. Also, a partial substitution of Na by Os was introduced as a starting structure model, but these values went to zero for the Os occupation during the refinements. From infrared measurements no hint for the presence of hydroxide in the structure was obtained, although NaOH was used as a mineralizer during the reaction.

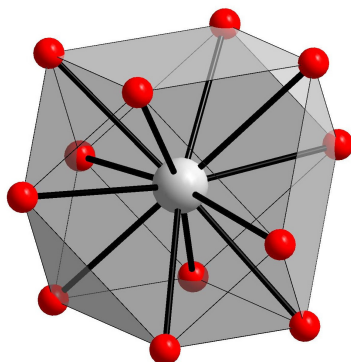


Figure 4-9 Coordination of the potassium atom in $K_2NaOsO_{5.5}$, a distorted cuboctahedron

For all the above mentioned reasons, we assume a composition $K_2NaOsO_{5.5}$ with fully occupied cation sites and a statistical disorder of oxygen vacancies in the crystal structure. Although the structure contains this unsatisfying disorder, the perovskite structure type matrix is able to stabilise the compound in equilibrium conditions, and provides access to this phase by a broad range of starting compounds and reaction conditions.

4.2.6 Magnetic measurements

Magnetic measurements were performed on polycrystalline powder samples using a SQUID-Magnetometer (MPMS 5.5, Quantum Design) between 5 and 350 K in magnetic fields up to 5 T. $K_2NaOsO_{5.5}$ has been found to be diamagnetic in accordance with the oxidation state of +8 for osmium, as suggested from the structure determination.

Similar diamagnetism has been found in other Os(VIII) oxides prepared by the same method, namely K_2OsO_5 and $Ag_{13}OsO_6$.

4.2.7 Conductivity measurements

Measurements of the electrical conductivity were performed by four-point-probe method (Van-der-Pauw) on pressed pellets (diameter: 6 mm, thickness: 1 mm). The compound behaves as an insulator in the investigated temperature range of 1.5 K to 350 K.

4.3 Na₃OsO₅, Sodium osmate(VII)

In the system Na-Os-O, only one ternary oxide, Na₅OsO₆ is reported till date [130], which is less compared to the number of ternary oxides reported for the homologous Na-Ru-O system. The trend is comprehensible due to the same reasons as for the potassium compounds (see section 4.1). The pyrochlore related oxides AOs₂O₆ (where A = K, Rb, Cs) [114-116] display superconductivity around 10 K and below. The T_c of these compounds decreases with increasing radius of the A cation, so the possibility of a higher T_c in a defect pyrochlore containing the smaller sized sodium is obvious. For this reason attempts were made to fit the smaller sized sodium into the pyrochlore lattice. However, attempts to explore and check the possibility of the formation of NaOs₂O₆ by applying different methods of preparation including the piston cylinder press, gave no clue for the existence of this compound. Also a possible sodium analogue for K₂OsO₅ was not obtained, however, while investigating this system, two new compounds, Na₃OsO₅ and the sodium hydroxy-osmate, Na₃OsO₄(OH)₂, were obtained. The latter, the hydrate of the title compound, is discussed in appendix as only a couple of crystals were obtained of this compound. The title compound was reported in 1963 by Scholder and Schatz [113]. However, no information on its structure data as well as magnetic behaviour was reported. The synthesis, crystal structure and characterisation of Na₃OsO₅ is discussed ahead.

4.3.1 Synthesis

Na₃OsO₅ was prepared by reaction of sodium peroxide and osmium powder in gold crucibles under oxygen flow. Stoichiometric amounts of Na₂O₂ (Sigma Aldrich) and osmium powder (Chempur, 99.9 %) were mixed in the ratio 1.5 : 1, finely ground in an agate mortar and pressed into pellets. The pellets were placed in gold crucibles which were sealed from one end and crimped from the other. Na₃OsO₅ was synthesised under an oxygen flow at 673 K for 2 days and by further cooling it down to room temperature at the rate of 15 K per hour. Several modifications of this procedure as well as reactions under oxygen flow were attempted to get the pure phase, however, the samples always contained a second phase of about 5 %, identified from X-ray patterns as Na₅OsO₆. The formation of Na₅OsO₆ is probably a result of losses of osmium evaporating as tetroxide after the formation of Na₃OsO₅. This volatilisation process is also observed at room temperature, so on exposure to atmosphere Na₃OsO₅ readily gives out OsO₄ fumes.

The synthesis of Na₅OsO₆ [130], reported by Betz and Hoppe to proceed from Na₂O and Os at higher temperatures of 1023 K followed by annealing at 1113 K for three weeks. Now, it was successfully performed at identical conditions as applied for Na₃OsO₅, and pure samples of Na₅OsO₆ have been obtained at a more moderate temperature of 673 K within two days. Possibly, the use of Na₂O₂ instead of Na₂O as reactant allows reducing the reaction time and temperature. From these experiments, it can be deduced that in the presence of Na₂O₂, the main parameter controlling the formation of these two compounds simply seems to be the Na/Os ratio given in the mixture of starting compounds.

4.3.2 Thermal analysis

The thermal analysis of Na₃OsO₅ was carried out by using the DTA/TGA equipment (STA 409, Netzsch, Selb) coupled with a quadruple mass spectrometer. The sample was heated at the rate of 10 K/min in a corundum crucible under a flow of dry argon. No intermediate decomposition was observed and no solid residue was left for investigation after 1473 K.

4.3.3 Raman spectroscopy

Raman spectrum was recorded with a Confocal Microscope Laser Raman System (Jobin-Yvon, excitation line 632 nm, power 4 mW), however, no spectra were obtained due to photoluminescence.

4.3.4 X-ray diffraction

X-ray diffraction powder data were collected with a Stoe Stadi-P diffractometer (Cu K α ₁, Ge monochromator, linear PSD) in steps of 0.01° over a 2 θ range from 0 to 90° for approximately 24 h with the samples sealed in glass capillaries of 0.2 mm diameter. The measured X-ray pattern is shown in Figure 4-10.

Single crystal data were collected on an IPDS-II diffractometer, Stoe & Cie, Darmstadt (MoK α Graphite monochromator, absorption correction by integration method). Further information concerning the data collection and processing, the crystallographic parameters, as well as details on structure solution and refinement are given in Table 4.10. The atomic coordinates and isotropic displacement parameters are given in Table 4.11, while the anisotropic displacement parameters are given in Table 4.12.

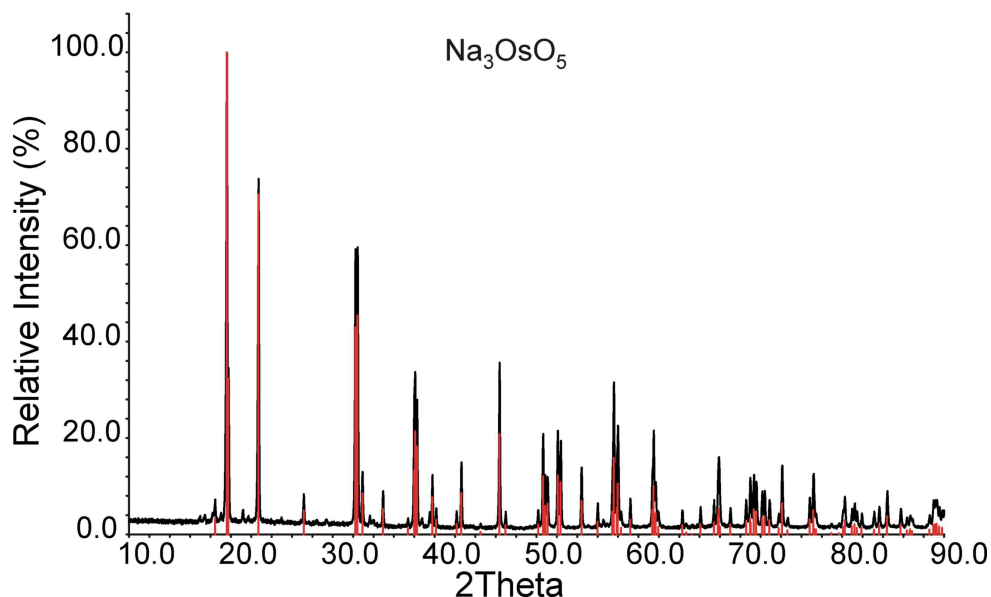


Figure 4-10 Measured X-ray pattern of Na₃OsO₅ (red reflections are the data from single crystal analysis, weak unindexed reflections are of Na₅OsO₆)

Table 4.10 Crystallographic data and details on the structure determination of Na₃OsO₅

Compound	Na ₃ OsO ₅
Crystal System	Hexagonal
Space group	<i>P</i> 3 ₁ 21 (no. 152)
Lattice parameters	<i>a</i> = 5.5529(2) Å <i>c</i> = 13.4726(8) Å
Formula units	3
Cell volume	359.77(3) Å ³
X-ray density	4.6961 g·cm ⁻³
Molar mass	1017.51
Absorption coefficient	26.776 mm ⁻¹
Absorption correction	integration
Diffractometer	IPDS-II (Stoe & Cie)
Wavelength	Mo-Kα (<i>λ</i> = 0.71073 Å)
Monochromator	Graphite
Temperature	293 K
Data collection mode	ω-Scan
Reciprocal lattice segments	Full sphere
2θ-region	8.48° < 2θ < 67.27°
hkl _{min} - hkl _{max}	-8 ≤ <i>h</i> ≤ 8; -8 ≤ <i>k</i> ≤ 8; -21 ≤ <i>l</i> ≤ 21
Number of measured reflections	5553
Number of unique reflections	958
Number of reflections > 4σ	955
Number of parameters	44
R _{int}	3.25%
R(F)(obs), R(F)(all)	0.0197, 0.0198
R _w (F ²)(obs), R _w (F ²)(all)	0.0427, 0.0427
Goodness-of-fit (all data)	1.169
Flack parameter	0.0032
Extinction coefficient	0.0015(3)
Difference density min./max.	-3.074 / 1.535 e · Å ⁻³

Table 4.11 Atomic coordinates and isotropic displacement parameters U_{iso} in \AA^2 of Na₃OsO₅ with standard deviations in parenthesis; U_{iso} is defined as $\exp[-8\pi^2 U(\sin^2\theta/\lambda^2)]$

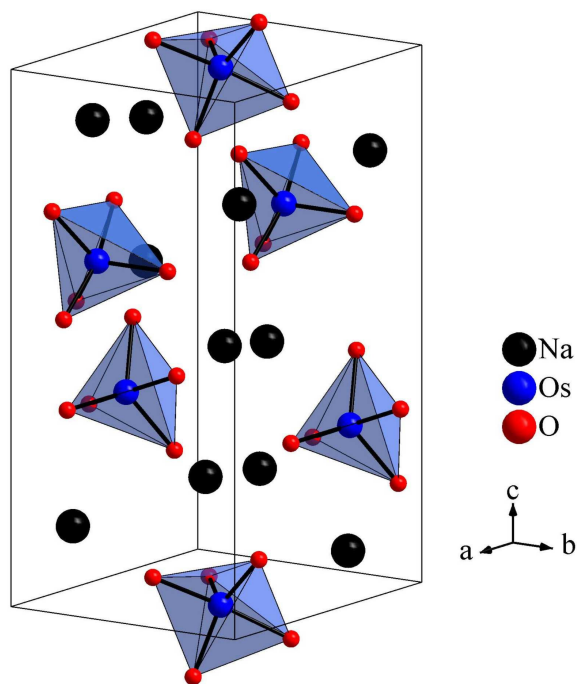
Atom	Wy.Pos.	x	y	z	U_{iso}
Na1	3b	0	0.2765(5)	0.1666(7)	0.0218(6)
Na2	6c	0.2953(5)	0.9176(5)	0.0851(16)	0.0237(5)
Os	3a	0.6157(4)	0.61572(4)	0	0.0092(7)
O1	3a	0.3002(9)	0.3002(9)	0	0.0185(11)
O2	6c	0.6823(9)	0.8426(8)	0.1053(3)	0.0217(8)
O3	6c	0.8200(9)	0.4834(9)	0.0649(3)	0.0221(9)

Table 4.12 Anisotropic displacement parameters for Na₃OsO₅. The U_{ij} are defined as $-2\pi^2 (U_{11}h^2a^{*2} + U_{22}k^2b^{*2} + U_{33}l^2c^{*2} + U_{12}hka^*b^* + U_{13}hla^*c^* + U_{23}klb^*c^*)$

Atom	U_{11}	U_{22}	U_{33}	U_{12}	U_{13}	U_{23}
Na1	0.0270(17)	0.0162(11)	0.0256(14)	0.0135(9)	-0.0092(11)	-0.0046(5)
Na2	0.0337(14)	0.0250(11)	0.0215(9)	0.0215(10)	-0.0028(9)	-0.0036(8)
Os	0.00921(9)	0.00921(9)	0.00996(9)	0.00518(8)	-0.00042(4)	0.00042(4)
O1	0.0094(16)	0.0094(16)	0.028(3)	-0.0018(19)	-0.0036(11)	0.0036(11)
O2	0.031(2)	0.0176(17)	0.0197(16)	0.0145(15)	-0.0067(15)	-0.0053(14)
O3	0.027(2)	0.030(3)	0.0197(17)	0.022(2)	-0.0034(15)	0.0016(15)

4.3.5 Structure description

Na₃OsO₅ is isostructural to that of Na₃ReO₅ [131]. The crystal structure consists of isolated OsO₅ trigonal bipyramids which are separated by sodium atoms, as shown in Figure 4-11. The Os atoms are packed analogous to a distorted cubic close packing, while the Na⁺ cations occupy the octahedral (Na1) and tetrahedral holes (Na2) of the fcc packing.

Figure 4-11 Unit cell of Na₃OsO₅

The Na₃Os cation arrangement is corresponding to the Li₃Bi type of structure [132], see Figure 4-12a. The structural relationship is further documented by the crystallographic *c* axis being identical with the diagonal of the pseudo-cubic cell, see Figure 4-12b. The same feature is also visible in Figure 4-13. The threefold symmetry of the cubic parent structure is retained in the trigonal arrangement in Na₃OsO₅.

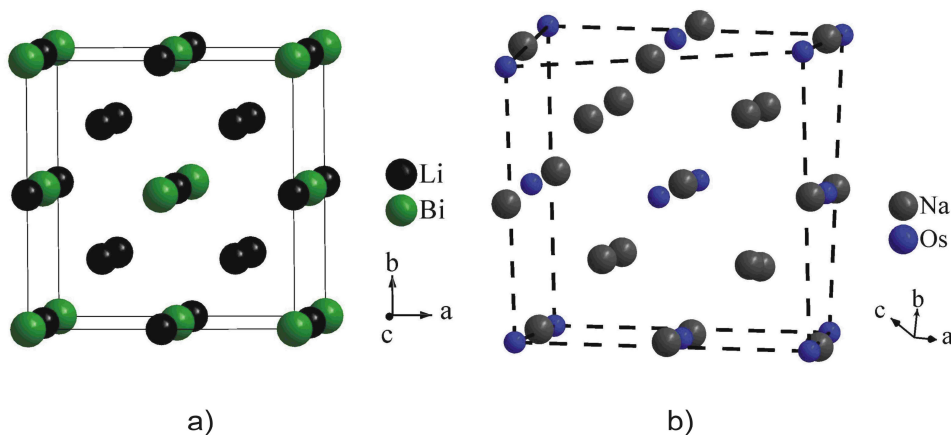


Figure 4-12 a) Unit cell of Li₃Bi, b) Li₃Bi analogue part of the cation partial structure of Na₃OsO₅

Osmium is coordinated by a trigonal bipyramid of five oxygen atoms (see Figure 4-14). The average distances to the equatorial oxygen atoms, 1.789 Å, are shorter than those of the axial ligands (1.851 Å).

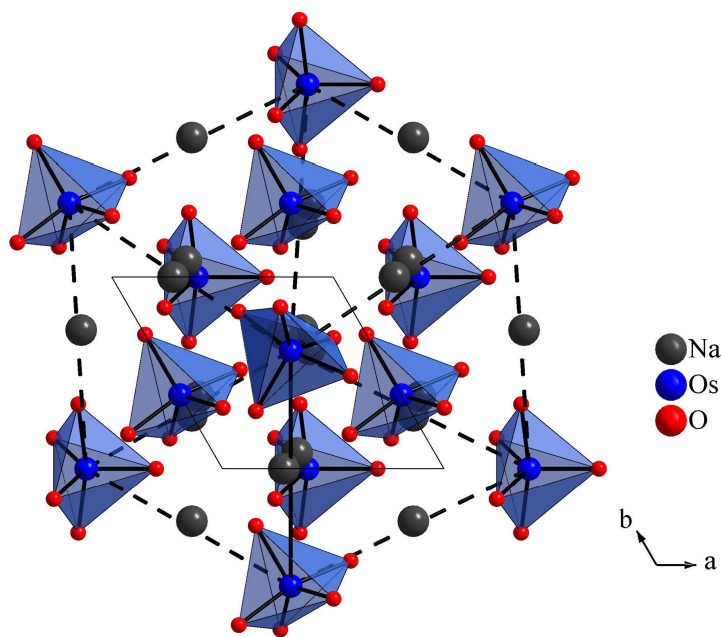


Figure 4-13 Crystal structure of Na₃OsO₅, view along the crystallographic *c* axis, the diagonal of the pseudo-cubic cell (dashed lines) of the Li₃Bi analogue cation packing, OsO₅ bipyramids and Na⁺ cations are drawn.

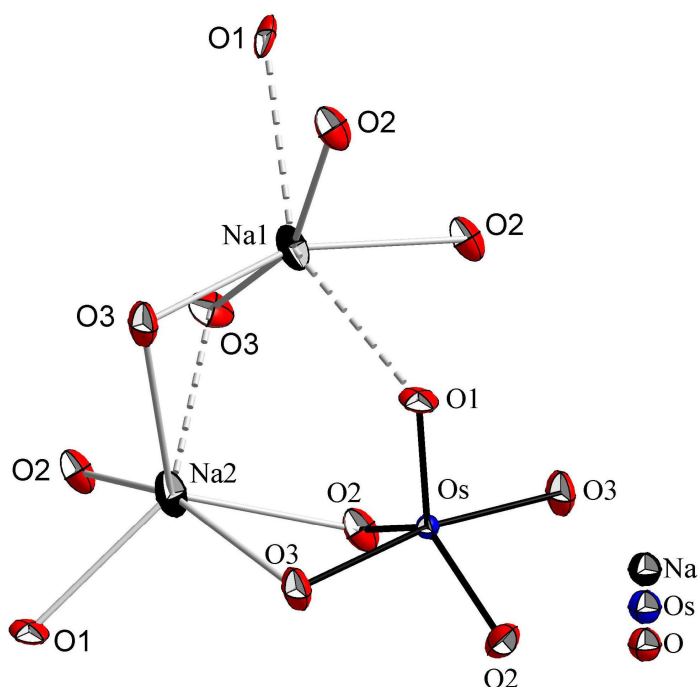


Figure 4-14 Coordination of cations in Na₃OsO₅, displacement ellipsoids are drawn at the 50 % probability level, dashed lines represent distances longer than 2.75 Å. Symmetry codes: (i) $y, x, -z$; (ii) $-x+1, -x+y+1, -z+1/3$; (iii) $x-1, y-1, z$; (iv) $x, y+1, z$; (v) $x-1, y, z$; (vi) $-x+1, -x+y, -z+1/3$; (vii) $-y, x-y, z+1/3$.

Regarding the bond angles of the OsO₅³⁻ anion, it just has a small deviation of 0.26% from the ideal polyhedron, calculated by the method applied to ReO₅ groups [131]. By considering the neighbours only at distances below 3 Å, both the independent sodium atoms are surrounded by irregular polyhedra of 4+2 (Na1) and 5+1 (Na2) oxygen atoms, distantly resembling the trigonal prisms (see Figure 4-14b). The bond distances and angles are listed in Table 4.13.

Table 4.13 Selected bond lengths (Å) and angles (°) for Na₃OsO₅

Atoms	Distances	Atoms	Angles
Os–O1	1.752(5)	O3–Os–O3 ⁱ	167.6(3)
Os–O2	1.809(4) [2x]	O1–Os–O3	96.20(14) [2x]
Os–O3	1.850(4) [2x]	O2–Os–O3 ⁱ	87.09(17) [2x]
Na1–O3 ⁱⁱ	2.313(4) [2x]	O2–Os–O3	87.33(3) [2x]
Na1–O2 ⁱⁱⁱ	2.313(4) [2x]	O1–Os–O2	116.77(14) [2x]
Na1–O1	2.760(18) [2x]	O2–Os–O2	126.5(3) [2x]
Na2–O2 ⁱⁱ	2.318(4)		
Na2–O2	2.400(5)		
Na2–O1 ^{iv}	2.402(3)		
Na2–O3 ⁱ	2.456(4)		
Na2–O3 ^v	2.547(5)		
Na2–O3 ⁱⁱ	2.758(5)		
Na2–Os	3.205(2)		
Na2–Na1 ^{xi}	3.276(3)		

Symmetry codes: (i) $y, x, -z$; (ii) $-x+1, -x+y+1, -z+1/3$; (iii) $x-1, y-1, z$; (iv) $x, y+1, z$; (v) $x-1, y, z$.

Similar OsO₅ groups, as observed here, were found in osmate(VIII) K₂OsO₅. The bond distances are slightly shorter as expected due to the higher oxidation state of Os, however, are in the same qualitative order, (average Os-O_{ax} 1.780 Å, av. Os -O_{eq} 1.766 Å).

As mentioned above, the crystal structures Na₃MO₅ with M = Os, Re are isostructural. The lattice parameters, the unit cell content, the packing of the different atoms, and the shortest bond distances are similar in both compounds. The MO₅ groups show similar bond lengths and angles, and the deviation from the ideal polyhedron is 0.26 % in both cases. Also, the coordination of the sodium atoms in both the compounds is almost identical, the Na₂ and Na₃ atoms in Na₃ReO₅ both correspond to Na₂ in Na₃OsO₅. However, Na₃ReO₅ is described in space group *P*3₁, a direct subgroup of *P*3₁21 as determined for Na₃OsO₅. After comparison of the two crystal structures, it was assumed that Na₃ReO₅ could also be described in *P*3₁21 space group, which then would be isotypic with Na₃OsO₅.

Concerning the oxidation state of osmium, so far only ternary osmates(VII) are known with sodium, while in the case of potassium only one osmate(VIII), K₂OsO₅, was obtained (section 4.1). K₂OsO₅ was obtained as a pure powder at similar conditions as the sodium compounds, however, in that case KO₂ was the potassium source which obviously acts as a stronger oxidant. The formation of osmates (VII) or (VIII) at moderate temperatures correlates with the presence of O₂⁻ or O₂²⁻ (also their oxidation power), respectively, and thus the thermal stability of the alkali compounds, Na₂O₂ and KO₂. It should be noted that formal hydrates of Na₃OsO₅ and K₂OsO₅, are also known, Na₃OsO₄(OH)₂ [133] and K₂OsO₄(OH)₂ [134], respectively. They contain osmium in the same valence states as the respective parent compounds, however, any hydrates of the hitherto hypothetical K₃OsO₅ and Na₂OsO₅ are not known.

4.3.6 Magnetic measurements

Magnetic measurements were performed on polycrystalline powder samples using a SQUID-Magnetometer (MPMS 5.5, Quantum Design) between 5 and 350 K in magnetic fields up to 5 T. Na₃OsO₅ displays paramagnetic behaviour with low temperature antiferromagnetic interactions at around 23 K and 6 K. The susceptibility plot is shown in Figure 4-15. The inverse magnetic susceptibility obey the Curie-Weiss Law down to about $T = 50$ K. Fitting the Curie and Weiss constants the values obtained are $C = 0.1994$ emu K/mol and $\theta \sim -10$ K. The effective magnetic moment is $\mu_{eff} = 1.26\mu_B$, which is less than the theoretical value of $1.73\mu_B$ for the d^1 system, Os⁷⁺ ion, due to spin orbit coupling.

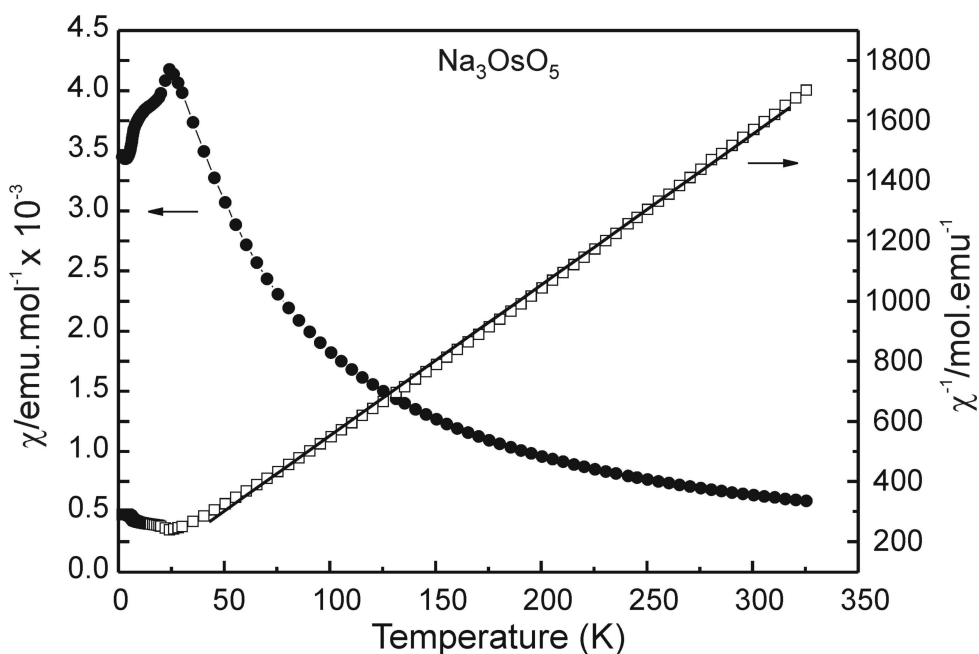


Figure 4-15 Magnetic susceptibility of Na₃OsO₅ represented as χ vs. T (circles) and χ^{-1} vs. T (squares) in an applied field of 5 T. The full line represents the linear fit using the Curie-Weiss law

The magnetic measurements are found to be similar to Li₅OsO₆ reported by Hoppe et. al. Na₃OsO₅ also contains a small impurity of Na₅OsO₆. Further purification and neutron studies are required in order to have a detailed overview on this compound.

4.4 CsOsO₄, Cesium osmate(VII)

The first tetraoxo-osmate(VII) mentioned in the literature, [AsPh₄][OsO₄] [135], was reported in 1984. Just one year later, the synthesis and IR spectroscopic data of the sodium, potassium, rubidium, and cesium tetraoxo-osmates(VII) were published [119], together with the lattice parameters of KOsO₄. Comparing all the X-ray powder patterns to CaWO₄ or to the corresponding periodates, the tetraoxo-osmates(VII) MOsO₄ (M = Na, K, Rb) were reported to crystallise tetragonally in the scheelite type of structure. However CsOsO₄, due to the larger size of cesium, was predicted to be orthorhombic. Nevertheless, none of the crystal structures are reported so far. In an article on the knowledge of AMO₄ type oxides, Hoppe et. al. have discussed the factors and the problems involved in the investigation of these structure types [136]. In the attempts to explore alkali metal oxo-osmates, CsOsO₄ was indeed found to crystallise in an orthorhombic lattice. For the preparation, here again the closed system of autoclaves under oxygen pressure was used. The synthesis, crystal structure and characterisation of CsOsO₄ are discussed ahead.

4.4.1 Synthesis

Polycrystalline samples of CsOsO₄ were synthesised from equimolar amounts of cesium peroxide and osmium metal at 873 K for 2 days at 29 MPa of oxygen pressure. The phase was obtained in the temperature range of 673 K to 873 K under 30 MPa to 50 MPa of oxygen pressure. Alternatively, the phase can also be obtained using stoichiometric amounts of cesium oxide and osmium metal. Single crystals suitable for X-ray diffraction studies were selected and sealed into glass capillaries of 0.3 mm diameter.

4.4.2 Thermal analysis

The thermal analysis of CsOsO₄ was carried out by using the DTA/TGA equipment (STA 409, Netzsch, Selb) coupled with a quadruple mass spectrometer. The sample was heated at the rate of 10 K/min in a corundum crucible under a flow of dry argon. As no residue was left after 1273 K, further investigation was not carried out.

4.4.3 Raman spectroscopy

Raman spectrum of CsOsO₄ was recorded with a Confocal Microscope Laser Raman System (Jobin-Yvon, excitation line 632 nm, power 4 mW). The spectrum is shown in Figure 4-16. The modes at 824.5 cm⁻¹ and 914.9 cm⁻¹ are assigned to the OsO₄ tetrahedra as reported in literature [78].

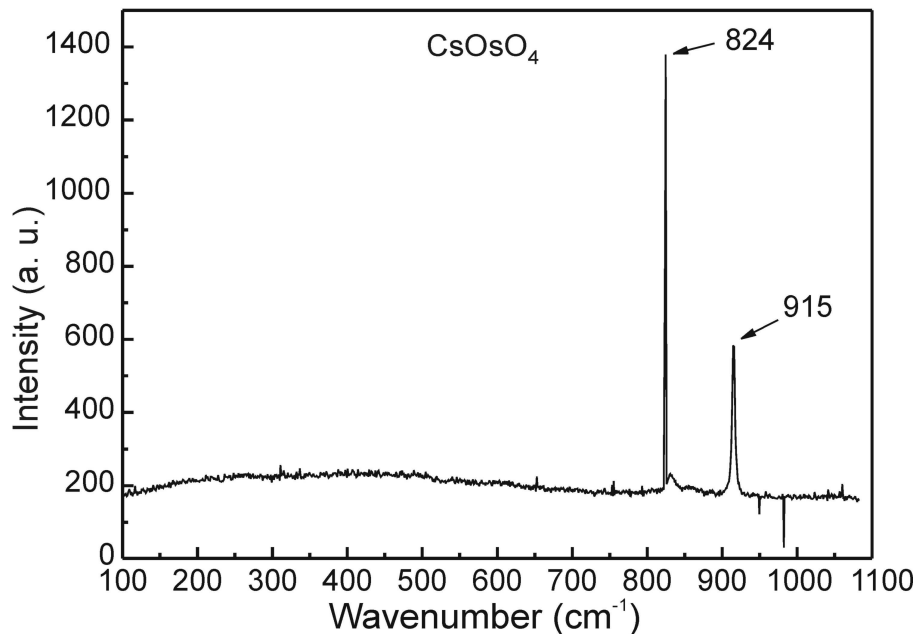


Figure 4-16 Raman spectrum of CsOsO₄

4.4.4 X-ray diffraction

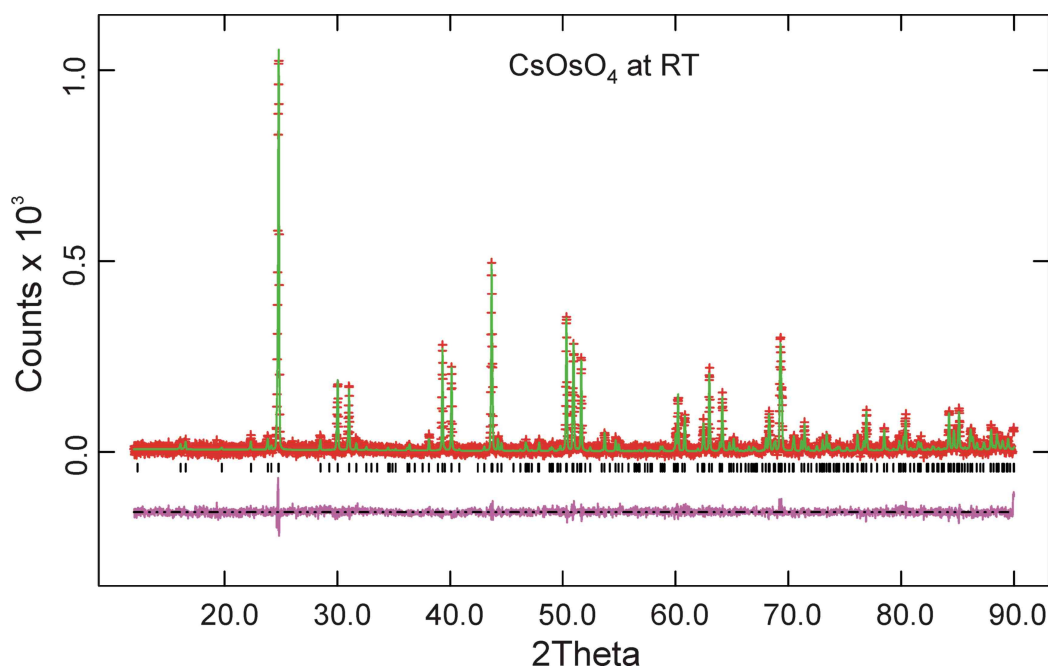
X-ray powder diffraction data for CsOsO₄ were collected with a Stoe Stadi-P diffractometer (Cu K α ₁, Ge monochromator, linear PSD) in steps of 0.01° over a 2 θ range from 0 to 90° for approximately 24 h with the samples sealed in glass capillaries of 0.2 mm diameter. CsOsO₄ was found to crystallise in an orthorhombic lattice, similar to CsReO₄ and CsIO₄, reported by Beintema in 1937, and it is also isostructural with CsTcO₄ [137,138]. Single crystal data were collected on a Bruker AXS with SMART-CCD (APEX) (MoK α Graphite monochromator, semi-empirical absorption correction with the program SADABS). Further information concerning the data collection and processing, the crystallographic parameters, as well as details on the structure solution and refinement are given in Table 4.14. The details of the Rietveld refinement are given in Table 4.15 and the refinement plot is shown in Figure 4-17.

Table 4.14 Crystallographic data and measurement details on the structure determination of CsOsO₄ from single crystal analysis

Compound	CsOsO ₄
Crystal system	orthorhombic
Space group	<i>Pnma</i> (no. 62)
Lattice parameters	a = 5.7835(2), b = 5.9378(2) c = 14.3895(5) Å
No. of formula units (Z)	4
Cell volume	494.15(3) Å ³
X-ray density	5.2030 g·cm ⁻³
Molar mass	1017.51
Diffractometer	Bruker SMART-APEX CCD
Wavelength	Mo-Kα (λ = 0.71073 Å)
Monochromator	Graphite
Temperature	293 K
Data collection mode	ω-Scan
Reciprocal lattice segments	Full sphere
2θ-region	5.12° < 2θ < 28.90°
hkl _{min} - hkl _{max}	-7 ≤ h ≤ 7; -8 ≤ k ≤ 8; -19 ≤ l ≤ 19
Number of measured reflections	1854
Number of unique reflections	348
Number of reflections > 2σ	296
Number of parameters	34
R _{int}	13.21%
Absorption coefficient	32.95 mm ⁻¹
R(F)(obs), R(F)(all)	0.0781, 0.0694
R _w (F ²)(obs), R _w (F ²)(all)	0.1677, 0.1636
Goodness-of-fit (all data)	1.183
Difference density min./max.	-5.171 / 2.948 e · Å ⁻³

Table 4.15 Rietveld refinement of powder data of CsOsO₄

Compound	CsOsO ₄
Crystal system	orthorhombic
Space group	<i>Pnma</i> (no. 62)
Lattice parameters at 298 K	a = 5.7536(6), b = 5.9425(6) c = 14.3524(13) Å
Unit cell volume	490.717(7) Å ³
No. of formula units (Z)	4
X-ray density (calculated)	5.239 g/cm ³
Least squares refinement data	
No. of refined parameters	30
Measurement range 2θ	11.98 – 90.01°
hkl-range	0 ≤ h ≤ 5, 0 ≤ k ≤ 5, 0 ≤ l ≤ 13
Measured reflections	7804
wR _p	10.97 %
R _p	8.32 %
Reduced χ ²	0.4355
R (F ²)	18.00

Figure 4-17 Rietveld refinement plot of CsOsO₄Table 4.16 Atomic coordinates and isotropic displacement parameters U_{iso} in \AA^2 of CsOsO₄ from single crystal and powder refinements

Single crystal refinement						
Atoms	Wyckoff Position	x	y	z	U_{eq}	
Cs	4c	0 0031(2)	0.25	0.12981(11)	0.0311(2)	
Os	4c	0.54867(14)	0.25	0.11866(7)	0.02676(12)	
O1	4c	0.8157(13)	0.75	0.0920(5)	0.06980(19)	
O2	4c	0.3349(21)	0.75	0.0327(10)	0.2097 (7)	
O3	8d	0.4989(6)	0.5030(9)	0.1857(4)	0.06292(11)	
Powder refinement						
Atoms	Wyckoff Position	x	y	z	U_{eq}	
Cs	4c	0 0256(8)	0.25	0.1261(5)	0.0417(17)	
Os	4c	0.4633(5)	0.25	0.8790(3)	0.0230(10)	
O1	4c	0.815 (5)	0.75	0.0901(19)	0.0210(8)	
O2	4c	0.362(5)	0.75	0.028(3)	0.0590(11)	
O3	8d	0.488(5)	0.518(4)	0.1807(17)	0.0730(9)	

Table 4.17 Anisotropic displacement parameters for CsOsO₄ from single crystal refinement. The U_{ij} are defined as $-2\pi^2 (U_{11}h^2a^{*2} + U_{22}k^2b^{*2} + U_{33}l^2c^{*2} + U_{12}hka^*b^* + U_{13}hla^*c^* + U_{23}klb^*c^*)$

Atom	U_{11}	U_{22}	U_{33}	U_{12}	U_{13}	U_{23}
Cs	0.011(4)	0.060(4)	0.022(4)	0.00000	0.009(2)	0.00000
Os	0.024(4)	0.0314(15)	0.025(2)	0.00000	0.006(2)	0.00000
O1	0.095(5)	0.0340(3)	0.080(5)	0.00000	-0.023(4)	0.00000
O2	0.129(9)	0.348(19)	0.152(11)	0.00000	-0.118(9)	0.00000
O3	0.041(2)	0.068(2)	0.080(3)	-0.0011(18)	0.0113(15)	0.022(3)

4.4.5 Structure description

The crystal structure was refined from the powder as well as from the single crystal data, the latter with anisotropic refinement of the thermal displacement parameters. Both

determinations reveal the same structure solution with similar structural characteristics. CsOsO₄ crystallises orthorhombic, in space group *Pnma*, isotypic to BaSO₄ (barite) [139]. The crystal structure consists of isolated tetrahedral OsO₄⁻ anions and Cs⁺ cations. The unit cell is shown in Figure 4-18.

The bond angles of the OsO₄ tetrahedron show fairly small deviations from tetrahedral angle, while the Os-O distances are obviously too short. Moreover, from single crystal analysis the thermal parameter for one oxygen atom was very large, and the refinement factors were deteriorated. The powder refinement yielded considerably better refinement factors compared to the single crystal analysis. The oxygen atoms display better thermal parameters, however still the thermal parameters were large.

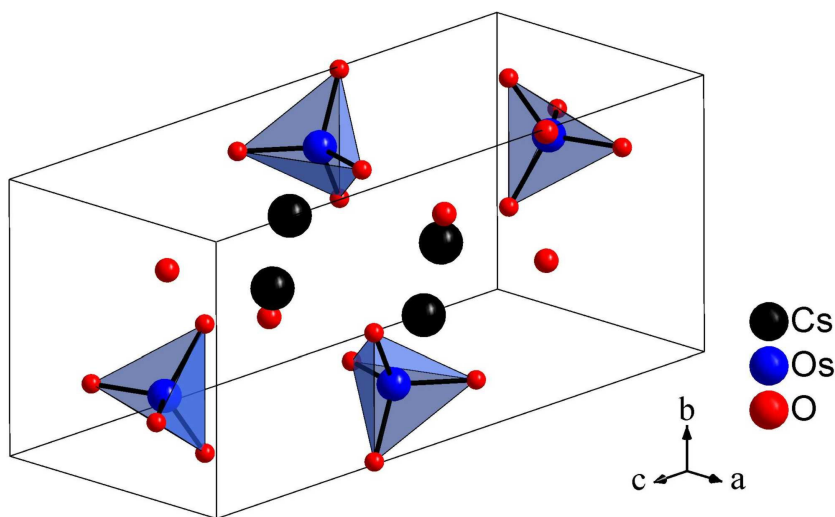


Figure 4-18 Unit cell of CsOsO₄

Both the large thermal parameters and the short bonds are expressions of librational disorder of the OsO₄⁻ anion, which is a result of weak attractive Coulomb interactions at relatively low temperatures in CsOsO₄. The OsO₄⁻ anion is just ineffectively fixed by the voluminous and thus soft Cs⁺ cation. Consequentially, the very large displacement parameter of O2 obtained from the single crystal data refinement can be explained by the weakest interaction to Cs⁺ cations of all oxygen atoms present in the asymmetric unit. While O1 and O3 have three Cs neighbours in a short distance, O2 has just one of them besides two Cs neighbours at a distance of 3.801 Å (dashed lines in Figure 4-19a). As expected, the main extension of the thermal displacement ellipsoid is perpendicular to the strongest bonds, O2-Os and O2-Cs (see. Figure 4-19a), while the Os-O2-Cs angle is 175°.

The cesium atoms are surrounded by 12 oxygen atoms forming a pentagonal prism where one pentagon is widened and capped by two O-atoms (see Figure 4-19b). The coordination polyhedra of cesium share common edges along [100] to form chains with Os⁷⁺ cations situated in between them. The distances obtained from the powder refinement as well as from the single crystal refinement are listed in Table 4.18.

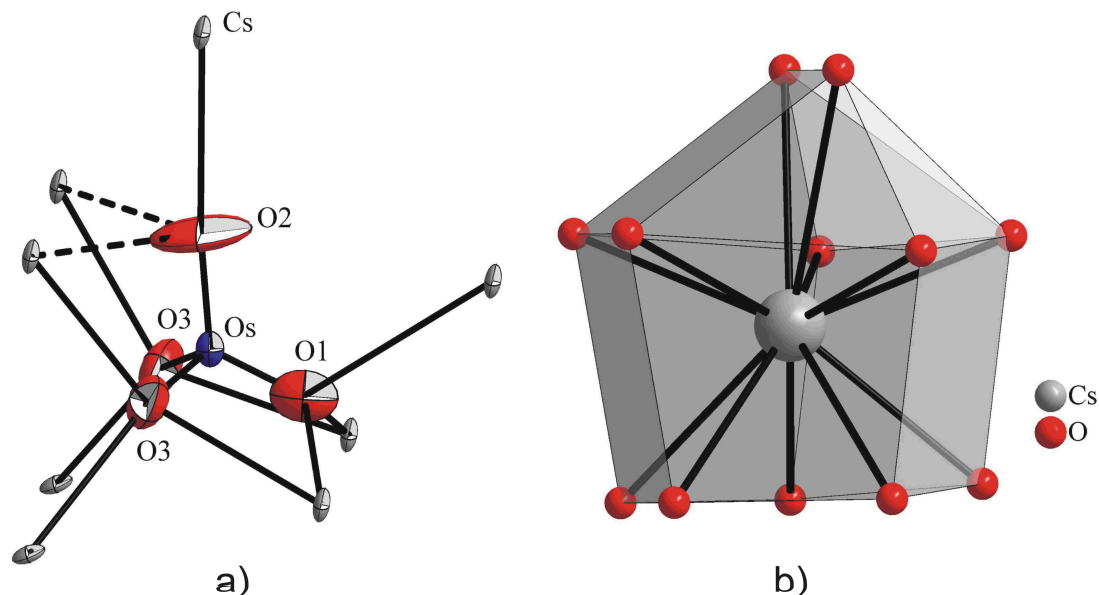


Figure 4-19 a) Cesium environment of the OsO₄ tetrahedron in CsOsO₄. Unlabelled atoms are Cs, ellipsoids are drawn at the 50 % probability level, dashed bonds represent Cs-O distances longer than 3.8 Å. Symmetry codes: (i): $-x, y + 0.5, -z$; (ii): $x, -y + 1.5, z$. b) Coordination polyhedron of Cs⁺ in CsOsO₄

Regarding the packing, the osmium atoms, the larger tetrahedral OsO₄ groups, and the cesium atoms are arranged in a tetragonally distorted diamond-like fcc packing. Each packing penetrates the other without any contact, as illustrated in Figure 4-20. This arrangement resembles the interpenetrating networks in Cu₂O, each of these networks having the anti-cristobalite structure which can also be derived from the diamond structure. From cesium tetraoxo salts CsMO₄, compounds with M = Mn, Tc, Re, Cl, Br, I are known. Most of them are described in the orthorhombic space group *Pnma*. The Re compound exhibits two modifications, orthorhombic α -CsReO₄, and at higher temperatures, tetragonal β -CsReO₄ [140,141]. CsIO₄ also displays more than one modification, CsBrO₄ crystallises only in the scheelite structure [142], and CsClO₄ is found in a cubic modification beneath the orthorhombic one [143].

All these phases tend to have short *M*-O bond distances and large thermal parameters for the oxygen atoms indicating weak interactions between the different ions.

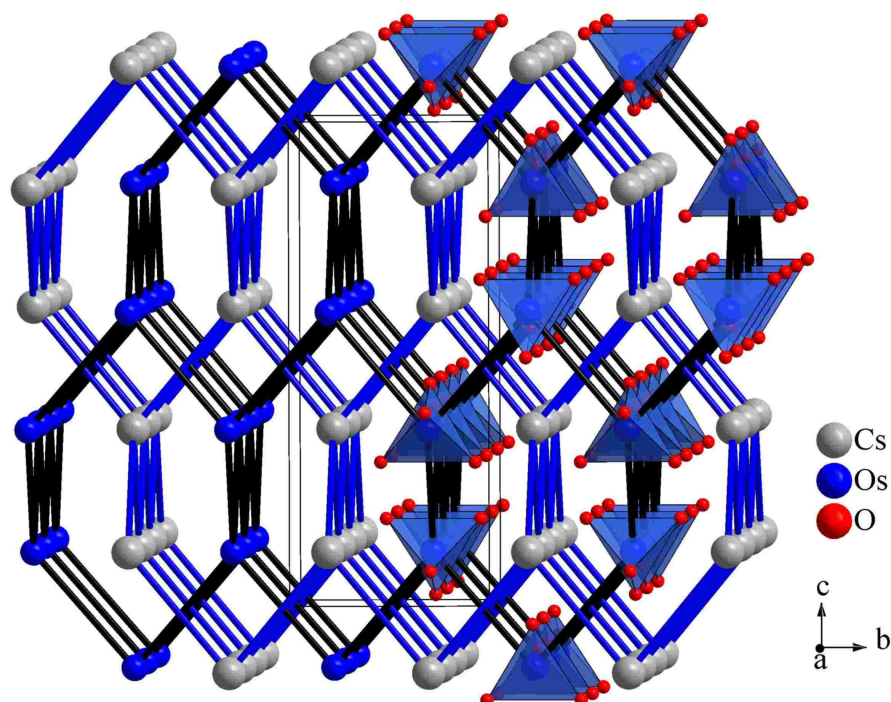


Figure 4-20 Packing of the metal atoms in CsOsO₄, in the right part, OsO₄ tetrahedra are drawn instead of Os atoms. To illustrate the diamond-like substructures, bonds have been drawn between cations of the same kind (blue: Cs network, black: Os network)

Table 4.18 Selected bond lengths (Å) and angles (°) for CsOsO₄ from single crystal and powder refinements

Bonds	Distances	
	Single crystal	Powder
Os–O1	1.591(8)	1.6615(3)
Os–O2	1.749(8)	1.670(4)
Os–O3	1.779(5)[2x]	1.650(3) [2x]
Cs–O2	3.048(8)	3.1419(4)
Cs–O3	3.051(5)[2x]	3.1982(3)[2x]
Cs–O1	3.207(3)[2x]	3.2501(12)[2x]
Cs–O3	3.335(5) [2x]	3.2050(3)[2x]
Cs–O1	3.359(8)	3.2357(3)
Cs–O3	3.377(4) [2x]	3.5662(3) [2x]
Cs–O2	3.801(11) [2x]	3.8148(3) [2x]
Atoms	Angles	
O1–Os–O2	178.32(6)°	
O1–Os–O3 [2x]	142.42(6)°	
O2–Os–O3 [2x]	116.30(8)°	
O3–Os–O3	115.36(2)°	

The single crystal measurement at lower temperatures is to be carried out to check whether the compound undergoes any structural transition.

4.4.6 Magnetic measurements

Magnetic measurements were performed on polycrystalline powder samples using a SQUID-Magnetometer (MPMS 5.5, Quantum Design) between 5 and 350 K in magnetic fields up to 5 T. From the measurements it was found that CsOsO₄ displays paramagnetic behaviour. The susceptibility plot of CsOsO₄ is shown in Figure 4-21. The inverse magnetic susceptibility obeys the Curie-Weiss Law down to about $T = 50$ K. The effective magnetic moment is $\mu_{eff} = 1.43\mu_B$, which is less than the theoretical value of $1.73\mu_B$ for the Os⁷⁺ ion with d¹ valence electron configuration, due to spin orbit coupling. The calculated magnetic moment is comparable with that reported for Ba₂MOsO₆ (M = Li, Na) [118,144] thus confirming the oxidation state +7 for osmium. The magnetic measurements also show a slight deflection in the inverse susceptibility plot (around 160 K), possibly indicating a structural transition. The magnetic moment was also calculated in two different temperature regions, 165 K to 300 K and 10 K to 160 K. The calculated moment in both these regions is around $1.50\mu_B$ and $1.43\mu_B$ respectively.

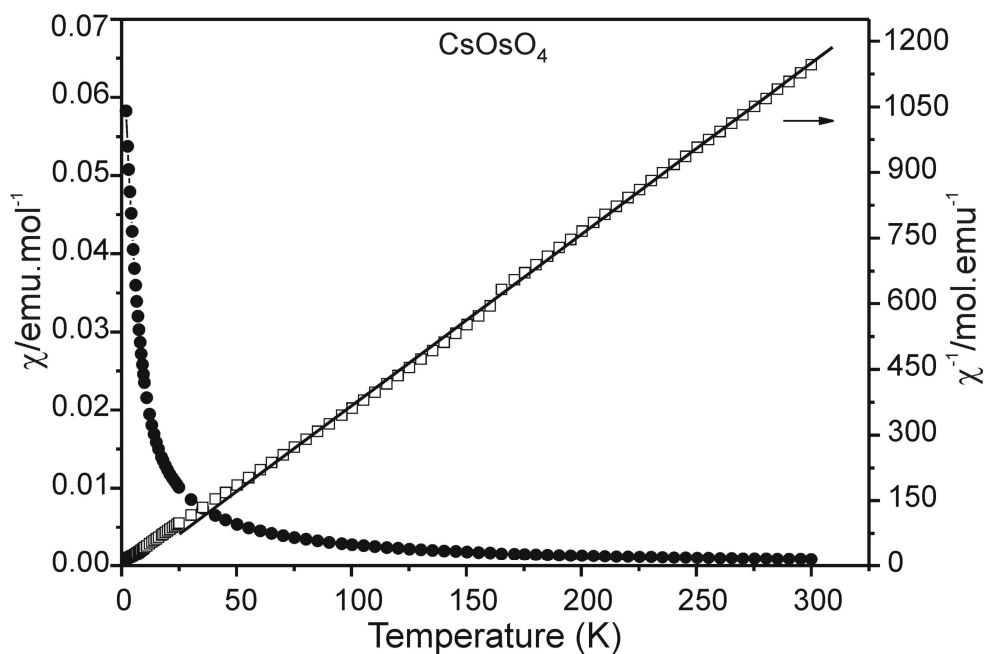


Figure 4-21 Magnetic susceptibility of CsOsO₄ represented as χ vs. T (circles) and χ^{-1} vs. T (squares) in an applied field of 5 T. The full line represents the linear fit using the Curie-Weiss law

4.5 $K_3NaOs_2O_9$, a triple perovskite

The current interest in triple perovskites containing transition metals is driven by its intriguing physical properties, in particular the electronic and magnetic properties. A number of mixed valent ruthenium(V/VI) and iridium(V/VI) containing triple perovskites have already been explored by zur Loye and co-workers [145,146]. Recently they also reported a couple of mixed iridium-ruthenium triple perovskites which exhibit interesting magnetic interactions [147,148]. Only one triple perovskite containing osmium is also explored containing divalent barium as the A cation and sodium as a B cation [149]. However, triple perovskites containing an alkali metal at the A sites, like $K_3NaRe_2O_9$ [150], are still very rare. Hence, an attempt has been made to replace the divalent barium cation on A site by the monovalent potassium cation in order to have an higher oxidation state for osmium. This resulted in the first osmium triple perovskite containing alkali metal cations at the A and B sites, exhibiting interesting magnetic interactions. The compound displays a transition to an antiferromagnetic state at around 140 K. Synthesis, crystal structure and characterisation of $K_3NaOs_2O_9$ is discussed in the following section.

4.5.1 Synthesis

For $K_3NaOs_2O_9$, KO_2 (synthesised from K and O_2) [92], Na_2O_2 and osmium powder (Chempur, 99.9 %) were mixed in the ratio 2 : 1 : 2, finely ground in an agate mortar and pressed into pellets. The pellets were put into gold crucibles which were sealed from one side and crimped from the other. Black, polycrystalline samples were obtained in stainless steel autoclaves under an oxygen pressure of 35 MPa at 873 K.

4.5.2 Thermal analysis

The thermal analysis of $K_3NaOs_2O_9$ was carried out by using the DTA/TGA equipment (STA 409, Netzsch, Selb) coupled with a quadruple mass spectrometer. The sample was heated at the rate of 10 K/min in a corundum crucible under a flow of dry argon till 1273 K. The compound starts losing oxygen at around 473 K. At 1273 K a possible composition of K_2OsO_4 is predicted from weight loss calculation along with Na_2O . Detailed investigation on this decomposition product was not continued further.

4.5.3 Raman spectroscopy

Raman spectrum of $K_3NaOs_2O_9$ was recorded with a Confocal Microscope Laser Raman System (Jobin-Yvon, excitation line 632 nm, power 4 mW). The spectrum is shown in

Figure 4-22. The structure consists of Os₂O₉ double octahedra, but no relevant spectral data were found in the literature.

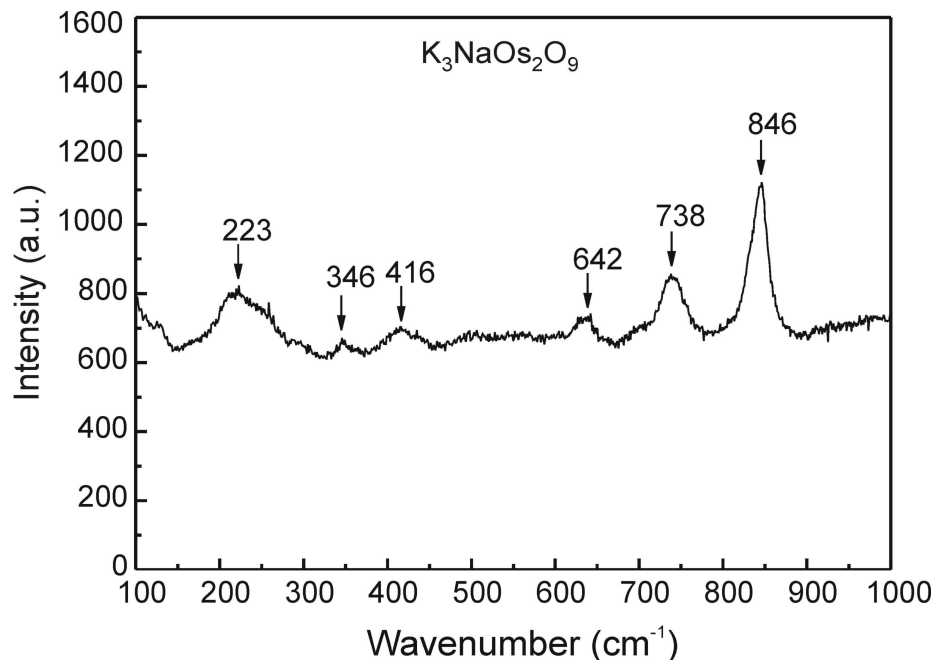


Figure 4-22 Raman spectrum of K₃NaOs₂O₉

4.5.4 X-ray diffraction

X-ray diffraction powder data were collected with a Stoe Stadi-P diffractometer (Cu K α ₁, Ge monochromator, linear PSD) in steps of 0.01° over a 2 θ range from 0 to 90° for approximately 24 h with the samples sealed in glass capillaries of 0.2 mm diameter. The measured X-ray pattern is shown in Figure 4-23.

Single crystal data were collected on a Bruker AXS with SMART-CCD (APEX) (MoK α ₁ Graphite monochromator, semi-empirical absorption correction with the program SADABS). Further information concerning the data collection and processing, the crystallographic parameters, as well as details on structure solution and refinement are given in Table 4.19. The atomic coordinates and isotropic displacement parameters are given in Table 4.20 while the anisotropic displacement parameters are listed in Table 4.21.

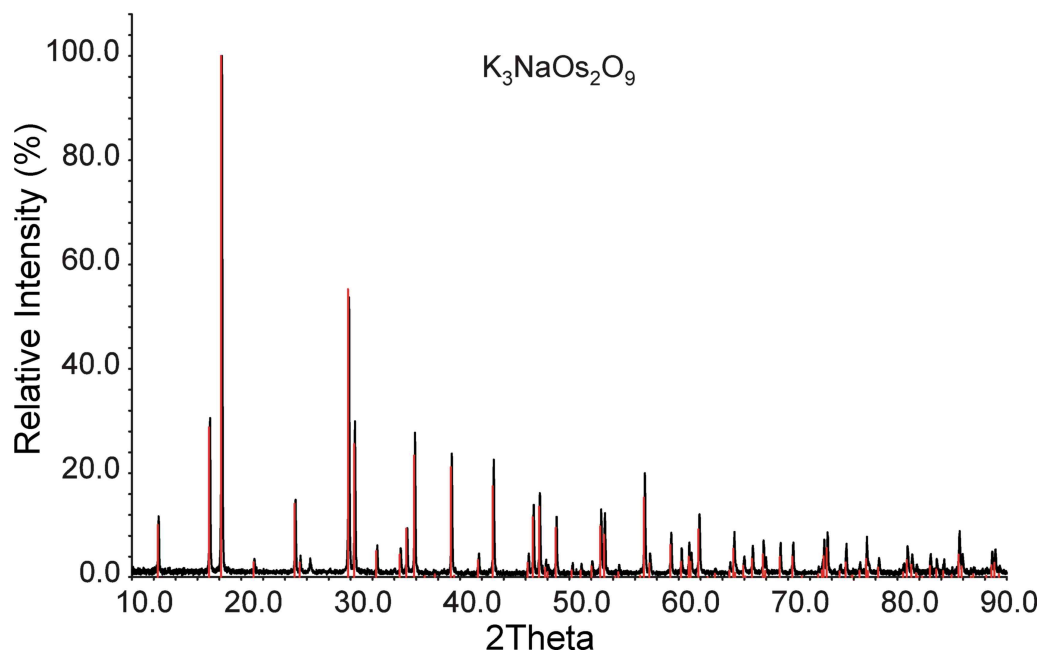


Figure 4-23 Measured X-ray pattern of K₃NaOs₂O₉, red reflections are the data calculated from single crystal analysis

Table 4.19 Crystallographic data and details on the structure determination of K₃NaOs₂O₉

Compound	K ₃ NaOs ₂ O ₉
Crystal system	Hexagonal
Space group	P6 ₃ /mmc (no. 194)
Lattice parameters	a = 5.9998(4) Å c = 14.3053(14) Å
Formula units	3
Cell volume	455.97(6) Å ³
Molar mass	1017.51
X-ray density	4.950 g·cm ⁻³
Absorption coefficient	29.939mm ⁻¹
Diffractometer	Bruker SMART-APEX CCD
Wavelength	Mo-Kα (λ = 0.71073 Å)
Monochromator	Graphite
Temperature	293 K
Data collection mode	ω-Scan
Reciprocal lattice segments	Full sphere
2θ-region	2.85° < 2θ < 29.95°
hkl _{min} - hkl _{max}	-8 ≤ h ≤ 8; -8 ≤ k ≤ 8; -20 ≤ l ≤ 20
Number of measured reflections	5187
Number of unique reflections	290
Number of reflections > 2σ	278
Number of parameters	22
R _{int}	4.26%
R(F)(obs), R(F)(all)	0.0285, 0.0304
R _w (F ²)(obs), R _w (F ²)(all)	0.0542, 0.0536
Goodness-of-fit (all data)	1.357
Difference density min./max.	-3.516 / 2.759 e · Å ⁻³

Table 4.20 Atomic coordinates and isotropic displacement parameters U_{iso} in Å² of K₃NaOs₂O₉ with standard deviations in parenthesis; U_{iso} is defined as $\exp[-8\pi^2 U(\sin^2\theta/\lambda^2)]$

Atom	Wy.Pos.	x	y	z	U_{iso}
K1	2 <i>b</i>	0	0	0.25	0.0225(10)
K2	4 <i>f</i>	0.3333	0.6667	0.1100(3)	0.0274(8)
Na	2 <i>a</i>	0	0	0	0.0158(17)
Os	4 <i>f</i>	0.6667	0.3333	0.1495(4)	0.0139(2)
O1	6 <i>h</i>	0.5305(8)	0.0610(17)	0.25	0.0175(18)
O2	12 <i>k</i>	0.3667(13)	0.1834(7)	0.0917(5)	0.0279(15)

Table 4.21 Anisotropic displacement parameters for K₃NaOs₂O₉. The U_{ij} are defined as $-2\pi^2(U_{11}h^2a^{*2} + U_{22}k^2b^{*2} + U_{33}l^2c^{*2} + U_{12}hka^*b^* + U_{13}hla^*c^* + U_{23}klb^*c^*)$

Atom	U_{11}	U_{22}	U_{33}	U_{12}	U_{13}	U_{23}
K1	0.0241(15)	0.0241(15)	0.0192(21)	0.01207(7)	0.00000	0.00000
K2	0.0233(11)	0.0233(11)	0.0356(19)	0.01167(5)	0.00000	0.00000
Na	0.0178(25)	0.0178(25)	0.0116(36)	0.00890(12)	0.00000	0.00000
Os	0.0147(2)	0.0147(2)	0.0123(3)	0.00733(1)	0.00000	0.00000
O1	0.0179(32)	0.0101(42)	0.0219(41)	0.00507(21)	0.00000	0.00000
O2	0.0150(32)	0.0340(30)	0.0283(30)	0.00751(16)	-0.0110(30)	-0.0055(15)

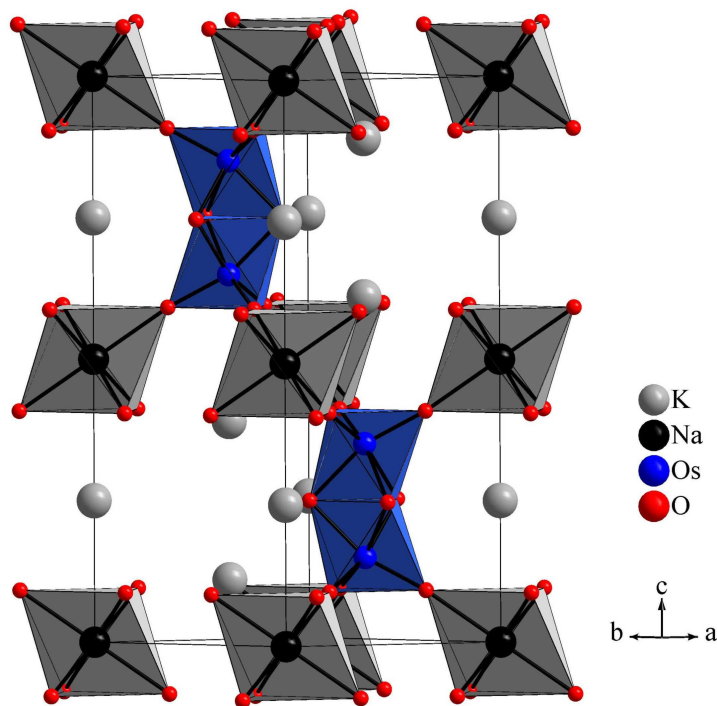
4.5.5 Structure description

According to single crystal analysis, the compound crystallises similar to the hexagonal 6*H*-BaTiO₃ type of structure, also known as triple perovskite. The crystal structure consists of isolated face sharing Os₂O₉ octahedra pairs. These octahedra pairs are linked by six common vertices to six NaO₆ octahedra. In-between these octahedra, the potassium atoms are situated in twelve-fold coordination. A schematic of the unit cell is shown in Figure 4-24. In terms of packing, the oxygen and potassium atoms in K₃NaOs₂O₉ form a close packing, as in the case of normal or double perovskites. However, in contrast to the ccp in double perovskite, a triple perovskite contains a combination of the hexagonal and cubic close packing. Their characteristic layer stacking is *ABAB* and *ABCABC* for hcp and ccp, respectively. The stacking found in the title compound is *ABACBC*. This packing creates octahedral voids between the layers, which are face-shared in the *B* layer and vertex-shared in the *A* and *C* layers. One quarter of these octahedra is filled in an ordered way by Os around *B* and by Na between *A* and *C*, respectively. Moreover the potassium atoms are surrounded by anti-cuboctahedra (K1) and cuboctahedra (K2) of oxygen atoms respectively (see Fig. 4.19). The Na-O distance of 2.3129(1) Å is in good agreement with the Na-O distance observed in the rhenium analogue, K₃NaRe₂O₉ (Na – O distance of 2.3256(2) Å). However, this Na – O distance is a bit longer as compared to the distance observed for Ba₃NaOs₂O₉ [2.259(5) Å] (with the similar sized Ba²⁺ instead of K⁺), and also for the cubic Ba₂NaOsO₆ [2.274(5) Å], both containing heptavalent osmium.

Table 4.22 Selected bond lengths (Å) and angles (°) for K₃NaOs₂O₉

Atoms	Distances	Atoms	Distances
Os–O1	2.0174(1) [3x]	K1–O1	3.0166(1) [6x]
Os–O2	1.7645(1) [3x]	K1–O2	2.9602(2) [6x]
		K2–O1	2.8650(2) [3x]
Na1–O1	2.3129(2) [6x]	K2–O2	3.0164(2) [6x]
		K2–O2	3.2789(3) [3x]
Os–Os	2.8760(3)		
Angles			
O1–Os–O2	162.5(3) [3x]	Os–O1–Os	90.90(3) [3x]
O1–Os–O1	74.80(3) [3x]		
O1–Os–O2	91.40(3) [3x]		
O2–Os–O2	99.80(3) [3x]		

Two different Os–O distances are observed within the octahedra pair, three long distances, each measuring 2.0174(1) Å, and three short distances, each measuring 1.7645(1) Å. The long Os–O distance is formed by the set of three oxygen atoms that are located in the shared face of the octahedra pair and the short Os–O distance is to the outer set of six oxygen atoms that corner share to the NaO₆ octahedra.

Figure 4-24 Unit cell of K₃NaOs₂O₉, approximate view along [1 1 0]

The short Os–O distances are comparable to distances measured for the OsO₆ octahedra with osmium in a high formal oxidation state such as +5, +6 or +7 as reported in the

literature. The Os-O distance measuring ~ 2.02 Å is typical for this set of M-O separations in triple perovskites.

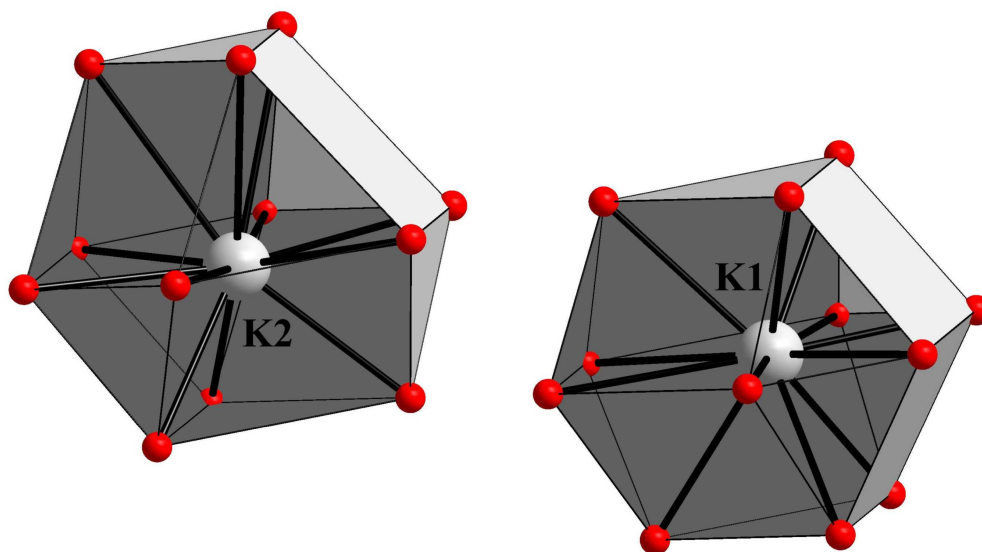


Figure 4-25 Coordination of potassium atoms in K₃NaOs₂O₉, a distorted cuboctahedron

The Os-Os interatomic distance of 2.8760 Å is considerably larger as compared to the Os-Os distances in osmium metal (2.675 Å) and in Ba₃NaOs₂O₉ (2.5491 Å). This deviation in the Os – Os bond distances is due to the charge of the osmium which is +7 in K₃NaOs₂O₉ and +5.5 in Ba₃NaOs₂O₉. However, the possibility of metal-metal interactions within the highly charged spin bearing osmium atoms cannot be ruled out, possibly via Os-O-Os superexchange interactions. Thus, the whole phenomenon gives rise to strong magnetic interactions with a transition to an antiferromagnetic state at around 140 K.

4.5.6 Magnetic measurements

Magnetic measurements were performed on polycrystalline powder samples using a SQUID-Magnetometer (MPMS 5.5, Quantum Design) between 5 and 350 K in the magnetic fields up to 5 T. K₃NaOs₂O₉ displays paramagnetic behaviour and undergoes a transition to an antiferromagnetic state at around 140 K. Susceptibility curves are shown in Figure 4-26. The inverse magnetic susceptibility obey the Curie-Weiss Law down to about $T = 150$ K. Further, the susceptibility increases till 25 K and further drops to zero with decrease in temperature. The effective magnetic moment is $\mu_{eff} = 1.739 \mu_B$. Fitting the Curie and Weiss constants the values obtained are $C = 0.3781$ emu K/mol and $\theta \sim -436$ K. The low Curie-Weiss temperature indicates strong interactions within the face sharing osmium octahedral pairs.

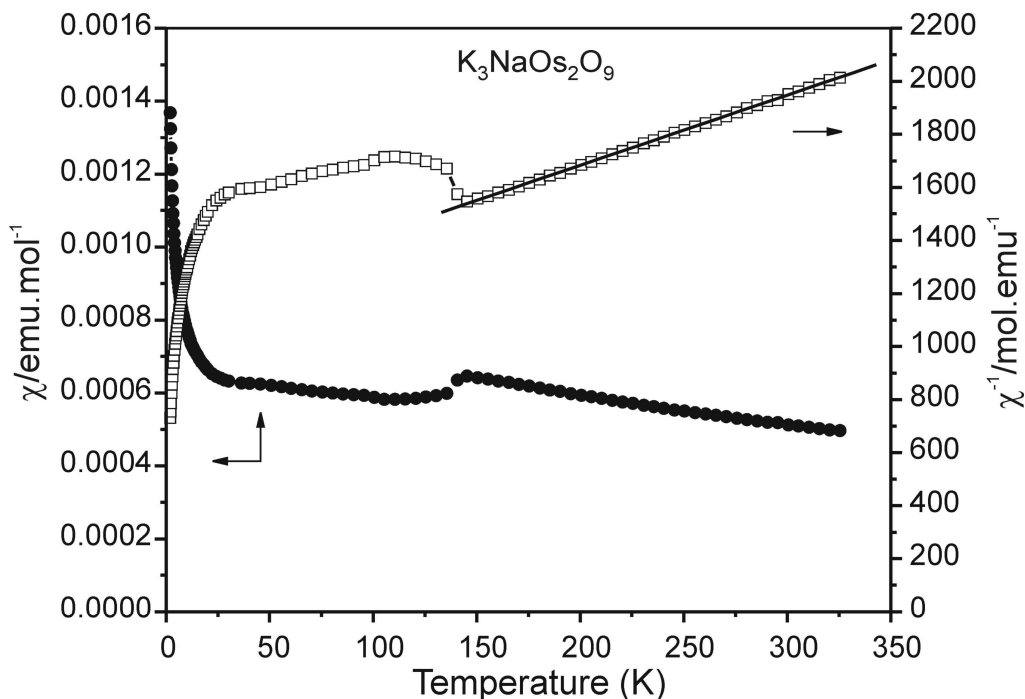


Figure 4-26 Magnetic susceptibility of K₃NaOs₂O₉ represented as χ vs. T (circles) and χ^{-1} vs. T (squares) in an applied field of 1 T. The full line represents the linear fit using the Curie-Weiss law

The high antiferromagnetic transition temperature suggests strong magnetic interactions as compared to Ba₃NaOs₂O₉. Further neutron studies are required to reveal the magnetic coupling and thus the magnetic structure of the compound.

4.5.7 Conductivity measurements

Measurements of the electrical conductivity were performed by four-point-probe method (Van-der-Pauw) on pressed pellets (diameter: 6 mm, thickness: 1 mm). The compound behaves as an insulator in the investigated temperature range of 1.5 K to 350 K.

5 Double perovskite

Double perovskites are studied since long time as they exhibit a variety of interesting electronic and magnetic properties. A double perovskite with osmium in the highest possible oxidation state is discussed in section 4.2. A main interest lies in such double perovskites which undergo a ferromagnetic transition at higher temperatures and display metallic or semi-conducting behaviour. A huge magnetoresistance effect is also observed in some double perovskites, as displayed by the manganites and Sr₂FeMoO₆. Several other analogues of osmium in Sr₂CrMO₆ ($M = \text{Mo, W, Re}$) [151-153] are reported in the literature amongst which Sr₂CrReO₆ displayed the highest Curie temperature, $T_c = 635$ K, till date in double perovskites. Recently, zur Loye reported a couple of double perovskites including Sr₂NiOsO₆, displaying antiferromagnetism around 50 K [154]. So, other than the high oxidation state compounds of osmium, one compound containing osmium in pentavalent state with chromium as the corresponding B cation was re-investigated. The compound displays the highest Curie temperature in the family of double perovskites till date. Neutron diffraction studies are also carried out on this compound.

5.1 Sr₂CrOsO₆

Sr₂CrOsO₆ was reported by Sleight and co-workers in 1962 for the first time, but only the X-ray data and an antiferromagnetic behaviour were referred. The title compound was synthesised to investigate the structure and magnetism in collaboration. The experiments revealed it to be ferromagnetic with the highest curie temperature known till date in the family of double perovskites, $T_c = 700$ K. The Neutron diffraction studies are being carried out in collaboration and are discussed in brief. A detailed analysis will be described elsewhere [155]. The synthesis, X-ray diffraction and magnetic measurements are discussed herein.

5.1.1 Synthesis

Polycrystalline samples of Sr₂CrOsO₆ were synthesised from stoichiometric amounts of SrO₂, CrO₂, and Os-metal powder at 1273 K in evacuated quartz tubes. The mixture was grinded thoroughly, pressed into pellets and put into a corundum crucible. The crucible was placed in quartz tube which was further evacuated and sealed under vacuum. The quartz tube was heated at 1273 K for 2 days. The obtained product was further heated

under oxygen flow at 673 K overnight to remove the excess of Os-metal as an impurity. The compound is insensitive to air.

5.1.2 Thermal analysis

The thermal analysis of Sr₂CrOsO₆ was carried out by using the DTA/TGA equipment (STA 409, Netzsch, Selb) coupled with a quadruple mass spectrometer. The sample was heated at the rate of 10 K/min in a corundum crucible under a flow of dry argon till 1573 K. The compound remains stable up to this temperature. The decomposition was also monitored under oxygen flow up to 1573 K. Osmium volatilises forming OsO₄ and the compound decomposes forming SrCr^{VI}O₄, Sr₈O(Cr^{VI}O₄)₄(Cr^{VI}O₄)₂ and Sr₂Cr^{IV}O₄, as identified by X-ray diffraction from the residues.

5.1.3 Raman spectroscopy

A Raman spectrum of Sr₂CrOsO₆ was recorded with a Confocal Microscope Laser Raman System (Jobin-Yvon, excitation line 632 nm, power 4 mW). The obtained spectrum is shown in Figure 5-1. The medium mode observed at 856 cm⁻¹ is similar to the mode observed for OsO₆ octahedra in literature [78].

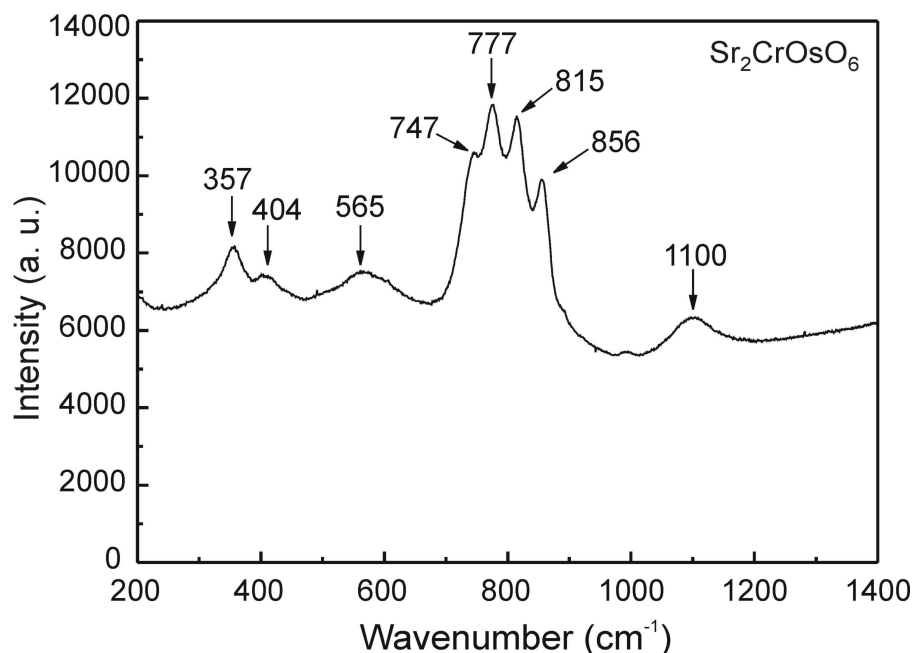


Figure 5-1 Raman spectrum of Sr₂CrOsO₆

Some of the modes obtained are comparable to the spectrum of the double perovskite K₂NaOsO_{5.5} (especially, those at 565, 777, 815, 856 cm⁻¹, see section 4.2.3), which also contain isolated OsO₆ octahedra as characteristic structure units.

5.1.4 X-ray diffraction, neutron diffraction and crystal structure

X-ray diffraction powder data were collected with a Stoe Stadi-P diffractometer (Cu K α_1 , Ge monochromator, linear PSD) in steps of 0.01° over a 2 θ range from 0 to 90° for approximately 24 h with the samples sealed in glass capillaries of 0.2 mm diameter. The measured X-ray pattern is shown in Figure 5-2. To gain further insight into the magnetic coupling, neutron data are necessary. The neutron data collection is in progress, the results will be discussed elsewhere. Further information concerning the data collection and processing, the crystallographic parameters, as well as details on structure solution and refinement are given in Table 5.1. The atomic coordinates and isotropic displacement parameters are given in Table 5.2.

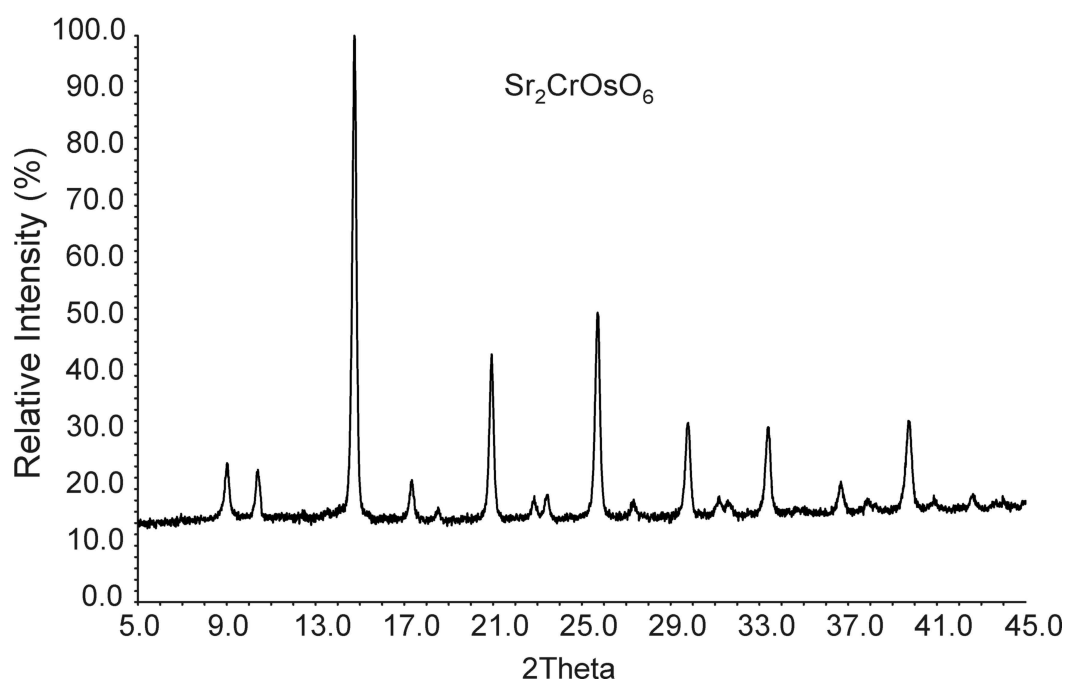


Figure 5-2 Measured X-ray pattern of Sr₂CrOsO₆

According to the powder refinement Sr₂CrOsO₆ crystallises as cubic double perovskite in space group Fm $\bar{3}$ m. The crystal structure consists of alternating CrO₆ octahedra and OsO₆ octahedra with twelve coordinate Sr cations separating the planes of chromium and osmium atoms. The osmium and chromium are in the formal oxidation states +5 and +3, respectively.

Table 5.1 Rietveld refinement of neutron powder data of Sr₂CrOsO₆ at 773 K

Compound	Sr₂CrOsO₆
Temperature	773 K
Crystal system	cubic
Space group	Fm $\bar{3}$ m (no. 225)
Lattice parameters	a = 7.8454(5) Å
Unit cell volume	482.89(3) Å ³
No. of formula units (Z)	4
X-ray density (calculated)	7.3422 g/cm ³
Wavelength	1.79714 Å
Least squares refinement data	
No. of refined parameters	12
Measurement range 2θ	-1.925 – 157.737°
hkl -range	-8 ≤ h ≤ 8, 0 ≤ k ≤ 5, 0 ≤ l ≤ 4
Measured reflections	66
R _p	3.74 %
wR _p	4.92 %
Reduced χ^2	2.0632

Table 5.2 Atomic coordinates and isotropic displacement parameters U_{iso} in Å² of Sr₂CrOsO₆, U_{iso} is defined as exp[-8π² U(sin²θ/λ²)] at 773 K

Atom	Wy.Pos.	x	y	z	Occupancy	U_{iso}
Sr1	8c	0.25	0.25	0.25	1.00000	0.0023(5)
Cr1	4a	0	0	0	0.99976	0.0023(5)
Os1	4b	0.5	0.5	0.5	0.99976	0.0023(5)
O	24e	0.2494(6)	0	0	0.99992	0.0146(6)

An example of the Rietveld refinement at 773 K is shown in Figure 5-3. The refinement of the magnetic structure is also being carried out at 2 K. The structural transition is observed at lower temperatures (below 550 K) where the compound crystallises orthorhombic. However, the interpretation is still in progress and will be discussed elsewhere in details.

Table 5.3 Selected bond lengths (Å) for Sr₂CrOsO₆ at 773 K

Atoms	Distances
Os–O	1.9473(1) [6x]
Cr–O	1.9755(1) [6x]
Sr–O	2.7739(1) [12x]

At room temperature the spins of chromium and osmium are aligned anti-parallel giving rise to antiferromagnetism. However, at higher temperatures the chromium and osmium spins are aligned parallel giving rise to ferromagnetic behaviour.

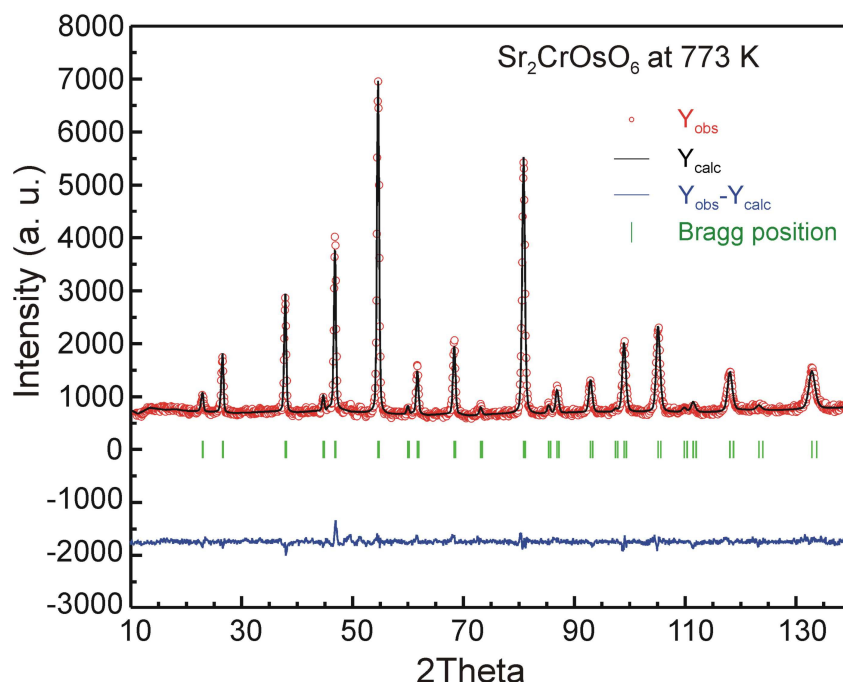


Figure 5-3 Rietveld refinement plot of neutron data for Sr₂CrOsO₆ at 773 K, with observed (red) and calculated (black) intensities, difference plot (blue) and the Bragg positions (green) are shown

In this compound the magnetic transition metal ion Cr³⁺ with a less localized 3d state and Os⁵⁺ ion with a delocalized 5d state enhance the hopping of the electrons between these sites. This process results in strong ferromagnetic exchange mechanism. The ordered double perovskites with cubic symmetry are the best candidates to have highly pronounced ferromagnetic interactions with high Curie temperatures. This is attributed to the exchange strength which depends upon the bond angles between the exchange pathways and is usually maximum for a 180° super-exchange (as observed in the case of the title compound, Cr-O-Os = 180°).

5.1.5 Magnetic measurements

Magnetic measurements were performed on polycrystalline powder samples using a SQUID-Magnetometer (MPMS 5.5, Quantum Design) between 5 and 1023 K in magnetic fields up to 5 T. The magnetic moment plot against temperature is shown in Figure 5-4. The ferromagnetic transition takes place around 700 K. The hysteresis loop measured at different temperatures is shown in Figure 5-5.

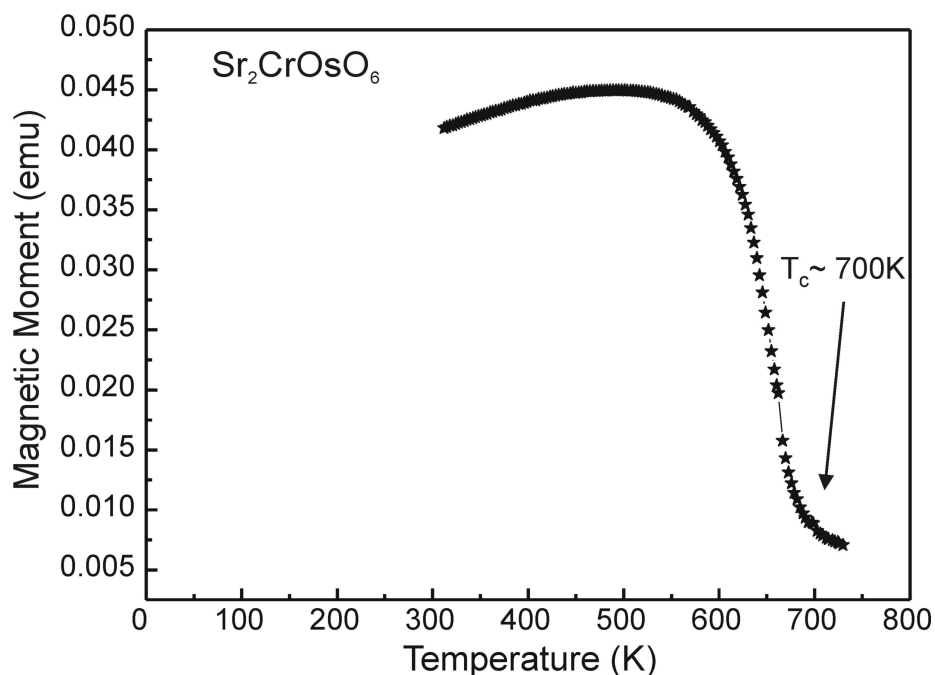


Figure 5-4 Plot of Magnetic moment vs. Temperature of Sr₂CrOsO₆ in an applied field of 0.1 T, ferromagnetic transition takes place with curie temperature(T_c) of around 700 K.

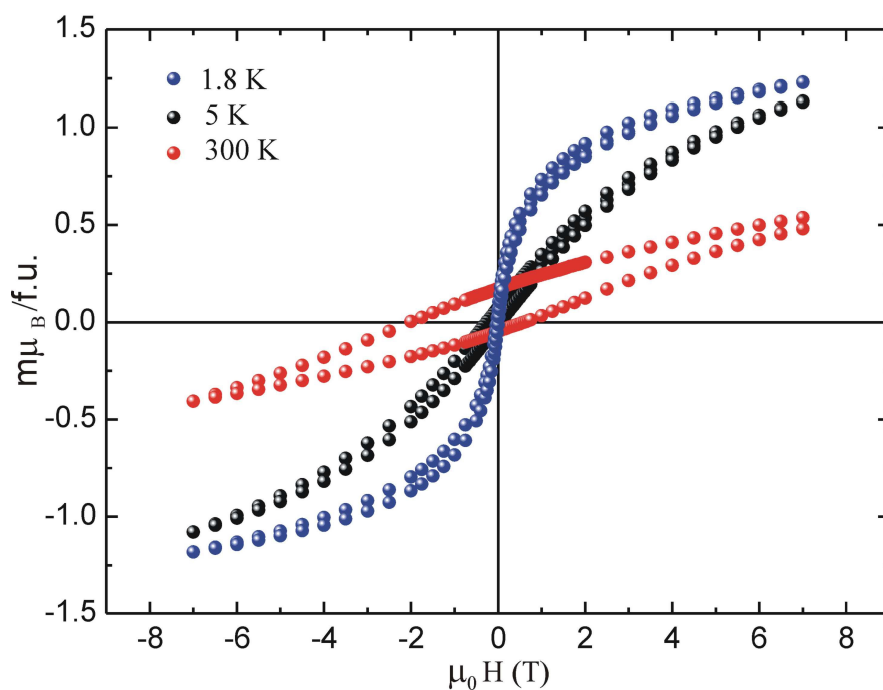


Figure 5-5 Hysteresis loop of Sr₂CrOsO₆ at different temperatures, 1.8 K, 5 K and 300 K

The net magnetic moment at higher temperatures decreases with decreasing temperature to result finally in an antiferromagnetic half-metallic ground state at lowest temperature. The hysteresis behaviour is remarkable at higher temperatures and thus Sr₂CrOsO₆ might be interesting for applications where large hysteresis loops are required at elevated

temperatures. Detailed analysis, description of the magnetic structure and the whole phenomenon is to be discussed elsewhere [155].

The double perovskites have gained immense interest due to their interesting magnetic interactions near room temperature. New materials are being synthesised to meet the demands of potential technological applications such as spintronics, magnetic random access memories (MRAM) and storage devices. This double perovskite with a very high Curie temperature contributes significantly to the ever increasing task of exploring application oriented perovskite type oxides.

Summary

The work carried out in the course of this thesis has focused in exploring new ternary and quaternary alkali metal oxo-ruthenates and osmates. Attempts have been made to stabilise high oxidation states of ruthenium and osmium. For the syntheses of these new compounds, besides conventional solid state methods, the autoclave technique was applied. The elevated oxygen pressures, achievable by this method, provide unique advantages to stabilise oxides at elevated temperatures and to reach even higher valence states. Thus, the technique is found to be extremely suitable to obtain hexavalent ruthenium compounds and heptavalent/ octavalent osmium compounds, and to deal with the poisonous osmium tetroxide formed as an intermediate during the reaction. In the closed system this tetroxide intermediate also provides a highly oxidising atmosphere in addition to the oxygen pressure generated in the autoclave. On the other hand, the technique also permits the use of alkali metal oxides/peroxides as starting materials at high temperatures.

In ternary and quaternary alkali metal oxo-ruthenates, the corresponding compounds are categorized based on the shortest Ru-Ru distances among the Ru^{6+} ions. Within this family, the compounds display a trend of increasing magnetic interactions with decrease in the size of alkali metals. Neutron diffraction studies are also carried out on Na_2RuO_4 , the ternary oxo-ruthenate displaying the highest magnetic transition temperature in this family. The low temperature magnetic structure has also been deduced from the same. Thus, the major part of the hexavalent alkali oxo-ruthenates is structurally investigated, along with their characterisation and magnetic properties which were not explored so far.

A number of new ternary and quaternary alkali metal oxo-osmates containing heptavalent and octavalent osmium have been explored. Some more high valent osmium containing oxides, which have been predicted and sketchily studied earlier, by spectroscopic methods, have now been characterised with their crystal structures and properties. Only a few double and triple perovskite oxides with alkali metal cations as the *A* and *B* cations are known till today. Some of the new compounds explored in this work belong to this family and represent the first osmium perovskites containing alkali metal cations at the *A* site.

$\text{Sr}_2\text{CrOsO}_6$, a cubic double perovskite is re-investigated and found to exhibit the highest Curie temperature known so far in the family of double perovskites. The compound

belongs to the increasing list of double perovskites with the task of discovering high ferromagnetic ordering temperature for potential technological applications.

The new compounds synthesised and characterised in the course of this work are discussed ahead in brief.

Na₂RuO₄

Na₂RuO₄ is prepared from Na₂O₂ and RuO₂ *via* high oxygen pressure synthesis. The compound crystallises in the monoclinic space group $P2_1/c$ ($a = 10.721(6)$, $b = 7.033(4)$, $c = 10.871(6)$ Å, $\beta = 119.10(4)^\circ$, $Z = 8$, 2503 unique reflections, $R_1 = 0.049$). Structure determination from single crystal data shows that the compound consists of infinite chains of RuO₅ trigonal bipyramids connected through their axial vertices. The Na cations connect the pseudo hexagonally close packed $^1_\infty[\text{RuO}_3\text{O}_{2/2}]$ chains and are coordinated by six or seven oxygen atoms, respectively. The magnetic properties are indicative for a largely one dimensional spin system showing an onset of significant exchange interactions at 200 K and a three dimensional antiferromagnetic ordering below 50 K. The neutron diffraction studies revealed that the Ru magnetic moments are coupled antiferromagnetically along the b -axis (along the RuO₄ chains) and are forming ferromagnetic planes along the a -axis.

K₂RuO₄ and Rb₂RuO₄

The compounds were synthesised more than a decade ago and are of β -K₂SO₄ structure type. However, the magnetic properties were not studied. In this work, polycrystalline samples of K₂RuO₄ and Rb₂RuO₄ are synthesised under an oxygen flow at 898 K for 2 days. Inverse magnetic susceptibilities obey the Curie-Weiss law down to about $T = 60$ K. Effective magnetic moments are $\mu_{\text{eff}} = 2.68 \mu_{\text{B}}$ for both compounds, which is 95 % of $\mu_{\text{SO}} = 2.83 \mu_{\text{B}}$, the ideal moment for the spin-only d^2 ($S = 1$) configuration, thus confirming the oxidation state +6 for ruthenium. Below 60 K, the inverse susceptibility curves diverge remarkably from the linear behaviour indicating the presence of antiferromagnetic interactions in both compounds, with $T_N = 14$ K and 4 K (2 transitions) for K₂RuO₄ and with $T_N = 9$ K for Rb₂RuO₄.

K₃Na(RuO₄)₂ and Rb₃Na(RuO₄)₂, Ruthenium Glaserites

K₃Na(RuO₄)₂ and Rb₃Na(RuO₄)₂ are prepared by solid state reactions of RuO₂, Na₂O₂, and RbO₂ or KO₂, respectively, at 873 K under oxygen atmosphere. K₃Na(RuO₄)₂ undergoes a

structural transition at 467 K and transforms from a monoclinic form at room temperature ($C2/c$, $a = 10.323(8)$, $b = 5.989(4)$, $c = 15.278(7)$ Å, $\beta = 90.49(5)^\circ$, $Z = 4$, single crystal data, 1231 independent reflections, $R_1 = 4.27\%$, $wR_2 = 8.95\%$) into a trigonal high temperature modification (Rietveld refinement from X-ray powder data, $P\bar{3}m1$, $a = 6.0164(1)$, $c = 7.6855(2)$ Å, $Z = 1$, 4053 data points, $R_p = 6.63\%$, $wR_p = 8.65\%$) which is isotypic to glaserite, $K_3Na(SO_4)_2$. According to a single crystal structure determination, $Rb_3Na(RuO_4)_2$ ($P\bar{3}m1$, $a = 6.0784(3)$, $c = 7.8994(6)$ Å, $Z = 1$, 281 independent reflections, $R_1 = 2.35\%$, $wR_2 = 5.51\%$) is isotypic to glaserite and the HT phase of $K_3Na(RuO_4)_2$. The rubidium analogue, $Rb_3Na(RuO_4)_2$, does not show a phase transition down to 100 K. Measurements of the inverse magnetic susceptibilities obey the Curie-Weiss law down to about 70 K. The effective magnetic moments of $\mu_{eff} = 2.85 \mu_B$ and $\mu_{eff} = 2.82 \mu_B$ for $K_3Na(RuO_4)_2$ and $Rb_3Na(RuO_4)_2$, respectively, are close to the ideal moment for the spin-only d^2 ($S = 1$) configuration, $\mu_{so} = 2.83 \mu_B$, thus confirming the hexavalent oxidation state for ruthenium. At lower temperatures, both compounds undergo an antiferromagnetic transition with $T_N \sim 28$ K in $K_3Na(RuO_4)_2$ and $T_N \sim 11$ K in $Rb_3Na(RuO_4)_2$. Raman measurements also confirm the tetrahedral coordination of ruthenium with oxygen. Both compounds exhibit an insulating behaviour.

Na₂RuO₃

Na_2RuO_3 is obtained from Na_2RuO_4 at 1123 K under a flow of argon. The structure is determined from X-ray powder diffraction. It is closely related to the α - $NaFeO_2$ and the Li_2SnO_3 structure types, layered variations of the NaCl type. The Na and Ru atoms are partially disordered. This partially disordered state is approximated by a two phase Rietveld refinement (Phase I: $R\bar{3}m$, $a = 3.12360(5)$, $c = 16.0370(4)$ Å, $Z = 2$; Phase II: $C2/c$, $a = 5.4141(4)$, $b = 9.3663(6)$, $c = 10.8481(4)$ Å, $\beta = 99.636(9)^\circ$, $Z = 8$). Inverse magnetic susceptibility obey the Curie-Weiss law down to about $T = 150$ K. The effective magnetic moment is $\mu_{eff} = 4.63\mu_B$, which is around 94% of $\mu_{SO} = 4.89 \mu_B$, the ideal moment for the spin-only d^4 ($S = 2$) configuration, thus confirming the oxidation state +4 for ruthenium. Na_2RuO_3 acts as a semi-conductor.

K₂OsO₅

K_2OsO_5 is obtained from reaction of osmium powder and KO_2 under elevated oxygen pressures. The compound crystallises in space group $P\bar{6}$ ($a = 10.7730(15)$, $c = 8.1453(16)$ Å, $Z = 6$, 1342 independent reflections, $R_1 = 1.91\%$, $wR_2 = 4.59\%$). Osmium is coordinated

by five oxygen atoms forming isolated OsO_5 trigonal bipyramids. These polyhedra are arranged in a hexagonal close packing, while potassium is occupying the octahedral voids and the centre of two face sharing tetrahedral voids. The OsO_5 groups are partially disordered, in which each second layer of the hexagonal close packing the bipyramids are observed in two possible orientations. Magnetic measurements show diamagnetic behaviour confirming the oxidation state +8 for osmium.

$\text{K}_2\text{NaOsO}_{5.5}$

$\text{K}_2\text{NaOsO}_{5.5}$ is prepared from KO_2 and osmium metal in autoclaves under oxygen pressure using NaOH as a mineralizer. The compound crystallises as a cubic double perovskite in space group $Fm\bar{3}m$ with $a = 8.41 \text{ \AA}$, containing perfectly ordered NaO_6 and OsO_6 octahedra. The cub-octahedron of potassium is slightly distorted due to the different size of the NaO_6 and OsO_6 octahedra, resulting in rectangles instead of squares and equilateral triangles of two different sizes as faces. Full occupation of all crystallographic sites participating in the double perovskite structure does not provide the charge neutrality, even while assuming the highest possible valence state for osmium. Hence, to achieve this, the occupancy of the oxygen atom was fixed to the exact composition $\text{K}_2\text{NaOsO}_{5.5}$ during the crystal structure refinements. The composition $\text{K}_2\text{NaOsO}_{5.5}$ is assumed with fully occupied cation sites and a statistical disorder of oxygen vacancies in the crystal structure. No hint for the presence of hydrogen was obtained from infrared measurements. Although, the structure contains this unsatisfying disorder, the perovskite structure type matrix is able to stabilise the compound in equilibrium conditions, and provides access to this phase by a broad range of starting compounds and reaction conditions.

Na_3OsO_5

Na_3OsO_5 is prepared by the reaction of sodium peroxide and osmium powder in gold crucibles under oxygen flow. According to single crystal structure determination the compound crystallises in the trigonal space group $P3_121$ (no. 152) with $a = 5.5529(2) \text{ \AA}$ and $c = 13.4726(8) \text{ \AA}$. The compound is isostructural to Na_3ReO_5 and contains isolated OsO_5 trigonal bipyramids. The osmium atoms form a distorted cubic close packing, where the sodium atoms occupy the octahedral and tetrahedral vacancies. This cation arrangement is similar to the Li_3Bi structure type. Na_3OsO_5 displays paramagnetic behaviour with low temperature antiferromagnetic interactions at around 23 K and 6 K.

CsOsO₄

CsOsO₄ is prepared from equimolar amounts of cesium peroxide and osmium metal at 873 K for 2 days at 29 MPa of oxygen pressure. The compound crystallises orthorhombic, in space group *Pnma* (no. 62) with $a = 5.7835(18)$, $b = 5.9378(19)$ and $c = 14.3895(47)$ Å, $Z = 4$, 348 unique reflections, $R = 8.27\%$. The structure consists of isolated OsO₄ tetrahedra, and is isotypic to the CsTcO₄ or CsIO₄. Also, similar to other CsMO₄ compounds, the thermal displacement parameters of the oxygen atoms are large and the Os-O bonds are too short to be reliable. These findings indicate a low fixation of the anion, and thus a weak interaction between OsO₄⁻ and the voluminous and soft Cs⁺ ions. Magnetic measurements exhibit a paramagnetic behaviour and Raman spectroscopy also confirms the presence of OsO₄ tetrahedra.

K₃NaOs₂O₉

K₃NaOs₂O₉ is prepared from stoichiometric amounts of KO₂, Na₂O₂ and excess of osmium metal powder in autoclaves under oxygen pressure. According to single crystal analysis, the compound crystallises hexagonally in space group *P6₃/mmc* (no. 194) with $a = 5.9998(4)$ and $c = 14.3053(14)$ Å. The structure is similar to the hexagonal 6*H*-BaTiO₃, also known as triple perovskite consisting of face sharing Os₂O₉ octahedra pairs which share six vertices to six NaO₆ octahedra. K₃NaOs₂O₉ displays paramagnetic behaviour and undergoes transition to an antiferromagnetic state at around 140 K. The inverse magnetic susceptibility obey the Curie-Weiss law down to about $T = 150$ K. Further, the susceptibility increases till 25 K and drops to zero with decrease in temperature. The effective magnetic moment is $\mu_{eff} = 1.739 \mu_B$. The very low Curie-Weiss temperature of -436 K indicates strong interactions within the face sharing osmium octahedra.

Sr₂CrOsO₆

Sr₂CrOsO₆ is prepared from stoichiometric amounts of SrO₂, CrO₂ and Os metal powder in corundum crucible placed in an evacuated quartz tube at 1273 K. Corresponding to the lattice parameters reported earlier in 1962, the compound crystallises as a cubic double perovskite in space group *Fm $\bar{3}$ m* with $a = 7.792$ Å. Magnetic measurements reveal robust ferromagnetism and the compound displays a strong ferromagnetic transition at 700 K. Neutron diffraction studies are still in progress to reveal the magnetic ordering phenomenon in the compound.

Na₃OsO₄(OH)₂

Na₃OsO₄(OH)₂ was obtained from NaOH and Os-metal powder at 673 K in autoclaves under oxygen pressure. The compound crystallises in the monoclinic space group $P2_1/m$ with $a = 5.7605(5)$, $b = 9.2995(7)$, $c = 5.9485(5)$ Å, $\beta = 118.168(2)^\circ$. The hydrogen atoms have been refined without any constraints resulting in plausible O-H distances. The crystal structure consists of osmium in octahedral coordination of four oxide and two hydroxide ions. These octahedral complexes are connected by hydrogen bridges to form infinite zigzag chains along the b axis.

Zusammenfassung

Im Rahmen dieser Arbeit wurden Synthese und Eigenschaften von neuen ternären und quaternären Alkalimetalloxoruthenaten und -osmaten untersucht. Dabei wurde versucht, Ruthenium und Osmium in hohen Oxidationsstufen zu stabilisieren. Für die Synthesen der neuen Verbindungen wurde, neben konventionellen festkörperchemischen Methoden, insbesondere die Autoklaventechnik angewandt. Die hohen Sauerstoffpartialdrücke, die mit Hilfe dieser Methode zugänglich sind, bieten außerordentliche Vorteile für die Stabilisierung von Oxiden bei erhöhten Temperaturen sowie zum Erreichen von hohen Valenzzuständen. Damit ist diese Technik sehr gut geeignet, um zu Verbindungen mit sechswertigem Ruthenium und sieben- und achtwertigem Osmium zu gelangen und ist eine sehr gute Methode zur sicheren Handhabung des toxischen, während der Reaktionen entstehenden Osmiumtetroxids. Das Tetroxid als Zwischenstufe im geschlossenen System erzeugt außerdem - zusätzlich zum Sauerstoffdruck - *in situ* eine stark oxidierende Atmosphäre während der Reaktion. Weiterhin ermöglicht diese Technik den Einsatz von luftempfindlichen Alkalimetallperoxiden und -hyperoxiden als Ausgangsverbindungen bei hoher Temperatur.

Die ternären und quaternären Alkalimetalloxo-ruthenate wurden anhand der kürzesten Ru-Ru-Abstände zwischen den Ru^{6+} -Ionen eingeordnet. Innerhalb dieser Substanzfamilie zeigen die Verbindungen zunehmende magnetische Wechselwirkungen bei gleichzeitig abnehmendem Radius des Alkalimetallkations. An Na_2RuO_4 , dem Oxoruthenat mit der höchsten magnetischen Übergangstemperatur, wurden Neutronenbeugungsuntersuchungen durchgeführt. Anhand dieser Experimente wurde auch die magnetische Struktur dieser Verbindung hergeleitet. Mit dieser Arbeit sind die Kristallstrukturen eines Großteils der sechswertigen Alkalioxo-ruthenate bekannt und deren Eigenschaften einschließlich des bisher unbekanntem Magnetismus untersucht.

Eine Reihe von ternären und quaternären Verbindungen mit sieben- oder achtwertigem Osmium wurde erstmals erhalten und charakterisiert. Von weiteren, hochvalenten Osmium enthaltenden Verbindungen, die bereits vorausgesagt oder mit Hilfe von spektroskopischen Methoden untersucht worden waren, sind jetzt auch Kristallstrukturen und Kenntnisse über sonstige Eigenschaften bekannt. Doppel- und Dreifachperowskite mit Alkalimetallkationen auf „A“- und „B“- Positionen sind bis heute nur in sehr geringer Anzahl bekannt. Die in dieser Arbeit untersuchten Verbindungen

gehören zu dieser Gruppe und stellen die ersten Osmiumperowskite mit Alkalimetallkationen auf der „A“-Position überhaupt dar.

$\text{Sr}_2\text{CrOsO}_6$, ein kubischer Doppelperowskit, wurde neu untersucht und zeigt die höchste, bisher gefundene Curie-Temperatur in dieser Verbindungsklasse. Die Verbindung gehört zur wachsenden Gruppe von Doppelperowskiten, bei denen hohe magnetische Ordnungstemperaturen entdeckt wurden und die sich für potentielle technologische Anwendungen anbieten.

Die wichtigsten Details der im Rahmen dieser Arbeit neu synthetisierten und charakterisierten Verbindungen werden im folgenden kurz aufgeführt.

Na_2RuO_4

Na_2RuO_4 wurde unter hohem Sauerstoffdruck aus Na_2O_2 und RuO_2 erhalten. Es kristallisiert monoklin in der Raumgruppe $P2_1/c$ ($a = 10,721(6)$, $b = 7,033(4)$, $c = 10,871(6)$ Å, $\beta = 119,10(4)^\circ$, $Z = 8$, 2503 symmetrisch unabhängige Reflexe, $R_1 = 0,0488$). Die Einkristallstrukturbestimmung zeigt, daß die Verbindung aus unendlichen Ketten trigonaler RuO_5 -Bipyramiden besteht, die über ihre axialen Atome verknüpft sind. Die Na-Kationen verbinden die hexagonal dicht gepackten ${}^1_\infty[\text{RuO}_3\text{O}_{2/2}]$ -Ketten und sind sechs- bzw. siebenfach von Sauerstoff koordiniert. Unterhalb von 200 K besteht Na_2RuO_4 aus einem hauptsächlich eindimensionalen Spinsystem und dreidimensionaler antiferromagnetischer Ordnung, die unterhalb von 50 K einsetzt. Wie Neutronenbeugungsexperimente belegen, sind die magnetischen Momente entlang der b -Achse, d. h. entlang der RuO_4 -Ketten, antiferromagnetisch gekoppelt und bilden ferromagnetische Schichten in der ac -Ebene.

K_2RuO_4 und Rb_2RuO_4

Die beiden, strukturell bereits seit geraumer Zeit aufgeklärten Verbindungen wurden auf ihre magnetischen Eigenschaften hin untersucht. Dazu wurden mikrokristalline Proben beider Substanzen innerhalb von 2 d bei 898 K im Sauerstoffstrom synthetisiert. Die inversen magnetischen Suszeptibilitäten gehorchen dem Curie-Weiss-Gesetz bis etwa 60 K. Das effektive magnetische Moment beträgt 2,68 μB für beide Verbindungen, also 95 % des idealen magnetischen Moments für den *spin-only*-Fall der d^2 -Valenzelektronenkonfiguration ($S = 1$), 2,83 μB , und belegt damit die Oxidationsstufe +6 für Ruthenium. Unterhalb von 60 K weicht die Kurve der magnetischen Suszeptibilität beträchtlich vom linearen Verlauf ab und verdeutlicht die Anwesenheit

antiferromagnetischer Wechselwirkungen unterhalb von 14 K bzw. 4 K für K_2RuO_4 (2 Übergänge) sowie 9 K für Rb_2RuO_4 .

$\text{K}_3\text{Na}(\text{RuO}_4)_2$ und $\text{Rb}_3\text{Na}(\text{RuO}_4)_2$, Ruthenium-Glaserite

Die beiden Verbindungen wurden aus Festkörperreaktionen von RuO_2 , Na_2O_2 und KO_2 bzw. RbO_2 bei 873 K unter Sauerstoffatmosphäre erhalten. $\text{K}_3\text{Na}(\text{RuO}_4)_2$ durchläuft einen Phasenübergang bei 467 K und wandelt sich aus einer monoklinen Form bei Raumtemperatur ($C2/c$, $a = 10,323(8)$, $b = 5,989(4)$, $c = 15,278(7)$ Å, $\beta = 90,49(5)^\circ$, $Z = 4$, Einkristalldaten, 1231 unabhängige Reflexe, $R_1 = 4,27$ %, $wR_2 = 8,95$ %) in eine trigonale Hochtemperaturmodifikation um (Rietveldverfeinerung aus Röntgenpulverdaten, $P\bar{3}m1$, $a = 6,0164(1)$, $c = 7,6855(2)$ Å, $Z = 1$, 4053 Datenpunkte, $R_p = 6,63$ %, $wR_p = 8,65$ %). $\text{Rb}_3\text{Na}(\text{RuO}_4)_2$ ist gemäß einer Einkristallstrukturanalyse ($P\bar{3}m1$, $a = 6,0784(3)$, $c = 7,8994(6)$ Å, $Z = 1$, 281 unabhängige Reflexe, $R_1 = 2,35$ %, $wR_2 = 5,51$ %) isotyp zu Glaserit, $\text{K}_3\text{Na}(\text{SO}_4)_2$, und der HT-Modifikation von $\text{K}_3\text{Na}(\text{RuO}_4)_2$. Die Rubidiumverbindung zeigt keinerlei Phasenübergang bis hinunter zu 100 K. Messungen der inversen magnetischen Suszeptibilität zeigen einen Curie-Weiss-Verlauf bis etwa 70 K. Die effektiven magnetischen Momente $\mu_{\text{eff}} = 2,82 \mu_B$ ($\text{K}_3\text{Na}(\text{RuO}_4)_2$) und $\mu_{\text{eff}} = 2,85 \mu_B$ ($\text{Rb}_3\text{Na}(\text{RuO}_4)_2$) befinden sich nahe am idealen Wert für eine d^2 -*spin-only*-Konfiguration und bestätigen die sechswertige Oxidationsstufe für Ruthenium. Bei niedrigen Temperaturen $T_N \sim 28$ K ($\text{K}_3\text{Na}(\text{RuO}_4)_2$) bzw. $T_N \sim 11$ K ($\text{Rb}_3\text{Na}(\text{RuO}_4)_2$) durchlaufen beide Verbindungen antiferromagnetische Übergänge. Raman-Messungen belegen die tetraedrische Koordination der Rutheniumatome. Beide Verbindungen sind Isolatoren.

Na_2RuO_3

Na_2RuO_3 wurde aus Na_2RuO_4 bei einer Temperatur von 1123 K im Argonstrom erhalten. Die Struktur wurde aus Röntgenpulverdaten bestimmt. Sie ist eng verwandt mit dem α - NaFeO_2 - und dem Li_2SnO_3 -Strukturtyp, die beide Schichtvarianten des NaCl-Typs sind, ist jedoch im Unterschied zu diesen durch partielle Fehlordnung der Kationen gekennzeichnet. Der partiell geordnete Zustand wurde über eine Zwei-Phasen-Rietveldverfeinerung angenähert (Phase I: $R\bar{3}m$, $a = 3,12360(5)$, $c = 16,0370(4)$ Å, $Z=8$; Phase II: $C2/c$, $a = 5,4141(4)$, $b = 9,3663(6)$, $c = 10,8481(4)$ Å, $\beta = 99,636(9)^\circ$, $Z = 8$). Die inverse magnetische Suszeptibilität gehorcht dem Curie-Weiss-Gesetz bis etwa 150 K. Das effektive magnetische Moment $\mu_{\text{eff}} = 4,63 \mu_B$ beträgt etwa 94 % des idealen Moments für

den *spin-only*-Fall der d^4 -Konfiguration, $\mu_{so} = 4,89 \mu\text{B}$, und belegt damit die Oxidationsstufe +4 für Ruthenium. Na_2RuO_3 verhält sich wie ein Halbleiter.

K_2OsO_5

K_2OsO_5 wurde erstmals aus einer Reaktion von Osmiumpulver und KO_2 unter erhöhtem Sauerstoffdruck erhalten. Die Substanz kristallisiert in der hexagonalen Raumgruppe $P\bar{6}$ ($a = 10,7730(15)$, $c = 8,1453(16) \text{ \AA}$, $Z = 6$, 1342 unabhängige Reflexe, $R_1 = 1,91\%$, $wR_2 = 4,59\%$). Osmium ist von fünf Sauerstoffatomen koordiniert, die in Form einer trigonalen Bipyramide angeordnet sind. Diese Polyeder sind hexagonal dicht gepackt, Kalium befindet sich darin in den Oktaederlücken sowie im Zentrum eines durch zwei flächenverknüpfte Tetraederlücken gebildeten Hohlraumes. Die OsO_5 -Bipyramiden sind in jeder zweiten Schicht der hexagonal dichten Packung fehlgeordnet, es werden jeweils zwei Orientierungen der Polyeder beobachtet. K_2OsO_5 verhält sich magnetischen Messungen zufolge diamagnetisch, was die Anwesenheit von Osmium in der Oxidationsstufe +8 bestätigt.

$\text{K}_2\text{NaOsO}_{5,5}$

$\text{K}_2\text{NaOsO}_{5,5}$ wurde aus KO_2 und Osmiumpulver in Edelstahlautoklaven unter erhöhtem Sauerstoffdruck mit NaOH als Mineralisator erhalten. Die Verbindung kristallisiert als kubischer Doppelperowskit in Raumgruppe $Fm\bar{3}m$ mit $a = 8,41 \text{ \AA}$ und enthält Na und Os ausgeordnet in den Oktaederlücken. Das Koordinationskuboktaeder um Kalium ist leicht verzerrt aufgrund der unterschiedlichen Größe der NaO_6 - und OsO_6 -Oktaeder, woraus Rechtecke anstatt von Quadraten und gleichseitige Dreiecke in zwei verschiedenen Größen als Begrenzungsflächen resultieren. Eine vollständige Besetzung aller an der Struktur des Doppelperowskits beteiligten, kristallographischen Lagen ergibt, auch unter Annahme des höchsten Valenzzustandes für Osmium, keine Ladungsneutralität. Um diese zu erreichen, wurde die Sauerstoffbesetzung im Verlauf der Verfeinerung auf die genaue Zusammensetzung $\text{K}_2\text{NaOsO}_{5,5}$ festgesetzt. Damit wird die Zusammensetzung $\text{K}_2\text{NaOsO}_{5,5}$ mit vollbesetzten Kationlagen und einer statistischen Fehlordnung der Sauerstoffleerstellen angenommen. Bei Infrarotmessungen an $\text{K}_2\text{NaOsO}_{5,5}$ wurden keinerlei Hinweis für die Anwesenheit von Hydroxid festgestellt. Obwohl die Kristallstruktur diese etwas unbefriedigende Art der Fehlordnung enthält, ist die Perowskitstruktur als Matrix in der Lage, die Verbindung unter Gleichgewichtsbedingungen zu stabilisieren, und ermöglicht

damit den Zugang zu dieser Phase über einen großen Bereich von Reaktionsbedingungen und Ausgangsverbindungen.

Na₃OsO₅

Na₃OsO₅ wird durch Reaktion von Natriumperoxid und Osmiumpulver in Goldampullen im Sauerstoffstrom synthetisiert. Gemäß einer Einkristallstrukturbestimmung kristallisiert die Verbindung in der trigonalen Raumgruppe *P*3₁21 (Nr. 152) mit $a = 5,5529(2) \text{ \AA}$ and $c = 13,4726(8) \text{ \AA}$. Die Verbindung enthält isolierte OsO₅-Bipyramiden und ist isostrukturell zu Na₃ReO₅. Die Osmiumatome bilden eine verzerrt kubisch dichte Packung, worin die Natriumatome alle Oktaeder- und Tetraederlücken besetzen, so daß die Kationenteilstruktur vom Li₃Bi-Strukturtyp abgeleitet werden kann. Na₃OsO₅ zeigt paramagnetisches Verhalten mit antiferromagnetischen Wechselwirkungen, die bei etwa 23 K sowie bei ca. 6 K einsetzen.

CsOsO₄

CsOsO₄ wurde aus äquimolaren Mengen von Cäsiumhyperoxid und Osmiumpulver innerhalb von zwei Tagen bei 873 K und 29 MPa Sauerstoffdruck dargestellt. Die Verbindung kristallisiert orthorhombisch in Raumgruppe *Pnma* (Nr. 62) mit $a = 5,7835(18)$, $b = 5,9378(19)$ und $c = 14,3895(47) \text{ \AA}$, $Z = 4$ (348 unabhängige Reflexe, $R1 = 8,27 \%$). Die Kristallstruktur enthält isolierte OsO₄-Tetraeder und ist isotyp zum CsTcO₄- bzw. CsIO₄-Strukturtyp. Die Temperaturfaktoren der Sauerstoffatome sind, wie auch in anderen CsMO₄-Verbindungen, recht groß und die Os-O-Abstände sehr kurz. Dies ist auf die schwache Fixierung der Anionen zurückzuführen und ist ein Anzeichen für die schwachen Wechselwirkungen zwischen den OsO₄-Gruppen und den voluminösen und weichen Cs⁺-Kationen. Magnetische Messungen zeigen paramagnetisches Verhalten. Mithilfe von Raman-Spektroskopie wird das Vorhandensein von tetraedrischen OsO₄-Baupgruppen bestätigt.

K₃NaOs₂O₉

K₃NaOs₂O₉ wurde aus stöchiometrischen Mengen von KO₂ und Na₂O₂ sowie einem Überschuß von Osmiumpulver in Edelstahlautoklaven unter Sauerstoffdruck dargestellt. Einer Einkristallstrukturanalyse gemäß kristallisiert die Verbindung hexagonal in der Raumgruppe *P*6₃/*mmc* (Nr. 194) mit $a = 5,9998(4)$ and $c = 14,3053(14) \text{ \AA}$. Die Kristallstruktur ähnelt derjenigen von 6*H*-BaTiO₃ und besteht aus flächenverknüpften

Os₂O₉-Oktaederpaaren, welche sechs gemeinsame Ecken mit sechs NaO₆-Oktaedern teilen. Die Kaliumatome sind kuboktaedrisch bzw. antikuboktaedrisch von jeweils zwölf Sauerstoffatomen umgeben. K₃NaOs₂O₉ zeigt paramagnetisches Verhalten und geht bei ungefähr 140 K in einen antiferromagnetischen Zustand über. Die inverse magnetische Suszeptibilität gehorcht dem Curie-Weiss-Gesetz bis etwa 150 K. Darunter steigt die Suszeptibilität bis 25 K an, um bei weiterer Temperaturerniedrigung schließlich auf Null zu fallen. Das effektive magnetische Moment beträgt 1.739 μB . Die hohe Curie-Weiss-Temperatur läßt auf starke Wechselwirkungen innerhalb der flächenverknüpften Os₂O₉-Doppeloktaeder schließen.

Sr₂CrOsO₆

Sr₂CrOsO₆ wurde aus stöchiometrischen Mengen von SrO₂, CrO₂ und Osmiummetallpulver in unter Vakuum in Quarzampullen eingeschlossenen Korundtiegeln bei 1273 K synthetisiert. Entsprechend den bereits früher publizierten Gitterkonstanten kristallisiert die Verbindung als kubischer Doppelperowskit in Raumgruppe $Fm\bar{3}m$ mit $a = 7,792 \text{ \AA}$. Magnetische Untersuchungen offenbaren einen widerstandsfähigen Ferromagnetismus sowie einen starken magnetischen Übergang bei 700 K. Neutronenbeugungsexperimente, die die magnetischen Ordnungsphänomene in Sr₂CrOsO₆ erhellen sollen, sind noch nicht abgeschlossen.

Na₃OsO₄(OH)₂

Na₃OsO₄(OH)₂ wurde aus NaOH und Osmiumpulver bei 673 K unter erhöhtem Sauerstoffdruck in Edelstahlautoklaven erhalten. Die Verbindung kristallisiert monoklin in der Raumgruppe $P2_1/m$ mit $a = 5,7605(5)$, $b = 9,2995(7)$, $c = 5,9485(5) \text{ \AA}$, $\beta = 118,168(2)^\circ$. Die Wasserstoffatome konnten frei verfeinert werden, wobei plausible O-H-Abstände gefunden wurden. In der Kristallstruktur ist Osmium oktaedrisch von zwei OH- und vier O-Liganden koordiniert. Diese oktaedrischen Komplexe sind über Wasserstoffbrücken zu unendlichen Zickzackketten parallel zur b -Achse verbunden.

Outlook

The goal of achieving new alkali transition metal oxides by stabilising high oxidation states is of utmost importance in the field of solid state chemistry. There is a necessity to improve our knowledge on detailed understanding of the structural and magnetic properties of these new oxides, especially the perovskite type oxides, as these materials are very important in potential technological applications. The oxidation state of a metal plays a crucial role in tuning a certain expected electrical or physical property of a particular material. Thus, synthesising new materials gives a pavement to explore its exciting magnetic and electronic properties and to understand their chemical and physical aspects from the application point of view.

The discovery of new alkali transition metal oxides for ruthenium and osmium in high oxidation state makes significant contributions in understanding the crystal chemistry of ternary/ quaternary alkali metal osmium and ruthenium oxides. The trend in the magnetic behaviour of these compounds, based upon the different high oxidation states enlightens in understanding their chemical and physical properties.

The ternary and the quaternary alkali metal oxo-ruthenates display an increasing trend in magnetic interactions as the distance between the spin bearing ruthenium atoms decreases.

This interesting trend necessitates exploring new ternary and quaternary oxo-ruthenates containing the smallest alkali metal cation, lithium. The hexavalent ruthenium containing oxides are still very rare and thus the exploration of these new compounds adds to the knowledge of realising new high oxidation states of ruthenium and hence in revealing their properties. Neutron diffraction studies are required to get an idea about the low temperature magnetic interactions.

Research in osmium containing oxides has taken a leap only since last few years, the probable reason being in dealing with the toxic nature of osmium metal. The higher oxidation state compounds of osmium are extremely hazardous, hence a great care is to be taken while dealing with such compounds and therefore reactions have to be carried out in closed systems. The quaternary alkali metal oxo-osmates stabilised in perovskite lattices display strong magnetic interactions at lower temperatures. Especially, in the case of $K_3NaOs_2O_9$, the antiferromagnetic transition temperature of around 140 K makes it necessary to explore this compound by neutron diffraction experiments.

In general, high oxidation state compounds are not investigated to a fuller extent, and thus it demands to explore more new materials with new oxidation states, in order to understand the hidden chemical and physical aspects.

The double perovskite, $\text{Sr}_2\text{CrOsO}_6$, exhibits the highest Curie temperature known till date in the family of double perovskites, which are in a great demand for potential technological applications. Neutron diffraction studies are still underway to understand the magnetic aspects. Thus, it challenges in the further discovery of new oxide materials with high curie temperatures.

Finally, to explore new high and unusual oxidation states, the alkali metals should be more frequently incorporated into the perovskite lattice.

List of Figures

Figure 2-1	Internal pressure in the autoclave using oxygen for high pressure syntheses with an effective autoclave volume of 0.02 litres.....	11
Figure 2-2	Schematic of the structure of oxygen high pressure autoclave	11
Figure 2-3	Oxygen high pressure autoclave (a) sub-assemblies; and (b) the assembled autoclave	12
Figure 2-4	Mechanism of generating oxygen pressure in the autoclave	13
Figure 2-5	Vacuum line	14
Figure 2-6	Schlenk apparatus (upper cross sections: LV of 29, remaining cross sections LV 14.5), a = ampoules sealing unit and b = capillary filling unit	14
Figure 3-1	Raman spectrum of Na_2RuO_4	23
Figure 3-2	X-ray pattern of Na_2RuO_4 (reflections in red is the pattern calculated from the single crystal structure determination).....	24
Figure 3-3	View of the crystal structure of Na_2RuO_4 along [010]. RuO_5 units are drawn as polyhedra. The ${}^1_\infty[\text{RuO}_3\text{O}_{2/2}]$ chains are arranged in a pseudo-hexagonal rod packing.....	26
Figure 3-4	Schematic drawing of two parallel ${}^1_\infty[\text{RuO}_3\text{O}_{2/2}]$ chains. The connecting Na^+ cations are indicated. Displacement ellipsoids have been drawn at the 50% probability level.....	27
Figure 3-5	Magnetic susceptibility of Na_2RuO_4 represented as χ^{-1} versus T and χ T versus T.....	30
Figure 3-6	Schematic of the Na_2RuO_4 crystal structure. RuO_5 trigonal bipyramids sharing apical oxygen atoms form one dimensional chains running along the b-axis ..	31
Figure 3-7	Rietveld refinement of Na_2RuO_4 powder neutron diffraction data from HRPT ($\lambda = 1.886 \text{ \AA}$) at 199 K. Experimental points, calculated profile and the difference curve are shown. The two rows of ticks at the bottom indicate the calculated peak positions for the main phase and the vanadium from the container material	31
Figure 3-8	Rietveld refinement of Na_2RuO_4 powder neutron diffraction data from DMC ($\lambda = 4.20 \text{ \AA}$) at 1.5 K. The experimental points, calculated profile and the difference curve are shown. Two rows of the ticks at the bottom indicate the calculated peak positions for the crystal and magnetic structures of Na_2RuO_4 ..	32
Figure 3-9	Portions of HRPT neutron diffraction patterns of Na_2RuO_4 collected at 1.5 K and 39 K and normalized to comparable scale.....	34
Figure 3-10	Temperature dependencies of the unit cell parameters a, b and c of Na_2RuO_4	35
Figure 3-11	Temperature dependence of the ordered Ru^{6+} magnetic moment magnitude in Na_2RuO_4 . Error bars are comparable to the symbol sizes, except for last few points (above 36 K) and are not shown for clarity. The solid line is a fit of the $M_{\text{Ru}}(\text{T})$ data to the empirical formula explained in equation (3.1) in the text ..	36
Figure 3-12	Low-temperature magnetic structure of Na_2RuO_4 . The antiferromagnetically ordered chains of Ru ions are couple ferromagnetically between each other. The magnetic Ru moments are aligned in the a-c plane with the dominant a- and minor c- components.....	36
Figure 3-13	Magnetic susceptibility of K_2RuO_4 represented as χ vs. T (circles) and χ^{-1} vs. T (squares) in an applied field of 5 T. The full line represents the linear fit using the Curie-Weiss law.....	38

Figure 3-14	Magnetic susceptibility of Rb_2RuO_4 represented as χ vs. T (circles) and χ^{-1} vs. T (squares) in an applied field of 5 T. The full line represents the linear fit using the Curie-Weiss law	39
Figure 3-15	Raman spectra of $\text{K}_3\text{Na}(\text{RuO}_4)_2$ (red) and $\text{Rb}_3\text{Na}(\text{RuO}_4)_2$ (black)	42
Figure 3-16	Measured X-ray pattern of $(\text{K}_3\text{NaRuO}_4)_2$. Room temperature (upper pattern) and 473 K (lower pattern). Asterisk marks indicate the reflections responsible for phase transition	43
Figure 3-17	X-ray diffraction patterns of $\text{K}_3\text{Na}(\text{RuO}_4)_2$ at different temperatures, asterisk (*) indicates the reflections responsible for the phase transition	43
Figure 3-18	Rietveld refinement of the HT phase of $\text{K}_3\text{Na}(\text{RuO}_4)_2$ (excluded region at $\sim 2\theta = 19^\circ$ is to avoid the spurious reflection arising from the detector)	45
Figure 3-19	Crystal structure of $\text{K}_3\text{Na}(\text{RuO}_4)_2$: a) HT phase above 467 K, view along $[-110]$; b) LT phase at room temperature, view along $[-100]$	46
Figure 3-20	Oxygen coordination of K^+ ions in a), b) HT phase and c), d) LT phase of $\text{K}_3\text{Na}(\text{RuO}_4)_2$, respectively	47
Figure 3-21	Sequence of RuO_4 and AO_x coordination polyhedra parallel to the c axis in a) $\text{Rb}_3\text{Na}(\text{RuO}_4)_2$ and b) LT- $\text{K}_3\text{Na}(\text{RuO}_4)_2$	50
Figure 3-22	Unit cell of $\text{Rb}_3\text{Na}(\text{RuO}_4)_2$	51
Figure 3-23	Specific heat of $\text{K}_3\text{Na}(\text{RuO}_4)_2$	53
Figure 3-24	Magnetic susceptibility of $\text{K}_3\text{Na}(\text{RuO}_4)_2$ represented as χ vs. T (circles) and χ^{-1} vs. T (squares) in an applied field of 5 T. The full line represents the linear fit using the Curie-Weiss law	56
Figure 3-25	Magnetic susceptibility of $\text{Rb}_3\text{Na}(\text{RuO}_4)_2$ represented as χ vs. T (circles) and χ^{-1} vs. T (squares) in an applied field of 5 T. The full line represents the linear fit using the Curie-Weiss law	56
Figure 3-26	Scattered X-ray intensities for Na_2RuO_3 as a function of diffraction angle 2θ . The observed patterns (cross), the best Rietveld fit profiles (line), difference curves (bottom line) are shown. Reflection positions of hexagonal (above) and monoclinic phase (below) are marked	60
Figure 3-27	Crystal structure of Na_2RuO_3 in a projection along the b -axis. RuO_6 octahedra and Na atoms are drawn	61
Figure 3-28	Magnetic susceptibility of Na_2RuO_3 represented as χ vs. T (circles) and χ^{-1} vs. T (squares) in an applied field of 5 T. The full line represents the linear fit using the Curie-Weiss law	62
Figure 4-1	Raman spectrum of K_2OsO_5	65
Figure 4-2	X-ray pattern of K_2OsO_5 , red peaks are calculated from the result of the crystal structure refinement	66
Figure 4-3	Perspective view of K_2OsO_5 along $[110]$. OsO_5 bipyramids and K^+ ions have been drawn, blue polyhedra: $z = 0$, green polyhedra: $z = 1/2$	69
Figure 4-4	View of the crystal structure of K_2OsO_5 along $[00-1]$. OsO_5 bipyramids and K^+ ions have been drawn, blue polyhedra: $z = 0$, green polyhedra: $z = 1/2$	69
Figure 4-5	Coordination of the two crystallographically independent osmium in K_2OsO_5 , a) trigonal bipyramidal OsO_5^{2-} group, b) split atom model of the two superimposed OsO_5 groups around the Os_2 atom	71
Figure 4-6	Raman spectra of $\text{K}_2\text{NaOsO}_{5.5}$	74
Figure 4-7	Measured X-ray pattern of $\text{K}_2\text{NaOsO}_{5.5}$, reflections in red is the pattern calculated from the single crystal structure determination. Weak unindexed reflections belong to $\text{K}_3\text{NaOs}_2\text{O}_9$, see section 4.5	75
Figure 4-8	Crystal structure of the double perovskite $\text{K}_2\text{NaOsO}_{5.5}$	77
Figure 4-9	Coordination of potassium atom in $\text{K}_2\text{NaOsO}_{5.5}$, a distorted cub-octahedron .	78

Figure 4-10 Measured X-ray pattern of Na ₃ OsO ₅ (red reflections are the data from single crystal analysis, weak unindexed reflections are of Na ₅ OsO ₆)	81
Figure 4-11 Unit cell of Na ₃ OsO ₅	82
Figure 4-12 a) Unit cell of Li ₃ Bi, b) Li ₃ Bi analogue part of the cation partial structure of Na ₃ OsO ₅	83
Figure 4-13 Crystal structure of Na ₃ OsO ₅ , view along the crystallographic c axis, the diagonal of the pseudo-cubic cell (dashed lines) of the Li ₃ Bi analogue cation packing, OsO ₅ bipyramids and Na ⁺ cations are drawn.	83
Figure 4-14 Coordination of cations in Na ₃ OsO ₅ , displacement ellipsoids are drawn at the 50 % probability level, dashed lines represent distances longer than 2.75 Å. Symmetry codes: (i) y, x, -z; (ii) -x+1, -x+y+1, -z+1/3; (iii) x-1, y-1, z; (iv) x, y+1, z; (v) x-1, y, z; (vi) -x+1, -x+y, -z+1/3; (vii) -y, x-y, z+1/3.	84
Figure 4-15 Magnetic susceptibility of Na ₃ OsO ₅ represented as χ vs. T (circles) and χ^{-1} vs. T (squares) in an applied field of 5 T. The full line represents the linear fit using the Curie-Weiss law	86
Figure 4-16 Raman spectrum of CsOsO ₄	88
Figure 4-17 Rietveld refinement plot of CsOsO ₄	90
Figure 4-18 Unit cell of CsOsO ₄	91
Figure 4-19 a) Cesium environment of the OsO ₄ tetrahedron in CsOsO ₄ . Unlabelled atoms are Cs, ellipsoids are drawn at the 50 % probability level, dashed bonds represent Cs-O distances longer than 3.8 Å. Symmetry codes: (i): -x, y + 0.5, -z; (ii): x; -y + 1.5, z. b) Coordination polyhedron of Cs ⁺ in CsOsO ₄	92
Figure 4-20 Packing of the metal atoms in CsOsO ₄ , in the right part, OsO ₄ tetrahedra are drawn instead of Os atoms. To illustrate the diamond-like substructures, bonds have been drawn between cations of the same kind (blue: Cs network, black: Os network).....	93
Figure 4-21 Magnetic susceptibility of CsOsO ₄ represented as χ vs. T (circles) and χ^{-1} vs. T (squares) in an applied field of 5 T. The full line represents the linear fit using the Curie-Weiss law.....	94
Figure 4-22 Raman spectrum of K ₃ NaOs ₂ O ₉	96
Figure 4-23 Measured X-ray pattern of K ₃ NaOs ₂ O ₉ , red reflections are the data from single crystal analysis	97
Figure 4-24 Unit cell of K ₃ NaOs ₂ O ₉ , approximate view along [1 1 0]	99
Figure 4-25 Coordination of potassium atom in K ₃ NaOs ₂ O ₉ , a distorted cub-octahedron	100
Figure 4-26 Magnetic susceptibility of K ₃ NaOs ₂ O ₉ represented as χ vs. T (circles) and χ^{-1} vs. T (squares) in an applied field of 1 T. The full line represents the linear fit using the Curie-Weiss law	101
Figure 5-1 Raman spectrum of Sr ₂ CrOsO ₆	103
Figure 5-2 Measured X-ray pattern of Sr ₂ CrOsO ₆	104
Figure 5-3 Rietveld refinement plot of Neutron data for Sr ₂ CrOsO ₆ at 773 K, with observed (red) and calculated (black) intensities, difference plot (blue) and the Bragg positions (green) are shown	106
Figure 5-4 Plot of Magnetic moment vs. Temperature of Sr ₂ CrOsO ₆ in an applied field of 0.1 T, ferromagnetic transition takes place with curie temperature(T _c) of around 700 K.	107
Figure 5-5 Hysteresis loop of Sr ₂ CrOsO ₆ at different temperatures, 1.8 K, 5 K and 300 K	107

List of Tables

Table 3.1	Crystallographic data and details on the structure determination of Na ₂ RuO ₄	25
Table 3.2	Atomic coordinates and isotropic displacement parameters U _{iso} in Å ² of Na ₂ RuO ₄ with standard deviations in parentheses; U _{iso} is defined as $\exp[-8\pi^2 U(\sin^2\theta/\lambda^2)]$	28
Table 3.3	Selected bond distances (Å) and angles (°) for Na ₂ RuO ₄ with standard deviations in parentheses	28
Table 3.4	Crystal structure parameters of Na ₂ RuO ₄ at T = 1.5 K and 199 K, refined from HRPT powder neutron data, space group P 21/c. The thermal parameters for the atoms of each sort were constrained to equality in the refinements	33
Table 3.5	Bond lengths of Ru-O in Å at selected temperatures	33
Table 3.6	Experimental X-ray powder data for K ₃ Na(RuO ₄) ₂ at RT with d > 1.4 Å	44
Table 3.7	Experimental X-ray powder data for Rb ₃ Na(RuO ₄) ₂ with d > 1.3 Å	44
Table 3.8	Powder refinement data of HT-K ₃ Na(RuO ₄) ₂	45
Table 3.9	Crystallographic data of K ₃ Na(RuO ₄) ₂ , at room temperature and at 473 K (HT), and Rb ₃ Na(RuO ₄) ₂ at room temperature	48
Table 3.10	Details of the single crystal refinement of K ₃ Na(RuO ₄) ₂ and Rb ₃ Na(RuO ₄) ₂	48
Table 3.11	Atomic coordinates and isotropic displacement parameters U _{iso} in Å ² of K ₃ Na(RuO ₄) ₂ (LT and HT) and Rb ₃ Na(RuO ₄) ₂ , U _{eq} is defined as $\exp[-8\pi^2 U(\sin^2\theta/\lambda^2)]$	49
Table 3.12	Anisotropic displacement parameters of LT-K ₃ Na(RuO ₄) ₂ and Rb ₃ Na(RuO ₄) ₂ . The U _{ij} are defined as $-2\pi^2 (U_{11}h^2a^{*2} + U_{22}k^2b^{*2} + U_{33}l^2c^{*2} + U_{12}hka^*b^* + U_{13}hla^*c^* + U_{23}klb^*c^*)$	49
Table 3.13	Selected bond lengths (Å) for LT- and HT-K ₃ Na(RuO ₄) ₂ and for Rb ₃ Na(RuO ₄) ₂	52
Table 3.14	M-O bond lengths at room temperature and phase transition temperatures of some compounds crystallising in the glaserite type of structure	55
Table 3.15	Neél-Temperatures and shortest Ru-Ru distances in some alkali ruthenates	57
Table 3.16	Crystallographic data and details on the structure determination of Na ₂ RuO ₃	59
Table 3.17	Atomic coordinates and isotropic displacement parameters U _{eq} of the two hypothetical phases of Na ₂ RuO ₃ (see text for explanation). U _{eq} is defined as one third of the trace of the orthogonalised U _{ij} tensor	59
Table 3.18	Selected bond lengths (Å) for Na ₂ RuO ₃ with standard deviations in parentheses	60
Table 4.1	Crystallographic data and details on the structure determination of K ₂ OsO ₅	67
Table 4.2	Atomic coordinates and isotropic displacement parameters U _{iso} in Å ² of K ₂ OsO ₅ , U _{iso} is defined as $\exp[-8\pi^2 U(\sin^2\theta/\lambda^2)]$	67
Table 4.3	Anisotropic displacement parameters for K ₂ OsO ₅ . The U _{ij} are defined as $-2\pi^2 (U_{11}h^2a^{*2} + U_{22}k^2b^{*2} + U_{33}l^2c^{*2} + U_{12}hka^*b^* + U_{13}hla^*c^* + U_{23}klb^*c^*)$	68
Table 4.4	Selected bond lengths (Å) for K ₂ OsO ₅	70
Table 4.5	Selected bond angles for K ₂ OsO ₅	70
Table 4.6	Crystallographic data and details on the structure determination of K ₂ NaOsO _{5.5}	76
Table 4.7	Atomic coordinates and isotropic displacement parameters U _{iso} in Å ² of K ₂ NaOsO _{5.5} , U _{iso} is defined as $\exp[-8\pi^2 U(\sin^2\theta/\lambda^2)]$	76
Table 4.8	Anisotropic displacement parameters for K ₂ NaOsO _{5.5} . The U _{ij} are defined as $-2\pi^2 (U_{11}h^2a^{*2} + U_{22}k^2b^{*2} + U_{33}l^2c^{*2} + U_{12}hka^*b^* + U_{13}hla^*c^* + U_{23}klb^*c^*)$	76
Table 4.9	Selected bond lengths (Å) for K ₂ NaOsO _{5.5}	77
Table 4.10	Crystallographic data and details on the structure determination of Na ₃ OsO ₅	81

Table 4.11	Atomic coordinates and isotropic displacement parameters U_{iso} in \AA^2 of Na_3OsO_5 with standard deviations in parenthesis; U_{iso} is defined as $\exp[-8\pi^2 U(\sin^2\theta/\lambda^2)]$	82
Table 4.12	Anisotropic displacement parameters for Na_3OsO_5 . The U_{ij} are defined as $-2\pi^2 (U_{11}h^2a^{*2} + U_{22}k^2b^{*2} + U_{33}l^2c^{*2} + U_{12}hka^*b^* + U_{13}hla^*c^* + U_{23}klb^*c^*)$	82
Table 4.13	Selected bond lengths (\AA) and angles ($^\circ$) for Na_3OsO_5	84
Table 4.14	Crystallographic data and measurement details on the structure determination of CsOsO_4 from single crystal analysis	89
Table 4.15	Rietveld refinement of powder data of CsOsO_4	89
Table 4.16	Atomic coordinates and isotropic displacement parameters U_{iso} in \AA^2 of CsOsO_4 from single crystal and powder refinements.....	90
Table 4.17	Anisotropic displacement parameters for CsOsO_4 from single crystal refinement. The U_{ij} are defined as $-2\pi^2 (U_{11}h^2a^{*2} + U_{22}k^2b^{*2} + U_{33}l^2c^{*2} + U_{12}hka^*b^* + U_{13}hla^*c^* + U_{23}klb^*c^*)$	90
Table 4.18	Selected bond lengths (\AA) and angles ($^\circ$) for CsOsO_4 from single crystal and powder refinements	93
Table 4.19	Crystallographic data and details on the structure determination of $\text{K}_3\text{NaOs}_2\text{O}_9$	97
Table 4.20	Atomic coordinates and isotropic displacement parameters U_{iso} in \AA^2 of $\text{K}_3\text{NaOs}_2\text{O}_9$ with standard deviations in parenthesis; U_{iso} is defined as $\exp[-8\pi^2 U(\sin^2\theta/\lambda^2)]$	98
Table 4.21	Anisotropic displacement parameters for $\text{K}_3\text{NaOs}_2\text{O}_9$. The U_{ij} are defined as $-2\pi^2 (U_{11}h^2a^{*2} + U_{22}k^2b^{*2} + U_{33}l^2c^{*2} + U_{12}hka^*b^* + U_{13}hla^*c^* + U_{23}klb^*c^*)$.	98
Table 4.22	Selected bond lengths (\AA) and angles ($^\circ$) for $\text{K}_3\text{NaOs}_2\text{O}_9$	99
Table 5.1	Rietveld refinement of neutron powder data of $\text{Sr}_2\text{CrOsO}_6$ at 773 K.....	105
Table 5.2	Atomic coordinates and isotropic displacement parameters U_{iso} in \AA^2 of $\text{Sr}_2\text{CrOsO}_6$, U_{iso} is defined as $\exp[-8\pi^2 U(\sin^2\theta/\lambda^2)]$ at 773 K.....	105
Table 5.3	Selected bond lengths (\AA) for $\text{Sr}_2\text{CrOsO}_6$ at 773 K.....	105

List of Abbreviations

a. u.: arbitrary units

CMR: Colossal Magneto Resistance

HT: High Temperature

RT: Room Temperature

EDX: Energy Dispersive X-ray spectrometry

XPS: X-ray Photoelectron Spectroscopy

DTA: Differential Thermal Analysis

TG: Thermogravimetry

MS- Mass Spectrometry

DSC: Differential Scanning Calorimetry

PSD: Position Sensitive Detector

SQUID: Spin Quantum Interference Device

T_N : Néel Temperature

T_C : Curie Temperature

(s): strong

(m): medium

(w): weak

Å: Angstrom

K: Kelvin

θ : Theta temperature in Kelvin

T: Tesla

References

- [1] A. F. Holleman, E. Wiberg, Inorganic Chemistry, 1st English edition, **2001**.
- [2] A. West, Solid State Chemistry and its applications, Wiley, New York, **1984**.
- [3] V. M. Goldschmidt, Str. Nor. Vidensk-Akad. Oslo, **1926**, 1, 1.
- [4] R. D. Shannon, Acta Crystallogr., Sect. A, **1976**, A32, 751
- [5] R.von Helmolt, J. Wecker, B. Holzapfel, L. Schultz, K. Samwer, Phys. Rev. Lett., **1993**, 71, 2331.
- [6] K. Chahara, T. Ohno, M. Kasai, Y. Kozono, Appl. Phys. Lett., **1993**, 63, 1990.
- [7] S. Jin, T. Tiefel, M. MacCormack, R. Fastnacht, R. Romesh, L. Chen, Science, **1994**, 264, 413.
- [8] K. I. Kobayashi, T. Kimura, H. Sawada, K. Tekura, Y. Tokura, Nature, **1998**, 395, 677.
- [9] N. S. Rogado, J. Li, A. Sleight, M. A. Subramanian, Adv. Mater., **2005**, 17, 2225.
- [10] M. A. Pena, J. L. G. Fierro, Chem. Rev. **2001**, 101, 1981.
- [11] J. G. Bednorz, K. A. Müller, Z. Phys. B: Condens. Matter, **1986**, 64, 189.
- [12] R. Hoppe, R. Homann, Naturwissenschaften, **1966**, 53, 501.
- [13] D. Kissel, R. Hoppe, Z. Anorg. Allg. Chem., **1988**, 559, 40.
- [14] N. A. Ezerskaya, I. N. Kiseleva, I. F. Golovneva, Koord. Khim., **1990**, 16, 1127.
- [15] D. -Y. Jung, P. Gravereau, G. Demazeau, Eur. J. Solid State Inorg. Chem., **1993**, 30, 1025.
- [16] D. -Y. Jung, G. Demazeau, J. Solid State Chem., **1995**, 115, 447.
- [17] Hk. Müller-Buschbaum, Z. Anorg. Allg. Chem., **2005**, 631, 1005.
- [18] G. Demazeau, High Pressure Chemical Synthesis, Elsevier, **1989**, Chapter 5, 101.
- [19] Y. M. Kiselev, Y. D. Tretiyakov, Russ. Chem. Rev., **1999**, 68, 365.
- [20] H. Flood, T. Forland, Acta Chem. Scand., **1947**, 1, 592.
- [21] H. Lux, Elektrochem., **1939**, 45, 303.
- [22] R. C. Weast, Handbook of Chemistry and Physics, 64th ed., CRC-Press Inc., **1983-84**.

- [23] W. Schlenk, A. Thal, Ber. Dtsch. Chem. Ges., **1913**, 46, 2840.
- [24] E. R. Wölfel, Theorie und Praxis der Röntgenstrukturanalyse, 3rd ed., Vieweg, Braunschweig, **1987**.
- [25] H. Krischner, B. Koppelhuber Bitschnau, Röntgenstrukturanalyse und Rietveldmethode, 5th ed., Vieweg, Braunschweig, **1994**.
- [26] W. Massa, Kristallstrukturbestimmung, 2nd ed., Teubner, Stuttgart, **1996**.
- [27] G. H. Stout, L. H. Jensen, X-ray Structure Determination, 2nd ed., Wiley & Sons, New York, **1989**.
- [28] K. Brandenburger, Crystal-Impact, Diamond V 2.1, Program for Displaying Crystal Structures, Bonn, **1998**.
- [29] ICSD, Inorganic Crystal Structure Database, FIZ Karlsruhe.
- [30] ICDD-JCPDS, Joint Committee on Powder Diffraction Standards, Swartmore, USA.
- [31] Stoe & Cie, WinXPOW, Version 1.2, Darmstadt, **2001**
- [32] Raytest-Isotopenmeßgeräte-GmbH, Software: Aida 2.0, **1998**.
- [33] H. M. Rietveld, J. Appl. Crystallogr., **1969**, 2, 65.
- [34] J. E. Post, Reviews in Mineralogy: Modern Powder Diffraction Vol. 20, Washington D. C., USA, **1989**, S278.
- [35] A. C. Larson, R. B. von Dreele, GSAS (Generalized Structure Analysis System), Los Alamos National Laboratory Report LAUR 86-748, Los Alamos National Laboratory; Los Alamos, NM, **1994**, 86.
- [36] J. Rodriguez-Carvajal, Program: Fullprof 2000, CEA-CNRS, **2000**.
- [37] J. Rodriguez-Carvajal, Physica B, **1993**, 192, 55.
- [38] Stoe & Cie, X-Area: Software for IPDS, Version 1.16, Darmstadt, **2002**.
- [39] Siemens-Analytical-X-ray-Instruments, SMART32, Version 5.618: Program for data collection, Madison, WI, USA, **1997**.
- [40] Stoe & Cie, X-RED: Data reduction for STADI4 and IPDS, Version 1.22, Darmstadt, **2001**.
- [41] Siemens-Analytical-X-ray-Instruments, SAINT32, Version 6.02: Program for data reduction, Madison, WI, USA, **1999**.
- [42] Stoe & Cie, X-SHAPE: Crystal Optimisation for Numerical Absorption Correction Version 1.06, Darmstadt, **1999**.

-
- [43] G. M. Sheldrick, Bruker-AXS, SADABS, Version 2.0: Area Detector Absorption Correction, Madison, WI, USA, **2001**.
- [44] G. M. Sheldrick, SHELXS97, a program for the solution of crystal structures, computer program, Universität Göttingen, Germany, **1997**.
- [45] G. M. Sheldrick, Bruker-AXS, SHELXTL, Version 6.12: Program for the Solution of Structures, Madison, WI, USA, **2001**.
- [46] A. Altomare, G. Cascarano, C. Giacovazzo, G. Guagliardi, A. G. G. Moliterni, M. C. Burla, G. Polidori, M. Camili, R. Spagna, SIR97 - a package for crystal structure solution by direct methods and refinement, Computer program, Dip. Geomineralogico, University of Bari, Italy, **1997**.
- [47] V. Petricek, M. Dušek, JANA2000 - crystallographic computing system, Institute of Physics, Academy of the Czech Republic, Praha, **2000**.
- [48] E. Krumova, M. I. Aroyo, J. H. Perez-Mato, J. M. Igartua, S. Ivantchev, Pseudo-A Program for a Pseudosymmetry Search, Acta Crystallogr., Sect. A, **2000**, 56 Suppl. Issue, 144; <http://www.cryst.ehu.es>.
- [49] P. Fischer, G. Frey, M. Koch, M. Könnecke, V. Pomjakushin, J. Schefer, R. Thut, N. Schlumpf, R. Bürge, U. Greuter, S. Bondt, and E. Berruyer, Physica B, **2000**, 276-278, 146.
- [50] P. Fischer, L. Keller, J. Schefer, and J. Kohlbrecher, Neutron News, **2000**, 11, 19.
- [51] P. E. Selwood, Magnetochemistry, 2nd ed., Interscience, New York, **1956**.
- [52] C. J. Smithells, Metals Reference Book, Butterworth & Co, London, **1967**.
- [53] A. Wert, R. M. Thomson, Physics of Solids, McGraw-Hill, New York, **1964**.
- [54] S. Chandra, "Superionic Solids - Principles and Applications", Amsterdam, **1981**.
- [55] M. Pompetzki, Dissertation, Universität Bonn, **2003**.
- [56] U. Köhler, Dissertation, Universität Hannover, **1987**.
- [57] U. Henseler, M. Jansen, Sigma-Messung: Ein Programm zur Auswertung von elektrischen Messungen an Festkörpern, Bonn, **1996**.
- [58] U. Henseler, M. Jansen, Sigma-Auswertung: Ein Programm zur Auswertung von elektrischen Messungen an Festkörpern, Bonn, **1996**.
- [59] B. A. Boukamp, Equivalent Circuit (EQUIVCRT.PAS), Version 4.55: The Computer Assisted Electrochemical AC-Immitance Data Analysis System, University of Twente, Niederlande, **1997**.

- [60] S. E. Livingstone, *The Chemistry of Ru, Rh, Pd, Os, Ir and Pt*, Pergamon Texts in Inorganic Chemistry, **1973**, Volume 25.
- [61] J. L. Howe, *J. Am. Chem. Soc.*, **1901**, 23, 777.
- [62] J. L. Howe, F. N. Mercer, *J. Am. Chem. Soc.*, **1925**, 47, 2926.
- [63] R. J. Meyer, E. Pietsch, *Gmelins Handbuch Der Anorganischen Chemie*, **1938**, No. 63, Ru, 8 Auflage, Verlag Chemie.
- [64] S. N. Putilin, E. V. Antipov, O. Chmaissem, M. Marezio, *Nature*, **1993**, 362, 226.
- [65] M. J. Davis, M. D. Smith, K. E. Stitzer, H.-C. zur Loye, *J. Alloys Compd.*, **2003**, 351, 95
- [66] W. R. Gemmil, M. D. Smith, H.-C. zur Loye, *Inorg. Chem.*, **2004**, 43, 4254.
- [67] P. Horsch, M. Sofin, M. Mayr, M. Jansen, *Phys. Rev. Lett.*, **2005**, 94, 076403.
- [68] M. L. Foo, W. L. Lee, T. Siegrist, G. Lawes, A. P. Ramirez, N. P. Ong, R. J. Cava, *Mater. Res. Bull.*, **2004**, 39, 1663.
- [69] J. Darriet, *Acta Crystallogr., Sect. B*, **1974**, 30, 1459.
- [70] I. S. Shaplygin, V. B. Lazarev, *Russ. J. Inorg. Chem.*, **1980**, 25 (12), 1837.
- [71] K.A. Regan, Q. Huang, R. J. Cava, *J. Solid State Chem.*, **2005**, 178, 2104.
- [72] J. Darriet, Jean Galy, *Bull. Soc. Fr. Min. Cristallogr.*, **1974**, 97, 3.
- [73] K. A. Regan, Q. Huang, M. Lee, A. P Ramirez, R. J. Cava, *J. Solid State Chem.*, **2005**, 179, 193.
- [74] M. O. Elout, W.G. Haije, W. J. A. Maaskant, *Inorg. Chem.*, **1988**, 27, 610.
- [75] T. C. Brunold, H. U. Güdel, *Inorg. Chem.*, **1997**, 36, 2084.
- [76] K. Nakamoto, *Infrared and Raman Spectra of Inorganic and Coordination Compounds*, 4th edition, Wiley New York, **1986**.
- [77] W. P. Griffith, *J. Chem. Soc. [London] A*, **1968**, 1663.
- [78] J. Weidlein, U. Müller, K. Dehnicke, *Schwingungsfrequenzen II, Nebengruppen-elemente*, Georg Thieme Verlag Stuttgart; New York, **1986**, 82.
- [79] P. Coppens, in *Crystallographic Computing*, ed. F. R. Ahmed, S. R. Hall and C. P. Huber, Munksgaard, Copenhagen, Denmark, **1970**, 255.
- [80] L. N. Becka, R. J. Poljak, *An. Asoc. Quim. Argent.*, **1958**, 46, 204.
- [81] D. Fischer, R. Hoppe, *Z. Anorg. Allg. Chem.*, **1990**, 591, 87.

- [82] D. Fischer, R. Hoppe, *Z. Anorg. Allg. Chem.*, **1992**, 617, 37.
- [83] D. Fischer, R. Hoppe, *Z. Anorg. Allg. Chem.*, **1991**, 601, 41.
- [84] T. Hansen; Proceedings of the IXth ECSSC, Stuttgart, Germany, **2003**, 02-06 Sept.
- [85] K. M. Mogare, D. Sheptyakov, R. Bircher, H. –U. Güdel, M. Jansen, *Eur. Phys. J B*, **2006**, *accepted*.
- [86] D. Fischer, Universität Gießen, Dissertation, **1992**.
- [87] M. T. Weller, M. J. Pack, N. Binsted, S. E. Dann, *J. Alloys Compd.*, **1999**, 282 76.
- [88] F. Daniel, J. Moret, E. Philippot, M. Maurin, *J. Solid State Chem.*, **1977**, 22, 113.
- [89] B. Kratochvíl, L. Jenšovský, *Acta Crystallogr., Sect. B*, **1977**, 33, 2596.
- [90] W. Klein, J. Curda, E.-M. Peters, M. Jansen, *Z. Anorg. Allg. Chem.*, **2005**, 631, 723.
- [91] B. Gossner, *Neues Jahrb. Mineral. Abt. A Beilageband*, **1928**, 57, 89.
- [92] A. Helms, W. Klemm, *Z. Anorg. Allg. Chem.*, **1939**, 242, 33.
- [93] K. M. Mogare, K. Friese, W. Klein, M. Jansen, *Z. Anorg. Allg. Chem.*, **2004**, 630, 547.
- [94] D. Fischer, R. Hoppe, K. M. Mogare, M. Jansen, *Z. Naturforsch., B: Chem. Sci.*, **2005**, 60, 1113.
- [95] K. Okada, J. Oosaka, *Acta Crystallogr., Sect. B*, **1980**, 36, 919.
- [96] J. Fábry, T. Breczewski, V. Petříček, *Acta Crystallogr., Sect. B*, **1993**, 49, 826.
- [97] J. Díaz-Hernández, J. M. Mañes, M. J. Tello, A. López-Echarri, T. Breczewski, I. Ruiz-Larrea, *Phys. Rev. B: Condens. Matter*, **1996**, 53, 14097.
- [98] T. Fukami, R. H. Chen, *Acta Phys. Pol., A*, **1998**, 94,795.
- [99] P. B. Moore, *Am. Mineral.*, **1973**, 58, 32.
- [100] W. Eysel, *Am. Mineral.*, **1973**, 58, 736.
- [101] P. B. Moore, *Bull. Mineral.*, **1981**, 104, 536.
- [102] K. Friese, M. I. Aroyo, C. L. Folcia, G. Madariaga, T. Breczewski, *Acta Crystallogr., Sect. B*, **2001**, 57, 142.
- [103] G. Madariaga, T. Breczewski, *Acta Crystallogr., Sect. C*, **1990**, 50, 2019.
- [104] J. Fábry, T. Breczewski, G. Madariaga, *Acta Crystallogr., Sect. B*, **1994**, 50, 13.

- [105] J. Fábry, V. Petříček, P. Vaněk, I. Císařová, *Acta Crystallogr., Sect. B*, **1997**, 53, 596.
- [106] M. S. Belkhiria, S. Laaribi, A. Ben Hadj Amara, M. Ben Amara, M., *Ann. Chim.*, **1998**, 23, 117.
- [107] W. Abriel, F. Rau, K.-J. Range, *Mater. Res. Bull.*, **1980**, 15, 1099.
- [108] L. Pontonnier, M. Caillet, S. Aléonard, *Mater. Res. Bull.*, **1972**, 7, 799.
- [109] N. Arumugam, M. Sofin, M. Jansen, *Z. Kristallogr., New Cryst. Struct.*, **2005**, 220, 531.
- [110] W. Urland, R. Hoppe, *Z. Anorg. Allg. Chem.*, **1972**, 392, 23.
- [111] G. Kreuzberg, F. Stewner, R. Hoppe, *Z. Anorg. Allg. Chem.*, **1970**, 379, 242.
- [112] M. Jansen, R. Hoppe, *Z. Anorg. Allg. Chem.*, **1973**, 397, 279.
- [113] R. Scholder, G. Schatz, *Angew. Chem.*, **1963**, 75, 417; *Angew. Chem. Int. Ed.*, **1963**, 2, 264.
- [114] S. Yonezawa, Y. Muraoka, Y. Matsushita, Z. Hiroi, *J. Phys.: Condens. Matter*, **2004**, 16, L9.
- [115] S. M. Kazakov, N. D. Zhigadlo, M. Bruehwiler, B. Batlogg, J. Karpinski, *Supercond. Sci. Technol.*, **2004**, 1169.
- [116] S. Yonezawa, Y. Muraoka, Z. Hiroi, *J. Phys. Soc. Jpn.*, **2004**, 73, 1655.
- [117] M. Wakeshima, Y. Hinatsu, *Solid State Commun.*, **2005**, 136, 499.
- [118] K. E. Stitzer, M. D. Smith, H.-C. zur Loye, *Solid State Sci.*, **2002**, 4, 311.
- [119] W. Levason, M. Tajik, M. Webster, *J. Chem. Soc. Dalton Trans.*, **1985**, 1735.
- [120] L. O. Avtomyan, V. G. Andrianov, M. A. Porai-Kohits, *Zh. Strukt. Khim.*, **1962**, 3, 685.
- [121] R. K. Murmann, C. L. Barnes, *Z. Krist. - New Cryst. Struct.*, **2002**, 217, 303.
- [122] S. Ahlert, W. Klein, O. Jepsen, O. Gunnarsson, O. K. Andersen, M. Jansen, *Angew. Chem.* 2003, 115, 4458, *Angew. Chem. Int. Ed.*, **2003**, 42, 4322.
- [123] H. C. Jewiss, W. Levason, M. Tajik, M. Webster, N. P. C. Walker, *J. Chem. Soc., Dalton Trans.*, **1985**, 199.
- [124] J. R. Plaisier, R. A. G. de Graaff, D. J. W. Ijdo, *Mater. Res. Bull.*, **1995**, 30, 1249.
- [125] J. P. Besse, G. Baud, G. Lévassieur, R. Chevalier, *Acta Crystallogr., Sect. B*, **1979**, 35, 1756.

- [126] M. S. Schriewer, W. Jeitschko, *J. Solid State Chem.*, **1993**, 107, 1.
- [127] T. Hansen, A. Le Bail, Y. Laligant, *J. Solid State Chem.*, **1995**, 120, 223.
- [128] G. Nowogrocki, F. Abraham, J. Trehoux, D. Thomas, *Acta Crystallogr., Sect. B*, **1976**, 32, 2413.
- [129] W.R. Gemmill, M. D. Smith, R. Prozorov, H. C. zur Loye, *Inorg. Chem.*, **2005**, 44, 2639.
- [130] T. Betz, R. Hoppe, *Z. Anorg. Allg. Chem.*, **1985**, 524, 17.
- [131] E. Vielhaber, R. Hoppe, *Z. Anorg. Allg. Chem.*, **1992**, 610, 7.
- [132] E. Zintl, G. Brauer, *Z. Elektrochemie*, **1935**, 41, 297.
- [133] K. M. Mogare, W. Klein, M. Jansen, *Acta Crystallogr., Sect. E*, **2006**, 62, i52.
- [134] B. Ivanov-Emin, *Russ. J. Inorg. Chem. (Engl. Transl.)*, **1983**, 28, 704.
- [135] E. Bilger, J. Pebler, R. Weber, K. Dehnike, *Z. Naturforsch., B: Chem. Sci.*, **1984**, 39, 259
- [136] R. Hoppe, D. Fischer, J. Schneider, *Z. Anorg. Allg. Chem.*, **1999**, 625, 1135.
- [137] J. Beintema, *Z. Kristallographie, Kristallogeometrie, Kristallphysik, Kristallchemie*, **1937**, 97, 300.
- [138] G. Meyer, R. Hoppe, *Z. Anorg. Allg. Chem.*, **1976**, 420, 40.
- [139] R. W. James, *Proc. R. Soc. A*, **1925**, 109, 598.
- [140] K. -J. Range, P. Rögner, *Z. Naturforsch., B: Chem. Sci.*, **1992**, 47, 1513.
- [141] P. Rögner, K. -J. Range, *Z. Naturforsch., B: Chem. Sci.*, **1993**, 48, 685.
- [142] E. Gebert, S. W. Peterson, A. H. Jr.Reis, E. H. Appelman, *J. Inorg. Nucl. Chem.*, **1981**, 43, 3085.
- [143] H. J. Berthold, H. G. Baethge, B. G. Hoelscher, H. J. Kienert, W. Ludwig, J. M. Molepo, R. Wartchow, *Phase Transition*, **1992**, 38, 127.
- [144] A. W. Sleight, J. Longo, R. Ward, *Inorg. Chem.*, **1962**, 1, 245
- [145] K. E. Stitzer, M. D. Smith, W. R. Gemmill, H. C. zur Loye, *J. Am. Chem. Soc.*, **2002**, 124, 13877
- [146] S. J. Kim, M. D. Smith, J. Darriet, H. C. zur Loye, *J. Solid State Chem.*, **2004**, 177, 1493.
- [147] M. Lufaso, H. C. zur Loye, *Inorg. Chem.*, **2005**, 44, 9143.

- [148] M. Lufaso, H. C. zur Loye, *Inorg. Chem.*, **2005**, 44, 9154.
- [149] K. E. Stitzer, A.E.Abed, M. D. Smith, Matthew J. Davis, S. J Kim, J. Darriet, H. C. zur Loye, *Inorg. Chem.*, **2003**, 42, 947.
- [150] K. -J. Range, A. Atzesdorfer, *Z. Naturforsch., B: Chem. Sci.*, **1998**, 48, 237.
- [151] A. Arulraj, K. Ramesha, J. Gopalakrishnan, C. N. R. Rao, *J. Solid State Chem.*, **2000**, 155, 233.
- [152] T. S. Chan, R. S. Liu, G. Y. Guo, S. F. Hu, J. G. Lin, J. -F, Lee, L. -Y Jang, C. -R. Chang, C. Y. Huang, *Solid State Commun.*, **2004**, 131, 531.
- [153] H. Kato, T. Okuda, Y. Okimoto, Y. Tomioka, Y. Takenoya, A. Ohkubo, M. Kawasaki, Y. Tokura, *App. Phys. Lett.*, **2002**, 81, 328.
- [154] R. Macquart, S. J. Kim, W. R. Gemmill, J. K. Stalick, Y. Lee, T. Vogt, , H. C. zur Loye, *Inorg. Chem.*, **2005**, 44, 9676.
- [155] Y. Krockenberger, K. M. Mogare, M. Jansen, L. Alff, *in preparation*.

Appendix

$\text{Na}_3\text{OsO}_4(\text{OH})_2$

The compound was obtained while exploring the Na-Os-O system in autoclaves. Only a few sodium hydroxy osmates are reported in the literature among which the crystal structure of only one compound is reported, $\text{Na}_2\text{OsO}_4(\text{OH})_2\text{H}_2\text{O}$ (Nevskii et. al., *Dokl. Akad. Nauk*, **1982b**, 266, 1138). The number of crystal structures containing osmium in higher oxidation states is still very limited. A few of them are explored in this work, described in respective sections and one was reported in the literature (Ahlert et. al. *Angew. Chem. Int. Ed.*, **2003**, 42, 4322). Only a small amount of $\text{Na}_3\text{OsO}_4(\text{OH})_2$ was obtained containing a couple of crystals and thus complete characterisation was not possible. X-ray diffraction and the crystal structure solved by single crystal analysis are discussed herein.

Synthesis

$\text{Na}_3\text{OsO}_4(\text{OH})_2$ was obtained via the reaction of sodium hydroxide and osmium powder in a molar ratio of 3:1 applying an elevated oxygen pressure. The mixture was filled in a gold crucible and annealed in an autoclave at 673 K for 48 hours and 28 MPa of oxygen pressure. The compound is hygroscopic.

X-ray diffraction

X-ray diffraction powder data were collected with a Stoe Stadi-P diffractometer (Cu $K\alpha_1$, Ge monochromator, linear PSD) in steps of 0.01° over a 2θ range from 0 to 90° for approximately 24 h with the samples sealed in glass capillaries of 0.2 mm diameter. The measured X-ray pattern is shown in Figure 1. The pattern shows weak reflections of an unknown phase with an amount close to the detection limit.

Single crystal data were collected on a Bruker AXS with SMART-CCD (APEX) $\text{MoK}\alpha_1$ Graphite monochromator, semi-empirical absorption correction with the program SADABS. Further information concerning the data collection and processing, the crystallographic parameters, as well as details on structure solution and refinement are given in Table 1. The atomic coordinates and isotropic displacement parameters are given in Table 2, while the anisotropic displacement parameters are listed in Table 3.

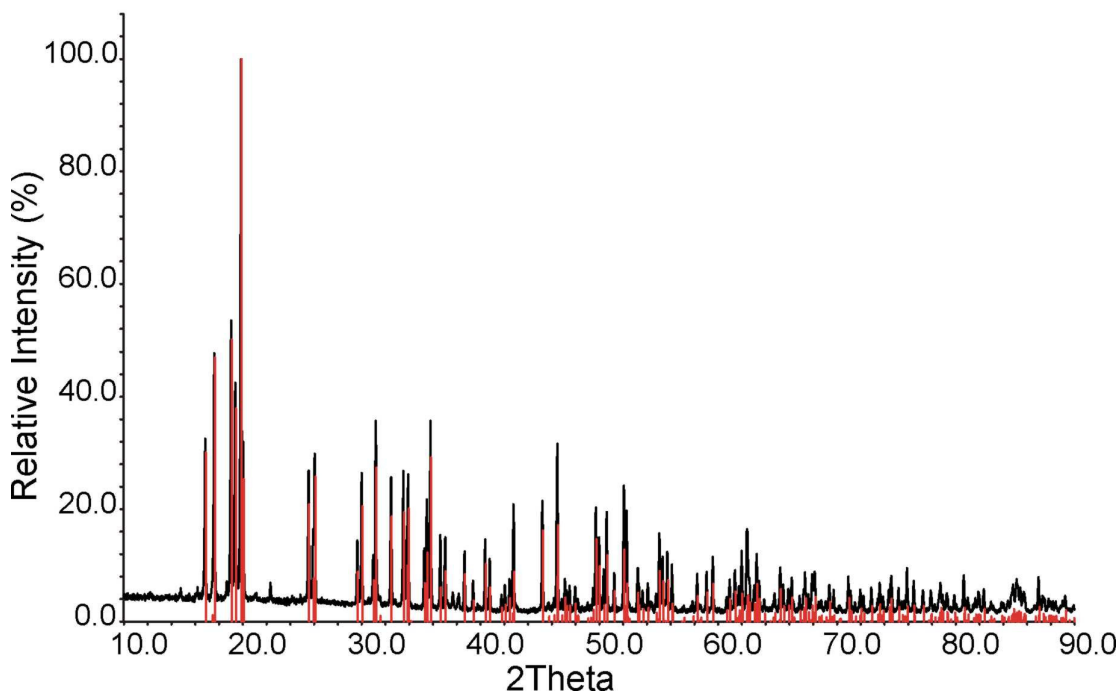


Figure 1 Measured X-ray pattern of $\text{Na}_3\text{OsO}_4(\text{OH})_2$ (red reflections are the data from single crystal analysis, few unindexed reflections is an unknown impurity phase)

Table 1 Crystallographic data and details on the structure determination of $\text{Na}_3\text{OsO}_4(\text{OH})_2$

Crystal System	Monoclinic
Space group	$P2_1/m$ (no. 11)
Lattice parameters	$a = 5.7605(5) \text{ \AA}$, $b = 9.2995(7) \text{ \AA}$ $c = 5.9485(2) \text{ \AA}$ and $\beta = 118.168(2)^\circ$
Formula units	2
Cell volume	$280.92(4) \text{ \AA}^3$
X-ray density	$4.223 \text{ g}\cdot\text{cm}^{-3}$
Molar mass	1017.51
Diffractometer	Bruker SMART-APEX CCD
Wavelength	Mo-K α ($\lambda = 0.71073 \text{ \AA}$)
Monochromator	Graphite
Temperature	293 K
Data collection mode	ω -Scan
2θ -region	$3.88^\circ < 2\theta < 29.99^\circ$
$hkl_{\min} - hkl_{\max}$	$-8 \leq h \leq 8$; $-13 \leq k \leq 13$; $-8 \leq l \leq 8$
Number of measured reflections	3488
Number of unique reflections	871
Number of reflections $> 2\sigma$	814
Number of parameters	57
R_{int}	0.065
Absorption coefficient	22.89 mm^{-1}
Extinction coefficient	0.0032(9)
$R(F)(\text{obs})$, $R(F)(\text{all})$	0.0235, 0.0258
$R_w(F^2)(\text{obs})$, $R_w(F^2)(\text{all})$	0.0519, 0.0528
Goodness-of-fit (all data)	1.031
Difference density min./max.	$-1.617 / 1.941 \text{ e} \cdot \text{\AA}^{-3}$

Table 2 Atomic coordinates and isotropic displacement parameters U_{iso} in \AA^2 of $\text{Na}_3\text{OsO}_4(\text{OH})_2$ with standard deviations in parenthesis; U_{iso} is defined as $\exp[-8\pi^2 U(\sin^2\theta/\lambda^2)]$

Atom	Wy.Pos.	x	y	z	Uiso
Na1	2e	0.0207(6)	1/4	-0.0150(6)	0.0293(7)
Na2	4f	0.4553(4)	0.0719(2)	0.7497(4)	0.0242(4)
Os	2e	0.78102(5)	1/4	0.38101(4)	0.01551(11)
O1	2e	1.1298(10)	1/4	0.521(1)	0.0227(10)
O2	2e	0.4624(10)	1/4	0.1089(10)	0.0278(12)
O3	4f	0.7415(7)	0.1095(4)	0.5701(7)	0.0242(8)
O4	4f	0.8200(7)	0.0850(4)	0.1473(7)	0.0217(7)
H	4f	0.958(13)	0.039(6)	0.241(11)	0.019(15)

Table 3 Anisotropic displacement parameters for $\text{Na}_3\text{OsO}_4(\text{OH})_2$. The U_{ij} are defined as $-2\pi^2 (U_{11}h^2a^* + U_{22}k^2b^* + U_{33}l^2c^* + U_{12}hka^*b^* + U_{13}hla^*c^* + U_{23}klb^*c^*)$

Atom	U_{11}	U_{22}	U_{33}	U_{12}	U_{13}	U_{23}
Na1	0.0198(14)	0.044(2)	0.0265(14)	0.00000	0.0132(12)	0.00000
Na2	0.0204(10)	0.0277(11)	0.0229(9)	-0.0027(8)	0.0088(8)	-0.0002(8)
Os	0.01277(14)	0.01910(18)	0.01401(14)	0.00000	0.00579(10)	0.00000
O1	0.017(2)	0.024(3)	0.023(2)	0.00000	0.0059(19)	0.00000
O2	0.018(2)	0.037(3)	0.023(2)	0.00000	0.006(2)	0.00000
O3	0.0270(19)	0.025(2)	0.0245(16)	0.0002(15)	0.0153(15)	0.0052(15)
O4	0.0179(19)	0.0245(19)	0.0184(15)	-0.0004(15)	0.0050(13)	-0.0036(14)

Structure description

According to single crystal analysis $\text{Na}_3\text{OsO}_4(\text{OH})_2$ contains osmium(VII), coordinated octahedrally by four oxide and two hydroxide ions. The crystal structure consists of $\text{OsO}_4(\text{OH})_2$ octahedra with the two OH groups coordinated in cis position. The octahedron is distorted in such a way that the edge formed by the OH groups is considerably longer [3.068(8) \AA] than the remaining ones [2.491(6)–2.767(6) \AA] and the osmium atom is shifted off-center due to the longer bond lengths to the hydroxide ligands (see Table 4). The Os - O distances vary depending upon on their functionality. The shortest Os - O distances are found to the O1 and O2 atoms which are not involved in hydrogen bonding, while O3 is involved as an acceptor in the O3ⁱⁱ --- H - O4 hydrogen bond to neighbouring OsO_6 octahedron and shows a slightly longer bond length to the osmium atom. The hydroxide groups form hydrogen bonds to two neighbouring octahedra, thus each octahedron participates in four bonds. The hydrogen bonds, shown in Figure 2, are unsymmetrical and nearly linear. The octahedra which are connected by these hydrogen bonds form chains parallel to [010], see Figure 3. The chains of OsO_6 octahedra are separated by sodium cations coordinated by a square pyramid of five (Na1) and an irregular polyhedron of six O atoms (Na2).

The hydrogen atoms were located in a difference Fourier map after anisotropic refinement of all non-hydrogen atoms and refined without any constraints in the final refinement, resulting in plausible O-H bond distances. The highest peak and the deepest hole in the final difference Fourier map are 0.82 and 0.86 Å, respectively, for the Os atom.

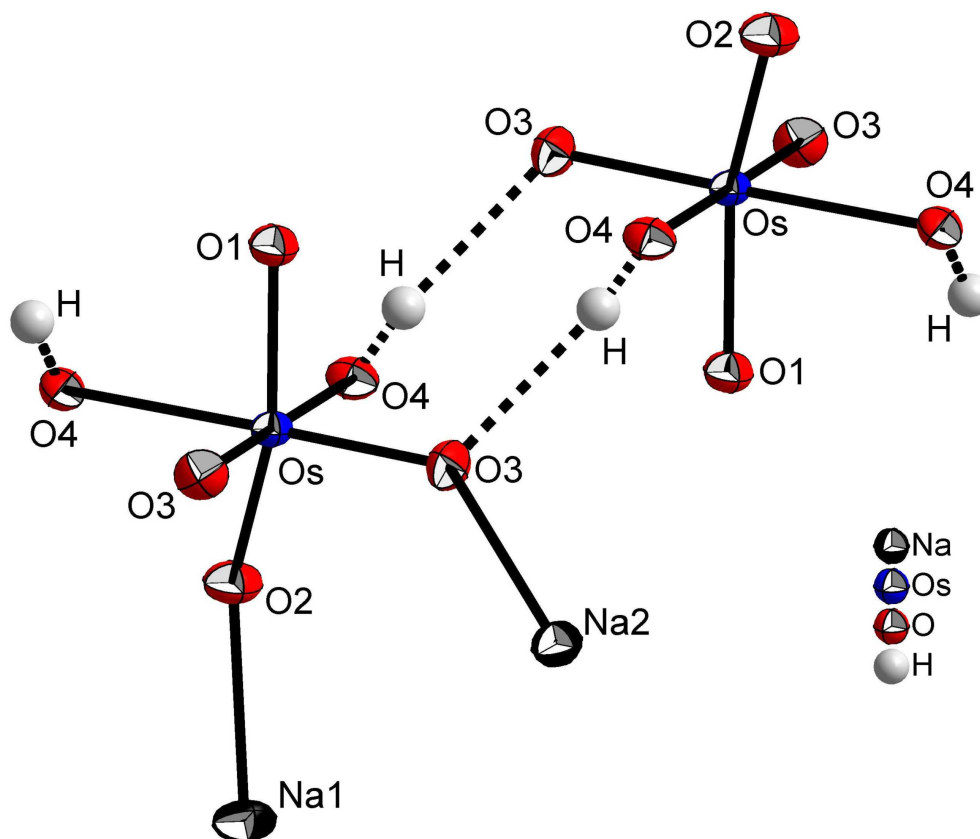


Figure 2 Details of the crystal structure of $\text{Na}_3\text{OsO}_4(\text{OH})_2$, displacement ellipsoids are shown at the 50 % probability level

Table 4 Selected bond lengths (Å) and angles (°) for $\text{Na}_3\text{OsO}_4(\text{OH})_2$

Atoms	Distances	Atoms	Distances
Os–O1	1.775(5)	Na2–O1	2.388(4)
Os–O2	1.784(5)	Na2–O2	2.689(5)
Os–O3	1.807(4) [2x]	Na2–O3	2.376(5)
Os–O4	2.152(4) [2x]	Na2–O3 ^x	2.390(5)
H–O4	0.84(6)	Na2–O4 ^{ix}	2.309(4)
H–O3	2.08(6)	Na2–O4 ^x	2.436(5)
Na1–O1	2.945(6)	Na1–Os ^v	3.183(3)
Na1–O2	2.291(6)	Na2–Os ^x	3.228(2)
Na1–O3	2.577(5) [2x]		
Na1–O4	2.383(5) [2x]		
Angles			
O2–Os–O3	98.92(2)		
O4–H–O3	169(5)		

Symmetry codes: (i) $x, 0.5-y, z$; (ii) $2-x, -y, 1-z$; (iii) $-1+x, 0.5-y, z$; (iv) $-1+x, y, z$; (v) $-1+x, y, -1+z$; (vi) $-1+x, 0.5-y, -1+z$; (vii) $x, 0.5-y, -1+z$; (viii) $x, y, -1+z$

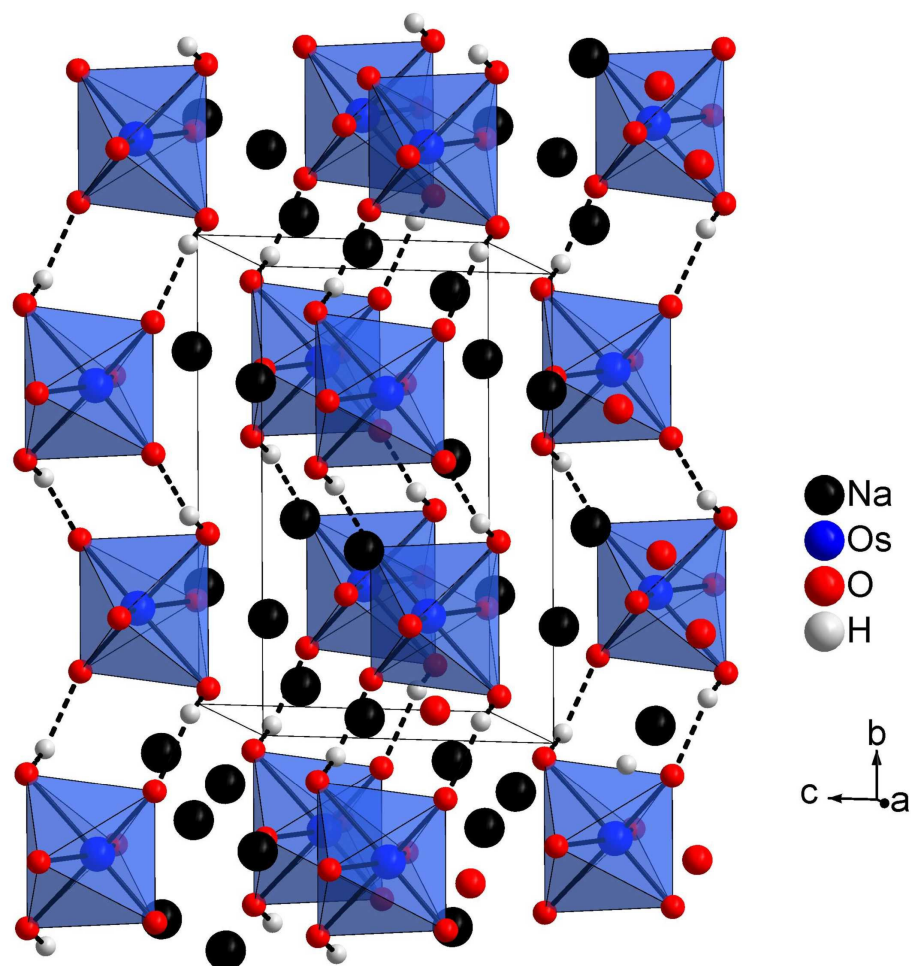


Figure 3 Crystal structure of $\text{Na}_3\text{OsO}_4(\text{OH})_2$, view along $[-100]$. OsO_6 octahedra, Na and H atoms are drawn. Dashed lines represent the hydrogen bonds

Among many postulated hydroxy-(oxo-)osmates, few of them have been structurally characterised (Nevskii et. al., *Dokl. Akad. Nauk*, **1982a**, 266, 628; Nevskii et. al., *Dokl. Akad. Nauk*, **1983**, 270, 1392; Jewiss et. al., *J. Chem. Soc. Dalton Trans.*, **1985**, 199; Murmann et. al., *Z. Kristallogr. New Cryst. Struct.*, **2002**, 217, 303). Within this family, only one sodium compound, formulated as $\text{Na}_2\text{OsO}_4(\text{OH})_2\text{H}_2\text{O}$ has been published without the location of any H atoms. Although this compound contains osmium in the oxidation state +VIII, the shape of the OsO_6 octahedron is very similar to that found in $\text{Na}_3\text{OsO}_4(\text{OH})_2$, that is, with one considerably longer edge and an off-center osmium atom with similar bond lengths. Nevertheless, the three dimensional arrangement of the octahedra and the most probable situation of H bonds is completely different.

Acknowledgements

I would like to express my sincere thanks to my doctoral advisor Prof. Dr. Dr. h. c. Martin Jansen for providing me with the opportunity to work under his guidance. Many thanks are due to him for the interesting topic, motivation and constant support.

My sincere thanks to Dr. Wilhelm Klein, my group leader, for his constant support throughout the course of my Ph.D., for crystal structure solutions and valuable discussions.

I would also like to thank Dr. Juergen Nuss, Dr. Karen Friese and Mrs. Eva Peters for crystal structure measurements. Thanks to Dr. Christian Oberndorfer for the DTA/TGA measurements. Thanks to Mr. Werner Giering for initial single crystal precession photographs, Mr. Ewald Schmidt for specific heat measurements and Mr. Klaus Hertel for Heat-Guinier measurements.

Special thanks to Mr. Jan Curda, his presence in the lab keeps cool atmosphere during work. Thanks to Mr. Claus Muehle for his valuable support during the initial stages of my Ph.D.. Thanks to Dr. Paul Balog and Mr. Frank Falkenberg for high pressure experiments.

Thanks to Mr. Wolfgang Koenig and Ms. Marie-Luise Schreiber for Infrared measurements. Thanks to Mr. Armin Schulz for the Raman measurements. Thanks to Mrs. Eva Bruecher and Mrs. Gisela Siegle for Magnetic and Conductivity measurements, respectively.

Thanks to my laboratory colleagues Andrei, Angelika, Carsten, Denis, Denitsa, Hanne, Martin SD, Nachi, Olivier Leynaud, Sanjeev, Stefan, my office colleagues Anton, Sascha and Timo for providing an enthusiastic atmosphere during work. Thanks to Ms. Jeanette Knapp for helping me in the administrative work. Thanks to all the Jansen group members for their constant support, encouragement and helpful discussions.

I am grateful to Prof. H. U. Guedel and Roland Bircher for their inputs in the magnetic studies of Na_2RuO_4 . Thanks are due to Dr. Denis Sheptyakov for neutron diffraction studies of Na_2RuO_4 . Thanks to Mr. Yoshiharu Krockenberger and Prof. Dr. Lambert Alff for the collaborative work on double perovskites.

I would also like to thank my dissertation committee members, Prof. Dr. Thomas Schleid and Prof. Dr. Helmut Bertagnolli.

My thanks are due to the Max Planck Society for the doctoral fellowship during my entire Ph.D. tenure.

My hearty thanks to Dr. S. Vijayalakshmi (IIT Bombay) for her constant motivation and support to pursue my PhD.

I am indebted to Dr. T. P. Makhija and Dr. J. M. Gadgil for their support during my undergraduate studies.

Thanks to all my friends, from Dahivali, Karjat, Mumbai, Pune, all the Indians at MPI and especially all my Buesnauer Platz friends for providing me a nice environment during my stay in Stuttgart.

Finally, I would like to thank my parents, grand parents, brothers and sisters for their encouragement and support. I feel myself lucky to be part of a family of such great and simple people. I express my deepest gratitude to my great uncle (Late) Madhav kaka for his love and affection throughout my life. Last but not the least I thank The Almighty for giving me an opportunity to explore and experience this wonderful world.

List of Publications

- **K. M. Mogare**, K. Friese, W. Klein, M. Jansen, Syntheses, Crystal structures and Properties of two new sodium ruthenates(VI), Na_2RuO_4 and Na_2RuO_3 , *Z. Anorg. Allg. Chem.* 630 (2004), 547.
- **K. M. Mogare**, W. Klein and M. Jansen, Synthesis, Crystal structure and Properties of potassium osmate(VIII), K_2OsO_5 , *Z. Anorg. Allg. Chem.* 631 (2005), 468.
- D. Fischer, R. Hoppe, **K. M. Mogare**, M. Jansen, Syntheses, Crystal Structures and Magnetic Properties of Rb_2RuO_4 and K_2RuO_4 , *Z. Naturforsch.* 60b (2005), 1113.
- **K. M. Mogare**, W. Klein and M. Jansen, Trisodium dihydroxy tetraoxo-osmate(VII), $\text{Na}_3\text{OsO}_4(\text{OH})_2$, *Acta Cryst. E* 62, (2006), i52-i54.
- **K. M. Mogare**, W. Klein, E. M. Peters, M. Jansen, $\text{K}_3\text{Na}(\text{RuO}_4)_2$ and $\text{Rb}_3\text{Na}(\text{RuO}_4)_2$, two new ruthenates with glaserite structure, *Solid State Sci.*, (2006), 8, 500.
- **K. M. Mogare**, D. Sheptyakov, R. Bircher, H.-U. Güdel, M. Jansen, Neutron Diffraction Study of the Magnetic Structure of Na_2RuO_4 , *Eur. Phys. J B*, (2006), *accepted*.
- **K. M. Mogare**, W. Klein H. Schilder, H. Lueken, M. Jansen, Synthesis and Crystal Structure and Magnetic Properties of Na_3OsO_5 , *Z. Anorg. Allg. Chem.*, (2006), *accepted*.
- **K. M. Mogare**, W. Klein, M. Jansen, Synthesis and Characterisation of two new alkali metal osmium perovskites, *manuscript in preparation*.
- **K. M. Mogare**, W. Klein and M. Jansen, Synthesis and Crystal Structure of Cesium oxo-osmate(VII), *manuscript in preparation*.
- Y. Krockenberger, **K. M. Mogare**, M. Jansen, Lambert Alff, A new perovskite displaying robust ferromagnetism, *manuscript in preparation*.

AUTOBIOGRAPHICAL STATEMENT

Kailash M. Mogare

Education

- Ph. D. in Inorganic Chemistry** **2002-2006**
Max-Planck Institute for Solid State Research, Stuttgart, Germany
Dissertation: 'New Ternary and Quaternary Metal Oxides of Ruthenium and Osmium'
Advisor: Prof. Dr. Dr. h. c. Martin Jansen
- M. Sc. in Polymer Chemistry** **1998-2000**
N. Wadia College, University of Pune, Pune, India
Thesis: 'Swelling Behaviour of Hydrogels'
Advisor: Dr. J. M. Gadgil
- B. Sc. in Chemistry** **1995-1998**
CHM College, University of Mumbai, Mumbai, India

Work Experience

- Research Assistant,** **2000-2001**
National Chemical Laboratories (NCL), Pune, India
Project: 'Water Soluble Polymers for Enhanced Oil Recovery'
- Research Assistant,** **2001-2002**
Indian Institute of Technology-Bombay (IIT), Mumbai, India
Project: 'Characterisation of Compounds using Gas Chromatography and Mass Spectrometry'

Personal Information

Date of Birth: 28th March 1978
Nationality: Indian
Gender: Male